High Resolution Polarimetric Imaging of Biophysical Objects Using Synthetic Aperture Radar

Sarah Caroline Mellows BROWN MEng(Hons)

A thesis submitted for the degree of Doctor of Philosophy

Department of Electronic and Electrical Engineering

University of Sheffield

November 1998

Summary

A synthetic aperture microwave near-field system is used to image biophysical objects in order to investigate the nature of radar-target interaction.

Two different imaging algorithms for focusing data collected over a two-dimensional planar aperture are investigated. The first of these is the single frequency backward propagation technique which is mathematically simple to implement and provides a high degree of resolution. Secondly, a multifrequency development of the backward propagation algorithm is presented and derived from two separate perspectives. This latter algorithm, known as the auto-focusing algorithm, requires no information about the range of the target from the aperture. Full characterisation by simulation of both algorithms is carried out and different filtering techniques are investigated.

The backward propagation algorithm is applied to the polarimetric imaging of three different leafless trees and a sugar beet plant at the X-band frequency of 10GHz. The images so produced demonstrate that the backscattered signal is dependent on the orientation of individual tree elements with respect to the polarisation. Furthermore, multiple scattering terms can be identified within the structure of the tree.

The auto-focusing algorithm is applied to the polarimetric imaging of two trees at 10GHz and repeat measurements are made over several months. As with the single frequency measurements, the backscattered signal is dependent on the orientation of individual tree elements relative to the polarisation. The relative contributions from the leaves and branches of the trees to the backscattered signal are assessed and found to be seasonally dependent.

Measurements are also carried out to investigate the variation of backscatter from a beech tree with varying incidence angle. It is demonstrated that at small angles of incidence, the leaves are the dominant source of backscatter but at large incidence angles, the branches and trunk of the tree have the greatest contribution.

Acknowledgements

I would like to thank my supervisor Dr John Bennett for his help and guidance on this project and his constant enthusiasm for the work. Thanks also to Dr Tony Whitaker for his help with the practical measurements and watering the trees!

Acknowledgements are also due to Dr Peter Mitchell of the Department of Animal and Plant Sciences for his helpful suggestions with regard to physiology of trees.

The work was funded by the University of Sheffield and latterly by the Engineering and Physical Sciences Research Council.

Publications

Brown, S.C.M. and Bennett, J.C., "High Resolution Microwave Imaging of the Backscatter of a Small Tree and its Variation with Incidence Angle", *International Geoscience and Remote Sensing Symposium*, 6-10 July 1998, Seattle, USA. pp. 2026-2028.

Bennett, J.C., Quegan, S., Morrison, K. and Brown, S.C.M., "The Representation of Vegetation Scattering Components in Models: Theory and Comparison", *Progress in Electromagnetics Research Symposium*, 13-17 July 1998, Nantes, France.

Brown, S.C.M. and Bennett, J.C., "High Resolution Microwave Polarimetric Imaging of Small Trees", *IEEE Transactions on Geoscience and Remote Sensing* (in press).

List of Principle Symbols and Abbreviations

a	Radius of a sphere
A	Effective area of receive antenna
B	Bandwidth of data
c	Speed of light, $3x10^8 ms^{-1}$
C( ), c( )	Cosine weighting function
df	Frequency sampling interval
dx, dy	Spatial sampling intervals
D	Aperture size, or the distance between two targets
D( )	Measured data
f	Frequency
f_o	Centre frequency
f_p	Frequency of correction factor peak
G( )	Correction Factor
G_t( )	Gain of transmit antenna
H( )	Propagation transfer function
HH	Horizontal transmit and receive polarisation
HV	Horizontal transmit and vertical receive polarisation
ISAR	Inverse Synthetic Aperture Radar
M( )	Actual recorded data
n_a, n_b	Probe aperture size in multiples of wavelength
N	Size of Fourier data array or number of point targets
P	Power transmitted by a radar
P( )	Pattern of probe antenna
r, R	Distance of target from aperture
R_{ff}	Far-field distance
RCS	Radar Cross Section
s, s_x, s_y	Spatial frequencies
S_c	Maximum spatial frequency used by auto-focusing algorithm
S_{max}	Maximum spatial frequency of a system
S( )	Frequency response of a system

SAR	Synthetic Aperture Radar
t	Time
U( )	Data transmitted from, or reflected by a target
U'( )	Corrected data
VH	Vertical transmit and horizontal receive polarisation
VV	Vertical transmit and receive polarisation
z	Range from aperture plane to target plane
α, β, γ	Direction cosines
γ	Depth of focus
δ	Resolution
$\delta( )$	Delta Function
Δ	Half the bandwidth of the data, or difference between f_o and f_p
λ	Wavelength
σ	Radar Cross Section
ΔR	Range resolution

Additional symbols are defined as introduced.

Table of Contents

Chapter 1

Introduction

1.1 Background

In recent years, the use of airborne and spaceborne sensors to generate detailed images of the Earth's surface has become commonplace. The data generated from these systems has a multiplicity of applications in many diverse fields ranging from weather forecasting to defence intelligence and from cartography to the monitoring of land use. Such systems have traditionally used optical wavelengths with great success but these are limited by their inability to see through cloud cover. This is a particular problem in northern latitudes and monsoon areas. Optical systems are also unable to see at night, further limiting their usefulness [1].

An alternative solution is to use active microwave systems such as synthetic aperture radar (SAR) to generate grey scale and false colour images of the Earth's surface. These systems can be used twenty four hours a day and in virtually all weather conditions. However, the images generated by these SAR systems represent the amount of microwave radiation or backscatter reflected from the Earth's surface and may not relate to what would be seen by the human eye. For example, a surface which appears rough to optical light may appear smooth to microwaves [2]. Consequently, the resulting data is very difficult to interpret. This is particularly true for biophysical targets such as agricultural crops and forested areas where the backscattered return depends on two main factors. Firstly, the backscatter is affected by the characteristics of the vegetation, such as the moisture content, the size, shape and orientation of the leaves and branches along with the underlying soil conditions. Secondly, the parameters of the radar system such as system wavelength, polarisation and the look angle used also need to be considered [3].

Remote sensing is not the only field in which it is important to understand the interaction between electromagnetic energy and vegetation. In radio communications, such as mobile phone systems and microwave links, it is vital to understand the nature of transmission through vegetation as well as the scattering from it. Such effects need to be considered when planning radio links so that site shielding, dead zones and multipath interference can be avoided.

1.2 Project Aims and Objectives

It is the aim of this work to investigate the nature of the interaction between biophysical objects and the microwave signals employed in radar systems. In particular, the scattering associated with forests and woodland areas are examined by generating high resolution near-field images of small individual trees at the X-band frequency of 10GHz. By so doing, the contributions of individual tree elements to the radar backscatter and their dependence on the system polarisation can be determined. The nature of scattering within the tree structure is also investigated. By monitoring individual trees over several months, the effects of seasonal changes, such as defoliation, in the backscattered return can also be observed. The effect of look angle on the backscatter is also examined. In addition, limited work to investigate the transmission through trees is carried out to determine the absorbing and forward scattering elements of such structures.

1.3 Review of Microwave Measurements of Trees

Extensive work has already been carried out into the scattering nature of individual and large groups of trees at a wide range of frequencies. These have examined both the reflection from, and the transmission through, different species of trees at different times during the year.

1.3.1 Scattering Measurements

Most reflection measurements have been carried out using ground based scatterometer measurements, based either indoors or outside, which can provide coarse information relating to the tree canopy and structure. The highest resolution achieved with such systems has been in the order of several wavelengths [4] which limits the ability of the system to examine individual elements of the tree structure. Nevertheless, these scatterometer measurements have proved to be useful in determining many characteristics of radar-tree interaction.

Backscatter levels obtained from individual trees vary greatly depending on the frequency of the illuminating radar. Measurements made at L, S, C and X bands have shown that as the frequency increases the ability of the microwave signal to penetrate

into a tree canopy decreases. Therefore, at low frequencies, backscatter from the branches dominates whilst at high frequencies the contributions of the leaves are more important [5][6][7]. This, however, is highly dependent on the structure of the tree itself. Consequently, at X band frequencies the backscatter is dependent on both the leaves and branches in a sparse canopy and just on the leaves for a more dense canopy [5][6].

The polarisation of the radar system used has also been found to be a factor in determining the backscattered levels from trees. It has been shown that like polarisations of vertical transmit and receive (VV) and horizontal transmit and receive (HH) systems produce relatively similar results for most situations, with variations of just a few decibels being common [5][6][8]. However, this is again dependent on the tree architecture and canopy density and Mougin *et al.* [7] have demonstrated that the VV and HH responses can be significantly different especially at the top of a tree where the branch structure is fairly simple.

The case of cross-polar responses (VH and HV) is somewhat different with much lower backscatter levels being recorded [6]. Cross-polar backscatter appears to be dependent not only on tree architecture and canopy density but also on the type of tree. At X-band, broadleaf and conifer trees have been shown to have very different cross-polar responses due to the different shapes of their leaves. On the whole, leaves are less dominant in X-band cross-polar returns [6] but the more needle-like the leaves, the greater the depolarisation of the incident signal [5][10].

Measurements to determine the azimuthal variations have been carried out by moving the position of transmitter and receiver around a group of trees [11][12]. These have demonstrated that the backscatter from trees has a fairly uniform angular distribution with variations in the region of 5dB about a mean value being recorded. Azimuthal variations in bistatic scattering [10][13] have also been shown to have a standard deviation of up to 6dB for like polarisations and 5dB for cross-polar results, although there are conflicting suggestions on whether this is due to tree structure or not.

The variation associated with different incidence angles has also been investigated for various coniferous trees but with mixed results. Some results [5][6] show little

variation with incidence angle whilst others show a decrease in backscatter with increasing incidence angle [8][7]. The lack of uniformity in these results is caused by differences in tree structure between the different trees and tree species examined. Ulaby and Dobson [9] have collated a number of published results and shown that there is indeed a fall of up to 5 dB in the backscatter levels as the incidence angle is increased. Such a result correlates well with the angular variation in backscatter obtained from a theoretical random surface [14].

There is considerable interest in the ability of radars to identify defoliated trees especially in large commercial forested areas. Consequently, a number of attempts have been made to establish the backscatter variations between foliated and defoliated trees. Most of these experiments have been made by measuring a healthy tree and then removing all its leaves and re-measuring it. These results have shown that backscatter usually decreases when a conifer tree is defoliated [6][15] although this is not always so evident for broad-leaved trees [16]. However, it has been suggested [17] that the manual removal of leaves and needles does not truly represent the defoliation that occurs due to disease or insect damage, hence questioning the results obtained for manual defoliation.

It is also important to understand the seasonal variations that occur in radar backscatter. Most results taken from plantations and forests so far seem to indicate that seasonal variations are no more than 5 or 6 dB in their entirety [11][12][13]. In particular, results obtained by Al-Nuaimi *et al.* [13] by illuminating an apple orchard from near ground level indicates that backscatter is highest when the trees are leafless. This is due to the fact that leaves are good absorbers as well as scatterers of microwave energy [4]. C-band measurements made over Canadian forests by Ahern [21] support this but Ulaby *et al.* [3] suggests that the backscatter from deciduous trees increases when they are in leaf. It is not just the degree of leaf coverage that determines the backscatter. Changes in the stem water content of a tree [18][19] may also affect the backscatter levels from both deciduous and coniferous trees. Furthermore, measurements indicate that the climate in which a tree grows may strongly affect this seasonal water content [20]. It has also been found that there is a diurnal variation of radar backscatter from trees in the region of 2 to 4dB [22][23].

Diurnal variations are induced by changes in the water content in the tree stem and leaves, and varies depending on the tree species and the weather [20][23][24].

It should be noted that data recorded over forested areas are subject to the weather conditions at the time of the measurements. Recent precipitation over an area often causes increases in backscatter especially of young plants and agricultural fields. However, the response from many tree canopies seems to decrease when wet since attenuation of the canopy layer is increased [25].

Other work has used scatterometer measurements to examine to backscatter from artificial trees [26][27][28]. Such an arrangement enables accurate repeatability and allows the parameters of the tree to be precisely defined and easily altered. However, most of the artificial trees had polycarbonate trunks and branches with aluminium leaves. Such an arrangement does not accurately simulate a real tree and generates some spurious results.

In the last couple of years, near-field imaging systems have been employed to generate two and three dimensional images of tree targets to aid understanding of the nature of radar-tree interaction. By employing such techniques, the scattering centres of tree targets can be more readily identified than if a scatterometer based system is used. Lang, Fortuny *et al.* [29][30][31] used a combination of ISAR and SAR techniques, discussed later in the chapter, to generate three dimensional images of a balsam fir tree. The measurements were made in an anechoic chamber at frequencies between 1 and 5.5GHz and demonstrated nature of scattering from different parts of the tree. In contrast, Kim *et al.* [32] used traditional ISAR techniques to generate two dimensional images of a maple tree at Ka band. They measured the tree with and without its leaves at VV polarisation, and were able to show that the backscatter of a bare tree was dominated by the response from the trunk but the leaves were the dominant scatterers when they were present.

1.3.2 Transmission Measurements

Most measurements of the transmission through, and the absorption by trees have been carried out in relation to mobile phone, broadcasting and other communications links.

Typically, measurements have been performed on orchards and small woods to determine the absorption rate through a canopy of trees. It is apparent that at small distances into the tree canopy, the attenuation rate is high, but at greater depths the attenuation rate is greatly reduced [11][13][33][34]. This is due to the fact that at small depths into the canopy, propagation is primarily along a strongly attenuated direct path whilst at greater depths, forward scattering becomes the dominant mode of operation.

It has also been shown that this transition between high and low attenuation rates occurs at a much greater distance into the canopy for leafless trees that it does for trees in leaf [11][33].

Measurements made at different heights have illustrated that attenuation close to the ground is less than higher up since tree trunks attenuate the signal less and forward scatter more than the tree canopy does [11][13][33]. Equally, measurements made at different times of the year show that in winter and spring, when trees are leafless, the attenuation through a wood or orchard is lower than when the trees are in leaf [11][13][34][35]. This would indicate that leaves are good absorbers of microwave energy.

Experiments have also established that attenuation increases with increasing frequency since at higher frequencies the leaves appear to be larger. Furthermore, there is little difference between HH and VV attenuation results and substantial depolarisation occurs at large vegetation depths [33].

As far as tree structure and species are concerned, it is clear that trees with a denser canopy have a greater attenuation on the propagated signal [10]. Measurements, made on whole orchards or copses of trees indicate that conifers absorb less than deciduous trees [34].

Finally, Al-Nuaimi *et al.* [35], have shown that singly distributed trees on a hilltop can actually improve a transmission path by means of forward scatter.

Much of the work on transmission measurements has been directed at finding a suitable model which will describe the attenuation of the signal at different depths within the canopy. The traditional approach is to assume that the decay is exponential

with distance into the canopy [13], although this is now considered to be unsatisfactory. A considerable amount of literature has been dedicated to finding new models [13][33][36] and to determining the suitability of existing ones [11][13][34][36][37].

1.4 Overview of Near-Field Imaging Systems

Since the aim of this work is to generate near-field images of tree targets, it is important to consider the different near-field imaging techniques that could be used.

Traditionally, most near-field imaging systems have been developed to aid investigations into the radar cross sections (RCS) of military targets [38] although there are numerous other applications. Many different imaging methods are available for this type of work and are based around four main types of imaging system. These are planar, cylindrical and spherical systems and compact ranges. Measurements are normally carried out in an anechoic chamber although a few systems are located outdoors. All near-field imaging systems use one, or a combination of two, of these systems [39] to generate and collect near-field data reflected from a target object. With the exception of compact ranges, which are not considered here, most near-field systems generate and collect data by means of a synthetic aperture. This is due to the fact that real aperture antennas are limited in resolution by their length and good azimuthal resolution can only be achieved with impractically long antennas [40]. Synthetic apertures provide higher resolution by scanning a co-located transmitter and receiver across the aperture, taking discrete measurement samples at regular intervals. In normal systems, a synthetic aperture is generated by moving the transmit and receive antennas around, or in a plane parallel to, a target. Evidently, this requires a complex control system and a high precision positioner unit. However, the problem can be circumvented by using an Inverse Synthetic Aperture Radar (ISAR) system which synthesises a synthetic aperture by the rotation of the target object about a fixed position as illustrated in Figure 1.1. The transmit and receive antennas are kept at a fixed location [41]. Since ISAR systems involve the circular motion of the target, they are equivalent to cylindrical or spherical scanning systems, depending on whether the target is rotated about one or two axes.

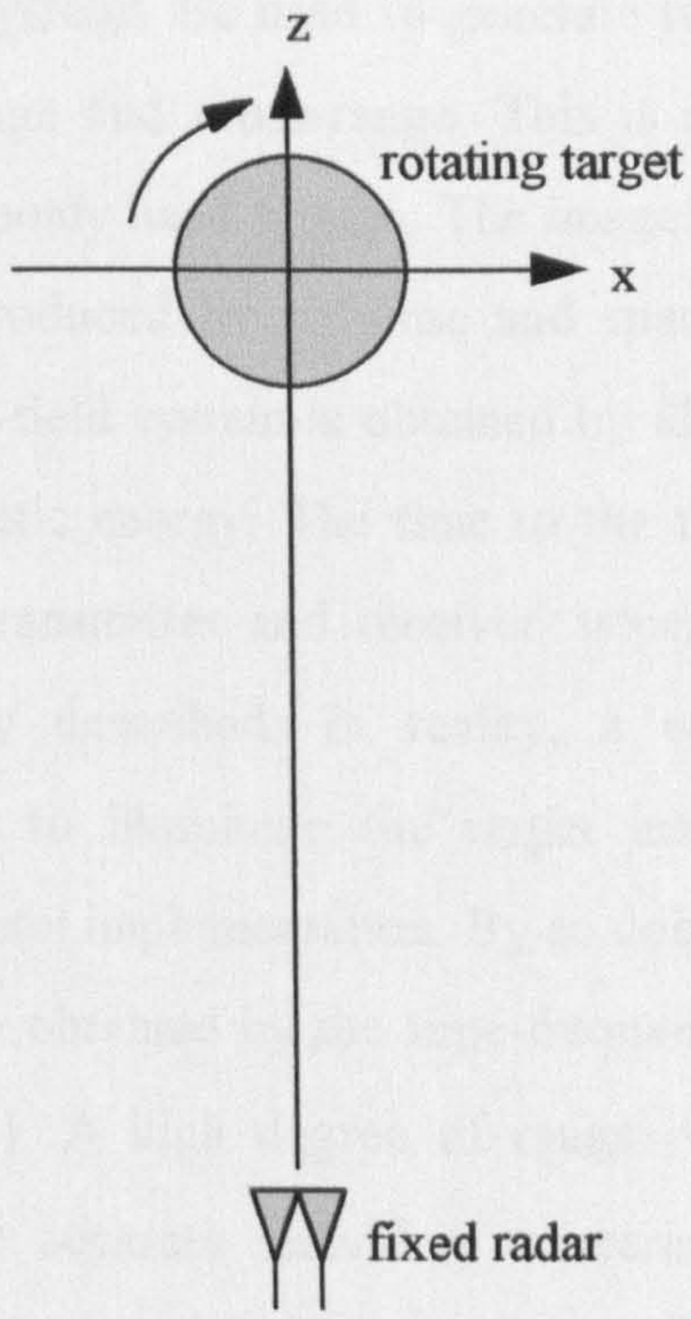

Figure 1.1 Schematic View of an ISAR Imaging System

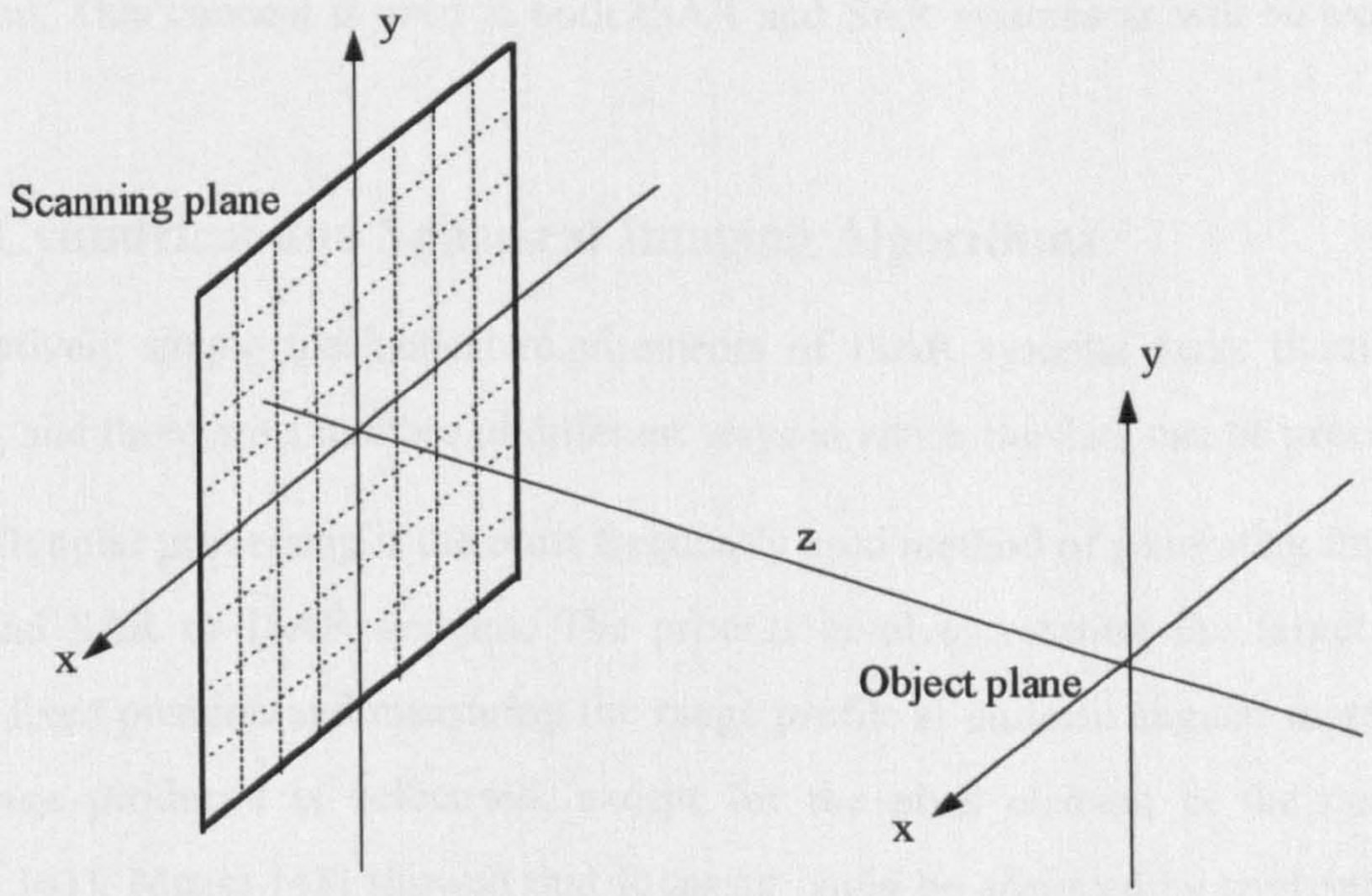

Figure 1.2 Schematic View of a Planar Near-Field Imaging System

The majority of near-field systems are used to generate two dimensional images of a target in terms of both range and cross-range. This is not always the case, but is certainly true of most commonly used system. The images produced are then directly comparable with images produced by airborne and spaceborne SAR systems. The range information in a near-field system is obtained by illuminating the target with a short pulse of electromagnetic energy. The time to the target can be measured and hence its range from the transmitter and receiver, which are considered to be co-located, can be accurately described. In reality, a series of stepped-frequency waveforms are often used to illuminate the target instead of short pulses, thus providing simpler experimental implementation. By so doing, the location of the target in the time domain is easily obtained by the time-frequency relationship provided by the Fourier Transform [42]. A high degree of range resolution, ΔR, is inevitably needed for this process to separate individual scattering centres in range. ΔR is dependent on the frequency bandwidth, B, so that

$$\Delta R = \frac{c}{2B} \tag{1-1}$$

Therefore, a wide bandwidth of data is often needed to achieve the desired range resolution. This concept is used in both ISAR and SAR systems as will be explained later.

1.4.1 Cylindrical and Spherical Imaging Algorithms

The relatively simple mechanical requirements of ISAR systems make them highly popular, and there are a number of different ways in which the data can be processed.

Range-Doppler processing is the most frequently used method of generating images in cylindrical SAR or ISAR systems. The process involves rotating the target object about a fixed position and measuring the range profile at uniform angular increments. The image produced is defocused, except for the pixel element at the centre of rotation [41]. Mensa [43] showed that focusing could be achieved by applying phase corrections to each signal sample to correct for the fact that they were displaced from the centre of rotation. However, the most straightforward way of focusing is to consider the two-dimensional data array of frequency profiles recorded for each

angular increment [44] and to perform a two dimensional Fourier transform on it. By so doing, a true down-range/cross-range image is obtained. The difficulty with this is that the data is in polar co-ordinates and the Fourier transform can only operate on Cartesian data. Nevertheless, by interpolating the data to Cartesian co-ordinates and then performing the transformation, an in-focus image can be obtained [45][46].

The cylindrical imaging scenario can also be analysed by means of tomographic processing. Tomography was originally developed for medical imaging of the human body but it can be equally well applied to radar imaging [47][48]. Tomographic projections of slices through a rotating target perpendicular to the radar line of sight can be related to an image of the target by means of the Fourier Slice Theorem [49]. In this theorem, the Fourier transform of a projection of the target is the centre-cross-section of the Fourier transform of an image of the target. [47]. Focusing of the data can be carried out in the frequency domain with a series of one dimensional Fourier transforms. However, a two-dimensional interpolation process is required in this method and it is more common to utilise a backprojection algorithm which operates in the spatial domain [47][49][50]. This allows individual one dimensional views to be merged sequentially so that each new view adds to the previously accumulated image. By using this system, in-focus imagery can be obtained with data collected at a single frequency although Mensa [51] has shown that such systems are improved if data is collected over a small bandwidth.

Another way of producing focused data from cylindrical ISAR systems is to use a system known as spherical backprojection [52][53] or coherent summation [54]. In this method, the energy reflected from a rotating target is again measured over a range of frequencies. The reflectivity of the image is determined by coherently summing the complex values of the signals from each scattering centre in the target. A focusing operator defined by the geometry of the system is applied to each scattered field measurement over a range of frequencies and angles [55][56]. This operator compensates for the changes in the amplitude and phase of the wave as it travels to and from the target object.

Fortuny [57] has recently extended this idea to a three-dimensional scenario. By rotating a target in one dimension and moving the transmit/receive antennas in an arc

over the target in another, a spherical scanning system is synthesised. The mathematics involved in focusing such a system are considerably more complex than in the cylindrical case. The advantage is that, given the use of a wide frequency bandwidth, three-dimensional images of targets can be produced.

More straightforward spherical scanning can be utilised to generate two dimensional images in a microwave eye type format [58]. In other words, the image is displayed in a horizontal cross-range against vertical cross-range format. There is no range axis since the data is recorded only at a single frequency. However, simple processing techniques used in standard cylindrical ISAR processing can be used to focus the data.

1.4.2 Linear SAR Measurements

The imaging process utilised in this work is not an ISAR system but a SAR system whereby images are generated using a vertical two-dimensional planar scanner located in an anechoic chamber as illustrated in Figure 1.2. Such a system can be analysed in terms of plane wave concepts, which are mathematically simple compared to the analysis of cylindrical and spherical systems. A brief synopsis of the principles of operation of a linear SAR system are presented here.

A plane wave can be described as a wave which has constant amplitude, phase and polarisation over a plane perpendicular to the direction of wave propagation [59]. Such a wave can never be generated in practice from a planar aperture since the energy contained in a plane wave is infinite and an infinite antenna aperture would be required to generate it. However, if a target lies within the illumination region of a large planar synthetic aperture, then it can be considered to be within the region of plane wave illumination. A mechanical positioning unit moves two small, low gain antennas, often called probe antennas, across the planar aperture. One probe transmits a spherical wave at each position along the aperture and whilst the second receives a reflected signal from a target. The sum of the signals transmitted as the probe moves over the aperture constitutes a plane wave [59]. The sum of the signals received by the second probe is generally thought of as the response of the target to plane wave illumination. Nevertheless, this is not strictly accurate. In a real array, the receiver measures the response incident across the whole aperture at one instant in time.

Therefore, the values received by the individual receiving elements are composed of signals transmitted by all elements. In a synthetic array, since each element is excited separately, the values received at the individual receiving elements are dependent only on the value transmitted from that element [43]. These differences can be observed in the mathematical equations for the signals received in both cases. Consider the case where a real aperture is modelled as an array of N elements. The data, U(x), recorded for an object located a distance r_n from the n^{th} element of a real array is then,

$$U(x) = \left[\sum_{n=1}^{N} \frac{\exp - j\left(\frac{2\pi r_n}{\lambda}\right)}{r_n} \right]^2 \qquad (1\text{-}2)$$

However, if the array elements are excited separately, as in a synthetic array, then the response is given by

$$U(x) = \sum_{n=1}^{N} \left[\frac{\exp - j\left(\frac{2\pi r_n}{\lambda}\right)}{r_n} \right]^2 \qquad (1\text{-}3)$$

Although the synthetic array clearly does not produce the same results as a real array, its use is justified since the target characteristics can still be determined from synthetically generated images. On the whole, synthetically generated images have better resolution than those generated from real arrays [43].

The near-field data recorded at a planar synthetic aperture does not produce in-focus imagery but requires the application of one of several imaging algorithms which are hereafter summarised.

The idea of using a focusing operator, discussed for cylindrical systems, is applicable to linear SAR systems, since the focusing operator is defined by the geometry of the system. Fortuny [60] and El Assad [54] have both used similar processes to generate two dimensional images.

However, the single frequency backward propagation method is perhaps the most straightforward planar near-field imaging system. Based on the angular spectrum of

plane waves [61], it is capable of imaging targets in the near field by backpropagating the wavefront of the received signal to the plane containing the target. Unfortunately it only has a very small depth of focus, severely restricting its use. Nevertheless, it is capable of producing high resolution images in a microwave eye format and acts as the basis to several other imaging algorithms. It is derived in full in Chapter 2.

The single frequency backward propagation algorithm has been extended to a multifrequency case by Bennett and Morrison [62]. By taking a set of multifrequency data they have demonstrated that the backward propagator can be applied at all frequencies to generate an in-focus image. This is achieved by converting the data to the spatial frequency domain and applying the propagator at all frequencies for a single distance from the aperture. The summation of this is converted back to the image domain and generates a single line of in-focus data. The whole process is repeated across a series of valid ranges from the aperture and hence a complete two-dimensional picture of range against cross-range is generated. The disadvantage of this system is that it requires a large bandwidth and is computationally intensive. However, it does produce an image comparable to that obtained from an airborne or spaceborne SAR system.

Finally in the 1980s, Ahmed Yamani developed a multifrequency imaging algorithm [63] from the single frequency backward propagation algorithm. This algorithm produces imagery in terms of horizontal and vertical cross-range, again generating a microwave eye type result. The uniqueness of this algorithm is that it is capable of automatically focusing an image without the need for range information. Furthermore, it requires a much smaller bandwidth than other algorithms mentioned above. This algorithm will be considered in detail in Chapter 3.

1.4.3 Choice of System

The choice of which imaging system to use for this work was governed by a number of factors. Due to the nature of the target, ISAR systems were considered to be unsuitable. This is because in ISAR systems, the target has to be rotated in azimuth and when the target is a small flexible tree, this may lead to unwanted target motion. After each angular increment it would have been necessary to wait until the target was

completely motionless before taking the next measurement. Hence, the data acquisition process would have been time consuming. Furthermore, if vertical cross-range information was required, the target would need to be rotated in elevation, which may cause the orientation of different tree components to change.

A SAR system, rather than an ISAR system, would therefore be the most sensible choice. Given the availability of a two-dimensional vertical planar scanner in an anechoic chamber, a planar SAR system was chosen for this work. In addition, by using the backward propagation algorithm, or a variant of it, data can be focused using intuitively simple mathematical processes.

1.5 Structure of Thesis

This work is divided into seven chapters of which this is the first.

Chapter 2 presents the theory of the single frequency backward propagation algorithm. The characteristics of the algorithm are investigated by simulation. This chapter, on the whole, does not present any new material.

The expansion of the backward propagation algorithm to a multifrequency auto-focusing scenario is investigated in Chapter 3. A new focusing algorithm is obtained and simulations to determine its characteristics are carried out and compared with the results from Chapter 2. The derivation of this multifrequency algorithm is new and novel although the end result is the same as that obtained by Yamani [63]. Rigorous characterisation and an understanding of the limitations of the algorithm are also new. In addition, the application of different filtering processes to the data are investigated.

Chapter 4 deals with the practical application of the backward propagation algorithm to an indoor experimental facility. Calibration of the system is explained and polarimetric purity measurements are presented. Experimental verification of the imaging algorithm is carried out and the system is applied to the imaging of various biophysical objects including several small trees. Experimental results are analysed and limitations of the algorithm are discussed. In addition, limited transmission measurements on one of the trees are carried out.

Chapter 5 considers the implementation of the auto-focusing algorithm in a real

experimental environment. In particular, the effect of the probe antennas on the final images is investigated and compensation to remove these effects is explained. Suitable probe antennas for the particular imaging geometry are designed. A description is provided of the experimental equipment and of the correction processes required to generate valid data from it. Finally, proof that the auto-focusing algorithm works correctly is presented by imaging a three-dimensional test target, and polarimetric investigations are also carried out.

The application of the auto-focusing algorithm to biophysical objects is presented in Chapter 6. Firstly, the response of a sycamore tree is measured and the auto-focusing algorithm applied to the recorded data. Different filtering procedures are applied to the focused data to determine the most appropriate technique. Results from measuring two trees, a larch and a beech tree, are then presented. The measurements are polarimetric and are measured over several months to determine any seasonal variations. The variation in backscatter with incidence angle from the beech tree is also investigated. Quantitative results are derived from the image data where appropriate.

The final chapter discusses many of the results obtained in chapters 4, 5 and 6 and attempts to draw some conclusions from them. The results obtained are compared, as far as is possible, with other published literature.

Chapter 2

Investigation of the Backward Propagation Imaging Algorithm

2.1 Introduction

The aim of this chapter is to present and develop a single frequency planar near-field system capable of imaging targets in an anechoic chamber. The focusing algorithm used, known as the backward propagation algorithm, is derived from first principles in the following sections and is based on the decomposition of recorded data into an angular spectrum of plane waves. Simulations of simple targets in both one and two dimensions are carried out to verify the validity of the algorithm and to develop a full characterisation of its properties, such as resolution and depth of focus. The response of more complex targets is also analysed along with investigations of multiple scattering within the target structure. Finally, the near-field images generated by this imaging algorithm are converted to a far-field quantity and are compared with expected radar cross section (RCS) values.

2.2 Derivation of the Backward Propagation Imaging Algorithm

All systems which generate images of a target scene work on the principles embodied in the human eye. They require an aperture across which the wavefront reflected, transmitted or emitted from an object, can be collected. This corresponds to the iris and lens in the human eye. The collected wavefront is then transformed to generate an image in the plane of the image sensor, i.e. at the retina in the case of the eye.

Electromagnetic imaging systems work on similar principles although the aperture can be used both to illuminate the target, and to the receive the wavefront reflected from it. A planar aperture provides the most straightforward way of achieving this and can be analysed by relatively simple mathematical processes. A planar synthetic aperture will be utilised for all of the following work and it is important to understand the nature of the aperture illumination and the propagation of electromagnetic energy from it. The best way of achieving this is by using the angular spectrum of plane waves [64][65][66][67] which is explained in the following section.

2.2.1 Plane Wave Propagation

In order to understand the propagation characteristics of electromagnetic waves, it is important to be able to analyse the constituent components of such waves. Fourier analysis provides a mathematically simplistic approach to achieving this in planar systems. It can be shown that if a planar complex field distribution is analysed by means of Fourier transformations, then the various spatial frequency components so generated can be identified as plane waves travelling in different directions. These components are known as the angular spectrum of plane waves. Fourier analysis is a powerful tool since a knowledge of the plane wave components at a particular point allows the field distribution at any other point in space to be calculated [61]. This is achieved by calculating the phase shift that each component has undergone in propagation to that point and then by adding the contributions of the different plane wave components.

To illustrate this, consider initially an object which is acting as a source of electromagnetic waves. The waves are received at an aperture located a distance z from the source as shown in Figure 1.2.

To quantify this, let U(x,y,0) represent the complex field distribution at the source, and let U(x,y,z) represent an unknown field distribution at a general point P with co-ordinates (x,y,z). If a two dimensional Fourier transform is applied to the field U(x,y,0) at the source, then the field can be decomposed into a series of simple exponential functions each propagating at a known angle. Therefore,

$$U(s_x, s_y, 0) = \iint U(x, y, 0).\exp\left(-j2\pi(s_x x + s_y y)\right) dxdy \qquad (2\text{-}1)$$

where s_x and s_y are the spatial frequencies in the x and y directions. Inversely, the source distribution can be described as the summation of these exponential functions, namely,

$$U(x, y, 0) = \iint U(s_x, s_y, 0).\exp\left(j2\pi(s_x x + s_y y)\right) ds_x ds_y \qquad (2\text{-}2)$$

It is also known that a unit-amplitude plane wave can be described by

$$A(x, y, z) = \exp\left(-j2\pi(\alpha x + \beta y + \gamma z)\right) \qquad (2\text{-}3)$$

where α, β and γ are direction cosines and γ is given by

$$\gamma = \sqrt{1-\alpha^2-\beta^2} \tag{2-4}$$

Thus across the plane of the source, where z = 0, a complex exponential function $\exp\left(j2\pi(s_x x + s_y y)\right)$ can be regarded as a plane wave propagating with direction cosines α, β and γ given by

$$\alpha = \lambda s_x \tag{2-5}$$

$$\beta = \lambda s_y \tag{2-6}$$

$$\gamma = \sqrt{1-(\lambda s_x)^2-(\lambda s_y)^2} \tag{2-7}$$

Consequently, equation (2-1) can be re-written in terms of its 'Angular Spectrum'

$$U\left(\frac{\alpha}{\lambda},\frac{\beta}{\lambda},0\right) = \iint U(x,y,0).\exp\left(-j2\pi\left(\frac{\alpha x}{\lambda}+\frac{\beta x}{\lambda}\right)\right)\,dxdy \tag{2-8}$$

In a similar manner, the angular spectrum of the field distribution across a plane parallel to the plane containing the source and a distance z from it is given by

$$U\left(\frac{\alpha}{\lambda},\frac{\beta}{\lambda},z\right) = \iint U(x,y,z).\exp\left(-j2\pi\left(\frac{\alpha x}{\lambda}+\frac{\beta x}{\lambda}\right)\right)\,dxdy \tag{2-9}$$

Conversely, the inverse Fourier transform shows how the measured field is composed of its angular spectrum.

$$U(x,y,z) = \iint U\left(\frac{\alpha}{\lambda},\frac{\beta}{\lambda},z\right).\exp\left(j2\pi\left(\frac{\alpha x}{\lambda}+\frac{\beta x}{\lambda}\right)\right)\,\frac{d\alpha}{\lambda}\frac{d\beta}{\lambda} \tag{2-10}$$

It is also known that the complex amplitude, U, of any electromagnetic wave propagating through space, must satisfy the Helmholtz equation, namely,

$$\nabla^2 U + k^2 U = 0 \tag{2-11}$$

If the Helmholtz equation is applied to equation (2-10) then a solution for $U\left(\frac{\alpha}{\lambda},\frac{\beta}{\lambda},z\right)$ can be given in terms of the angular spectrum of the field at the source

U(x,y,0), as shown below [61].

$$U\left(\frac{\alpha}{\lambda},\frac{\beta}{\lambda},z\right)=U\left(\frac{\alpha}{\lambda},\frac{\beta}{\lambda},0\right).\exp\left(-j\frac{2\pi z}{\lambda}\sqrt{1-\alpha^2-\beta^2}\right) \tag{2-12}$$

or in terms of spatial frequencies as

$$U\left(s_x,s_y,z\right)=U\left(s_x,s_y,0\right).\exp\left(-j\frac{2\pi z}{\lambda}\sqrt{1-\left(\lambda s_x\right)^2-\left(\lambda s_y\right)^2}\right) \tag{2-13}$$

However, this is only true if

$$(\lambda s_x)^2+(\lambda s_y)^2<1 \tag{2-14}$$

The waves produced when this condition is true are called homogeneous waves. If the reverse is true so that

$$(\lambda s_x)^2+(\lambda s_y)^2>1 \tag{2-15}$$

then the wave components will be strongly attenuated and will not travel far. These waves are known as evanescent waves.

It can be seen from equation (2-13) that the effect of propagation over a distance z is simply a change in the relative phase of each plane wave component in the field. This occurs since each plane wave component travels at a different angle and hence covers a different distance to reach a given point. The exponential term of this equation is known as the forward propagator.

This result is dependent on the sense in which plane wave propagation is taken to occur. Here plane wave propagation is taken to be in the form of exp(-jkr). However, in other literature [68] it has been taken to be exp(jkr) in which case the exponential term in equation (2-13) would be replaced by its complex conjugate.

It should also be noted that the spatial frequencies, s_x and s_y, are defined by the limits of the Fourier Transform. It is well known [69] that, if aliasing is to be avoided in near-field measurements, then the data must be sampled at intervals of, dx and dy, where

$$dx\le\frac{\lambda}{2}\quad\text{and}\quad dy\le\frac{\lambda}{2} \tag{2-16}$$

Therefore, the data in the spatial frequency domain will be limited to values S_{maxx} and S_{maxy}, which are defined as

$$S_{maxx} = \frac{1}{2dx} \quad \text{and} \quad S_{maxy} = \frac{1}{2dy} \tag{2-17}$$

for a two-sided array. For simplicity, dx and dy are always taken to be the same value in this work, and hence S_{maxx} and S_{maxy} are identical and are referred to as S_{max}.

2.2.2 Propagation as a Spatial Filter

From equation (2-13), it is possible to consider the forward propagator as a transfer function $H(s_x,s_y,z)$ as shown below.

$$H(s_x, s_y, z) = \frac{U(s_x s_y, z)}{U(s_x s_y, 0)} = \exp\left(\frac{-j2\pi z}{\lambda}\sqrt{1-(\lambda s_x)^2-(\lambda s_y)^2}\right) \tag{2-18}$$

If the distance z is at least several wavelengths long, then the evanescent waves can be ignored, yielding a transfer function,

$$H(s_x, s_y, z) = \begin{cases} \exp\left(\frac{-j2\pi z}{\lambda}\sqrt{1-(\lambda s_x)^2-(\lambda s_y)^2}\right) & s_x^2 + s_y^2 < 1/\lambda^2 \\ 0 & \text{otherwise} \end{cases} \tag{2-19}$$

Hence, propagation can be thought of as a linear spatial filter with a finite spatial frequency bandwidth. The transmission of the filter is zero outside a circular region (i.e. bandwidth) of $1/\lambda$. Inside the region the modulus of the transfer function is unity but spatial frequency dependent phase shifts are introduced. This is illustrated in Figure 2.1a for a target at a distance of z=1m from a 1m wide aperture.

2.2.3 Backward Propagation

Equation (2-13) can also be re-written as

$$U(s_x, s_y, 0) = U(s_x, s_y, z).\exp\left(j\frac{2\pi z}{\lambda}\sqrt{1-(\lambda s_x)^2-(\lambda s_y)^2}\right) \tag{2-20}$$

to obtain an expression for the angular spectrum of the field distribution at a source in terms of the angular spectrum a distance z away from it. In this equation, the complex exponential term is often called the backward propagator. Therefore, the distribution

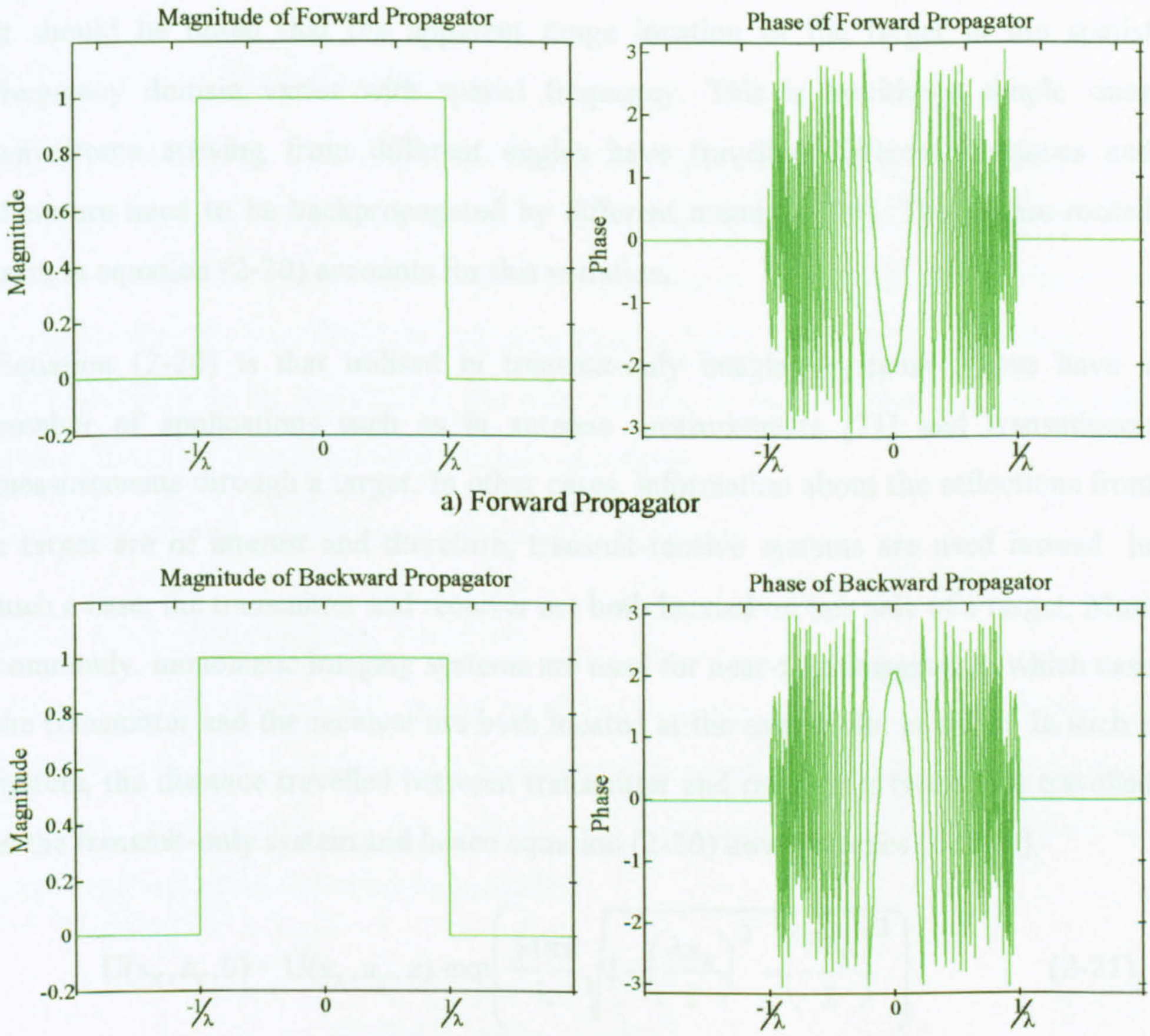

Figure 2.1 Illustration of Forward and Backward Propagators

of an unknown source can be determined by measuring the field distribution a distance z away from it, and applying the backward propagator to the angular spectrum of measured data. The process is known as backward propagation.

It should be noted that the apparent range location of the target in the spatial frequency domain varies with spatial frequency. This is intuitively simple since wavefronts arriving from different angles have travelled different distances and therefore need to be backpropagated by different amounts [70]. The square-rooted term in equation (2-20) accounts for this variation.

Equation (2-20) is that utilised in transmit-only imaging systems. These have a number of applications such as in antenna measurements [71] and transmission measurements through a target. In other cases, information about the reflections from a target are of interest and therefore, transmit-receive systems are used instead. In such a case, the transmitter and receiver are both located on one side of a target. Most commonly, monostatic imaging systems are used for near-field imaging, in which case the transmitter and the receiver are both located at the same point in space. In such a system, the distance travelled between transmitter and receiver is twice that travelled in the transmit-only system and hence equation (2-20) now becomes [63][68],

$$U(s_x, s_y, 0) = U(s_x, s_y, z).\exp\left(\frac{j4\pi z}{\lambda}\sqrt{1-\left(\frac{\lambda s_x}{2}\right)^2-\left(\frac{\lambda s_y}{2}\right)^2}\right) \qquad (2\text{-}21)$$

and the backward propagator is now

$$H^{-1}(s_x, s_y, z) = \exp\left(\frac{j4\pi z}{\lambda}\sqrt{1-\left(\frac{\lambda s_x}{2}\right)^2-\left(\frac{\lambda s_y}{2}\right)^2}\right) \qquad (2\text{-}22)$$

and is illustrated in Figure 2.1b.

The backward propagation algorithm for a transmit-receive system can be summarised as follows

i. Record data U(x, y, z) a distance z from the target

ii. Perform a forward Fourier transform to give $U(s_x, s_y, z)$

iii. Multiply by the backward wave propagator $H^{-1}(s_x,s_y,z)$ to give $U(s_x, s_y, 0)$

iv. Inverse Fourier transform to give the field distribution U(x, y, 0) in the plane of the target

2.3 System Simulation

In order to verify the validity of this backward propagation algorithm, a simulation of a suitable imaging system was generated on a Unix based computer system. Such a system enables the characteristics of the algorithm to be determined. Considerable work has already been done on this algorithm [63][67] but since it is the basis of a new algorithm, to be explained in the next chapter, it was important to simulate the system to act as a reference with this new algorithm.

All simulations are carried out at a frequency of 10GHz.

2.3.1 One Dimensional Imaging

Initially, a one dimensional planar synthetic aperture system was developed for simplicity and ideal isotropic point scatterers were used as the targets to be imaged. The data, U(x), representing the recorded field at the aperture reflected from the point scatterers was generated using the equation

$$U(x) = \sum_{n=1}^{N} \frac{\exp - j\left(\frac{4\pi r_n}{\lambda}\right)}{r_n^{\,2}} \qquad (2\text{-}23)$$

where r_n is the distance of the n^{th} point scatterer from each aperture element and N is the total number of scatterers. Hence the contributions of all N scatterers need to be summed to give the total data. The backward propagation algorithm can then be applied as described in Section 2.2.3.

Figure 2.2 illustrates the application of the backward propagation algorithm to a single point scatterer located 1.5m away from a scanning aperture. The scatterer is assumed to be infinitely small and re-radiates the energy incident on it as a spherical wavefront. The aperture is 1m in width and the frequency of operation is 10GHz. The first sidelobe levels of the reconstructed image are at -14dB. It is apparent from this

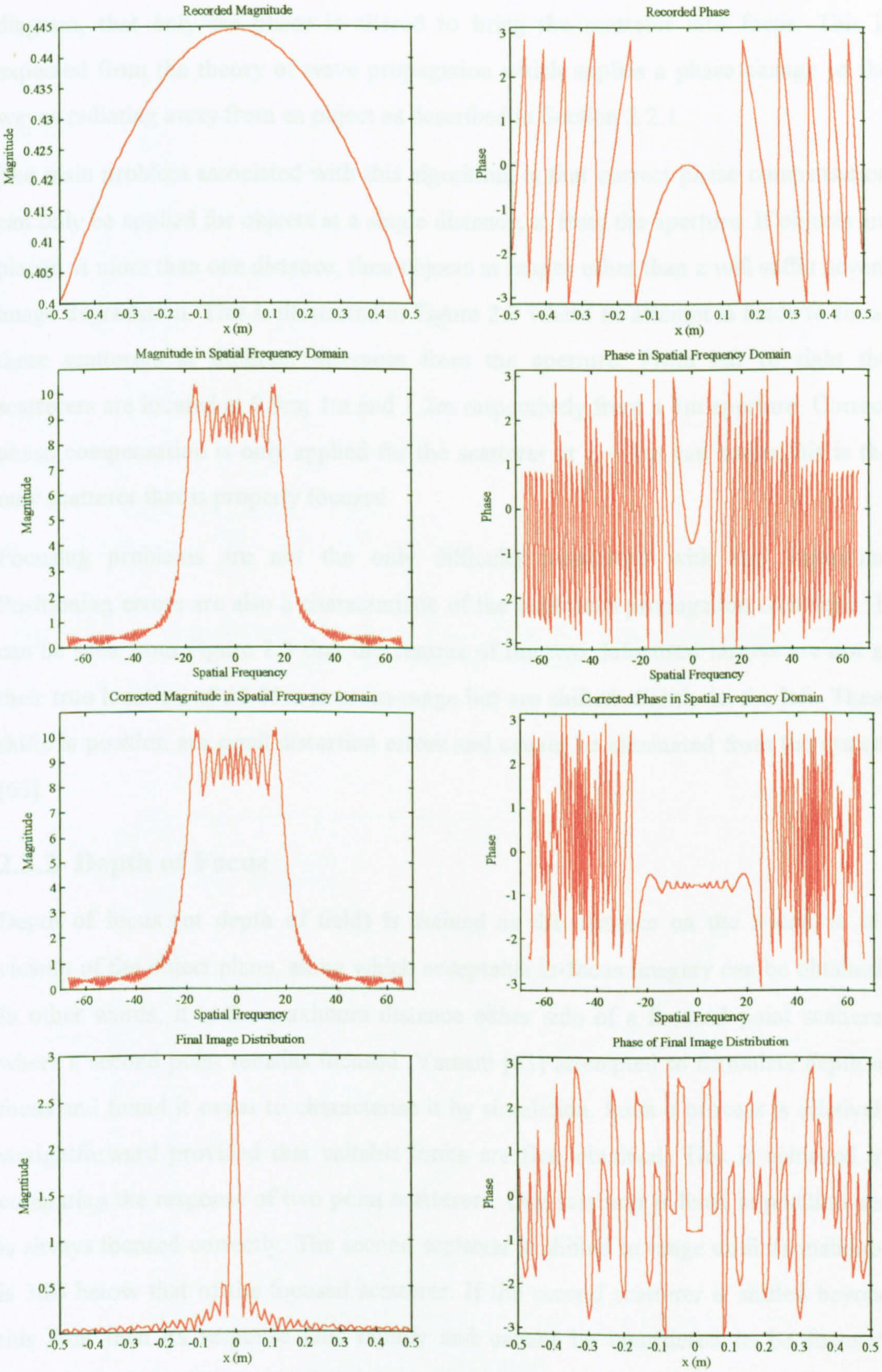

Figure 2.2 Magnitude and Phase Response of a Single Point Scatterer Before and After Application of the Backward Propagation Algorithm

diagram, that only the phase is altered to bring the scatterer into focus. This is expected from the theory of wave propagation which applies a phase change to the waves radiating away from an object as described in Section 2.2.1.

The main problem associated with this algorithm, is that correct phase compensation can only be applied for objects at a single distance, z, from the aperture. If objects are placed at more than one distance, then objects at ranges other than z will suffer severe image degradation. This is illustrated in Figure 2.3 where an attempt is made to focus three scatterers at different distances from the aperture. From left to right the scatterers are located at 0.9m, 1m and 1.2m respectively from a 1m aperture. Correct phase compensation is only applied for the scatterer at z = 1m and hence this is the only scatterer that is properly focused.

Focusing problems are not the only difficulty associated with this algorithm. Positioning errors are also a characteristic of the backward propagation technique. It can be seen from Figure 2.3 that the centres of the two defocused targets are not at their true location of ±0.25m in cross-range but are shifted slightly to the left. These shifts in position are small distortion errors and cannot be eliminated from the system [63].

2.3.2 Depth of Focus

Depth of focus (or depth of field) is defined as the distance on the z-axis, in the vicinity of the object plane, along which acceptable in-focus imagery can be obtained. In other words, it is the maximum distance either side of a focused point scatterer where a second point remains focused. Yamani [63] attempted to formulate depth of focus and found it easier to characterise it by simulation. Such a process is relatively straightforward provided that suitable limits are first obtained. This is achieved by comparing the response of two point scatterers. One scatterer is fixed in position and is always focused correctly. The second scatterer is shifted in range until its mainlobe is 3dB below that of the focused scatterer. If the second scatterer is shifted beyond this limit then its response falls rapidly and cannot be considered to be focused. Figure 2.4 shows the results of such simulations by plotting range against depth of focus for both a 1m and a 2m aperture. It is apparent that the depth of focus close to

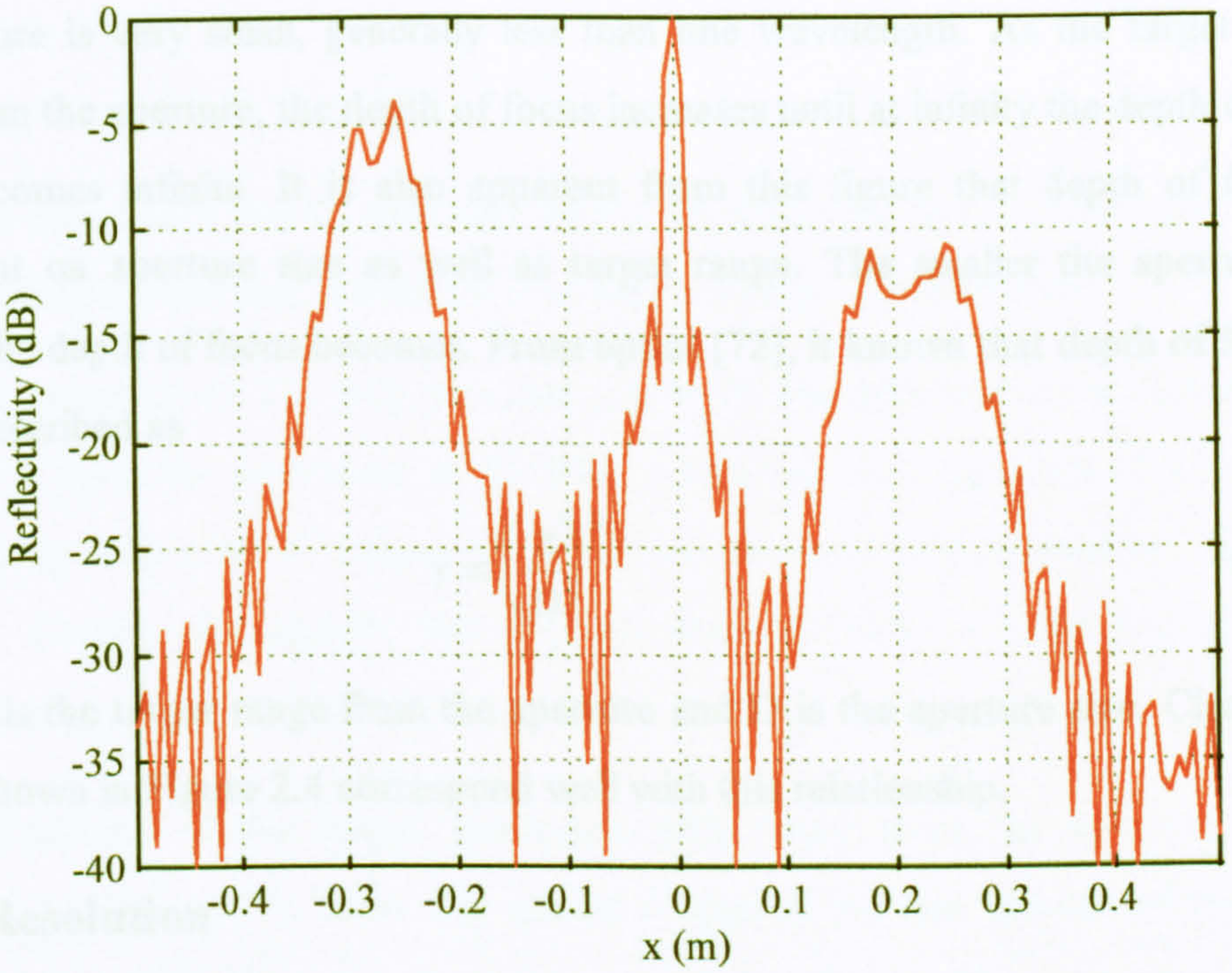

Figure 2.3 Reconstructed Image of Three Point Scatterers Located at 0.9m, 1m and 1.2m from the Aperture

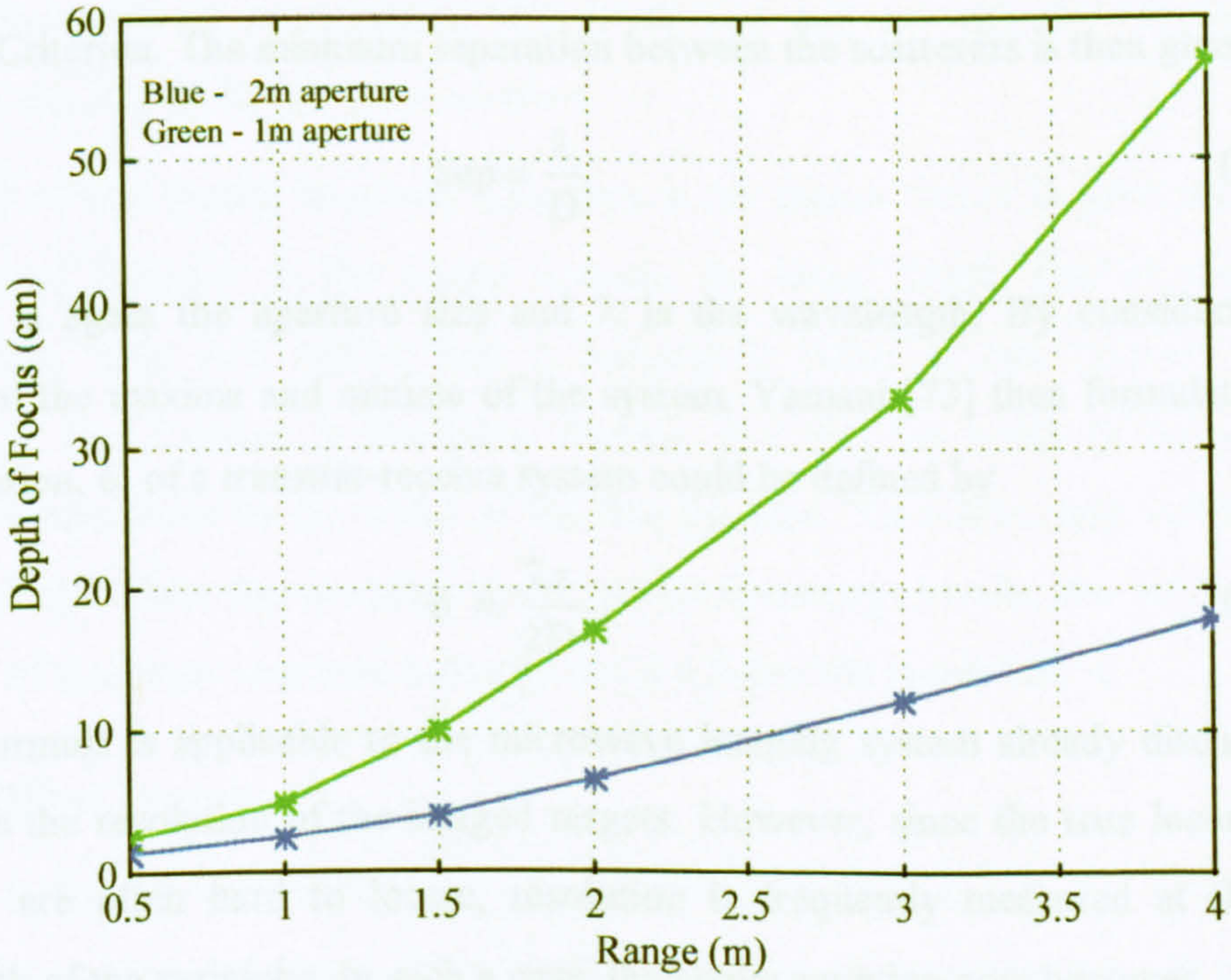

Figure 2.4 Variation of Depth of Focus with Target Range

an aperture is very small, generally less than one wavelength. As the target moves away from the aperture, the depth of focus increases until at infinity the depth of focus itself becomes infinite. It is also apparent from this figure that depth of focus is dependent on aperture size as well as target range. The smaller the aperture, the greater the depth of focus becomes. From optics [72], it known that depth of focus, γ, is best described as

$$\gamma \propto \left(\frac{z}{D}\right)^2 \tag{2-24}$$

where z is the target range from the aperture and D is the aperture size. Clearly, the results shown in Figure 2.4 correspond well with this relationship.

2.3.3 Resolution

Resolution was first formulated by Lord Rayleigh to help predict the ability of an optical system to distinguish two stars. He proved that two point targets could be resolved if the maximum of one target was located at the same point as the first minimum of the second target [72]. If the targets are closer than this minimum separation then they cannot be distinguished from each other. This is known as the Rayleigh Criterion. The minimum separation between the scatterers is then given by,

$$\text{Sep} = \frac{\lambda}{D} \tag{2-25}$$

where D is again the aperture size and λ is the wavelength. By considering the location of the maxima and minima of the system, Yamani [73] then formulated that the resolution, δ, of a transmit-receive system could be defined by

$$\delta = \frac{\lambda z}{2D} \tag{2-26}$$

Such a formula is applicable to the microwave imaging system already discussed to determine the resolution of the imaged targets. However, since the true locations of the nulls are often hard to locate, resolution is frequently measured at the 3dB beamwidth of the mainlobe. In such a case, the above equation now becomes

$$\delta_{3dB} = 0.89\frac{\lambda z}{2D} \tag{2-27}$$

From this equation it can be seen that resolution decreases as the target moves away from the aperture and that resolution increases for larger aperture sizes.

However, equation (2-27) only provides a straight line approximation of resolution. Figure 2.5 plots the resolution at 10GHz, calculated from equation (2-27) against range, along with a set of values for resolution obtained from simulations for a 3m aperture. Clearly, the straight line approximation provides a good approximation except at ranges that are close to the aperture.

The degradation of the target resolution with range from the aperture can be explained by Figure 2.6. Here the spatial frequency domain spectra of two point targets at two different ranges from the aperture are shown. The nearer target has a broad spectrum containing higher spatial frequencies than the target further away. This occurs since most of the energy scattered from near targets is received at the aperture, whereas the energy scattered from targets further away is spread over a wider range of angles by the time it reaches the aperture. Consequently, the higher spatial frequencies of more distant targets are lost and can only be recovered by increasing the size of the scanning aperture.

The width of this spatial frequency spectrum is the critical factor in determining the resolution of a target in the image domain. By using simple Fourier transform relationships, it is well known that a rectangular pulse in one Fourier domain generates a sinc function in the other domain, and that the width of the pulse is inversely proportional to the width of the sinc function. Therefore, with reference to Figure 2.6, the wider the spectrum in the spatial frequency domain, the narrower the mainlobe of the target response becomes and the better the resolution is.

2.3.3.1 Offset Targets

Figure 2.5 also demonstrates that if objects are offset from x = 0 (i.e. towards the edge of the scanning aperture), the measured resolution diverges further still from the approximation provided by equation (2-27). This effect can be explained by

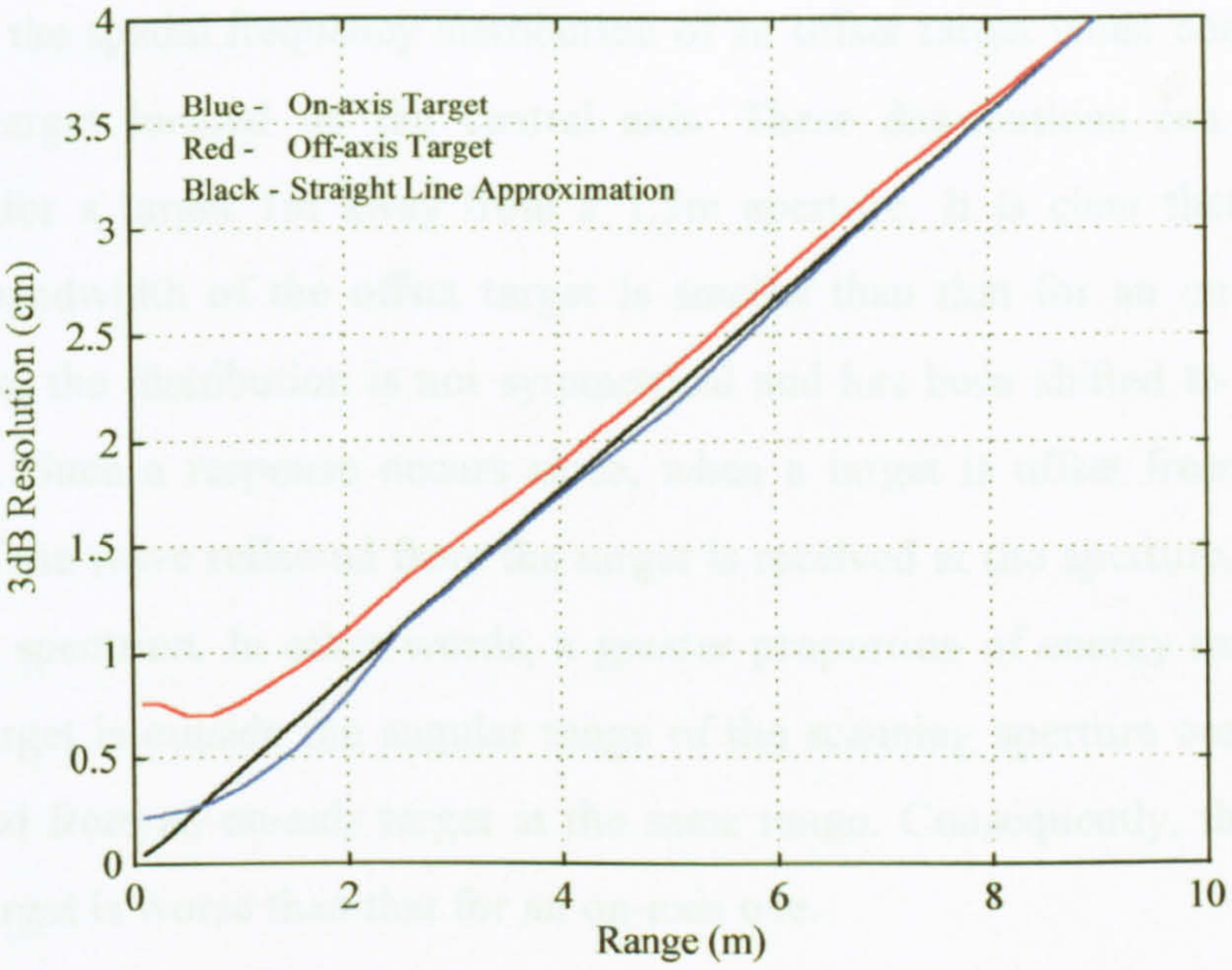

Figure 2.5 Comparison of Measured and Calculated Resolution with Target Range

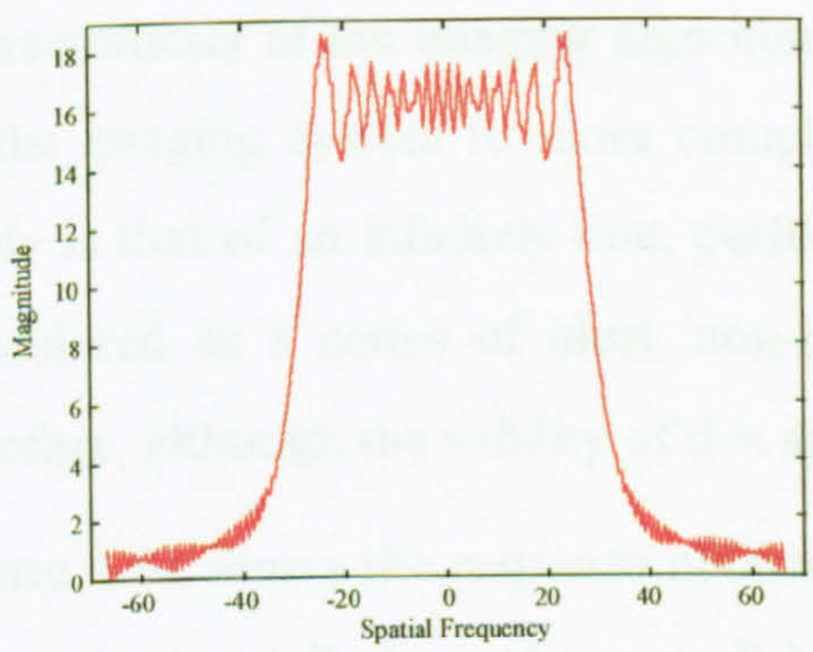

Target at z = 1m

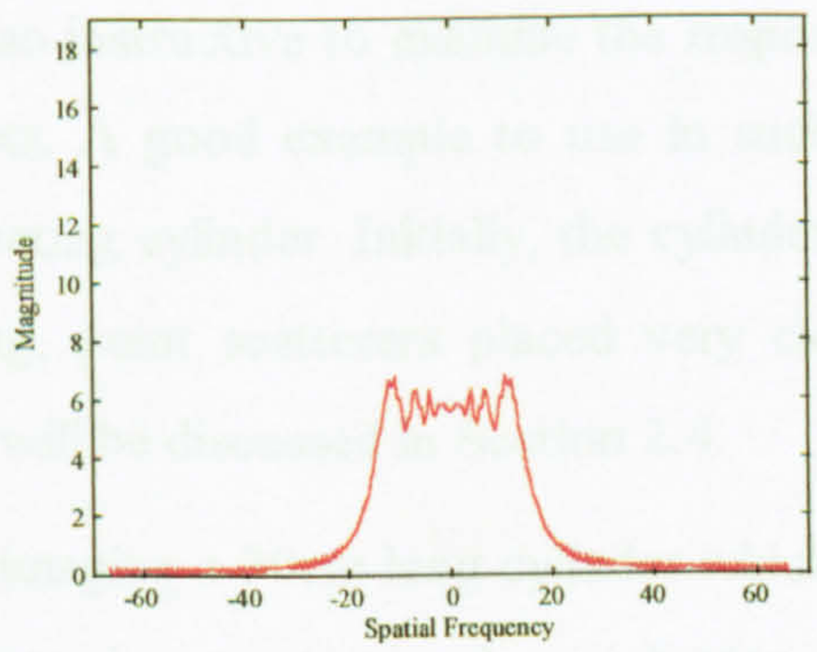

Target at z = 2m

Figure 2.6 Spatial Frequency Distributions of Two Point Scatterers at Two Different Ranges from the Aperture

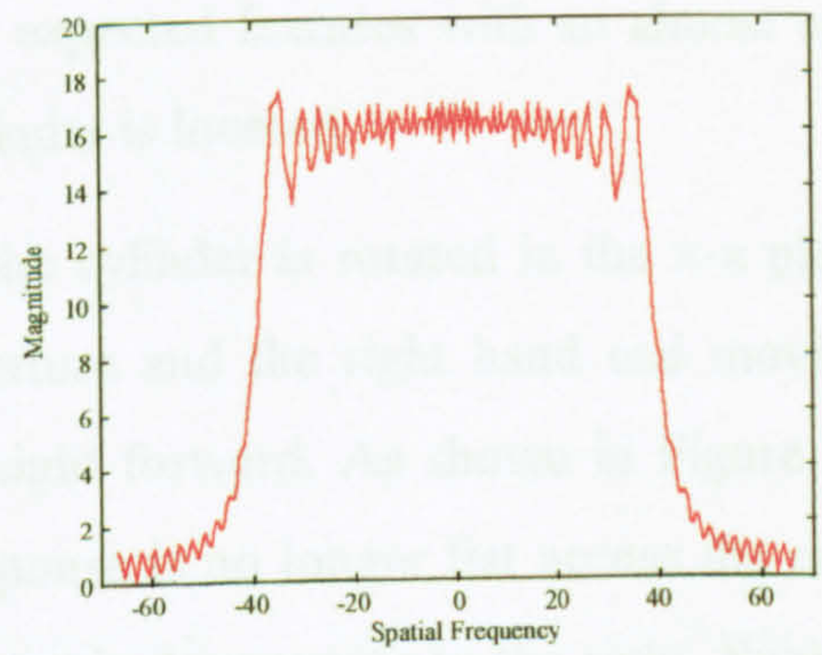

Target at x = 0m

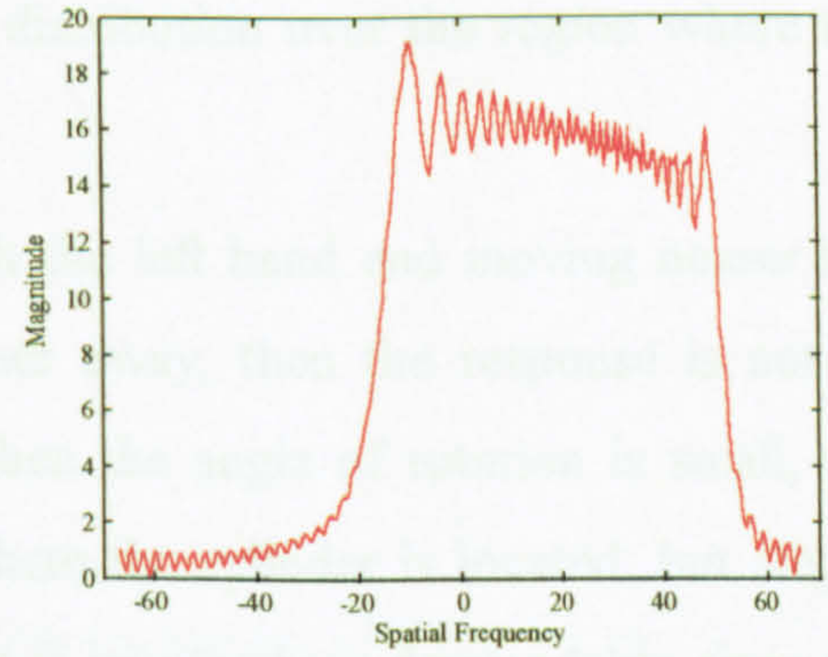

Target at x = 0.5m

Figure 2.7 Spatial Frequency Distributions of Two Point Scatterers at Two Different Cross-Ranges

considering the spatial frequency distribution of an offset target when compared with that of a target located on the central axis. These distributions can be seen in Figure 2.7 for a target 1m away from a 1.5m aperture. It is clear that the spatial frequency bandwidth of the offset target is smaller than that for an on-axis target. Furthermore, the distribution is not symmetrical and has been shifted to one side of the domain. Such a response occurs since, when a target is offset from the central axis, less of the wave reflected from the target is received at the aperture, resulting in a deformed spectrum. In other words, a greater proportion of energy reflected from an offset target is outside the angular range of the scanning aperture compared with that received from an on-axis target at the same range. Consequently, the resolution of such a target is worse than that for an on-axis one.

2.3.4 Complex Targets

Whilst the simulation of ideal point scatterers provides valuable information about the characteristics of the imaging algorithm, it is also instructive to examine the response of the imaging system to more complex targets. A good example to use in such a study is that of an infinitely thin, perfectly reflecting cylinder. Initially, the cylinder is considered as a series of ideal, non-interacting, point scatterers placed very close together, although the validity of this approach will be discussed in Section 2.4.

Figure 2.8a shows the response obtained from imaging a 30cm long cylinder which is placed horizontally in a plane parallel to the scanning aperture and at a distance of 1.5m from it. The cylinder is composed of 40 scatterers each separated by a quarter of a wavelength. The reconstructed response of the cylinder after focusing demonstrates the expected features with an almost constant distribution over the region where the cylinder is located.

If the cylinder is rotated in the x-z plane, with the left hand end moving nearer the aperture and the right hand end moving further away, then the response is not as straight forward. As shown in Figure 2.8b, when the angle of rotation is small, the response is no longer flat across the region where the cylinder is located, but slopes unevenly downwards to the right. Such a result is intuitively understandable since the right hand end is moving away from the aperture and hence a smaller angular

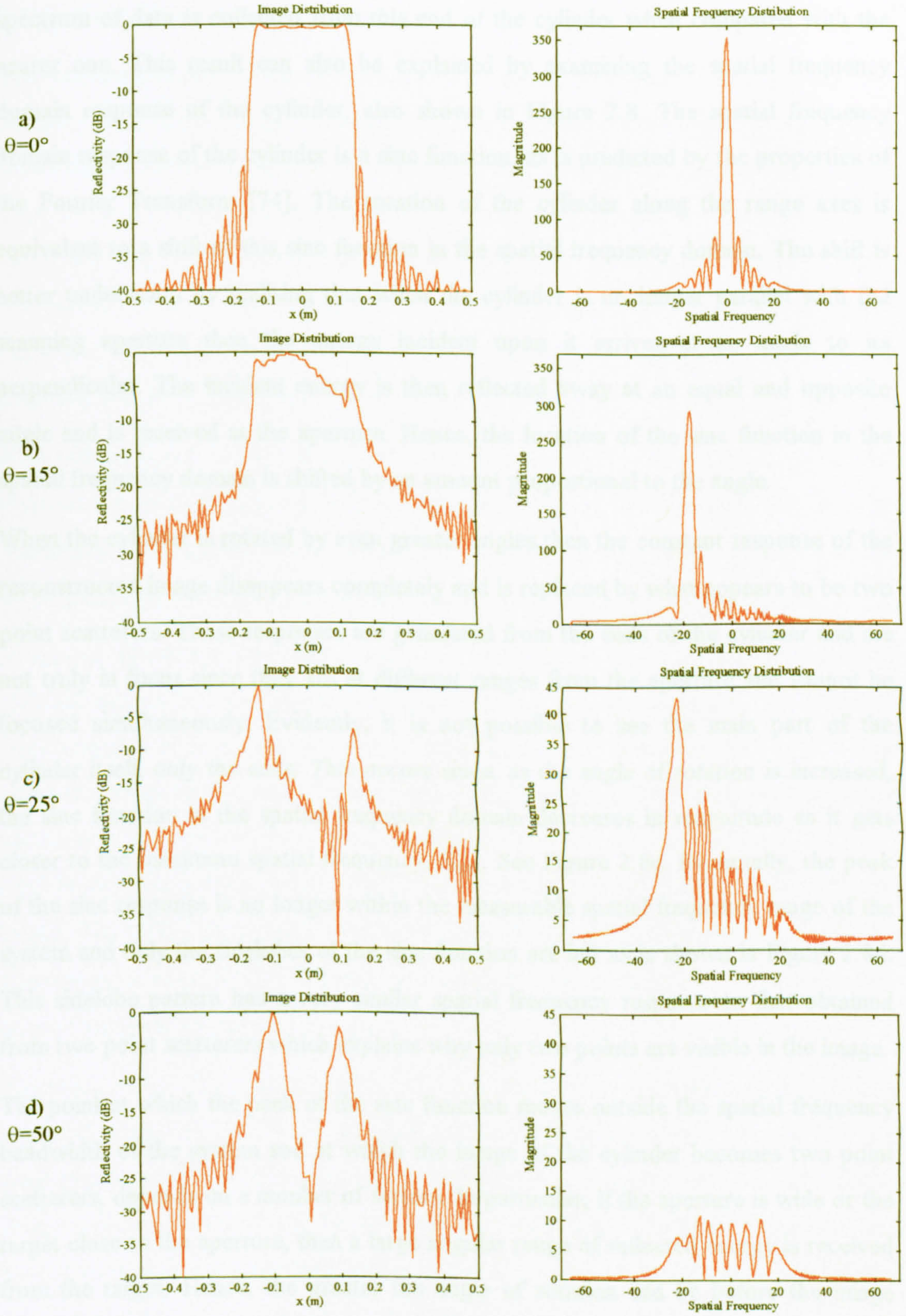

Figure 2.8 Reconstructed Image and Spatial Frequency Domain Response of a Rotated Horizontal Cylinder

spectrum of data is collected from this end of the cylinder when compared with the nearer one. This result can also be explained by examining the spatial frequency domain response of the cylinder, also shown in Figure 2.8. The spatial frequency domain response of the cylinder is a sinc function, as is predicted by the properties of the Fourier Transform [74]. The rotation of the cylinder along the range axes is equivalent to a shift of this sinc function in the spatial frequency domain. The shift is better understood by realising that when the cylinder is no longer parallel with the scanning aperture then the energy incident upon it arrives at an angle to its perpendicular. The incident energy is then reflected away at an equal and opposite angle and is received at the aperture. Hence, the location of the sinc function in the spatial frequency domain is shifted by an amount proportional to the angle.

When the cylinder is rotated by even greater angles then the constant response of the reconstructed image disappears completely and is replaced by what appears to be two point scatterers. These responses are generated from the ends of the cylinder and are not truly in focus since they are at different ranges from the aperture and cannot be focused simultaneously. Evidently, it is not possible to see the main part of the cylinder itself, only the ends. This occurs since, as the angle of rotation is increased, the sinc function in the spatial frequency domain decreases in magnitude as it gets closer to the maximum spatial frequency, S_{max}. See Figure 2.8c. Eventually, the peak of the sinc response is no longer within the measurable spatial frequency range of the system and only the sidelobes of the sinc function are left as is shown in Figure 2.8d. This sidelobe pattern has a very similar spatial frequency response to that obtained from two point scatterers which explains why only two points are visible in the image.

The point at which the peak of the sinc function moves outside the spatial frequency bandwidth of the system and at which the image of the cylinder becomes two point scatterers, depends on a number of factors. In particular, if the aperture is wide or the target close to the aperture, then a large angular range of reflected energy is received from the target. Hence, the greater the angle of rotation can be before the image deteriorates to two points. For the 30cm long cylinder simulated, it was found that the image of the cylinder becomes two points when the angle of rotation was approximately 25°.

2.3.5 Two-Dimensional Simulations

Two-dimensional simulations of the system are also required to help predict the characteristics of the image produced by a real synthetic aperture system. Figure 2.9 shows the two-dimensional case for three point scatterers placed at, from left to right, 0.9m, 1m and 1.2m in range, and where correct phase compensation has been applied to the target at 1m. It can be seen that the target at 1m is the only scatterer in focus and that it has four sidelobe regions emanating outwards from the main response. These are the result of the data being limited to a square aperture [74]. The first sidelobes are -15dB below the main response.

It should be noted that the image of Figure 2.9 has been interpolated in the spatial frequency domain by placing it in a large array prior to the final inverse Fourier Transform. This allows clearer details of the reconstructed image to be observed without altering the results and will be utilised for all future simulations.

A second simulation was then carried out to simulate three cylinders located at different orientations and angles with respect to the scanning aperture. The cylinders were arranged in such as way as to represent the trunk of a tree and two branches in order to anticipate the measurements made in Chapter 4. The trunk was arranged vertically in a plane parallel to the scanning aperture and was 1m in length. The left hand branch was inclined away from the aperture at an angle of 20° and was 0.5m in length. The right hand branch was also 0.5m in length and was inclined towards the aperture at an angle of 10°. Focusing was applied in the plane of the trunk which was located 1m from a 1.5m by 1.5m aperture.

The result of this simulation is shown in Figure 2.10. The main trunk is all in focus, as expected, whilst the right hand branch is visible but is partially out of focus. The left hand branch, is also visible, although its left hand end is badly out of focus and the image is deteriorating to a point as previously explained. This occurs since the left hand branch is at a greater angle to the plane of focusing than the right hand branch and consequently, the peak of the response from this branch could not be captured within the angular range of the system as was explained in Section 2.3.4.

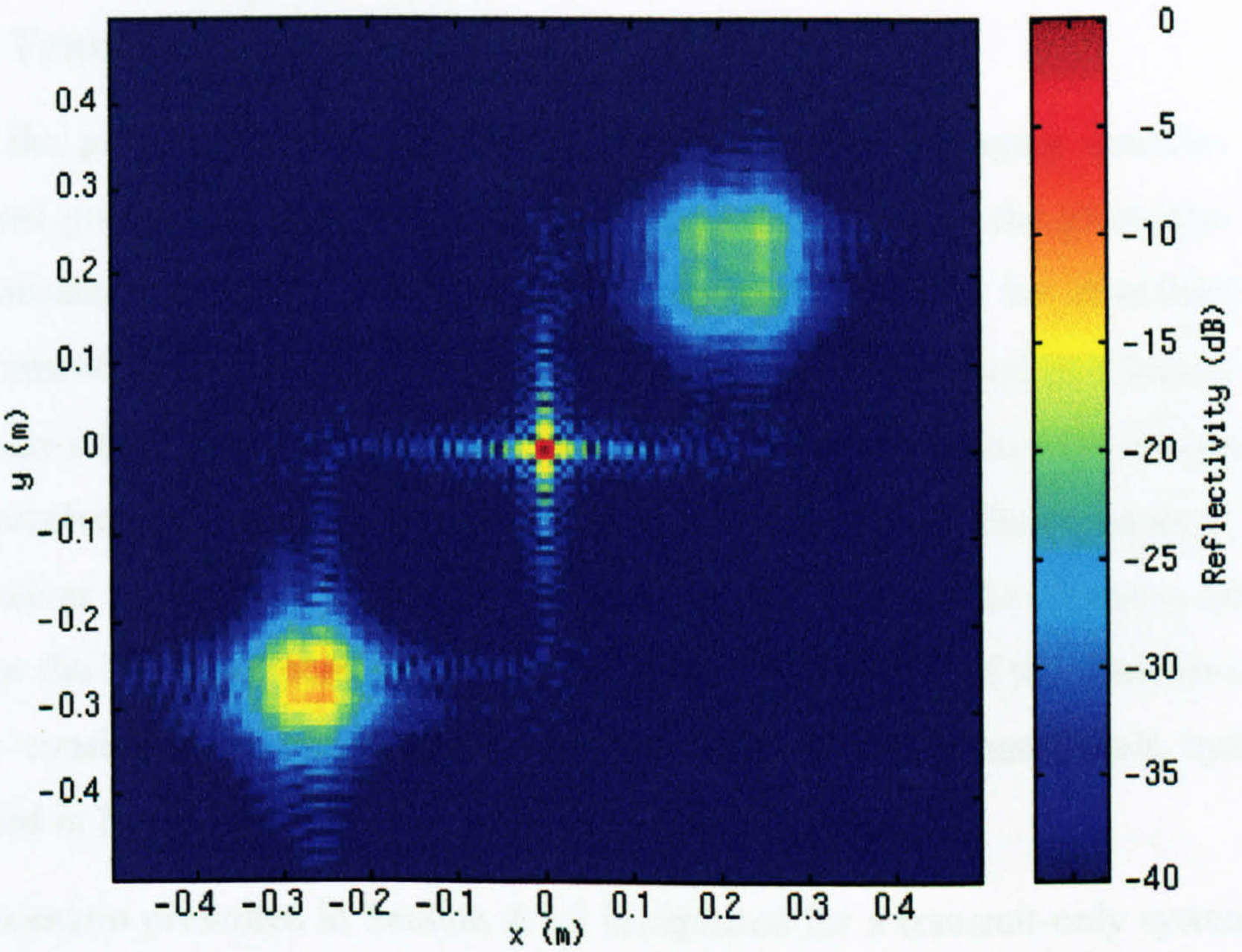

Figure 2.9 Two Dimensional Image of Three Point Scatterers Located at Three Different Ranges from the Aperture

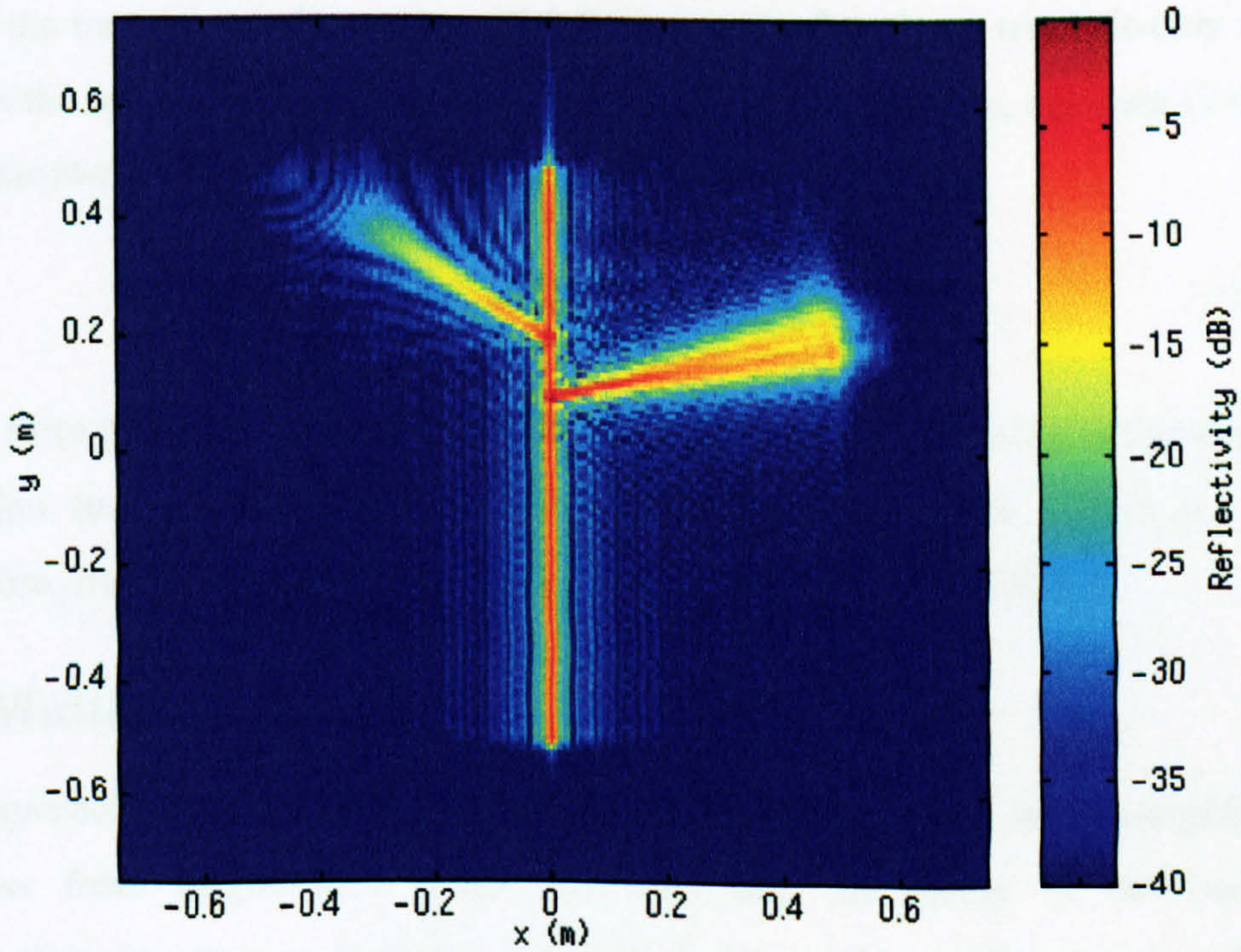

Figure 2.10 Two Dimensional Image of a Simulated Tree Composed of Three Cylinders

2.3.6 Transmission Simulations

Whilst the principal aim of this chapter is to examine the imaging qualities of the backward propagation algorithm for a transmit-receive system, the properties of the complementary transmit-only imaging system also need to be examined since measurements of transmission through a target will be described in Chapter 4. As previously explained, in transmit-only systems, the transmitter is not in the same plane as the receiver. Instead, the target is illuminated from behind by the transmitter, whilst the receiver is placed a distance z in front of the target. The distance travelled between the source of scattering and the receiver is half that of the transmit-receive system considered in previous sections. Focusing of the transmit only system is explained in Section 2.2.1.

If the scenario presented in Section 2.3.1 is repeated for a transmit-only system, then a single point scatterer at 1m from the aperture is taken to be the source of the scattered field. The backward propagator as described by equation (2-20) is used to focus the data, and the resulting image is shown in Figure 2.11. Comparison of this with Figure 2.3 clearly shows that the transmit-only system has a resolution of half that of the transmit-receive system. This is due to the fact that a transmit-only system has half the spatial bandwidth of a transmit-receive system. Hence, equation (2-27) for the transmit-receive system resolution now becomes,

$$\delta_{3dB} = 0.89\frac{\lambda z}{D} \qquad (2\text{-}28)$$

Apart from this change in resolution, the characteristics of the backward propagation algorithm for both transmit-only and transmit-receive systems remain the same. Therefore, transmit-only systems are also limited in their depth of focus.

2.4 Multiple Scattering

The approach adopted in this work to date has been limited to investigating the response from simple ideal point scatterers and the ability of the backward propagation algorithm to focus them. Section 2.3.4 considered the response of arrays composed of closely spaced point scatterers. Such an approach is useful but far from accurate since it fails to account for the interaction that occurs within complex target

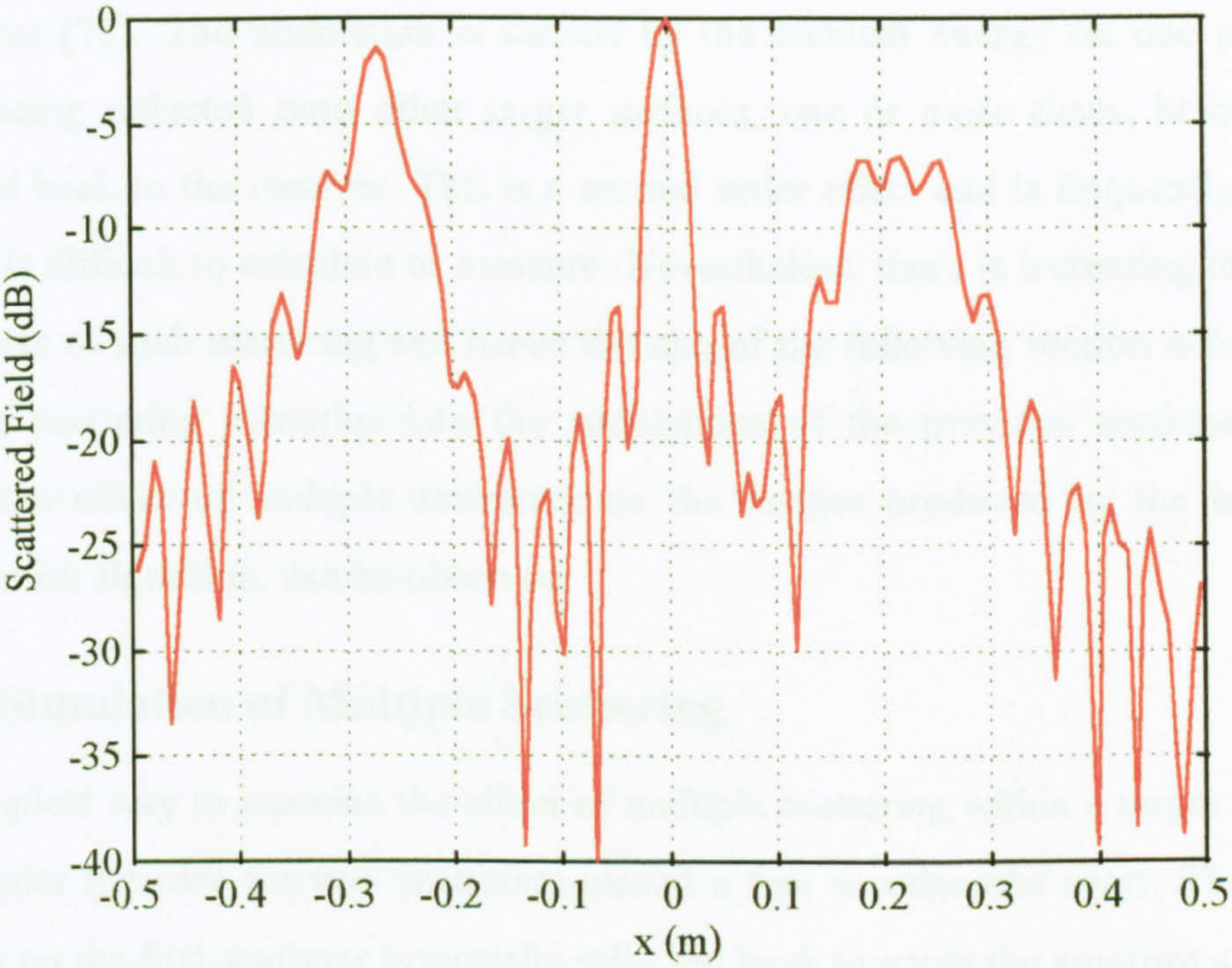

Figure 2.11 Reconstructed Image of Three Point Scatterers Located at Three Different Ranges from the Aperture for a Transmit-Only System

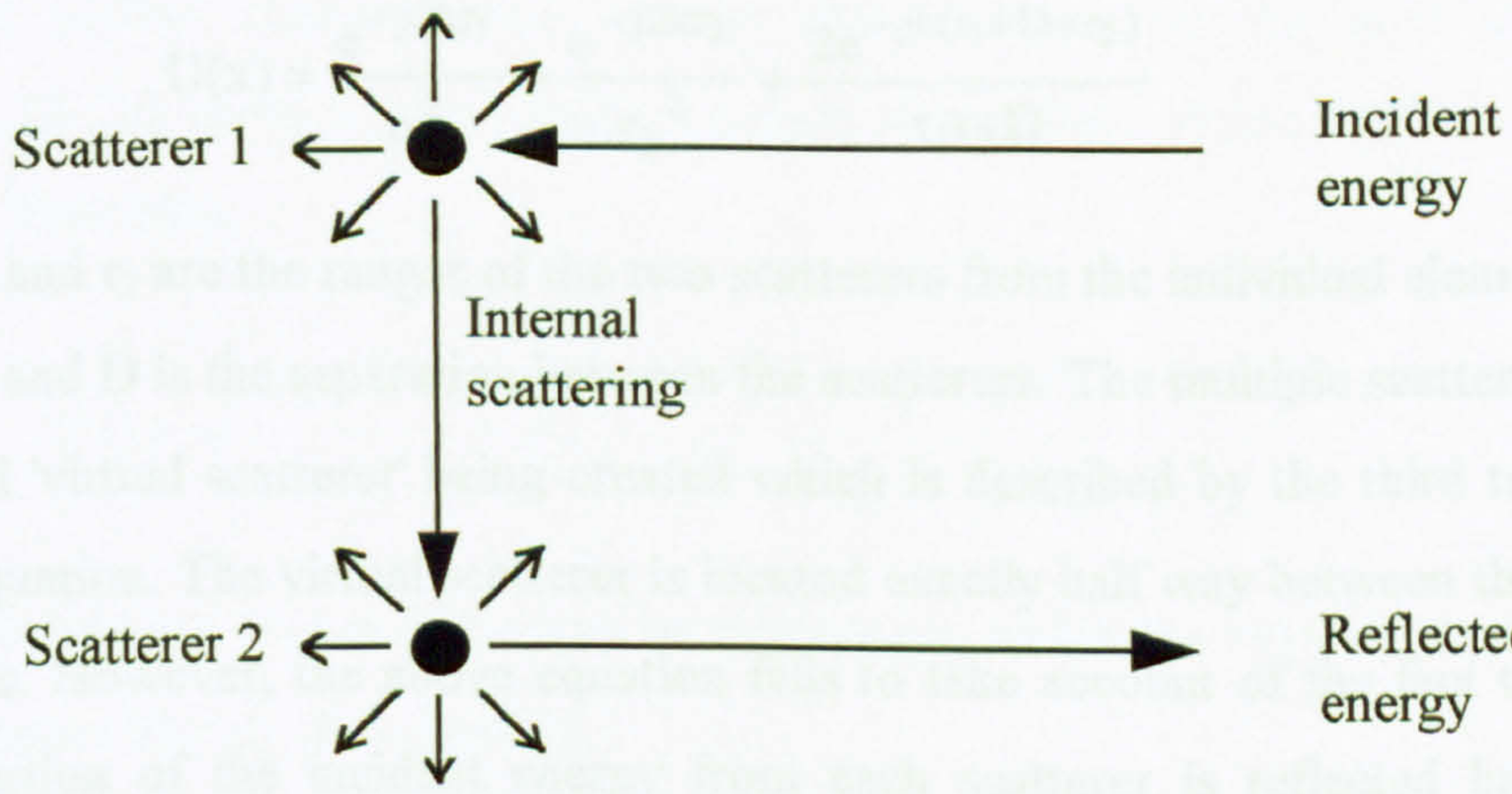

Figure 2.12 Illustration of Internal Scattering Between Two Point Scatterers

structures [75]. The interaction is caused by the incident energy on one part of a target being reflected onto other target surfaces, one or more times, before being reflected back to the receiver. This is a second order effect and is frequently ignored since it is difficult to calculate or measure. Nevertheless, there is increasing interest in the effects of such scattering and hence the aim of the following section is to include multiple scattering scenarios into the simulations of the previous sections. By so doing, the effect of multiple scattering on the images produced by the backward propagation algorithm, can be observed.

2.4.1 Simulation of Multiple Scattering

The simplest way to examine the effect of multiple scattering within a target object is to consider the case for two scatterers placed a few wavelengths apart. The energy incident on the first scatterer is partially reflected back towards the aperture as normal but some of the energy may be reflected towards the second scatterer. When it hits the second scatterer it is reflected back towards the aperture, as shown in Figure 2.12. The mechanism is repeated for energy incident on the second scatterer, which is reflected from the first scatterer. This process can be described by a development of equation (2-23), namely,

$$U(x) = \frac{e^{-j2kr_1}}{r_1^{\,2}} + \frac{e^{-j2kr_2}}{r_2^{\,2}} + \frac{2e^{-jk(r_1+D+r_2)}}{r_1 r_2 D} \qquad (2\text{-}29)$$

where r_1 and r_2 are the ranges of the two scatterers from the individual elements of the aperture and D is the separation between the scatterers. The multiple scattering results in a third 'virtual scatterer' being created which is described by the third term of the above equation. The virtual scatterer is located exactly half way between the two real scatterers. However, the above equation fails to take account of the fact that only a small portion of the incident energy from each scatterer is reflected back to the receiver and an even smaller amount is reflected in the direction of the second scatterer. In short, the above equation needs to take account of the nature of the scattering at the targets. This can be described in terms of radar cross section, σ, which will be fully explained in the following section.

If two targets are located an arbitrary distance, R, from a co-located transmitter and

receiver, then the power reflected back from the first target is given by

$$\frac{PG_t\sigma A}{\left(4\pi R^2\right)^2} \tag{2-30}$$

where P is the power transmitted by the radar, G_t is the gain of the transmit antenna and A is the effective area of the receive antenna. If multiple scattering occurs, then a second signal is reflected from the first target onto the second and then back to the receiver. The received signal from this route is described by

$$\frac{PG_t\sigma^2 A}{\left(4\pi R^2\right)^2\left(4\pi D^2\right)} \tag{2-31}$$

where D is again the separation between the targets. Ignoring all common terms, the powers received at the receiver are

from first scatterer σ (2-32)

from first scatterer via the second $\frac{\sigma^2}{\left(4\pi D^2\right)}$ (2-33)

and the received fields are the square roots of these values. An equal process occurs from the second scatterer back to the first. Substituting the field values into equation (2-29) gives a much more accurate description of the multiple scattering process. Therefore,

$$U(x) = \sqrt{\sigma}\frac{e^{-j2kr_1}}{r_1^2} + \sqrt{\sigma}\frac{e^{-j2kr_2}}{r_2^2} + \frac{\sigma}{D\sqrt{\pi}}\frac{e^{-jk(r_1+D+r_2)}}{r_1 r_2 D} \tag{2-34}$$

The scatterers can be considered to be spheres for which the radar cross section, σ_s, can be approximately described by,

$$\sigma_s = \pi a^2 \tag{2-35}$$

where 'a' is the radius of the sphere.

Using this equation to simulate suitable data, the effect of multiple scattering on the reconstructed image of two scatterers can be demonstrated, as shown in Figure 2.13.

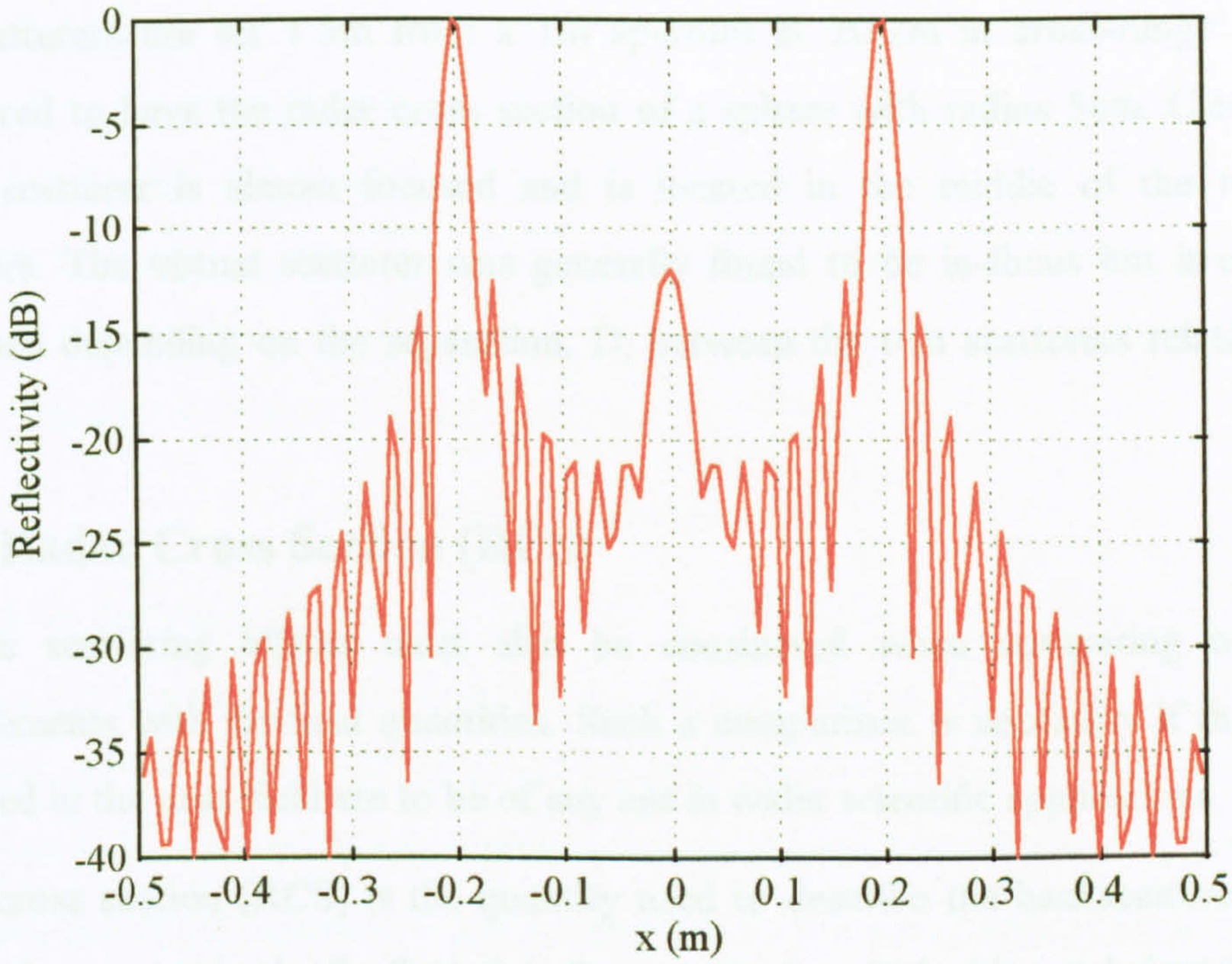

Figure 2.13 Reconstructed Image of Multiple Scattering Occurring Between Two Point Targets

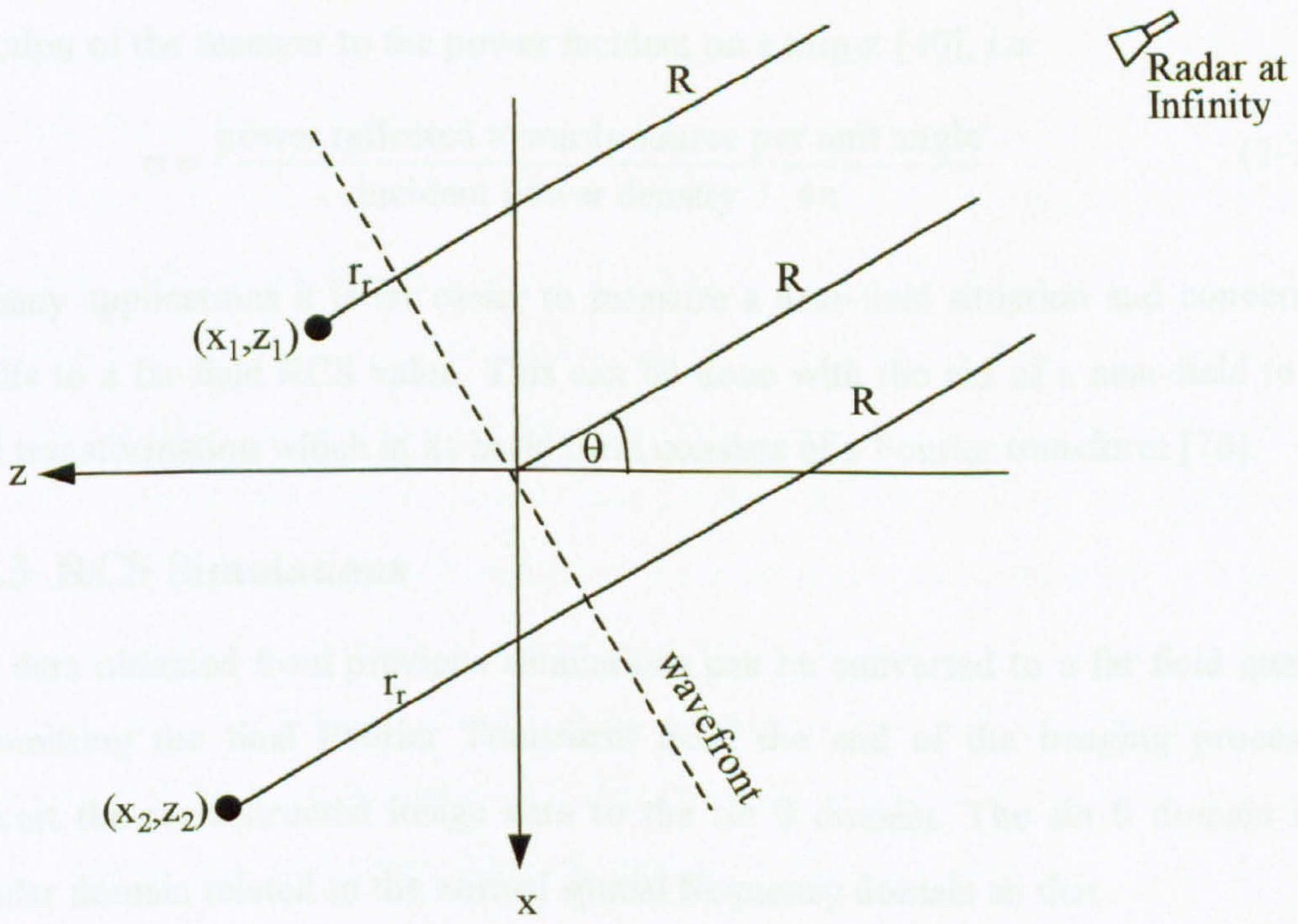

Figure 2.14 Geometry of a True RCS System

The scatterers are set 1.5m from a 1m aperture at ±0.2m in cross-range and are considered to have the radar cross section of a sphere with radius 5cm. Clearly, the virtual scatterer is almost focused and is located in the middle of the two real scatterers. The virtual scatterer was generally found to be in-focus but it could be defocused depending on the separation, D, between the two scatterers relative to r_1 and r_2.

2.4.2 Radar Cross Section (RCS)

Multiple scattering effects must also be considered when comparing near-field measurements with far-field quantities. Such a comparison is necessary if the values measured in the near-field are to be of any use in wider scientific applications.

Radar cross section (RCS) is the quantity used to describe the backscattered return from a given target in the far-field. It is the quantity by which ships and aircraft can be identified at long distances from a radar. It is highly dependent on the area of the target visible to the radar at a given point in time and is consequently a highly complex function, being built up from the scattering of energy on the surfaces of the target. RCS can be defined as the ratio of power reflected from a target in the direction of the receiver to the power incident on a target [40], i.e.

$$\sigma = \frac{\text{power reflected towards source per unit angle}}{\text{incident power density } / \ 4\pi} \tag{2-36}$$

In many applications it is far easier to measure a near-field situation and convert the results to a far-field RCS value. This can be done with the aid of a near-field to far-field transformation which in its basic form consists of a Fourier transform [76].

2.4.3 RCS Simulations

The data obtained from previous simulations can be converted to a far field quantity by omitting the final Fourier Transform from the end of the imaging process to convert the reconstructed image data to the sin θ domain. The sin θ domain is an angular domain related to the normal spatial frequency domain so that

$$\sin\theta = \frac{s\lambda}{2} \tag{2-37}$$

To determine the accuracy of the results so obtained, the data focused by the backward propagation algorithm needs to be compared with true RCS data which can be simulated using equation (2-23) provided that the near field range r_n is replaced with a far field range r_r. This range, r_r, is defined from Figure 2.14 where the radar is placed at infinity. From basic geometry, the distance from the radar to a general scatterer located at (x,z) is

$$R + z\cos\theta + x\sin\theta \tag{2-38}$$

where R is the distance from the radar to the wavefront nearest the target and θ describes the direction of wavefront propagation. However, the system in question is a transmit-receive system, so the actual distance travelled by the wave is double this. Furthermore, R is common to all terms, and since only the changes in phase of the wavefront are of any interest, it can be ignored. So the path length r_r for a true RCS system is effectively,

$$r_r = 2(z\cos\theta + x\sin\theta) \tag{2-39}$$

The true RCS response of two scatterers set 0.2m apart at a distance of 1m from a 1m aperture is shown in Figure 2.15. It is assumed that the targets are spheres with a radius of 5cm. Also shown is the RCS response generated from the single frequency near-field image data. Clearly the near-field data produces a result that is close to that for the real RCS data. In contrast, Figure 2.16 illustrates the results for the same two scatterers when multiple scattering is present between the two scatterers. Clearly, these results are not the same and hence the near-field data is unable to generate real RCS data in this case. When multiple scattering is present, the variation between the true RCS data and the data obtained from the near-field data varies depending on the separation D between the two scatterers. In some cases, the separation is such that, even when multiple scattering is present, the correct answer may be obtained from the near field data. Mensa and Vaccaro [76] illustrated the problem by measuring the near-field and far-field response of a dihedral and attempted to convert one to the other. Again, the scattering inherent within a dihedral structure resulted in an inaccurate transformation. They also demonstrated that real transmit-receive arrays, where all the elements are excited simultaneously, provide data which can be

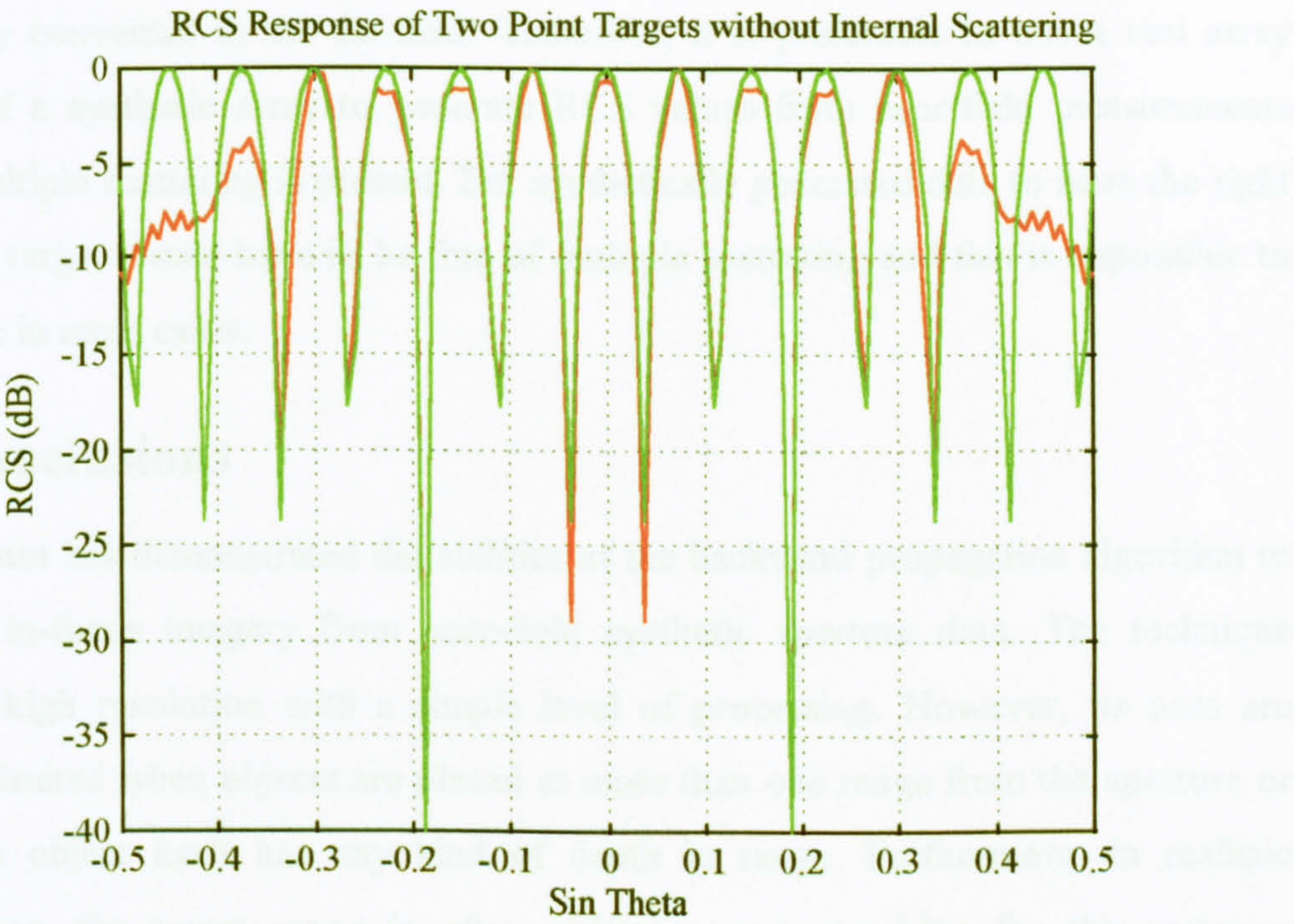

Figure 2.15 RCS Response of Two Point Targets Without Multiple Scattering

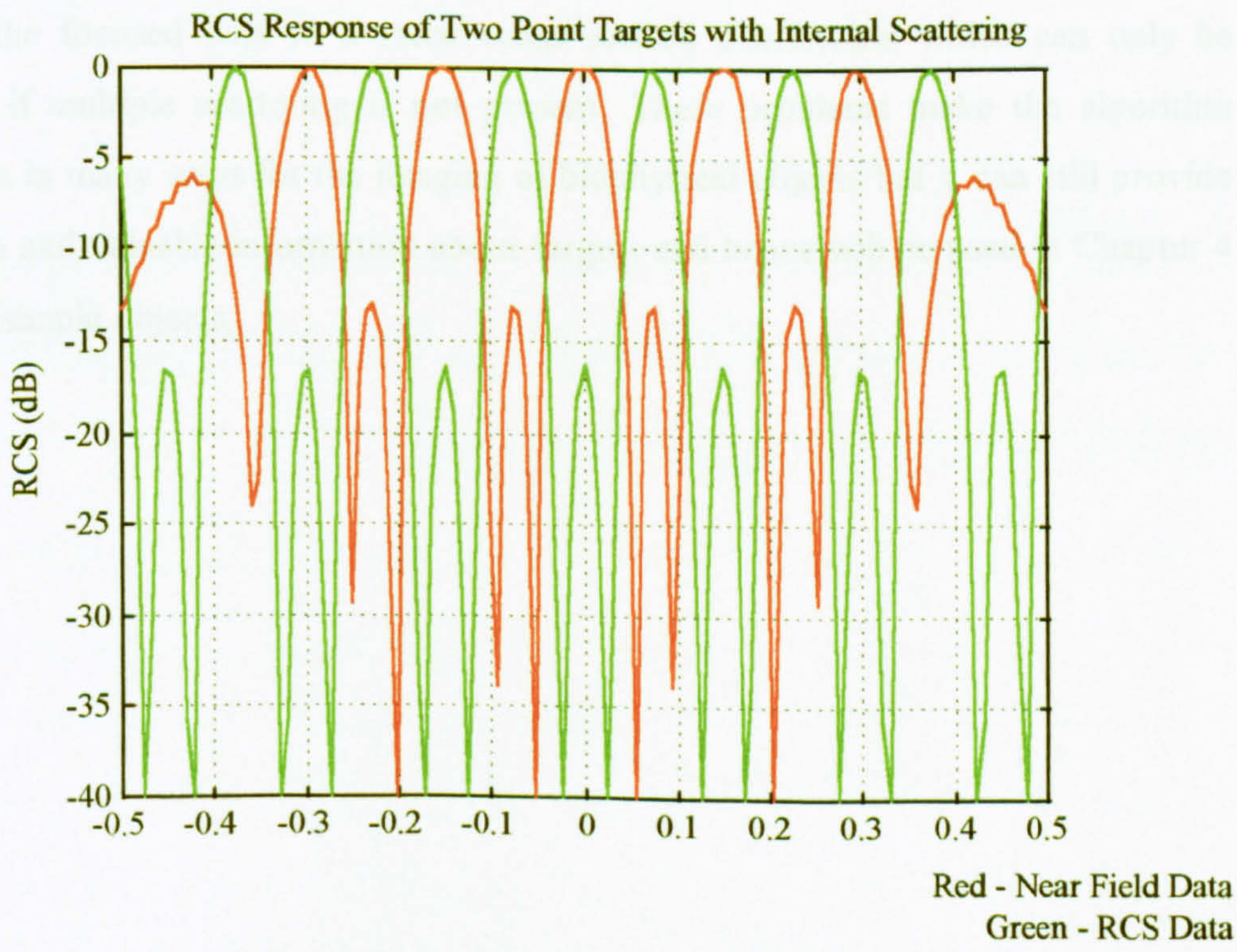

Figure 2.16 RCS Response of Two Point Targets With Multiple Scattering

accurately converted to the far-field. Therefore, it is preferable to use a real array instead of a synthetic array to generate RCS values from near-field measurements where multiple scattering is present. For synthetically generated data to have the right RCS, the target would have to be free of multiple scattering and this is impossible to determine in most cases.

2.5 Conclusions

This chapter has demonstrated the abilities of the backward propagation algorithm to generate in-focus imagery from near-field synthetic aperture data. The technique provides high resolution with a simple level of processing. However, its uses are severely limited when objects are placed at more than one range from the aperture or when the object itself has any kind of depth in range. Furthermore, in realistic applications, the target range is often unknown and searching for the optimum focusing condition can cause incorrect interpretation of the image. The responses of simple and complex targets were examined in both one and two dimensions by simulation. Multiple scattering within target structures was also examined and found to give rise to virtual images which may be focused. Attempts were also made to convert the focused data to a radar cross section distribution which can only be achieved if multiple scattering is not present. These problems make the algorithm unsuitable in many ways for the imaging of biophysical objects but it can still provide valid data and valuable information about targets and hence will be used in Chapter 4 to image simple objects.

Chapter 3

Development of a Multifrequency Auto-Focusing Imaging Algorithm

3.1 Introduction

In the previous chapter, it was shown that the single frequency backward propagation algorithm successfully focused the image of a point target. However, it failed to focus objects placed at more than one range from the aperture, or objects with a depth in range greater than the depth of focus. It also introduced distortion errors. To overcome these problems, a multifrequency implementation of the backward propagation algorithm is proposed which focuses all targets up to a maximum range. The advantage of this auto-focusing technique is that it provides in-focus imagery without any prior information about the location of the target in range. It also uses a small frequency bandwidth in comparison to other multifrequency algorithms.

The algorithm to be employed is analogous to one proposed by Ahmed Yamani [63] in the early 1980s. He provided a substantially different approach which resulted in an identical focusing procedure. The new approach is more concise and provides an intuitively simple understanding of the focusing mechanism.

This chapter presents a full derivation of both approaches to this automatic focusing algorithm and demonstrates the effectiveness of the algorithm for focusing point targets at different ranges. The characteristics of the algorithm are fully investigated in both one and two dimensions and the effect of scattering within target structures on the focusing capabilities of the algorithm is examined. The relationship of the generated images to radar cross section is discussed and improvements made to enhance the algorithm are described. A discussion on suitable filtering techniques is also included.

3.2 Development of an Auto-Focusing Imaging Algorithm

This section describes a development of the single frequency backward propagation imaging algorithm to a multifrequency scenario.

Initially, it is convenient to consider only a one-dimensional system. In Chapter 2, it was shown that the backward propagator term, $H^{-1}(s)$, given in equation (2-22), can be used to focus a set of single frequency data collected over a planar aperture. $H^{-1}(s)$ is defined as

$$H^{-1}(s) = \exp\left(\frac{j4\pi z}{\lambda}\sqrt{1-\left(\frac{\lambda s}{2}\right)^2}\right) \tag{3-1}$$

and the target range z is defined as

$$z = \frac{ct}{2} \qquad \text{where } t = \frac{(n-1)}{N.df} \tag{3-2}$$

df is the frequency sampling interval and N is the size of the Fourier data array used. It should be noted that the above relationship between time, t, and range, z, is only valid in the image domain and is not valid in the spatial frequency domain as will be shown later. The location of a given target in the spatial frequency range domain varies with spatial frequency and the effect is compensated for by the square-root term in equation (3-1) [70].

The same approach used in the single frequency example can also be used to focus a multifrequency data set U(s,f) collected over a planar aperture. The data must be converted to the range domain and multiplied by a correction factor to produce in-focus imagery. In this case, the correction factor, G(s,z), needed to focus the image is given by,

$$G(s,z) = \exp\left(\frac{j4\pi f_o z}{c}\sqrt{1-\left(\frac{sc}{2f_o}\right)^2}\right) \tag{3-3}$$

where f_o is the centre frequency of a small bandwidth. It can be seen that this is the same as the focusing operator, $H^{-1}(s)$, used in the single frequency case.

Given that z is still defined by equation (3-2), since the variation of target location with spatial frequency is accounted for by the square root term, then the above equation can be re-written as a time domain correction factor, namely.

$$G(s,t) = \exp\left(j2\pi f_o t\sqrt{1-\left(\frac{sc}{2f_o}\right)^2}\right) \tag{3-4}$$

Hence, in-focus imagery can be obtained by multiplying the time domain data, U(s,t), by the above focusing term. The corrected data, U'(s,t), is then Fourier transformed

with respect to time to the frequency domain where the centre frequency is extracted to give $U'(s,f_o)$. Finally, an inverse Fourier transform with respect to spatial frequency is applied to generate the final image distribution, $U'(x,f_o)$. The centre frequency is extracted as it is the only frequency at which truly in-focus imagery is obtained. The reason for this will be explained in the following section. The whole imaging process is illustrated in Figure 3.1 and validation that it produces in-focus imagery is given in Section 3.2.2. If a synthetic pulse system, as described in Chapter 1, is used, then this focusing operation requires the data to undergo four Fourier transformations. Obviously, this a time consuming and computationally intensive process and is therefore not desirable.

It is possible to simplify the focusing procedure for a synthetic pulse system by making use of the knowledge that multiplication in the time domain is equivalent to convolution in the frequency domain [74]. Therefore, if the focusing operator of equation (3-4) is transformed to the frequency domain, then convolution can be carried out in the frequency domain without the need for the data to be converted to its time domain form. The correction factor in the frequency domain is obtained by applying a Fourier transform to equation (3-4) so that

$$G(s,f) = \int_0^{1/df} \exp j2\pi f_o t \sqrt{1-\left(\frac{sc}{2f_o}\right)^2} \exp -j2\pi ft \, dt \qquad (3\text{-}5)$$

which yields

$$G(s,f) = \frac{1}{df} \exp\left(-j\frac{\pi}{df}\left\{f - f_o\sqrt{1-\left(\frac{sc}{2f_o}\right)^2}\right\}\right) \frac{\sin\frac{\pi}{df}\left\{f - f_o\sqrt{1-\left(\frac{sc}{2f_o}\right)^2}\right\}}{\frac{\pi}{df}\left\{f - f_o\sqrt{1-\left(\frac{sc}{2f_o}\right)^2}\right\}} \qquad (3\text{-}6)$$

Once G(s,f) has been convolved with the frequency domain data then the centre frequency can be extracted as before and inverse Fourier transformed to give $U'(x,f_o)$. This process is illustrated in Figure 3.2.

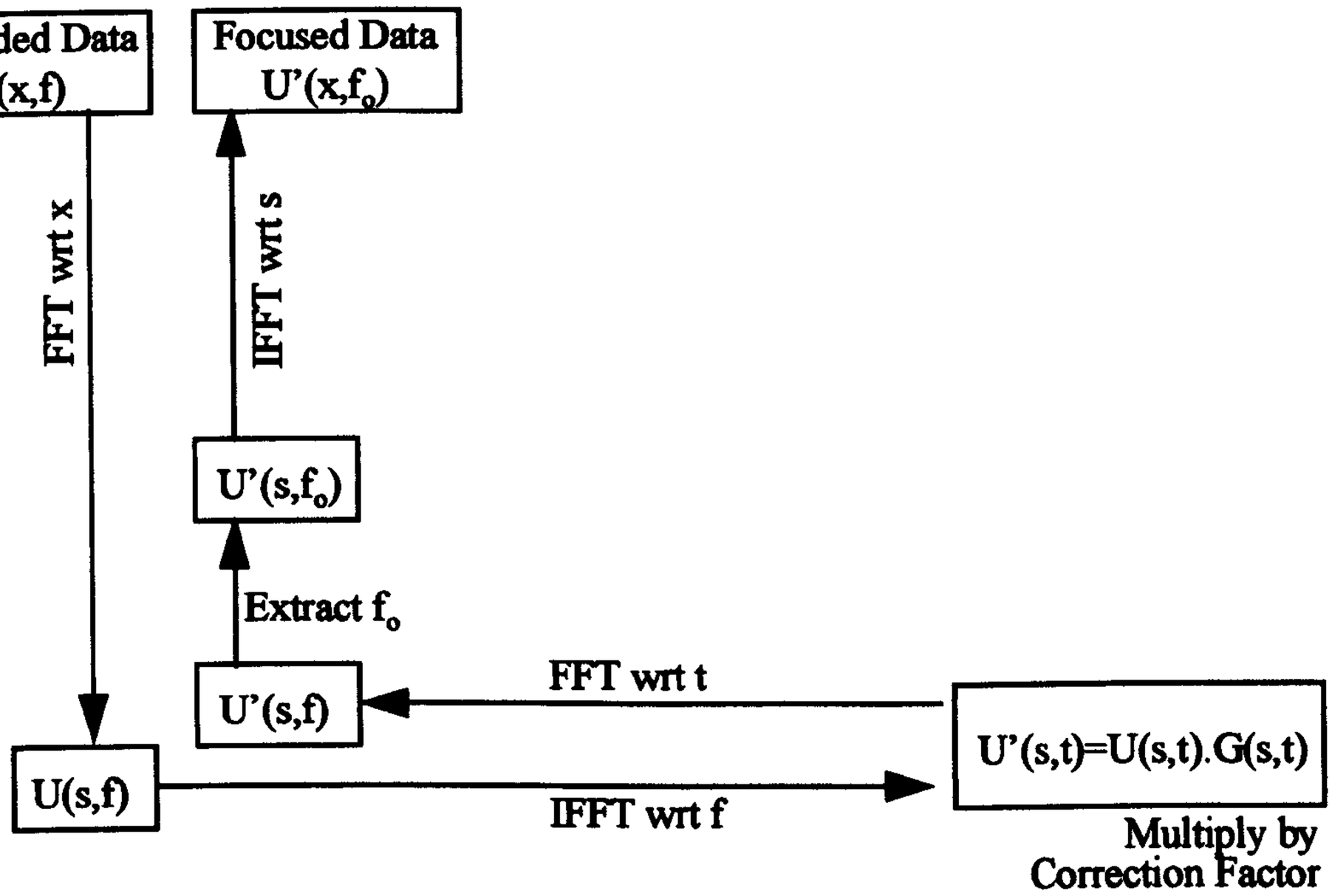

Figure 3.1 Illustration of the Auto-Focusing Algorithm

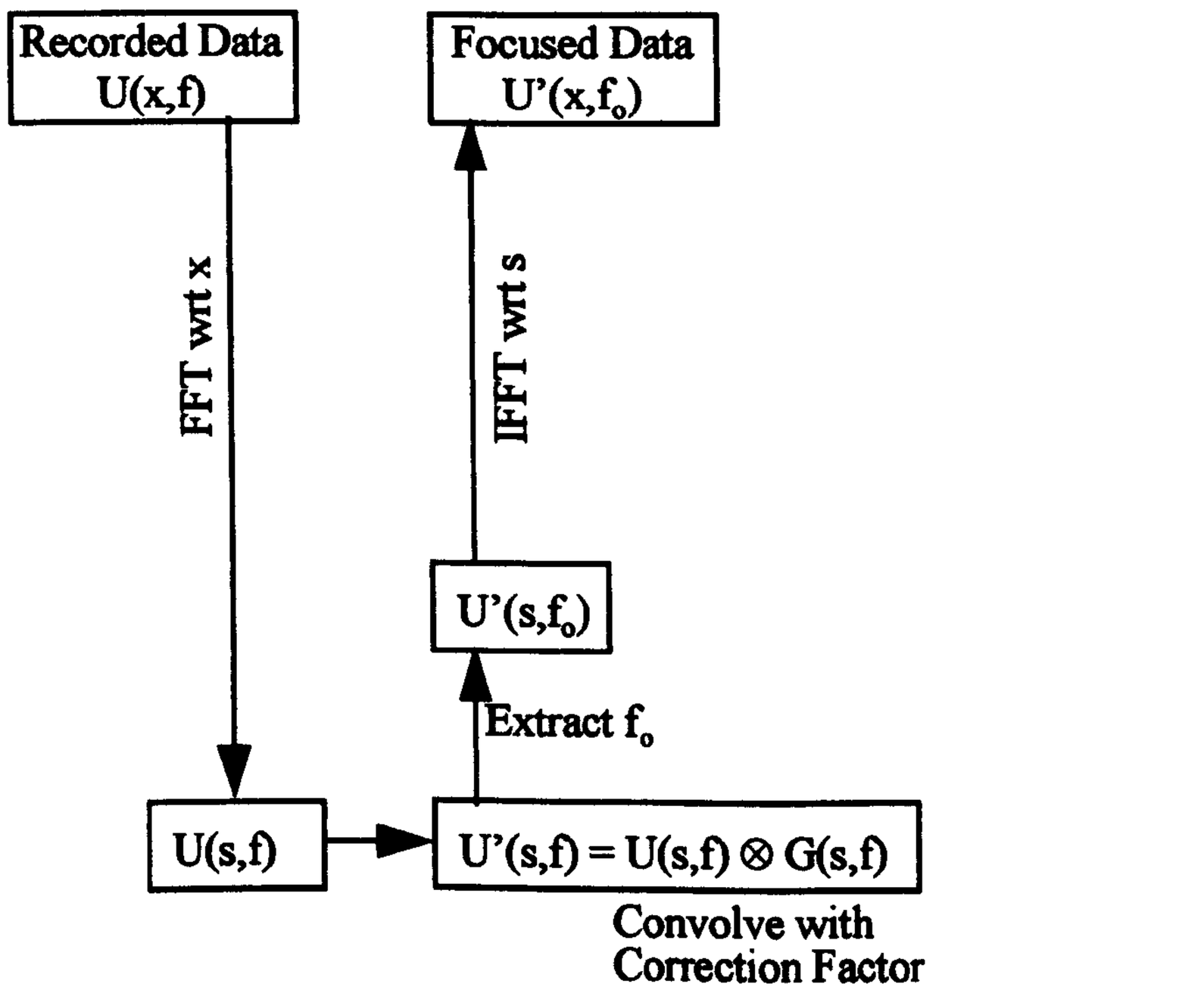

Figure 3.2 Illustration of the Convolutional Auto-Focusing Algorithm

Both the time domain and frequency domain correction processes are identical but the second one reduces the number of Fourier transforms required from four to two. Furthermore, the frequency domain approach employs a partial convolution process to obtain the centre frequency which is a fast and efficient implementation. Consequently, it is this second method that is utilised for the rest of the work.

3.2.1 Alternative Approach

In the early 1980s, Ahmed Yamani [63] also addressed the problem of multifrequency imaging and derived an auto-focusing algorithm from the backward propagation technique. Unsurprisingly, this derivation results in the same equations as described by equation (3-3) but approaches the problem from a completely different perspective. As such, it illustrates certain characteristics of the algorithm which are not easily understood from the previous approach and hence it is important to derive it in full here.

Using the concept of backward propagation developed in the previous chapter, equation (2-21) can be rewritten for a multifrequency system as

$$U(s,f,z) = U(s,f,0).\exp\left(\frac{-j4\pi fz}{c}\sqrt{1-\left(\frac{sc}{2f}\right)^2}\right) \qquad (3\text{-}7)$$

$$= U(s,f,0).\exp - j\phi(s,f)$$

Consider first just the exp-$j\phi(s,f)$ term of equation (3-7). It is this term that describes the change in phase which occurs during the propagation of the wave and which, in turn, brings about the defocusing of the image. Figure 3.3 shows a plot of the phase $\phi(s,f)$ against a range of frequencies for three point scatterers which are located at three different ranges, z_1, z_2 and z_3, from the aperture. From this, it can be seen that the phase is non linear with respect to frequency. However, over a small bandwidth, the phase for each scatterer can be approximated to the tangent of the phase at $f = f_o$ where f_o is the centre frequency.

The equation of the tangent of the phase can be obtained from the normal equation for a straight line, i.e.

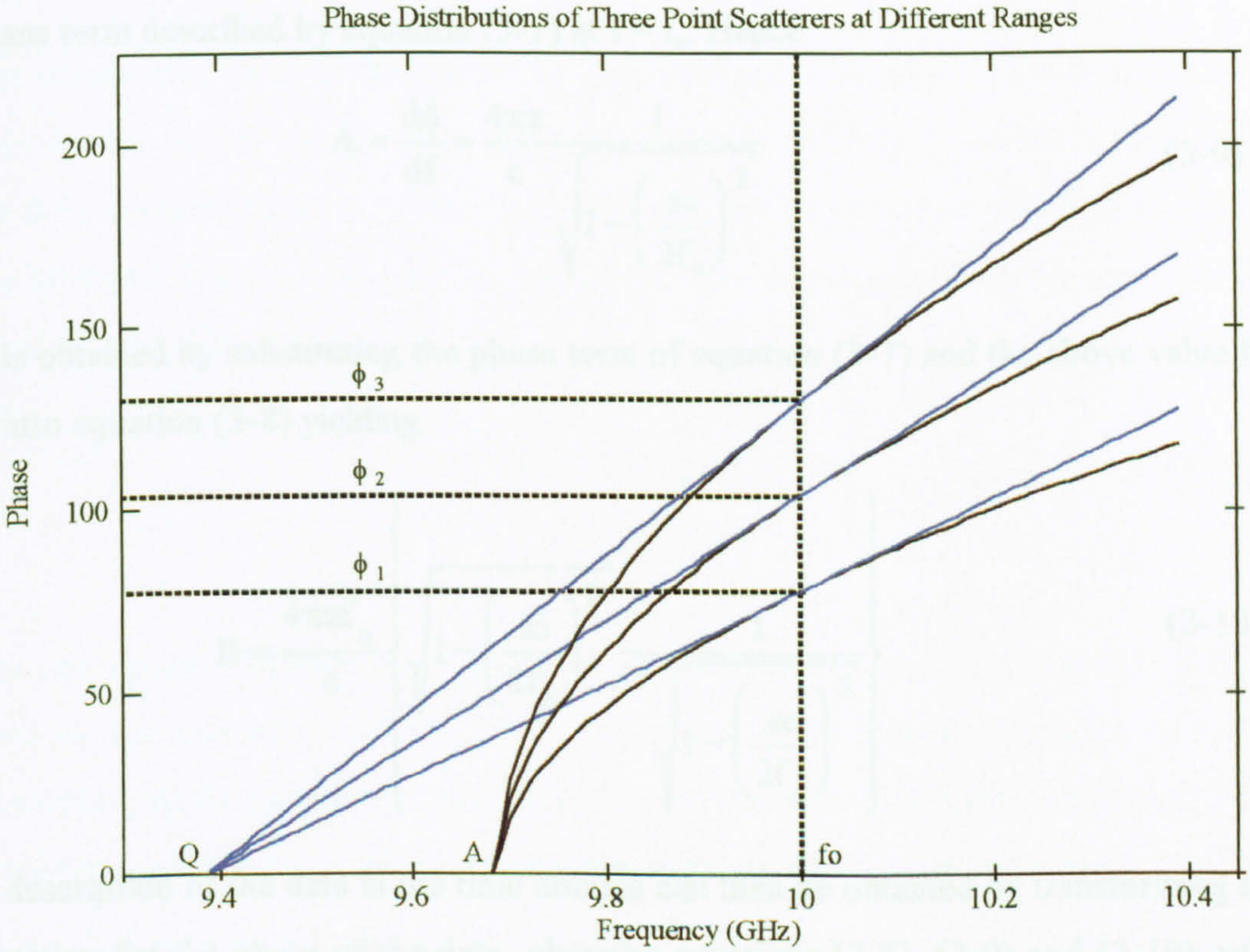

Points Q and A are given as $Q = f_o\left(\frac{sc}{2f_o}\right)^2$

$$A = \frac{sc}{2}$$

Figure 3.3 Phase Distribution of Three Point Scatterers at Three Different Ranges from the Aperture and their Tangents at $f=f_o$

$$\phi = Af + B \tag{3-8}$$

where ϕ is the phase, A is the gradient of the line at f_o and B is the point where the tangent line crosses the y axis. The gradient, A, can be obtained by differentiating the phase term described by equation (3-7) at $f = f_o$. Hence

$$A = \frac{d\phi}{df} = \frac{4\pi z}{c} \frac{1}{\sqrt{1 - \left(\frac{sc}{2f_o}\right)^2}} \tag{3-9}$$

B is obtained by substituting the phase term of equation (3-7) and the above value for A into equation (3-8) yielding

$$B = \frac{4\pi z f_o}{c} \left\{ \sqrt{1 - \left(\frac{sc}{2f_o}\right)^2} - \frac{1}{\sqrt{1 - \left(\frac{sc}{2f_o}\right)^2}} \right\} \tag{3-10}$$

A description of the data in the time domain can then be obtained by transforming the equation for the phase of the data, given by equations (3-8), (3-9) and (3-10), with respect to frequency f. Therefore,

$$U(s,t) = \int_{f_o-\Delta}^{f_o+\Delta} \exp - j(Af + B) \exp j2\pi ft \, df$$

$$= \int_{f_o-\Delta}^{f_o+\Delta} \exp - j\frac{4\pi z}{c} \left\{ \frac{(f - f_o)}{\sqrt{1 - \left(\frac{sc}{2f_o}\right)^2}} - f_o \sqrt{1 - \left(\frac{sc}{2f_o}\right)^2} \right\} \exp j2\pi ft \, df \tag{3-11}$$

which yields

$$U(s,t) = 2\Delta \exp \frac{-j4\pi f_o}{c} \left\{ zw - \frac{ct}{2} \right\} \frac{\sin\left\{ \frac{4\pi\Delta}{c} \left(\frac{z}{w} - \frac{ct}{2} \right) \right\}}{\frac{4\pi\Delta}{c} \left(\frac{z}{w} - \frac{ct}{2} \right)} \tag{3-12}$$

$$\text{where } w = \sqrt{1 - \left(\frac{sc}{2f_o}\right)^2}$$

In this case, Δ is used to denote half the bandwidth of the data.

The exponential term of the above equation represents the phase of the target in the time domain whilst the sinc term gives its amplitude. It is the phase term that causes the defocusing of the target. The time, t, for the signal to travel to and from the target can be found from this equation by setting the term in parentheses in the sinc function equal to zero. Therefore,

$$t = \frac{2z}{c} \frac{1}{\sqrt{1 - \left(\frac{sc}{2f_o}\right)^2}} \qquad (3\text{-}13)$$

The relationship between range and time provided by this equation is clearly not the same as that defined in equation (3-2). This is due to the fact that equation (3-2) is a description of the time-range relationship in the space domain whilst equation (3-13) provides a representation of the relationship in the spatial frequency domain.

Having established this relationship, the discussion of the focusing operation can be resumed. Referring once again to Figure 3.3, it can be seen that if the scatterers are to be focused at frequency f_o, then the data for the scatterers at z_1, z_2 and z_3, needs to be corrected by ϕ_1, ϕ_2 and ϕ_3 respectively. In the single frequency backward propagation technique, this cannot be done. However, it can be achieved in the multifrequency case, if the common intersection point Q shown in Figure 3.3 is shifted so that it is located at f_o. In such a case, the phase for all three targets would be zero at f_o. Therefore, correct compensation can be applied at f_o for all scatterers simultaneously.

The point of intersection, Q, of the tangent line with the frequency axis of Figure 3.3 (i.e. when $\phi = 0$) is then found to be

$$Q = f_o \left(\frac{sc}{2f_o}\right)^2 \qquad (3\text{-}14)$$

The shift in frequency, δf, needed to move the intersection point, Q, of the tangent

lines to the centre frequency can now be found.

$$\delta f = f_o - Q = f_o - f_o\left(\frac{sc}{2f_o}\right)^2 \tag{3-15}$$

Using the translation property of the Fourier transform [74], this shift in frequency can be considered as a time domain correction factor G(s,t) where

$$G(s,t) = \exp j2\pi f_o t\left(1-\left(\frac{sc}{2f_o}\right)^2\right) \tag{3-16}$$

Given that this equation has been derived from a spatial frequency domain representation of the recorded data, time t, is defined by equation (3-13). Substitution of this equation into equation (3-16) above gives,

$$G(s,z) = \exp\left(\frac{j4\pi f_o z}{c}\sqrt{1-\left(\frac{sc}{2f_o}\right)^2}\right) \tag{3-17}$$

which is identical to equation (3-3). Therefore, the analysis presented by Yamani is, once again, the application of the backward propagator to a multifrequency set of data. The algorithm hereafter is referred to as the multifrequency auto-focusing algorithm.

3.2.2 Time Domain Focusing

An examination of the focusing procedure in the spatial frequency time domain can be used to prove that the auto-focusing algorithm does indeed generate in-focus data. This is achieved by multiplying equation (3-12) for time domain data by the focusing operator of equation (3-4). Hence,

$$U'(s,t) = U(s,t).G(s,t) \tag{3-18}$$

which results in

$$U'(s,t) = 2\Delta\exp - j2\pi f_o t\frac{\sin\left\{\frac{4\pi\Delta}{c}\left(\frac{z}{w}-\frac{ct}{2}\right)\right\}}{\frac{4\pi\Delta}{c}\left(\frac{z}{w}-\frac{ct}{2}\right)} \tag{3-19}$$

$$\text{where } w = \sqrt{1 - \left(\frac{sc}{2f_o}\right)^2}$$

This equation consists of a sinc function at the location of the target and a fast varying phase term denoted by the exponential term. This high frequency phase term is not important and can be ignored since it is common to all targets. In other words, there is no range dependent phase shift associated with the data and hence the data is in-focus.

3.2.3 Analysis of the Correction Factor

For a full understanding of the focusing operation, the nature of the correction factor in the frequency domain is also investigated.

From equation (3-6) it can be seen that, in the frequency domain, the correction factor needed to shift the intersection of the phase values to f_o includes a sinc function. Given that frequency, f, and spatial frequency, s, are the only two variables in this equation, then the position of the central peak of the sinc function moves with varying spatial frequency.

Figure 3.4 shows the magnitude of the correction term G(s,f) plotted against frequency over a range of spatial frequencies, and clearly characterises the movement of the central peak of the correction factor.

When the correction factor is convolved with the recorded data, it is evident from Figure 3.5 that the correction factor is only convolved with part of the data (the area shaded grey). If the frequency bandwidth is increased then the range of spatial frequencies of the data available for the convolution process is increased and this in turn affects the resolution as will be demonstrated later. The data not convolved with the correction factor is ignored and therefore information is lost.

3.2.4 Determination of Convolution Limit

It is clearly important to establish the limits of the region where convolution occurs between the data and the correction factor. This can be achieved by determining the maximum spatial frequency of the region.

The maximum spatial frequency at which the data and the correction factor are

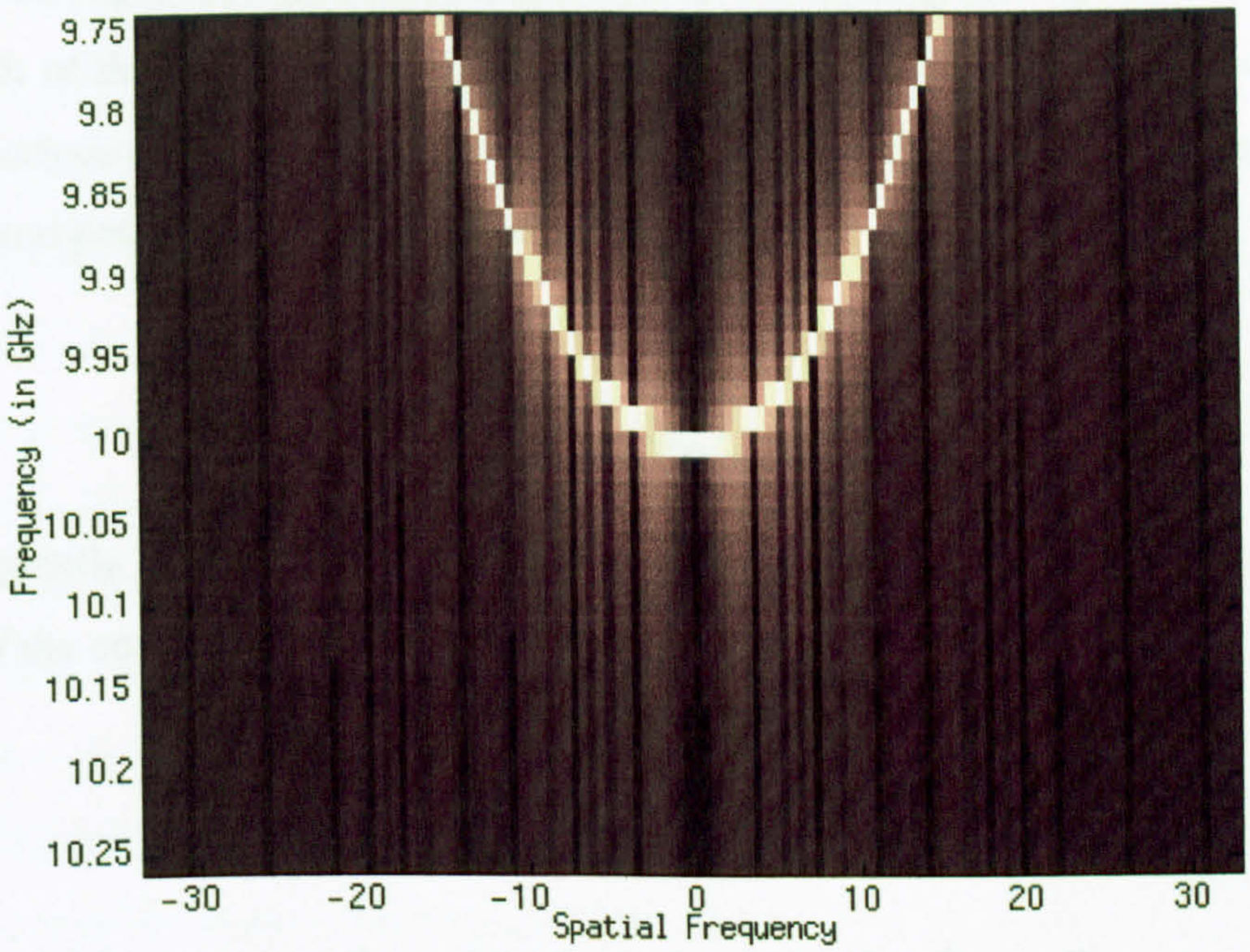

Figure 3.4 Magnitude of the Correction Factor G(s,f) Against Frequency and Spatial Frequency

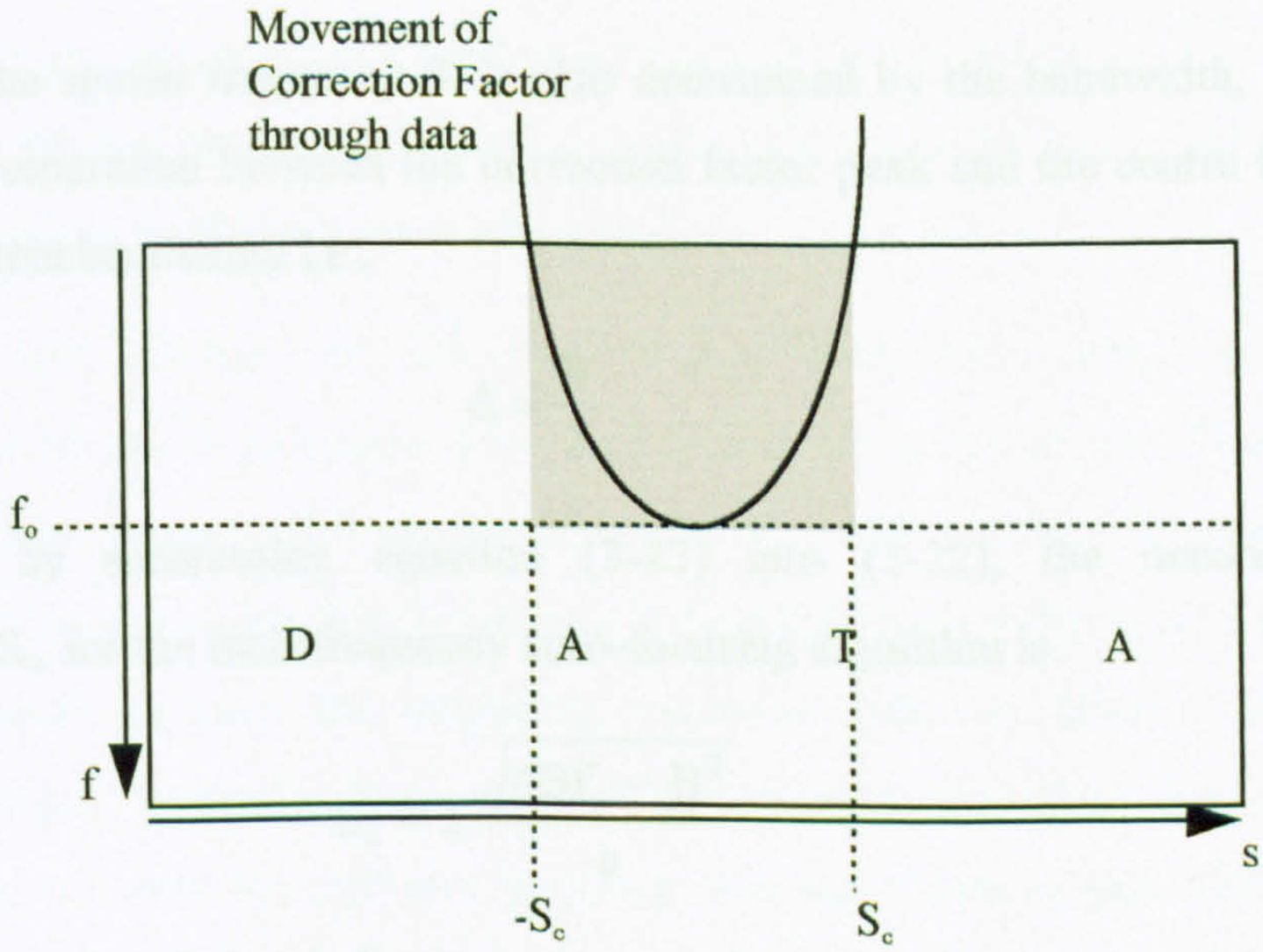

Figure 3.5 Representation of the Movement of the Correction Factor Peak Through the Recorded Data in the Spatial Frequency Domain

convolved together, S_c, can be formulated by considering the separation, Δ, between the peak of the correction factor, at $f=f_p$, and the centre frequency of the system, at $f=f_o$. Analysis of the sinc function of equation (3-6) shows that the frequency at which the central peak of the correction factor occurs is

$$f_p = f_o\sqrt{1-\left(\frac{sc}{2f_o}\right)^2} \tag{3-20}$$

Consequently, the frequency difference, Δ, between the centre frequency, f_o, and the peak of the correction factor, f_p, is given by

$$\Delta = f_o - f_p = f_o - f_o\sqrt{1-\left(\frac{sc}{2f_o}\right)^2} \tag{3-21}$$

The spatial frequency at the point where the correction factor first enters the data is termed S_c. At this point the separation between the correction factor peak and the centre frequency is

$$\Delta = f_o - f_p = f_o - f_o\sqrt{1-\left(\frac{S_c c}{2f_o}\right)^2} \tag{3-22}$$

However, the spatial frequency S_c is also determined by the bandwidth, B. In other words, the separation between the correction factor peak and the centre frequency is half the system bandwidth i.e.,

$$\Delta = \frac{B}{2} \tag{3-23}$$

Therefore, by substituting equation (3-23) into (3-22), the maximum spatial frequency, S_c, for the multifrequency auto-focusing algorithm is

$$S_c = \pm\frac{\sqrt{4Bf_o - B^2}}{c} \tag{3-24}$$

It can be seen that S_c is wholly dependent on the centre frequency and bandwidth of the system. It is not dependent on the range between the aperture and the target.

3.3 System Simulation

Simulation of the multifrequency auto-focusing algorithm is necessary to determine more about the nature of the algorithm and its characteristics. Initially, a one-dimensional system was considered and a single point scatterer was simulated and focused as is illustrated in Figure 3.6. The target is set 1m from a 1m aperture. The maximum spatial frequency marking the edge of the region of convolution is clearly visible and it is evident that the resolution of a single point scatterer is worse than that for the single frequency system. This will be discussed further in Section 3.3.1. The first sidelobe levels of the point target are slightly higher than those obtained using the backward propagation algorithm although not significantly so. However, the remaining sidelobes of the reconstructed multifrequency image are noticeably higher than those of the single frequency system.

The ability of the algorithm to automatically focus data at all ranges from an aperture is demonstrated in Figure 3.7. In this, three point scatterers at different ranges from a scanning aperture were simulated and then focused. The targets were placed, from left to right, at 0.9m, 1m and 1.2m from a 1m scanning aperture. As can be seen from the figure, all the targets are in focus although they have different amplitudes. The targets furthest from the aperture have the lowest value. The two offset scatterers appear at exactly ±0.25m and hence the distortion errors inherent in the backward propagation method described in Chapter 2 are eliminated.

There are two reasons for the loss of amplitude with target range. Firstly, electromagnetic waves propagate according to an inverse square law. Therefore, for a transmit-receive system, the amplitude received at the aperture is proportional to $1 / \text{range}^2$. To correct for this, the data can be multiplied by the square of the range and this greatly reduces the amplitude variations between different scatterers at different ranges. Secondly, as a scatterer is moved further from the aperture, the energy reflected from the scatterer becomes distributed over angles outside the field of view of the aperture and hence information is lost. This cannot be corrected for although its total effect on the reconstructed image is small due to the limiting effect of S_c.

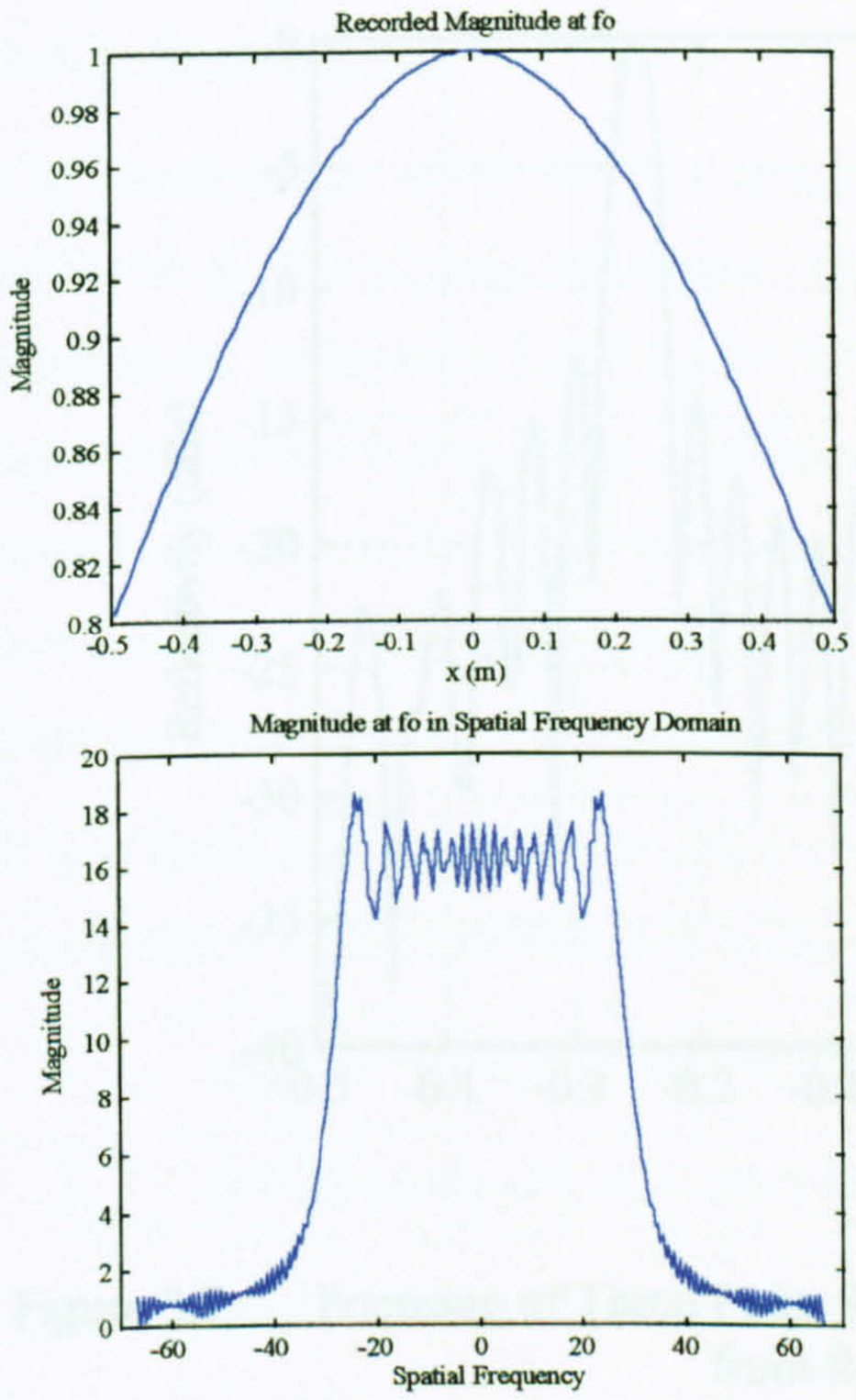

Figure 3.6 Magnitude and Phase Response of a Single Point Scatterer Before and After Application of the Auto-Focusing Algorithm

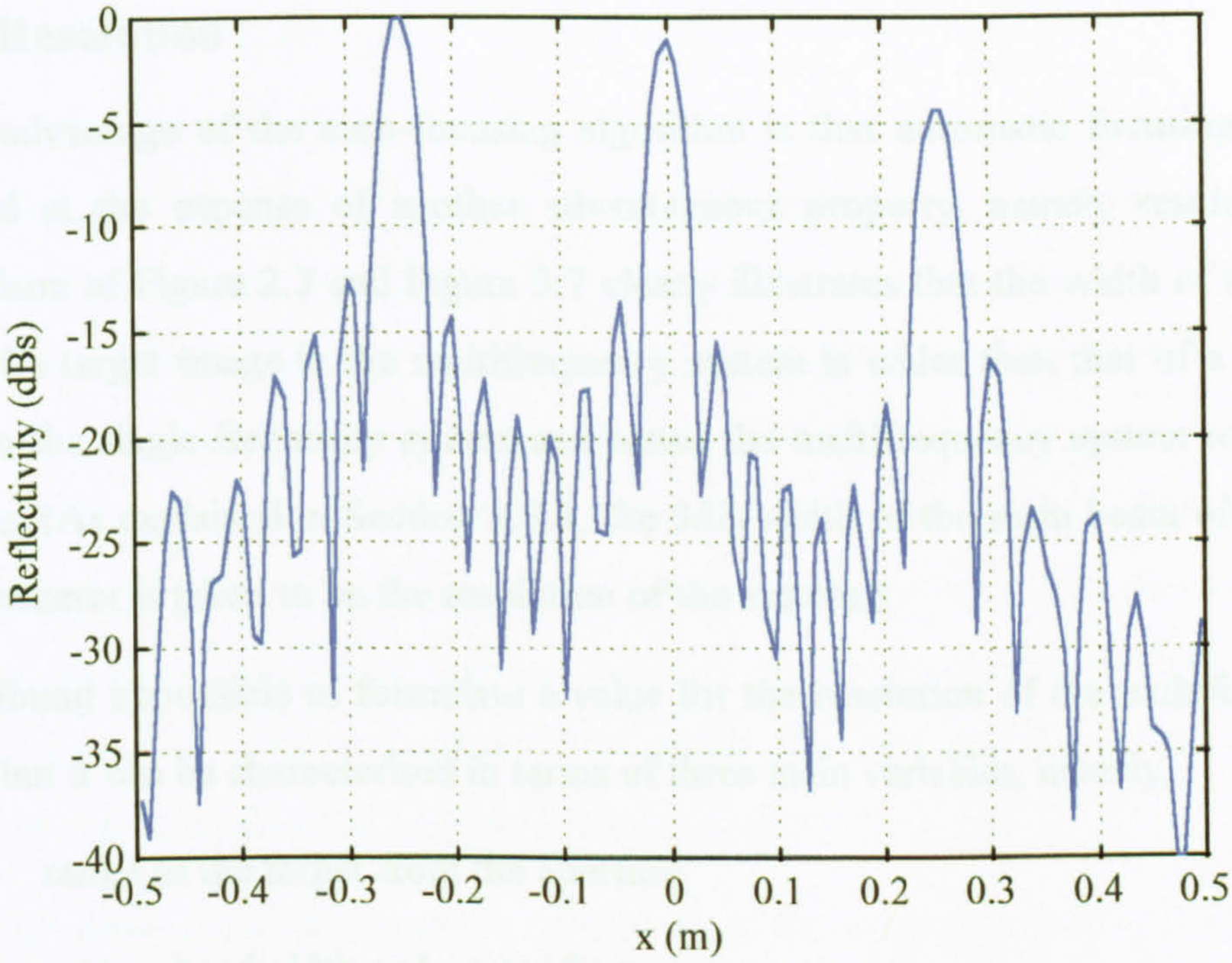

Figure 3.7 Focusing of Three Point Scatterers Located at Three Different Ranges from the Aperture

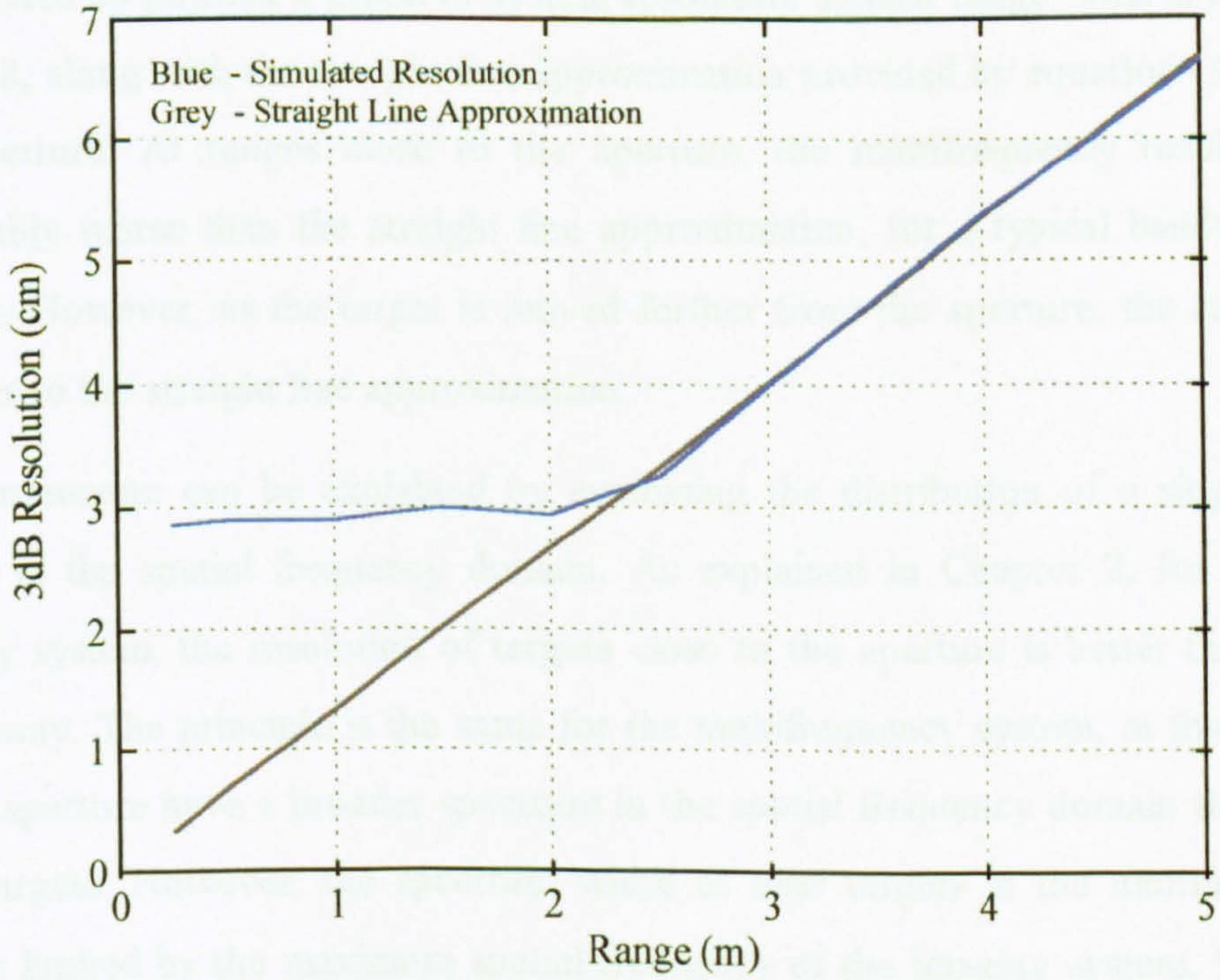

Figure 3.8 Resolution of the Multifrequency System Against Range

3.3.1 Resolution

The disadvantage of the auto-focusing algorithm is that automatic focusing is only achieved at the expense of another advantageous property, namely resolution. A comparison of Figure 2.3 and Figure 3.7 clearly illustrates that the width of the main beam of a target image in the multifrequency system is wider than that of a focused target in the single frequency system and hence the multifrequency system resolution is worse. (As explained in Section 2.3.3, the 3dB width of the main beam of a single point scatterer is taken to be the resolution of the system.)

It was found impossible to formulate a value for the resolution of the multifrequency system but it can be characterised in terms of three main variables, namely,

i. range of the target from the aperture

ii. system bandwidth and centre frequency

iii. aperture size.

Each of these three variables were examined in turn.

Firstly, the variation with respect to the range of the target from the aperture is demonstrated by plotting a graph of system resolution against range. This is shown in Figure 3.8, along with the straight line approximation provided by equation (2-27) for a 1m aperture. At ranges close to the aperture, the multifrequency resolution is considerably worse than the straight line approximation, for a typical bandwidth of 0.51GHz. However, as the target is moved further from the aperture, the resolution converges to the straight line approximation.

This phenomenon can be explained by examining the distribution of a single point scatterer in the spatial frequency domain. As explained in Chapter 2, for a single frequency system, the resolution of targets close to the aperture is better than those further away. The principle is the same for the multifrequency system, in that targets near the aperture have a broader spectrum in the spatial frequency domain than more distant targets. However, the spectrum width of near targets in the multifrequency system is limited by the maximum spatial frequency of the imaging system, S_c. Since S_c is constant then the resolution of near targets is constant. Targets further away are

not limited since the whole of their target spectra fall within $\pm S_c$.

The dependence of resolution on the system bandwidth is illustrated in Figure 3.9 where resolution for a 1m aperture is plotted against range for three different bandwidths along with the straight line approximation. It can be seen that larger bandwidths exhibit much better resolutions and that ultimately, the resolution of all bandwidths converges to the straight line approximation. Evidently, as the system bandwidth, B, is increased, then S_c, as defined by equation (3-24), also increases allowing higher spatial frequencies of the data to be convolved with the correction factor. It can therefore be seen that the choice of system bandwidth involves a trade-off between using a large bandwidth to obtain the best resolution and using a bandwidth that minimises the amount of data required.

Finally, the dependence of resolution on the size of the scanning aperture is illustrated in Figure 3.10 for three aperture sizes and a bandwidth of 0.51GHz. As expected from the single frequency results, the larger the aperture, the better the resolution. However, this is only true for distances away from the aperture. Close to the aperture, all the graphs converge to one line. This is due to the limiting effect that S_c has on the spatial frequency domain data of near targets as S_c is fixed regardless of aperture size.

Since the value of S_c has already been formulated, it is possible to derive an equation for the maximum resolution achieved for on-axis targets close to the aperture. Consider the diagram shown in Figure 3.11 which shows a rectangular function in the spatial frequency domain and its resulting image. It is well known that the dimension of the rectangular function in one domain governs the width of the sinc mainlobe in the other. In other words, the ratio of dimension B over dimension A is the same as the number of samples to the first null of the sinc function. In the case of the auto-focusing algorithm, A is $2S_c$ and B is $2S_{max}$ so the width to the first null, η, of the sinc function is

$$\eta = \frac{S_{max}}{S_c} dx \tag{3-25}$$

and the maximum 3dB resolution, δ_m, is given by

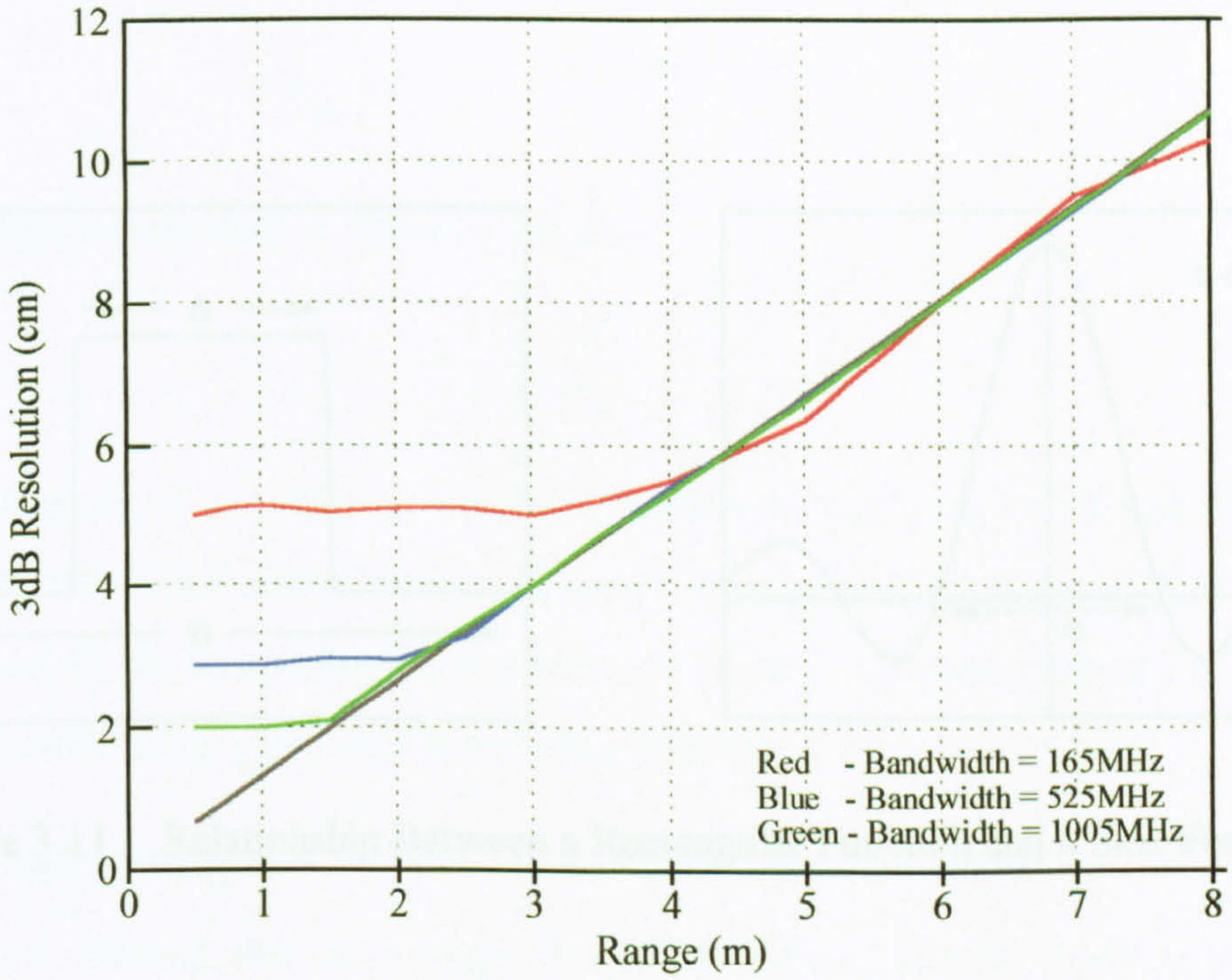

Figure 3.9 Resolution of the Multifrequency System for Different Bandwidths

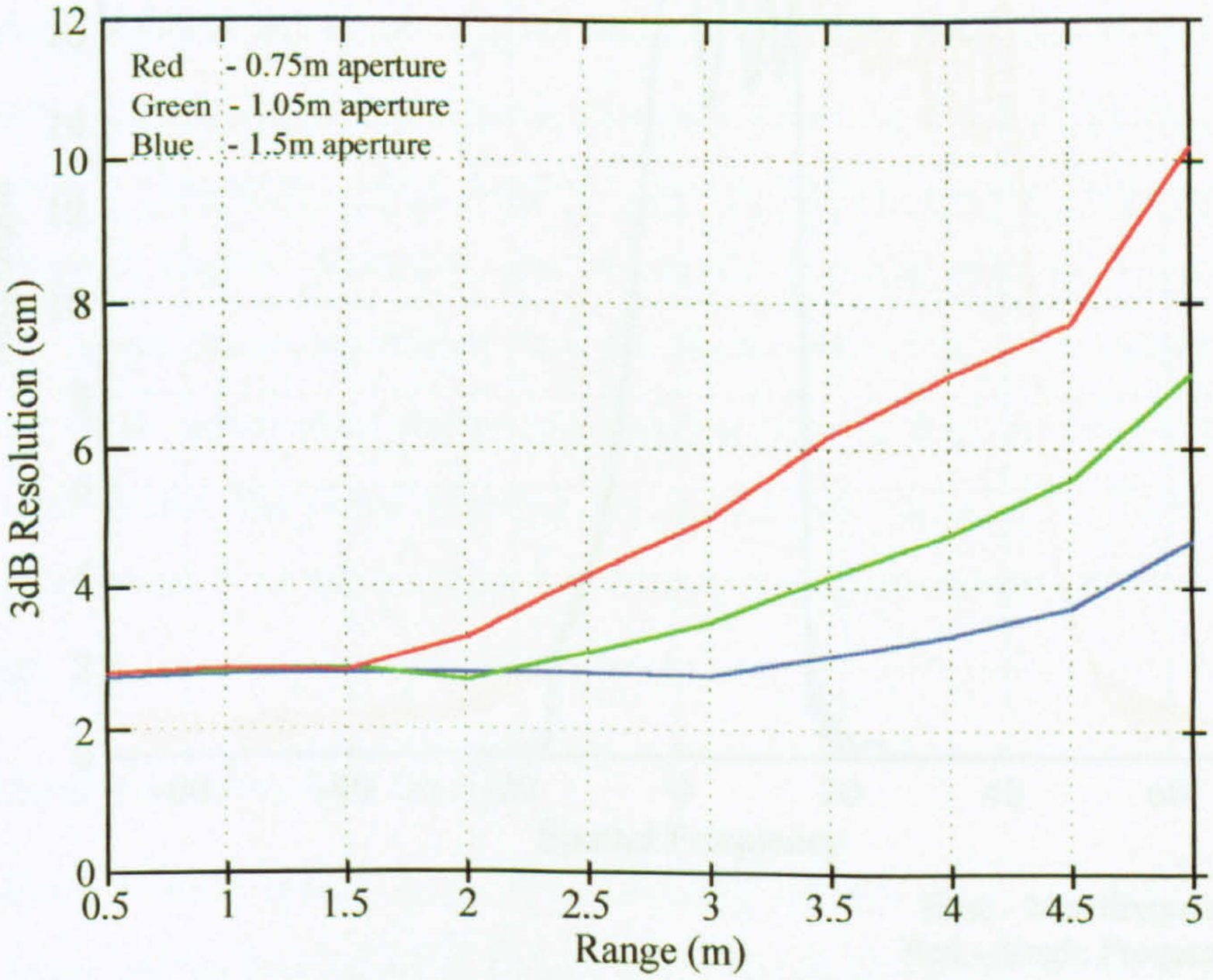

Figure 3.10 Resolution of the Multifrequency System for Different Aperture Sizes

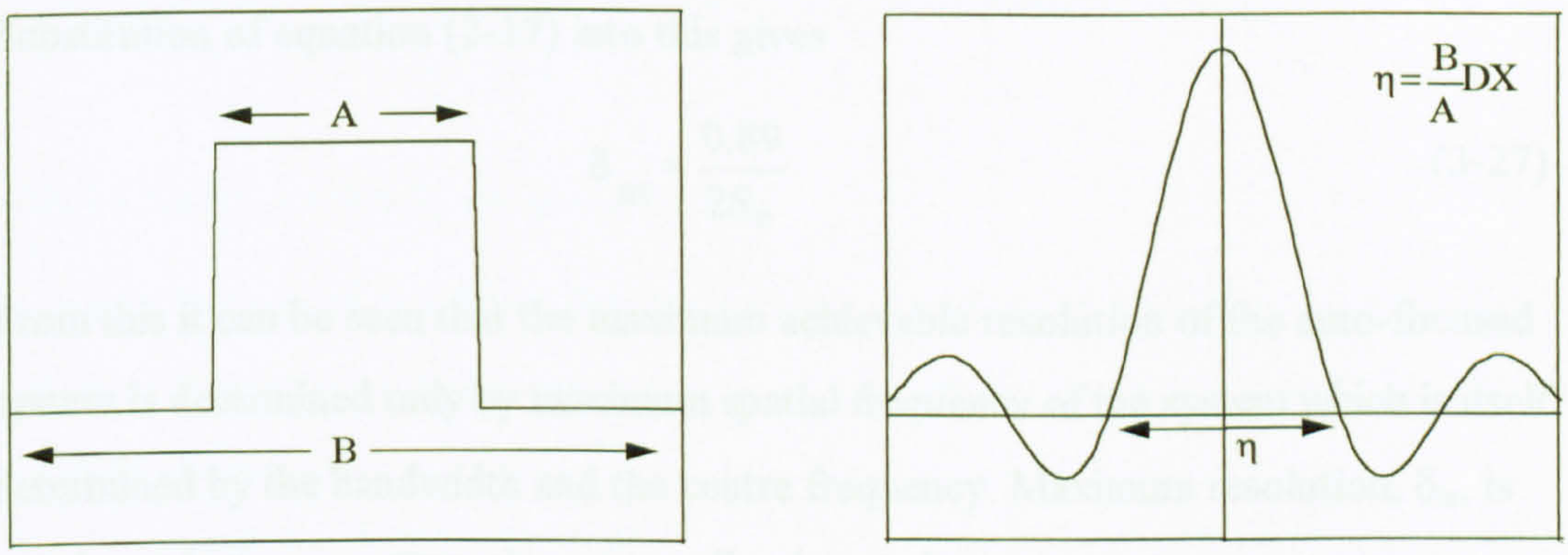

Figure 3.11 Relationship Between a Rectangular Function and a Sinc Function

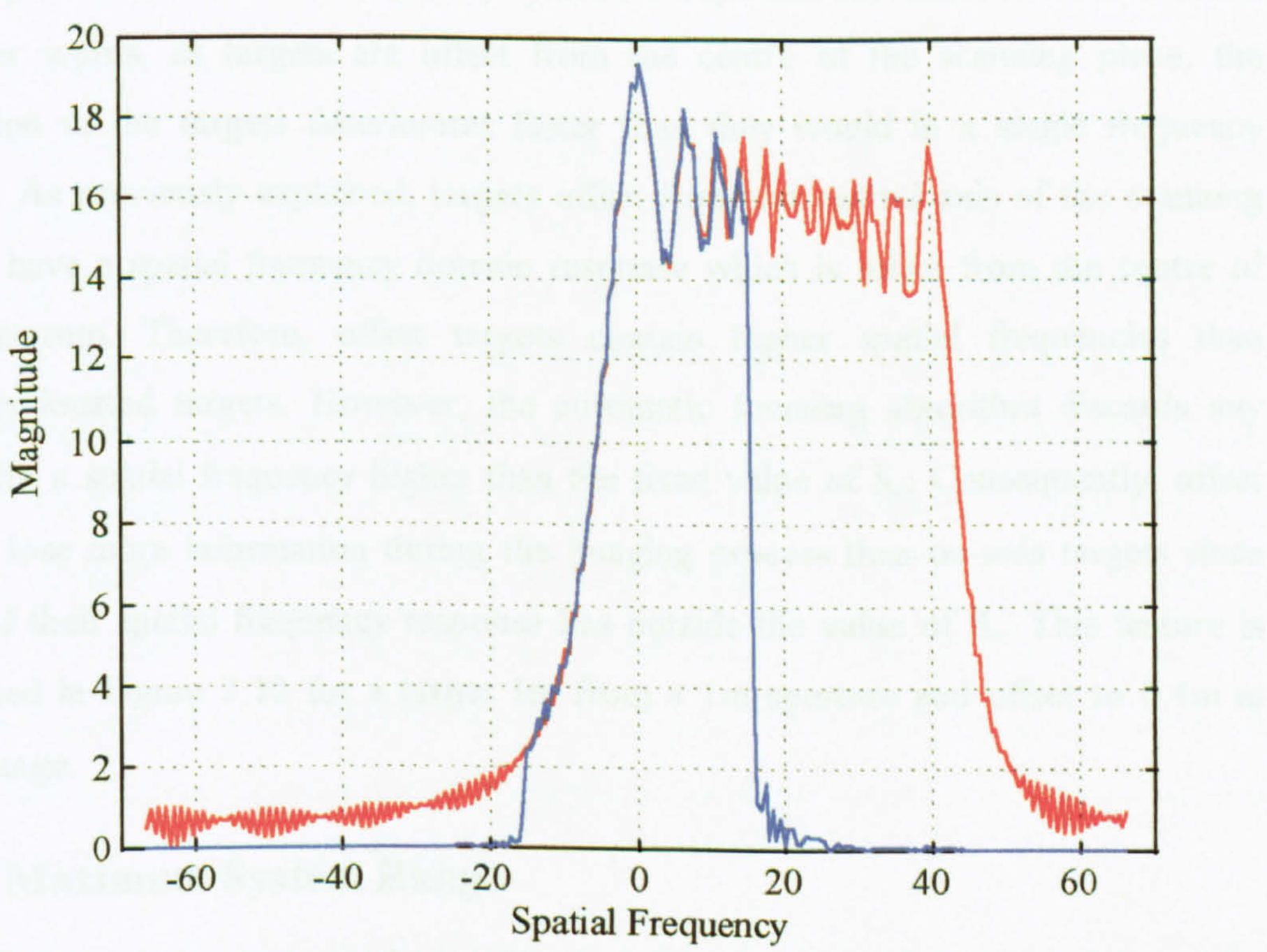

Blue - Multifrequency System
Red - Single Frequency System

Figure 3.12 Spatial Frequency Domain Response of an Offset Target

$$\delta_m = 0.89\eta = \frac{0.89 S_{max}}{S_c} dx \qquad (3\text{-}26)$$

Substitution of equation (2-17) into this gives

$$\delta_m = \frac{0.89}{2S_c} \qquad (3\text{-}27)$$

From this it can be seen that the maximum achievable resolution of the auto-focused system is determined only by maximum spatial frequency of the system which is itself determined by the bandwidth and the centre frequency. Maximum resolution, δ_m, is not dependent on aperture size or sampling interval.

3.3.1.1 Offset Targets

Figure 2.5 showed that in a single frequency system, targets at the edge of the scanning aperture have a worse resolution than those on the central axis. The same difficulty occurs in the multifrequency system, except that the effect is more evident. In other words, as targets are offset from the centre of the scanning plane, the resolution of the targets deteriorates faster than they would in a single frequency system. As previously explained, targets offset from the central axis of the scanning system have a spatial frequency domain response which is offset from the centre of the spectrum. Therefore, offset targets contain higher spatial frequencies than centrally located targets. However, the automatic focusing algorithm discards any data with a spatial frequency higher than the fixed value of S_c. Consequently, offset targets lose more information during the imaging process than on-axis targets since more of their spatial frequency response lies outside the value of S_c. This feature is illustrated in Figure 3.12 for a target 1m from a 1m aperture and offset to 0.4m in cross range.

3.3.2 Maximum System Range

The maximum system range, R_{max}, of an imaging system is the maximum range at which a target can be located from an aperture and still be focused correctly. In most systems, this value is determined by the limits of the Fourier Transform. In the time domain, the limits of the Fourier Transform are defined as

$$\text{limit} = \begin{cases} 0..\dfrac{1}{df} & \text{for a one - sided transform} \\ \dfrac{-1}{2df}..\dfrac{1}{2df} & \text{for a two - sided transform} \end{cases} \tag{3-28}$$

where df is the frequency sampling interval.

To make full use of the limits Fourier domain, a one-sided transform is used. Given that time is related to range via equation (3-2) then the maximum range that can be achieved is given by

$$R_{max} = \frac{c}{2df} \tag{3-29}$$

If the maximum target range from the aperture is known, then the above equation determines the maximum frequency sampling interval that can be used to collect the data.

3.3.3 Complex Targets

As has been discussed in the previous chapter, it is important to simulate the results obtained from targets more complex than individual point scatterers. Therefore, a 30cm long cylinder composed of 40 point scatterers, each set quarter of a wavelength apart, was simulated. The cylinder was placed horizontally in a plane parallel to the scanning aperture and at a distance of 1.5m from it. Figure 3.13a shows the reconstructed response of such a cylinder obtained by application of the auto-focusing imaging algorithm along with the cylinder's distribution in the spatial frequency domain. The response is almost identical to that obtained using the single frequency backward propagation algorithm, shown in Figure 2.8a, with an almost constant distribution over the region where the cylinder is located, except that in this case, the sidelobe levels are just slightly higher.

If the cylinder is rotated in the x-z plane, with the left hand end moving closer to the aperture and the right hand end moving further away, then the image rapidly starts to slope down at the right hand end. This is due to the right hand end of the target being further from the aperture and therefore a smaller angular spectrum of data is received.

a)
θ=0°

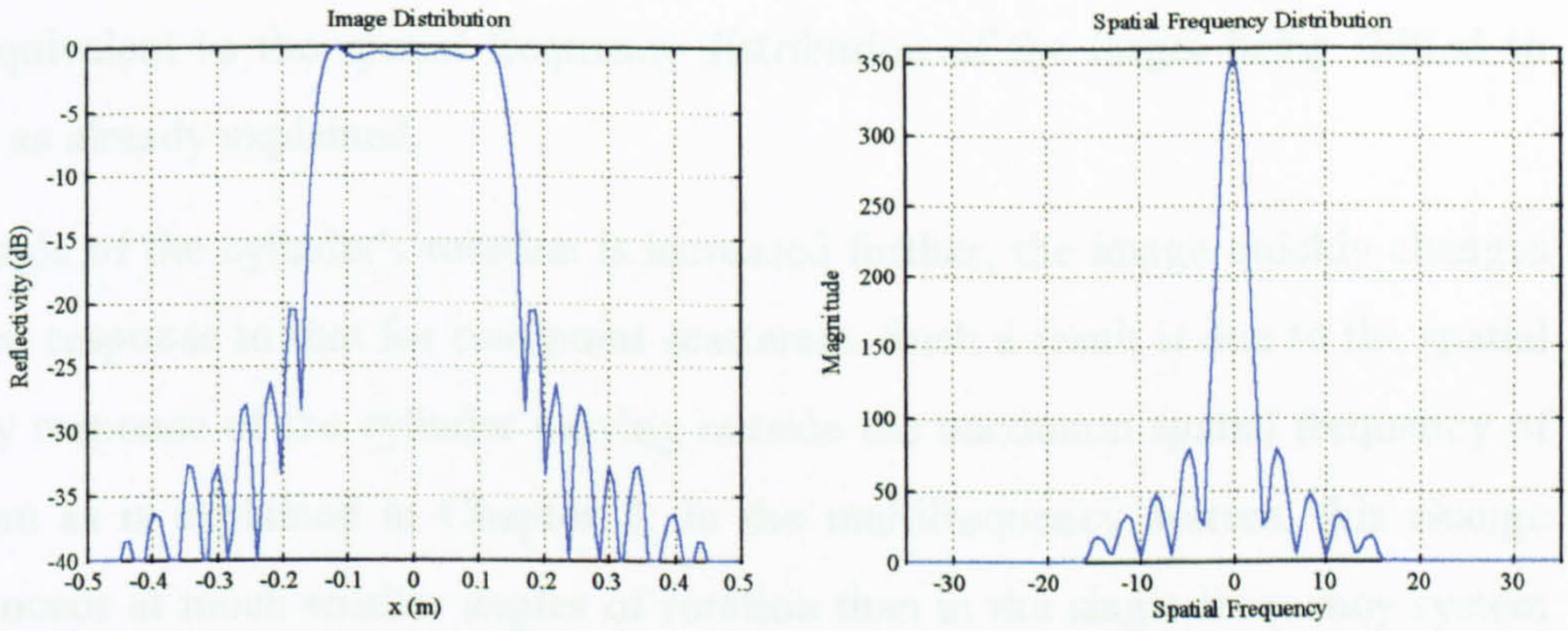

b)
θ=10°

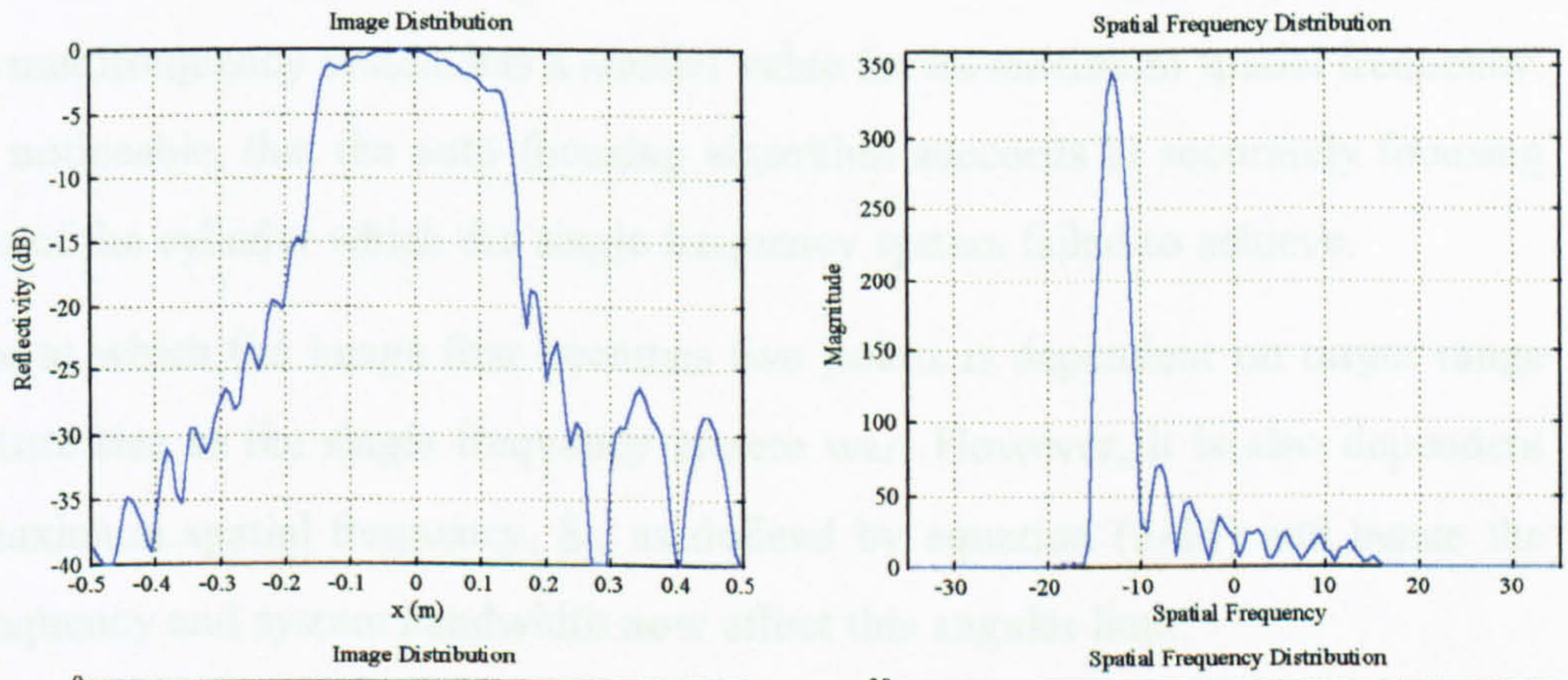

c)
θ=25°

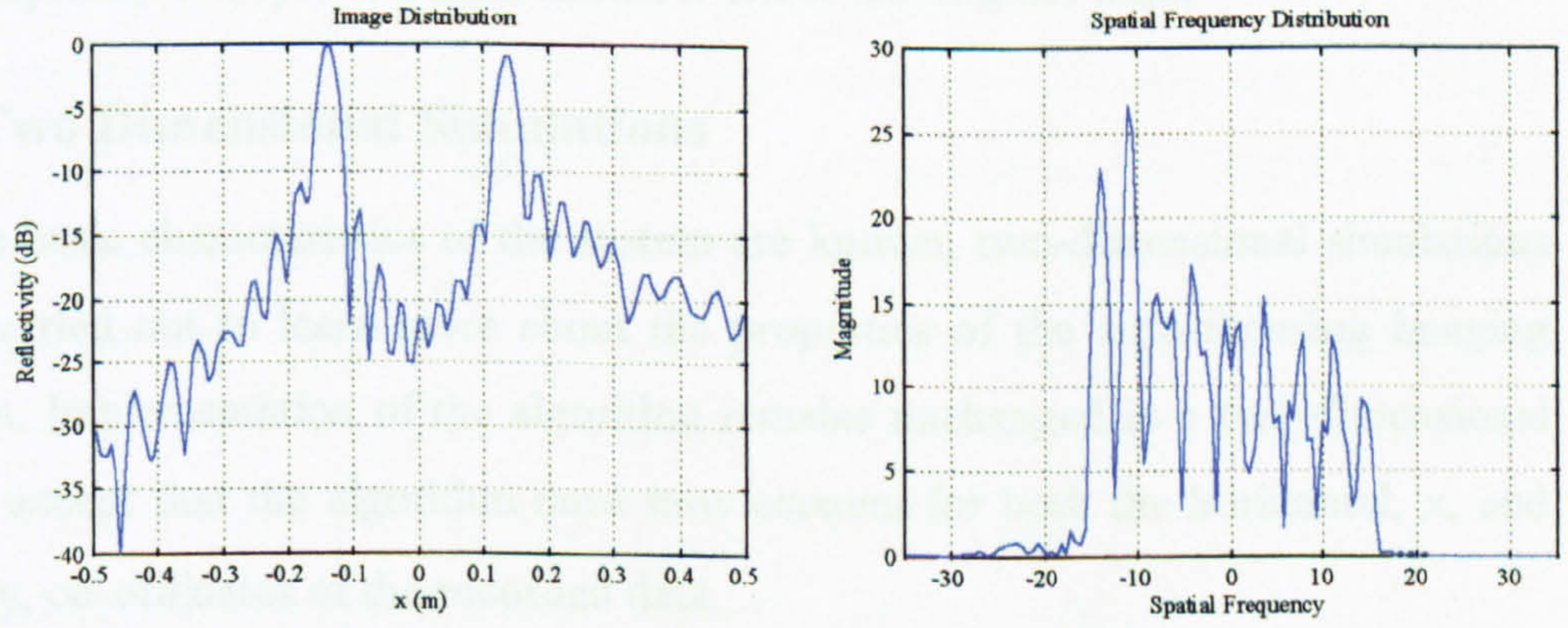

d)
θ=50°

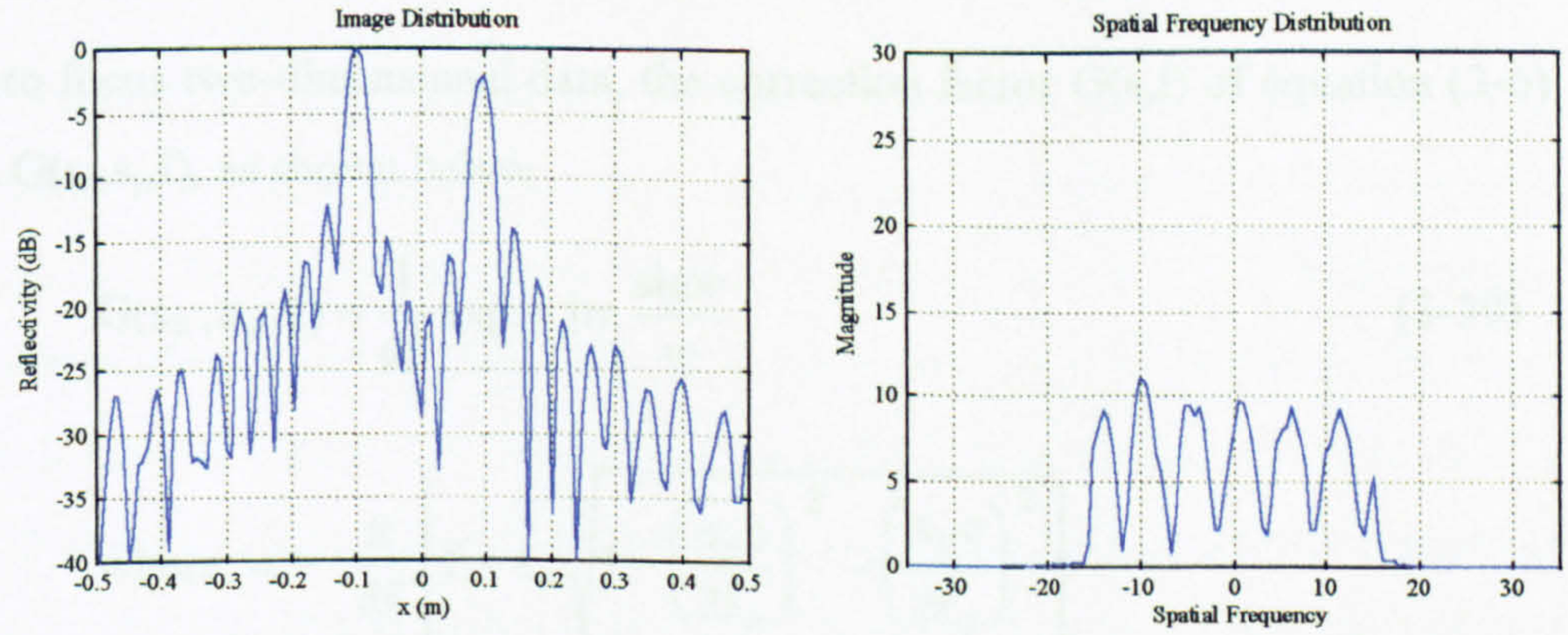

Figure 3.13 Reconstructed Image and Spatial Frequency Domain Response of a Rotated Horizontal Cylinder

This is equivalent to the spatial frequency distribution of the target being shifted to one side, as already explained.

As the angle of the cylinder's rotation is increased further, the image quickly changes from a flat response to that for two point scatterers. Such a result is due to the spatial frequency response of the cylinder moving outside the maximum spatial frequency of the system as is explained in Chapter 2. In the multifrequency system, this change starts to occur at much smaller angles of rotation than in the single frequency system since the multifrequency system has a smaller value for its maximum spatial frequency. It is also noticeable, that the auto-focusing algorithm succeeds in accurately focusing both ends of the cylinder which the single frequency system failed to achieve.

The angle at which the image first becomes two points is dependent on target range and aperture size as the single frequency system was. However, it is also dependent on the maximum spatial frequency, S_c, as defined by equation (3-24) and hence the centre frequency and system bandwidth now affect this angular limit.

3.3.4 Two Dimensional Simulations

Once the basic characteristics of the system are known, two-dimensional simulations can be carried out to learn more about the properties of the auto-focusing imaging algorithm. Implementation of the algorithm remains unchanged in a two-dimensional scenario except that the algorithm must now account for both the horizontal, x, and vertical, y, co-ordinates of the recorded data.

In order to focus two-dimensional data, the correction factor G(s,f) of equation (3-6) becomes $G(s_x,s_y,f)$, as shown below

$$G(s_x, s_y, f) = \frac{1}{df} \exp - jw.\frac{\sin w}{w} \qquad (3\text{-}30)$$

$$\text{where } w = \frac{\pi}{df}\left\{ f - f_o\sqrt{1-\left(\frac{s_x c}{2f_o}\right)^2 - \left(\frac{s_y c}{2f_o}\right)^2} \right\}$$

Similarly, equation (3-24) for the maximum spatial frequency is now expanded to give the maximum spatial frequencies in s_x and s_y, i.e. S_{xc} and S_{yc}.

$$S_{xc}^{\ 2} + S_{yc}^{\ 2} = \frac{4Bf_o - B^2}{c^2} \tag{3-31}$$

This is the equation of a circle with a radius ω, of

$$\omega = \frac{\sqrt{4Bf_o - B^2}}{c} \tag{3-32}$$

Therefore, it can be seen that when the data is convolved with the two dimensional correction factor, the data becomes limited to a circle of radius ω.

Figure 3.14 shows the two-dimensional image of a point scatterer focused by means of the auto-focusing algorithm. The first sidelobe levels of the focused point scatterer are only slightly higher than those obtained from the two-dimensional single frequency results. However, the sidelobes extend for a wide region around the mainbeam. It can also be seen in this image that there are two sets of sidelobes. Firstly, there is a set of concentric circular sidelobes surrounding the main beam of the scatterer. These are the result of the Fourier transform of a circular boundary [61] caused by the spatial frequency domain data being limited to a circle. Secondly, there are four spikes emanating outwards from the main beam. These are caused by the Fourier transform of a square bounded region [74]. Simulations show that the nature of the sidelobe structure nearly always contains the elements of both square and circular transforms, but the contributions of each of these varies with both range of the target from the aperture and its offset from the central axis of the imaging system.

Consider initially, the spatial frequency domain response of a target located on the central axis of the system. In a two-dimensional system, the amplitude of a target in this domain is in the form of a square function extending over s_x and s_y with a ripple running across the top of the response. This was previously illustrated in the one-dimensional case in Figure 3.6. As already described, targets that are close to the aperture contain a wide range of spatial frequencies. The highest spatial frequency generated by the scatterer is higher than the maximum spatial frequency used by the imaging system, S_c. Therefore, the scatterer response is limited to a circle when the scatterer is convolved with the correction factor. This is shown in Figure 3.15 and results in an image of the scatterer where the circular sidelobes dominate. However, if

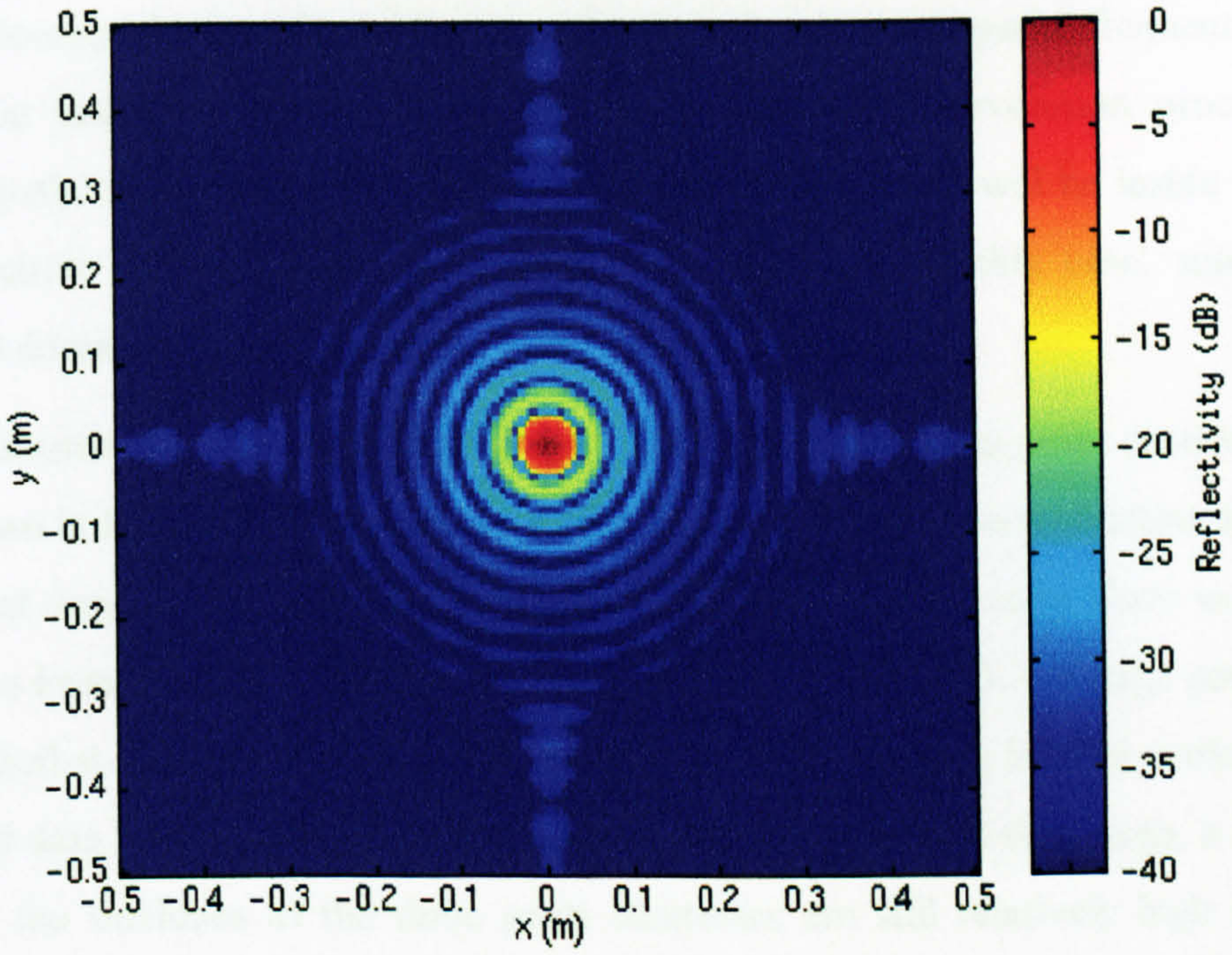

Figure 3.14 Two Dimensional Image of a Single Point Scatterer, 1m from a 1m Aperture, Focused with the Auto-Focusing Algorithm

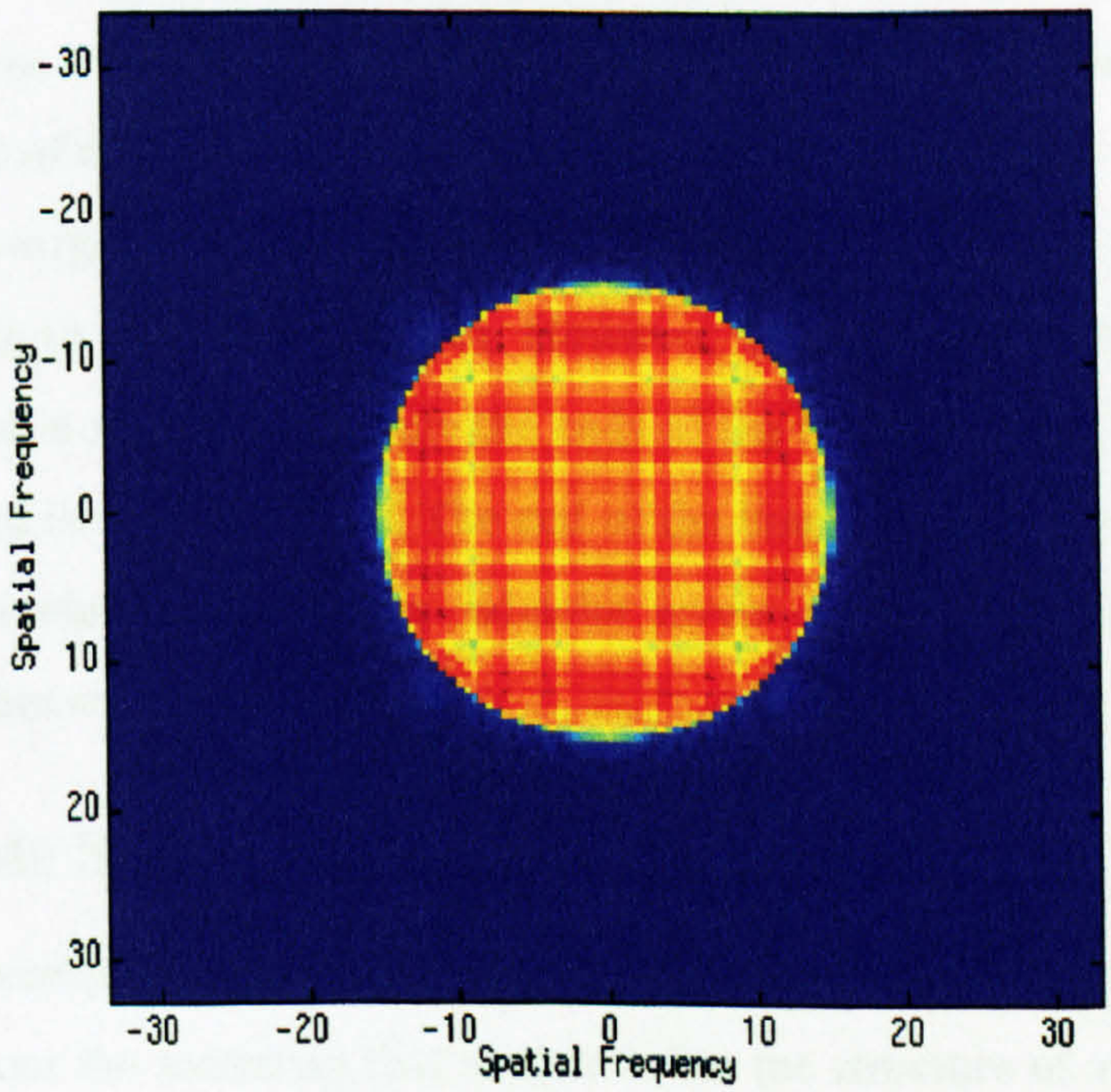

Figure 3.15 Two Dimensional Spatial Frequency Domain Spectrum of the Data After Focusing

the target is located further away from the aperture, then all the spatial frequencies describing that target will be less than S_c. Hence when the convolution process occurs, the spatial frequency domain of the whole target response will be inside the convolution circle and will keep its naturally square shape. In this case, square sidelobes will dominate.

Figure 3.16 illustrates a two-dimensional representation of the three point scatterers formerly shown in Figure 3.7. It can be seen that the peak value of each scatterer is at the same level despite the different ranges from the target. This occurs since range correction has been carried out on the data as described in Section 3.3. Range gating was also applied at the same time to limit the sidelobes. Range gating is most useful in real measured data to remove unwanted environmental reflections. In the image, it can be seen that the sidelobes of the three point scatterers are still relatively high and hence it is preferable to remove them by filtering. Suitable filtering techniques will be described in Section 3.6.

Finally, a third two-dimensional simulation was carried out to simulate three cylinders located at different orientations and angles with respect to the scanning aperture. This was a repeat of the simulation carried out in Section 2.3.5 for the single frequency system with three cylinders arranged to represent the trunk and two branches of a tree. The results of the multifrequency simulation are shown in Figure 3.17. Clearly all elements of the target structure are in focus, whereas in the single frequency case, it was not possible to focus the branches. However, one of the branches is not visible since it is angled in range so that only the ends of the branch can be seen and not the main response of the cylinder itself. The end of the branch can be seen to be in-focus. The reduced resolution and higher sidelobe levels associated with this particular imaging algorithm are also noticeable.

3.4 Multiple Scattering

Section 2.4 investigated the ability of the single frequency backward propagation algorithm to focus the scattering that occurs within the structure of a target object. A similar investigation must also be considered for the automatic focusing algorithm. This can be done by examining the case of two targets placed a few centimetres apart.

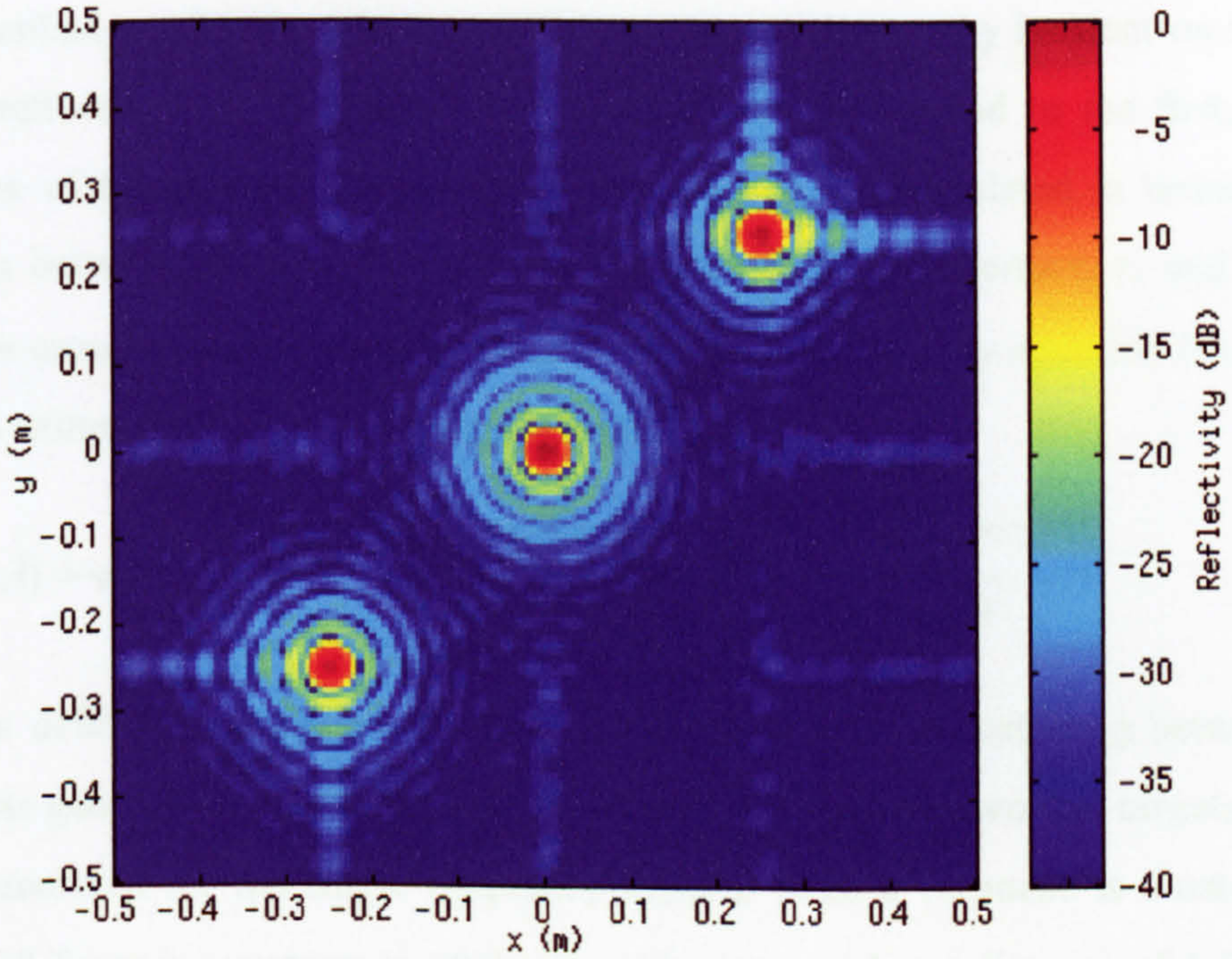

Figure 3.16 Two Dimensional Image of Three Point Scatterers Located at Three Different Ranges from the Aperture

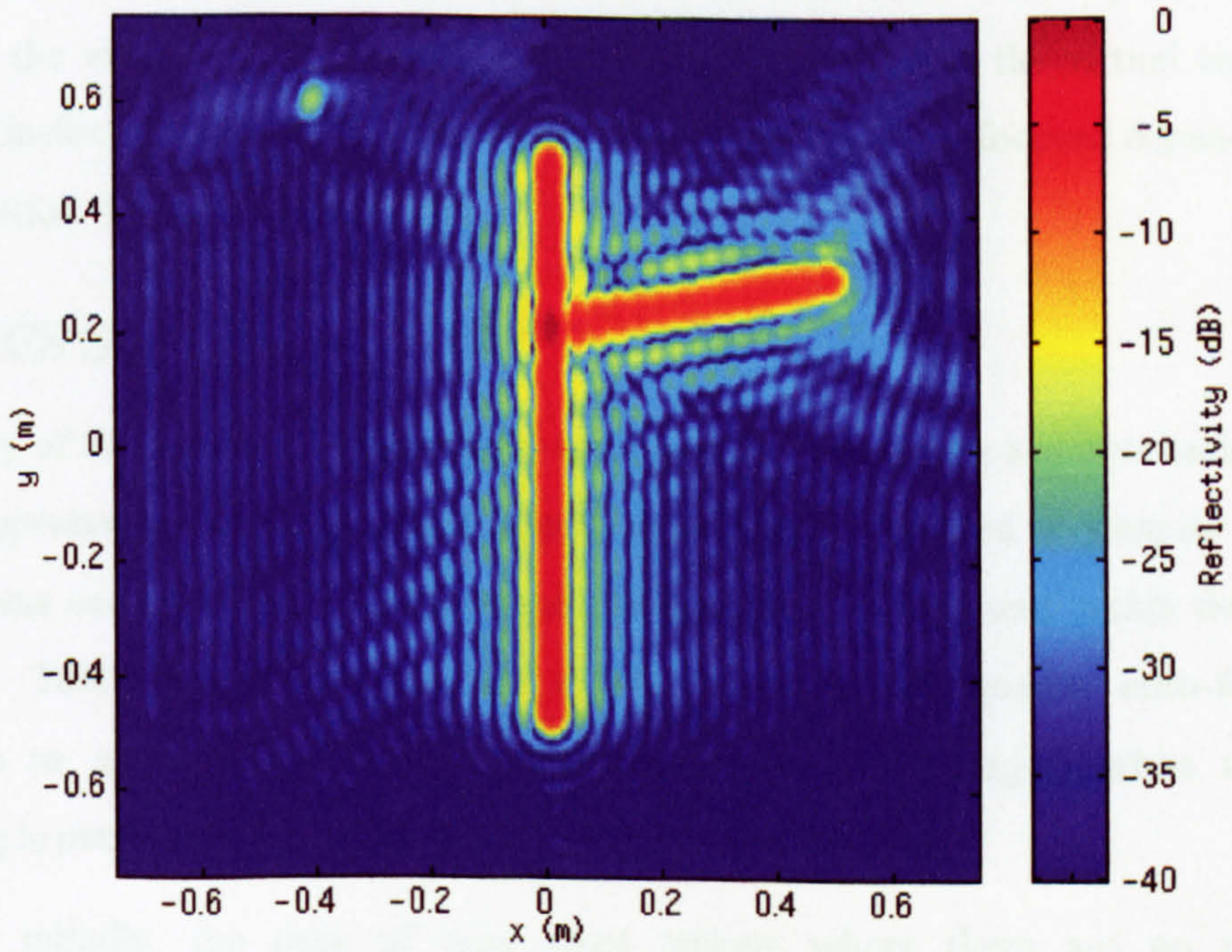

Figure 3.17 Two Dimensional Image of a Simulated Tree Composed of Three Cylinders

If, as described previously, it is assumed that some of the energy incident on the first target is reflected from the second and equally from the second to the first, then a description of the signal received at the aperture can be formulated in terms of the separation between the targets, D, their distances from the aperture, r_1 and r_2, and their radar cross section, σ. This is described in Section 2.4.1 by equation (2-34) and can be re-written for a multifrequency systems as,

$$U(x,f) = \sqrt{\sigma}\frac{e^{-j2\pi f r_1/c}}{r_1^{\,2}} + \sqrt{\sigma}\frac{e^{-j2\pi f r_2/c}}{r_2^{\,2}} + \frac{\sigma}{D\sqrt{\pi}}\frac{e^{-j\pi f(r_1+D+r_2)/c}}{r_1 r_2 D} \qquad (3\text{-}33)$$

σ is again defined by equation (2-35). It was found that the scattering between the two targets generates a 'virtual scatterer' half way between the two real targets similar to that generated for the single frequency system. Such a response is illustrated in Figure 3.18 for two scatterers at ±0.2m in cross-range and at a distance of 1.5m from a 1m aperture. It is assumed that the targets are spheres with a radius of 5cm. It can be seen that the virtual scatterer is in-focus although its first sidelobe levels are fairly high. As the two real targets are moved closer together, the response of the virtual target increases. This can be explained by examination of the above equation. As the separation between the scatterers, D, decreases, the third term in the equation, which describes the virtual target, increases. Simulations showed that the virtual term was generally in-focus, although in some cases, it was found to be defocused depending on the separation, D, relative to r_1 and r_2.

3.4.1 RCS Simulations

The ability of the backward propagation technique to generate an accurate radar cross section representation of two point targets was also investigated in Chapter 2. The attempt was successful except when multiple scattering was present within the target structure. This section examines the ability of the multifrequency auto-focusing algorithm to generate the correct radar cross section of targets when multiple scattering is present.

Consider initially, the case of two point targets where there are no multiple interactions present. The targets are set 0.2m apart at a distance of 1m from a 1m

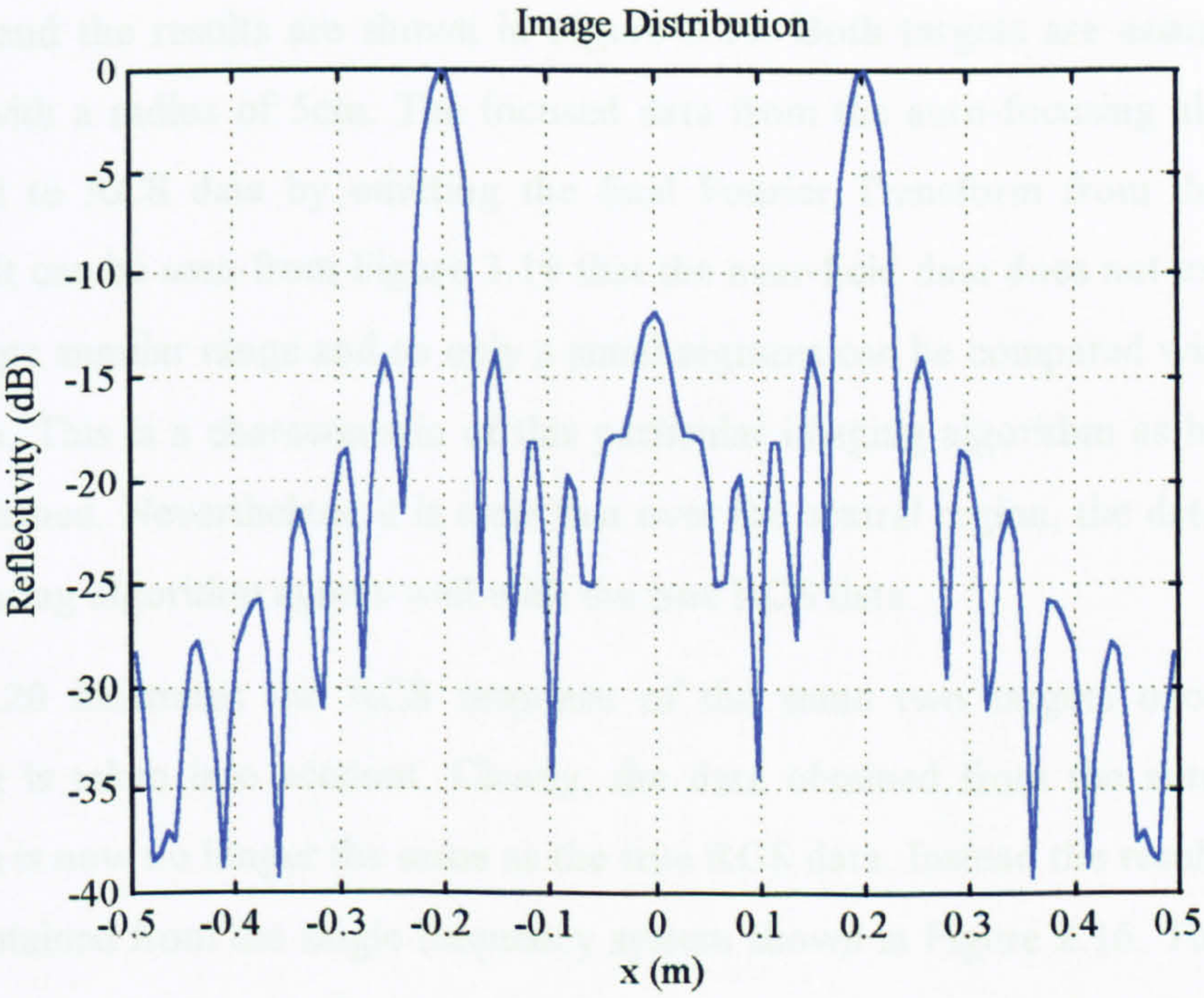

Figure 3.18 One Dimensional Image of Multiple Scattering Occurring Between Two Point Targets

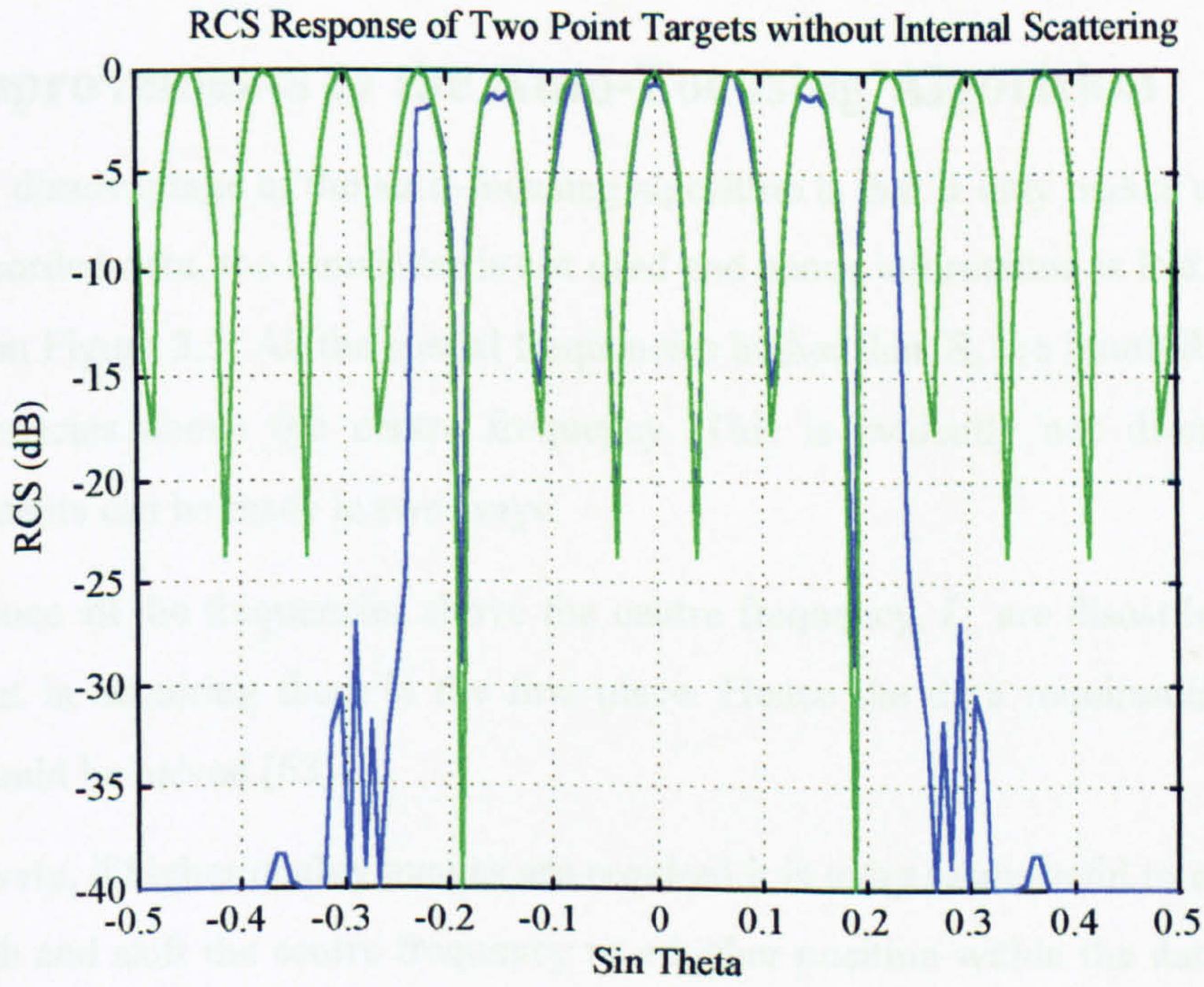

Blue - Multifrequency Data
Green - RCS Data

Figure 3.19 RCS Response of Two Point Targets Without Multiple Scattering

aperture and the results are shown in Figure 3.19. Both targets are assumed to be spheres with a radius of 5cm. The focused data from the auto-focusing algorithm is converted to RCS data by omitting the final Fourier Transform from the imaging process. It can be seen from Figure 3.19 that the near-field data does not extend over a very large angular range and so only a small segment can be compared with the true RCS data. This is a characteristic of this particular imaging algorithm as has already been explained. Nevertheless, it is clear that over the central region, the data from the auto-focusing algorithm agrees well with the true RCS data.

Figure 3.20 illustrates the RCS response of the same two targets once multiple scattering is taken into account. Clearly, the data obtained from the auto-focusing algorithm is now no longer the same as the true RCS data. Instead the result is similar to that obtained from the single frequency system shown in Figure 2.16. The problem arises since the third term of equation (3-33) does not represent the equation of a true point target and hence it cannot be correctly focused. Therefore, the auto-focusing algorithm, in common with the backward propagation algorithm, is unable to generate true RCS data when multiple scattering occurs within in the target structure.

3.5 Improvements to the Auto-Focusing Algorithm

The main disadvantage of the auto-focusing algorithm is that it only makes use of part of the recorded data, the remainder is not used and hence information is lost. This was depicted in Figure 3.5. All the spatial frequencies higher than S_c are ignored, as are all the frequencies above the centre frequency. This is evidently not desirable, and improvements can be made in two ways.

Firstly, since all the frequencies above the centre frequency, f_o, are discarded there is little point in acquiring them in the first place. Hence the data requirements of the system could be halved [63].

Alternatively, if higher quality images are required it is more resourceful to use the full bandwidth and shift the centre frequency to a higher position within the data block as illustrated in Figure 3.21. This shift of the centre frequency is equivalent to using a larger bandwidth and the correction factor travels through a larger portion of the data. Consequently, S_c increases and the system resolution is improved.

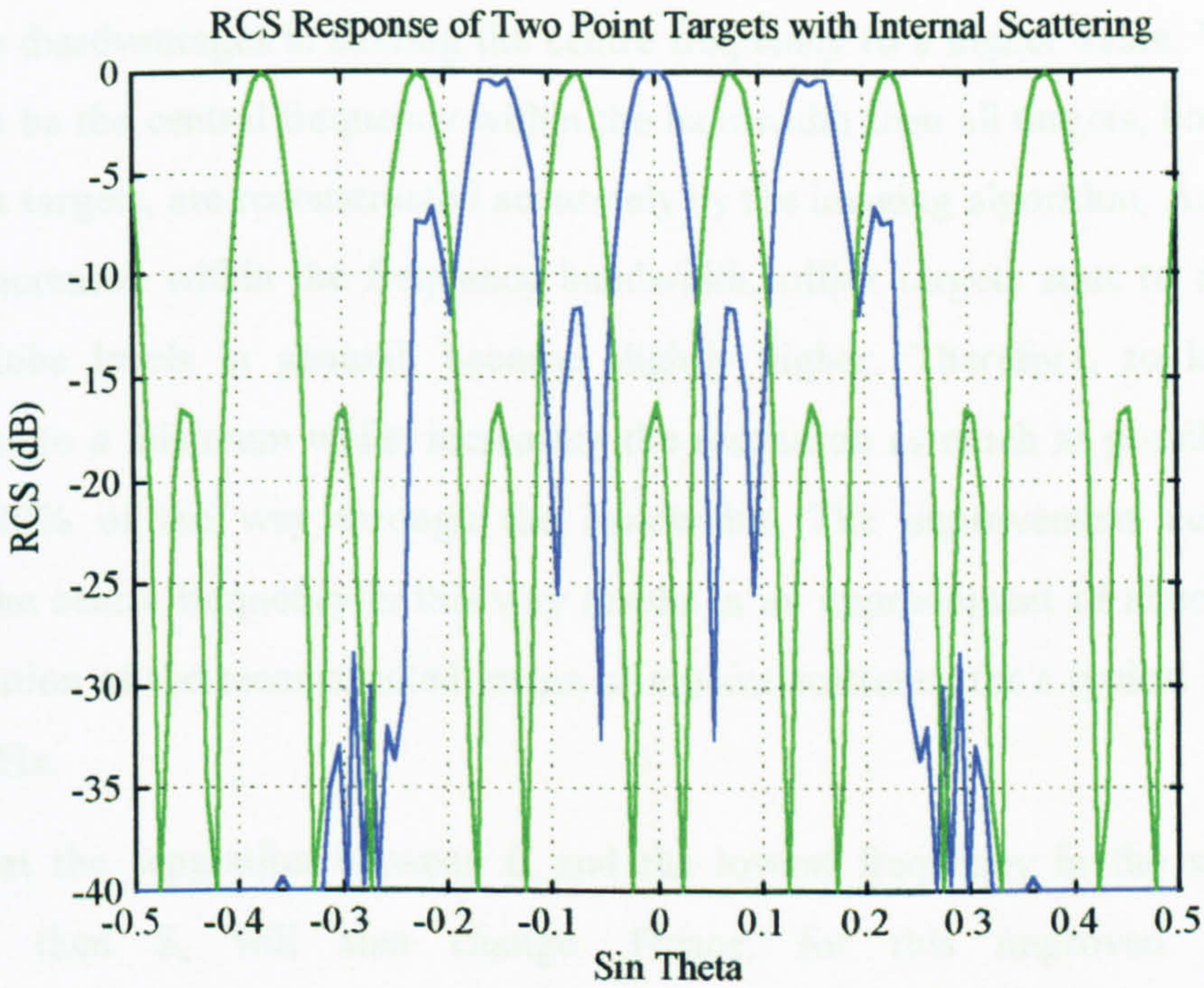

Figure 3.20 RCS Response of Two Point Targets With Multiple Scattering

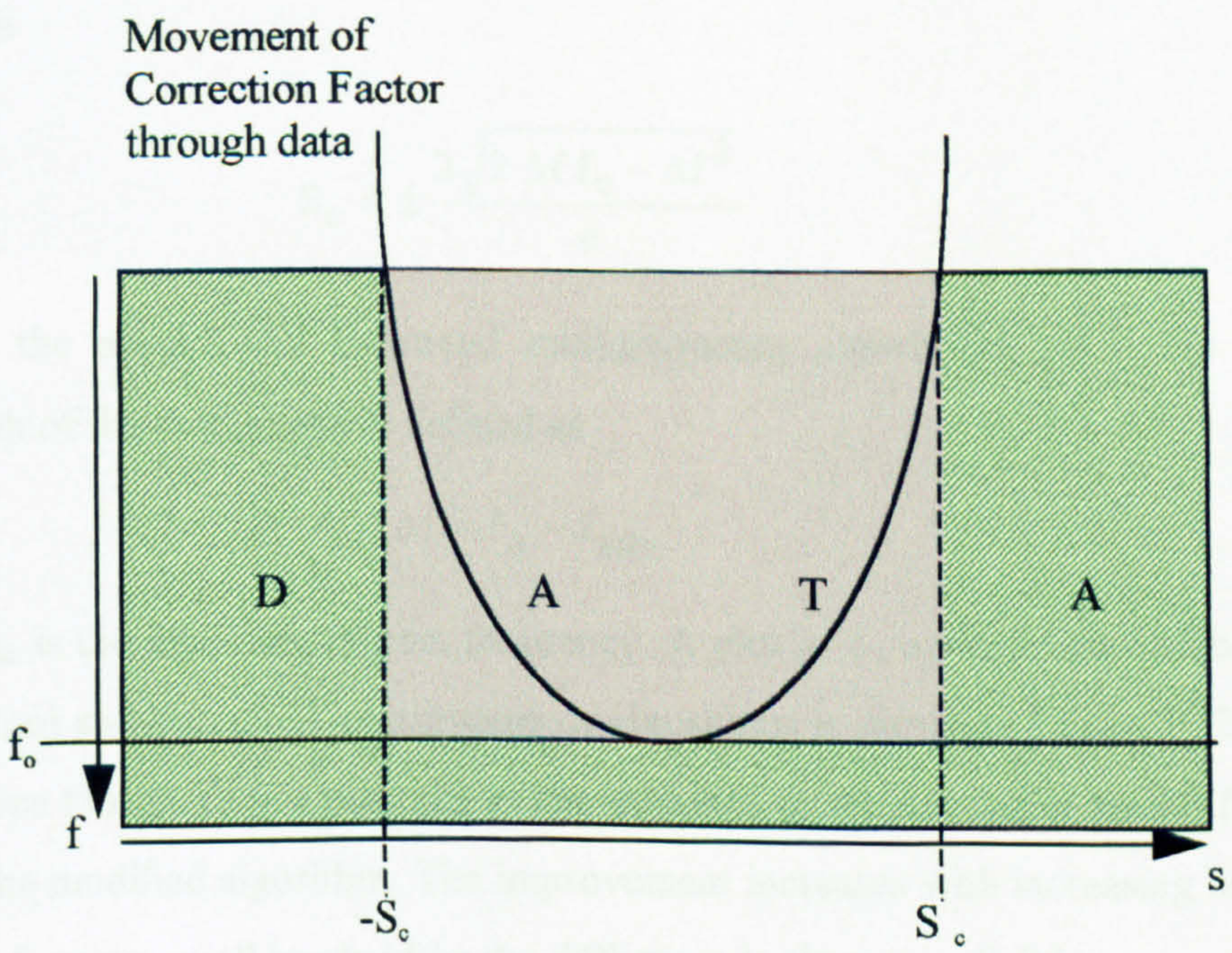

Figure 3.21 Shift of Centre Frequency to a Higher Value Within the Bandwidth

There are disadvantages in shifting the centre frequency to a higher value. When f_o is chosen to be the central frequency within the bandwidth then all targets, both on-axis and offset targets, are reconstructed accurately by the imaging algorithm. As the value of f_o is increased within the frequency bandwidth, offset targets start to deteriorate and sidelobe levels in general, become slightly higher. Therefore, to keep these distortions to a minimum whilst increasing the resolution as much as possible, f_o was located 80% of the way through the bandwidth. The improvement achieved by shifting the centre frequency in this way results in an improvement of almost 27% in the resolution of the reconstructed image of a point scatterer, for a typical bandwidth of 0.51GHz.

Given that the separation between f_o and the lowest frequency in the system has changed, then S_c will also change. Hence, for this improved algorithm, equation (3-24) now becomes

$$S_c = \pm \frac{4\sqrt{10Bf_o - 4B^2}}{5c} \tag{3-34}$$

where f_o is the new shifted centre frequency. In general, the above equation can be re-written as

$$S_c = \pm \frac{2\sqrt{2\,\Delta f\, f_o - \Delta f^2}}{c} \tag{3-35}$$

for both the normal and improved multifrequency algorithms. Δf is the effective bandwidth of the system and is defined as

$$\Delta f = f_o - f_{min} \tag{3-36}$$

where f_{min} is the minimum system frequency. A plot of S_c against bandwidth for both the standard and improved multifrequency algorithms is shown in Figure 3.22 where it can be seen that there is a reasonable improvement in the maximum spatial frequency S_c with the modified algorithm. The improvement increases with increasing bandwidth although for very small bandwidths the difference is almost negligible.

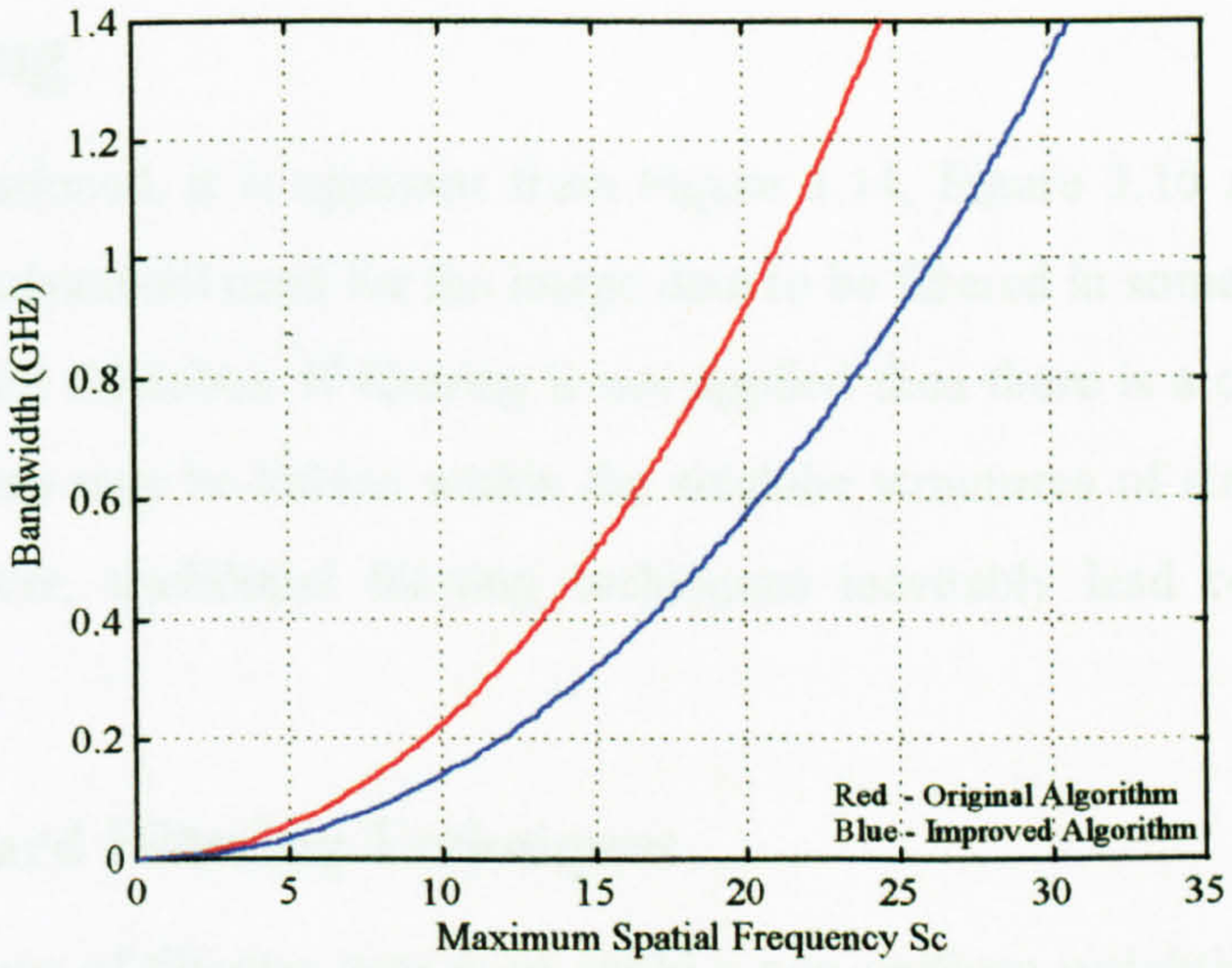

Figure 3.22 Variation in Maximum Spatial Frequency Against Bandwidth

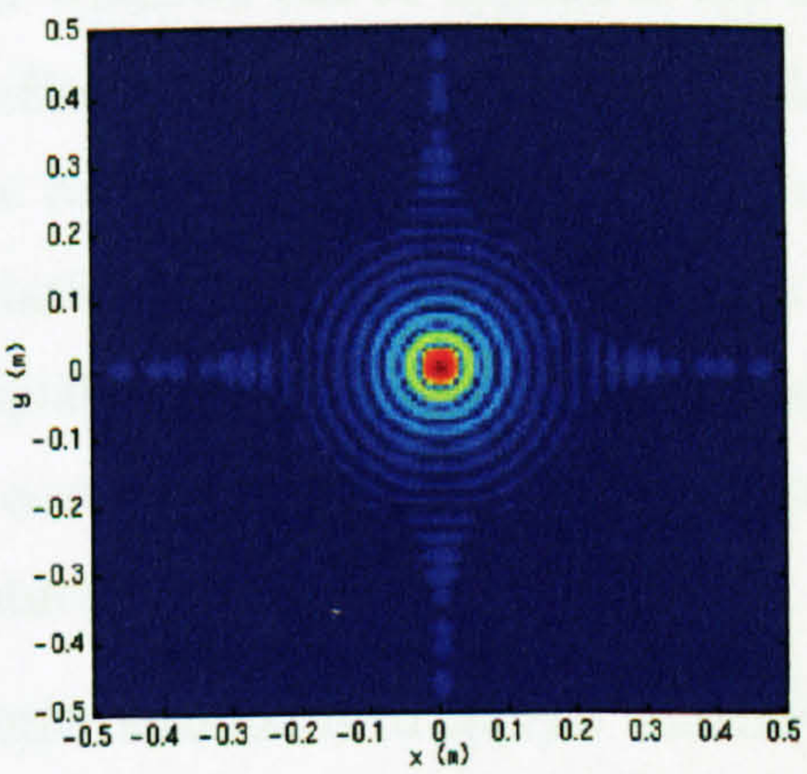

a) Unweighted

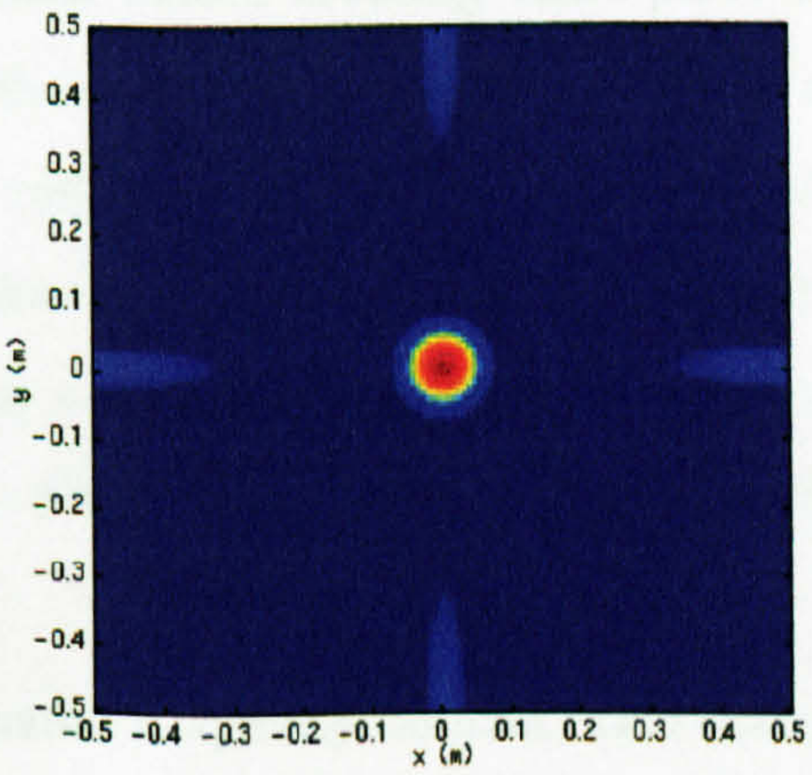

b) Hanning Weighted

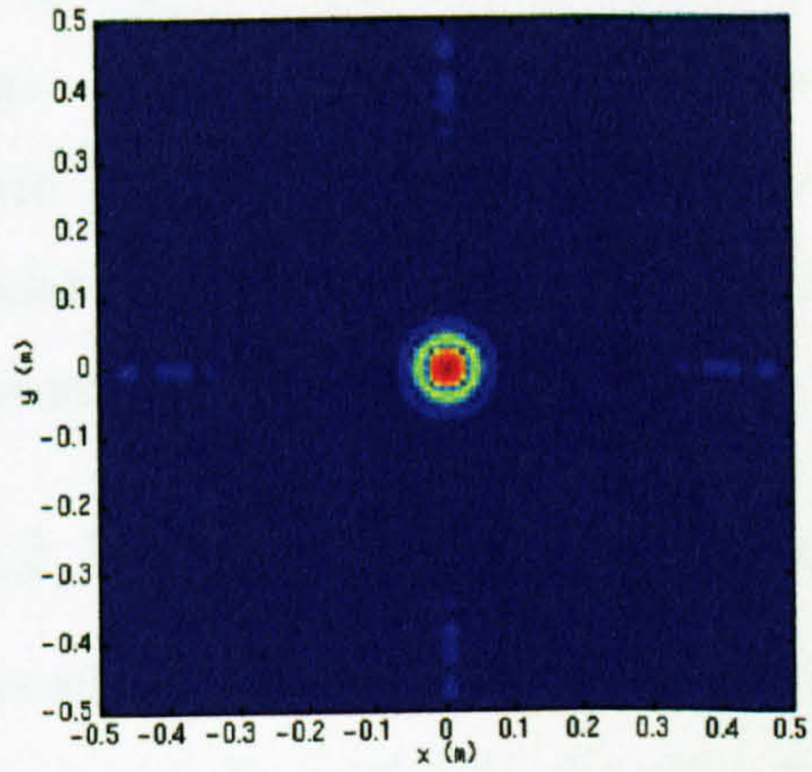

c) Dual Apodized

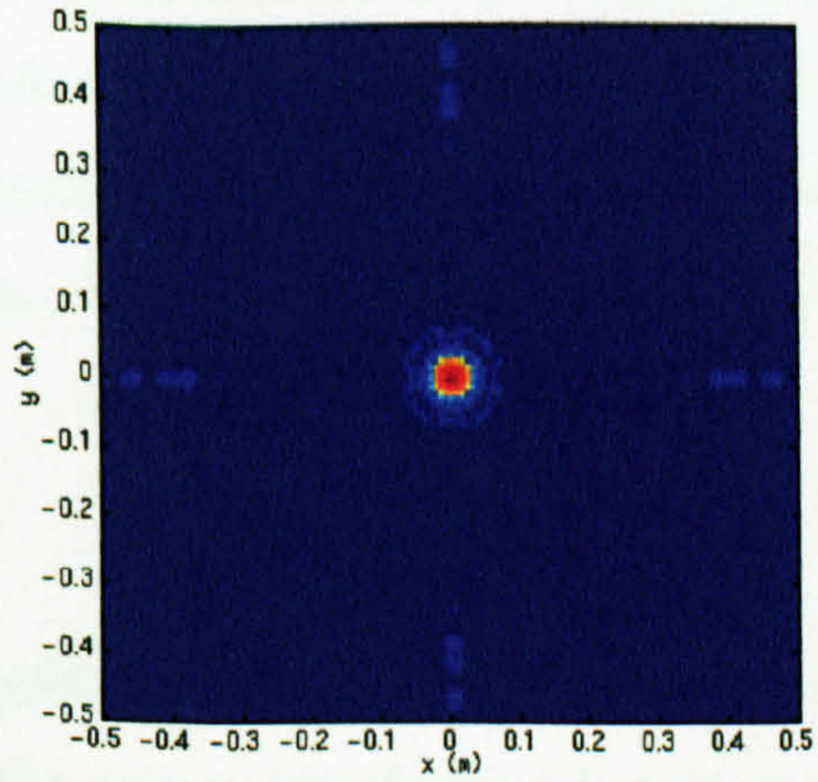

d) Tri-Apodized

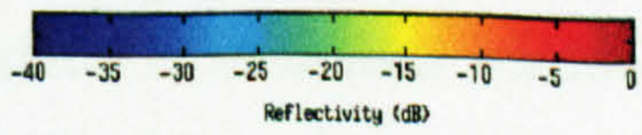

Figure 3.23 Application of Different Filtering Processes to a Single Point Scatterer.

3.6 Filtering

As already mentioned, it is apparent from Figure 3.14, Figure 3.16 and Figure 3.17 that there is a substantial need for the image data to be filtered in some way to remove the higher valued sidelobes. If filtering is not applied then there is a considerable risk that weak targets may be hidden within the sidelobe structures of strongly reflecting targets. However, traditional filtering techniques inevitably lead to some loss of resolution [77].

3.6.1 Standard Filtering Techniques

The simplest way of filtering data is to apply a non-uniform weighting across to the data. Suitable weighting functions normally have an amplitude that decreases monotonically and symmetrically away from the centre of the aperture.

Filter windows can be applied in the image domain before focusing takes place and are effective at reducing the sidelobe levels of the final image. When the targets are close to the aperture, such filtering causes a roll-off effect on the amplitude and resolution of targets at the edge of the image, thus degrading the image more than is acceptable. The roll-off can be avoided by using a large aperture so that the targets are not near the edges of the aperture, or by placing the target further from the aperture.

A better solution is to apply a window in the spatial frequency domain. This reduces the high spatial frequencies and results in lower sidelobe levels in the reconstructed image. The result of applying a Hanning window to a point target is shown in Figure 3.23b. It is particularly effective at removing the sidelobes generated by the circular aperture in the spatial frequency domain, although a loss in resolution of the reconstructed target, is noticeable.

3.6.2 Simple Apodization Techniques

None of these techniques are completely successful at removing all the sidelobes of a point target. In particular, the sidelobes from the square transforms inherent in the auto-focusing algorithm are resilient to most filter windows. Furthermore, the loss of resolution inherent in tradition filtering techniques is highly undesirable and can be

overcome by using a technique known as apodization. Apodization is a sidelobe reduction technique that does not cause any loss in the resolution of the mainbeam of the system impulse response. It has been used for many years in astronomy to help separate closely spaced targets but has only been applied to synthetic aperture radar systems in recent years [78].

There are several different apodization techniques, the simplest of which is dual apodization [79]. This technique uses two processed images generated from the same data set as its inputs. One image is an unweighted (i.e. unfiltered) image and the second is a filtered version of the same image. Normally, a Hanning weighting function is used in the spatial frequency domain to generate the filtered image. The apodization process compares the two images on a pixel by pixel basis and selects the minimum value of each pixel pair as the final image pixel. In this way, sidelobe reduction equal to that of the filtered image is obtained whilst the resolution of the unweighted image is maintained as shown in Figure 3.23c. It can be seen that although the sidelobe levels are reduced without loss in resolution, the first sidelobe level is unaffected by the filtering process as it falls within the main beam of the filtered image.

The dual apodization process can be expanded to include more than one filter window. Therefore, three input images constitutes tri-apodization and so on. The greater the number of input images, the lower the sidelobes become, although extra windows only introduce small improvements over the original dual apodization. Nevertheless, the addition of a specially designed filter window to the dual apodization process to reduce the first sidelobe level, has been found to be advantageous. This is illustrated in Figure 3.23d.

By comparison with Figure 3.23a, it is evident that the apodization process removes a large proportion of the sidelobes produced by the circular transformation and limits those generated by a square transform. The improvements achieved using this technique are valuable and will be applied to the imaging of biophysical objects in Chapter 6.

3.6.3 Spatially Variant Apodization (SVA)

In more recent years, an alternative to dual apodization has been developed at the Environmental Research Institute of Michigan. The technique, known as spatially variant apodization (SVA) is, as its name suggests, a non-linear procedure that applies a spatially varying filter across the final image distribution. This results in a non-uniform impulse response over the image. Unlike conventional filtering techniques, SVA does not apply a uniform reduction in sidelobes across an entire image by weighting the spatially frequency domain.

3.6.3.1 One Dimensional SVA

The basic concept behind SVA is relatively straightforward, in that each pixel in an image receives its own spatial frequency domain weighting function from a continuum of possible weighting functions [78]. In particular, SVA makes use of the special properties of a cosine-on-a-pedestal weighting function applied to complex Nyquist sampled imagery. Consider, initially a one dimensional case. The family of cosine-on-a-pedestal weighting functions for an aperture of N pixels can be described by

$$C(n) = 1 + 2w\cos\left(\frac{2\pi n}{N}\right) \tag{3-37}$$

When w is zero, the weighting is uniform (all pedestal) and when w is 0.5, the weighting is Hanning (all cosine). The discrete Fourier transform of C(n) is

$$c(m) = \delta(m) + w\delta(m-1) + w\delta(m+1) \tag{3-38}$$

where $\delta(m)$ is a delta function. Operating in the image domain, the SVA algorithm convolves c(m) with each line of pixels in the image. The algorithm can be applied to the real and imaginary parts of the image data together or separately. The latter approach yields the better results [78][80] and is the only case considered here.

Consider an unweighted Nyquist sampled image with complex valued samples, g(m). The SVA algorithm convolves g(m) with the weighting function c(m) to give

$$g'(m) = w(m)g(m-1) + g(m) + w(m)g(m+1) \tag{3-39}$$

To provide the optimum filtering, the algorithm selects $w(m)$ which minimises g'(m)

subject to the constraint that $w(m) \leq 0.5$. The value of $w(m)$ where this occurs, $w_u(m)$, is obtained by differentiating equation (3-39) with respect to $w(m)$, setting it equal to zero, and solving for $w(m)$. Hence,

$$w_u(m) = \frac{-g(m)}{g(m-1) + g(m+1)} \tag{3-40}$$

If $w(m)$ is required to be in the interval from 0.0 to 0.5, then the value g'(m) for the real or imaginary component of the m^{th} output pixel is,

$$g'(m) = \begin{cases} g(m) & \text{for } w_u(m) < 0 \\ 0 & \text{for } 0 \leq w_u(m) \leq 0.5 \\ g(m) + 0.5\left[g(m-1) + g(m+1)\right] & \text{for } w_u(m) > 0.5 \end{cases} \tag{3-41}$$

Therefore, for the real and imagery components of every pixel in the image, g(m), the above equation applies a unique filter weight to that pixel which gives a filtered pixel, g'(m).

Considering equation (3-40), it can be seen that the pixel g(m) must have the same sign as the sum of its neighbours for $w_u(m)$ to be negative. This is only true in a Nyquist-sampled sinc function if the pixel, g(m), is in the mainlobe. In this case one of the neighbouring pixels will be in a sidelobe and have a negative value whilst the other neighbour will be in the mainlobe and have a positive value. This is shown in Figure 3.24. When $w_u(m)$ has a value between 0 and 0.5, the input pixel, g(m), has the opposite sign of its neighbours. For a Nyquist-sampled sinc function, this occurs if g(m) is in the sidelobes, as shown in Figure 3.25. Therefore, the SVA algorithm sets the corresponding output pixel, g'(m), to zero to remove the sidelobe. When $w_u(m)$ is greater than 0.5, g(m) again has the opposite sign from the sum of the neighbouring pixels. In this case, the sum of the neighbouring pixels is not significantly greater than the value of the centre pixel which suggests that g(m) is in a mainlobe but contains energy from sidelobes of other scatterers. Hence, the algorithm applies Hanning weighting to g(m) in an attempt to reduce the influence of the sidelobes.

The whole SVA process is computationally efficient and although designed to work at the Nyquist rate, it has been shown to be effective at non-integer multiples of the

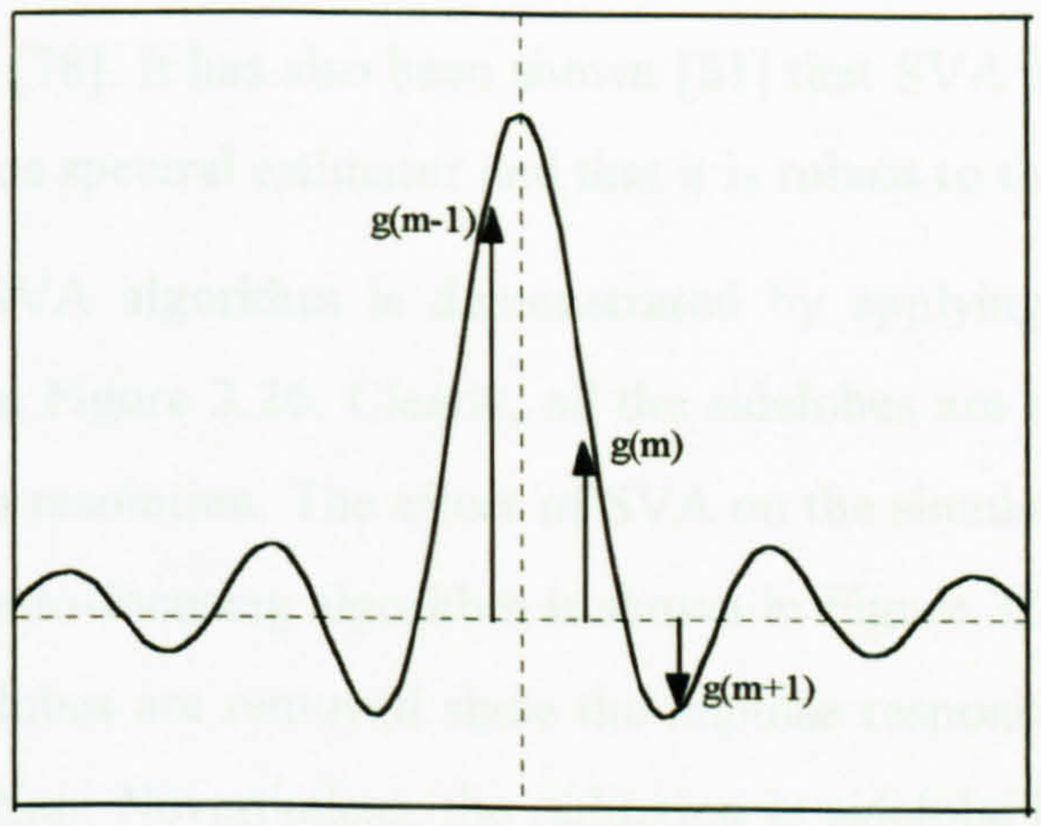

Figure 3.24 Example of Mainlobe Pixels in the SVA Algorithm

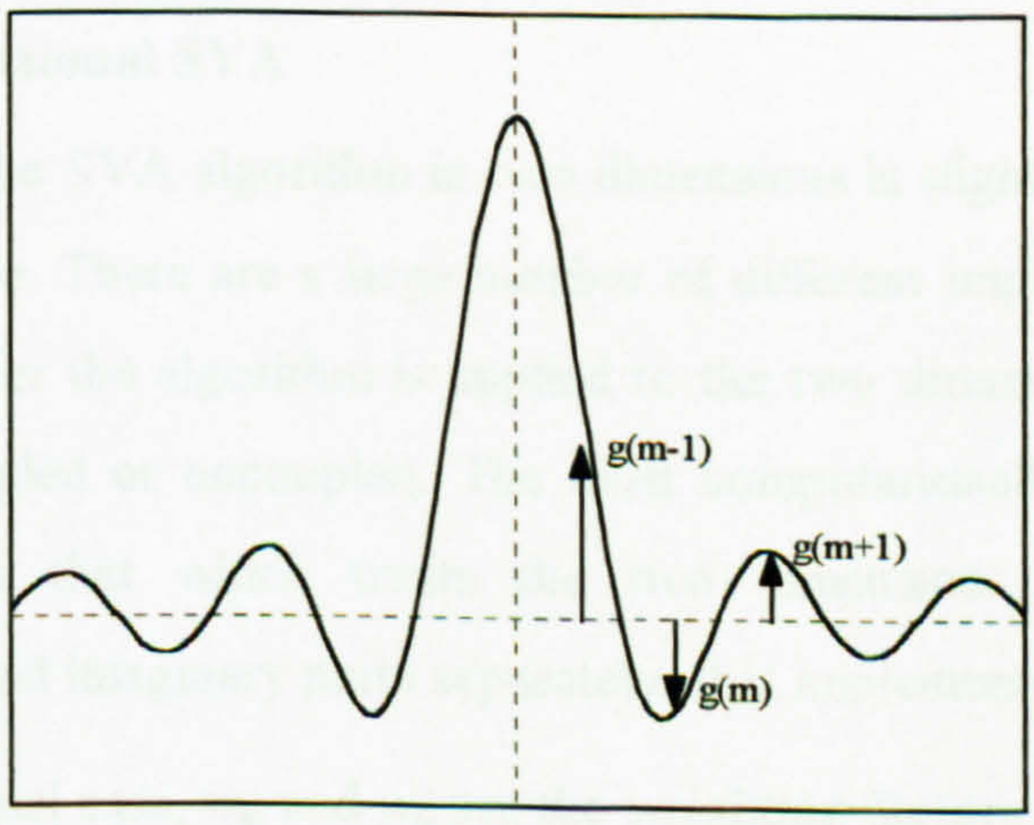

Figure 3.25 Example of Sidelobe Pixels in the SVA Algorithm

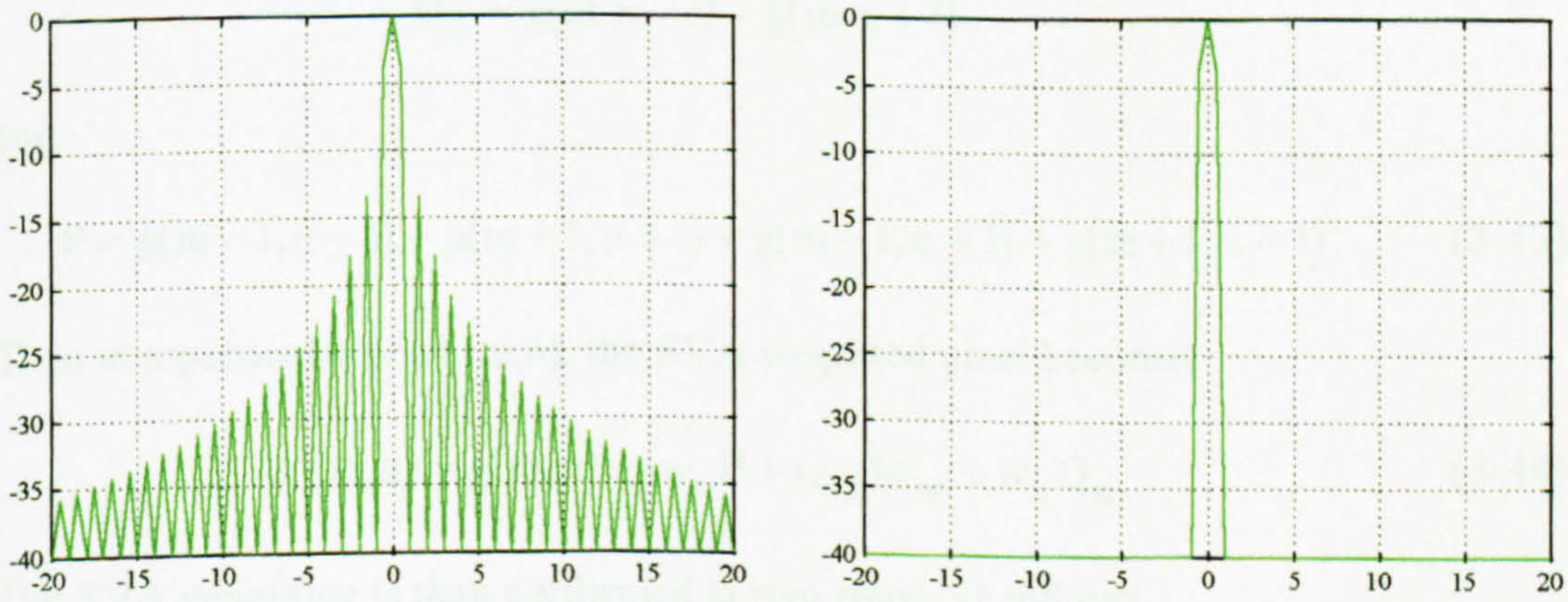

Figure 3.26 One Dimensional SVA Algorithm Applied to a Sinc Function

Nyquist rate as well [78]. It has also been shown [81] that SVA is a special version of the minimum variance spectral estimator and that it is robust to the addition of noise.

Validation of the SVA algorithm is demonstrated by applying it to an ideal sinc function as shown in Figure 3.26. Clearly, all the sidelobes are removed and there is no loss of mainbeam resolution. The effect of SVA on the simulation of a single point scatterer using the auto-focusing algorithm is shown in Figure 3.27. Here it is evident that not all the sidelobes are removed since the impulse response of the algorithm is not a true sinc function. Nevertheless, the reduction in sidelobe levels is considerable when compared with an unweighted image with all sidelobes being reduced to less than -30dB.

3.6.3.2 Two Dimensional SVA

Implementation of the SVA algorithm in two dimensions is slightly different from the one-dimensional case. There are a large number of different implementation methods depending on whether the algorithm is applied to the two dimensions sequentially or simultaneously, coupled or uncoupled. The most computationally efficient and most effective version is that which treats the two dimensions simultaneously and uncoupled for real and imaginary parts separately. It is implemented as follows [78].

In the two-dimensional case, w_m and w_n are the weighting factors in the m (horizontal) and n (vertical) directions. These weighting factors arise from a family of Nyquist-sampled separable raised-cosine weighting functions. Next, let

$$\begin{aligned} Q_m &= g(m-1,n) + g(m+1,n) \\ Q_n &= g(m,n-1) + g(m,n+1) \end{aligned} \tag{3-42}$$

and

$$P = g(m-1,n-1) + g(m+1,n+1) + g(m-1,n+1) + g(m+1,n-1) \tag{3-43}$$

Then at a particular pixel (m,n), the SVA weighted pixel becomes

$$g'(m,n) = g(m,n) + (w_n P + Q_m) w_m + w_n Q_n \tag{3-44}$$

The SVA weighting is then performed in two steps, as follows

i. Compute g'(m,n) for $(w_m,w_n) = (0,0.5)$, (0.5,0) and (0.5,0.5). If any of these have a

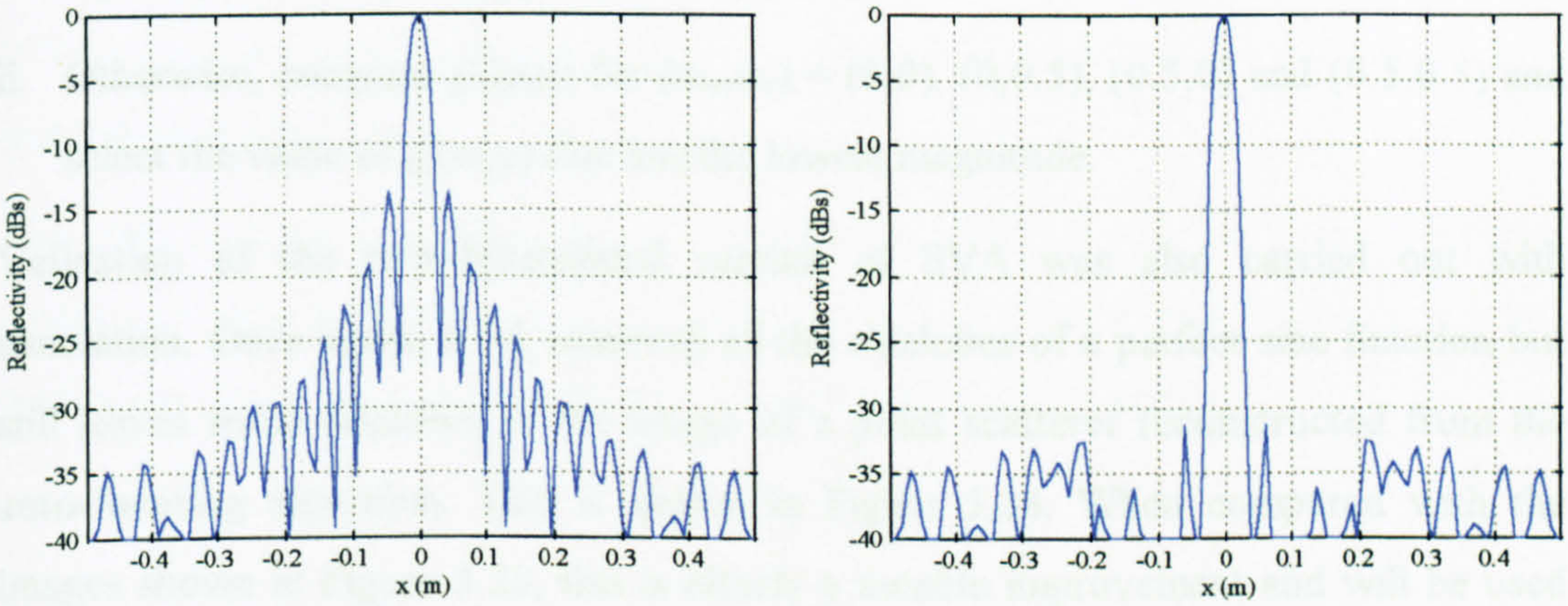

Figure 3.27 One Dimensional SVA Algorithm Applied to a Point Scatterer Focused Using the Auto-Focusing Algorithm

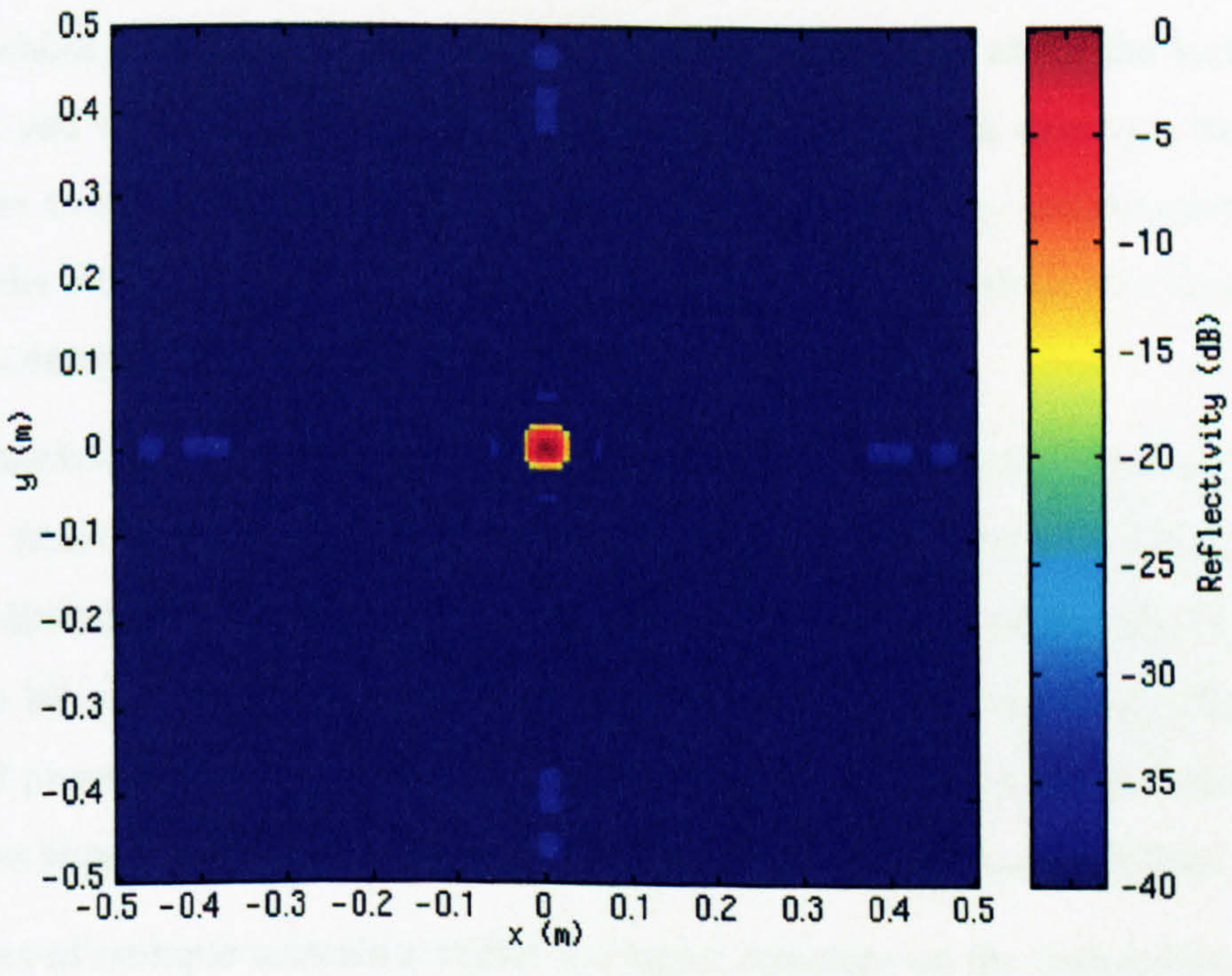

Figure 3.28 Two Dimensional SVA Algorithm Applied to a Point Scatterer Focused with the Auto-Focusing Algorithm

sign opposite to that of g(m,n), then g'(m,n) = 0.

ii. Otherwise, compute g'(m,n) for (w_m,w_n) = (0,0), (0,0.5), (0.5,0) and (0.5,0.5) and select the value of g'(m,n) that has the lowest magnitude.

Validation of the two-dimensional version of SVA was also carried out with simulation. Once again, SVA removed all the sidelobes of a perfect sinc function but still leaves some sidelobes in the image of a point scatterer reconstructed from the auto-focusing algorithm. This is shown in Figure 3.28. When compared with the images shown in Figure 3.23, this is clearly a notable improvement and will be used further in Chapter 6.

3.7 Conclusions

This chapter has shown that a development of the backward propagation imaging algorithm can be used to focus multifrequency data collected over a planar aperture. This algorithm provides automatic focusing without knowledge about the location of the target and which is achieved by multiplication of time domain data by a backward propagator term. Alternatively, the algorithm can be deduced by examination of the phase in the frequency domain. Focusing can be carried out in either the time or the frequency domain, although the latter is generally more efficient.

The characteristics of the auto-focusing algorithm have been investigated and its ability to focus all targets within a certain range has been demonstrated in both one and two dimensions. It has been shown that images focused using the auto-focusing algorithm have a worse resolution than those generated from the single frequency backward propagation algorithm. Investigations were also carried out into the ability of the auto-focusing algorithm to cope with complex targets such as cylinders.

The effects of multiple scattering within the target structure on the focused image and the reconstructed far-field were presented. It was found that the algorithm could focus some multiple scattering terms but was unable to convert them to a far-field quantity. Improvements were made to improve the resolution of the system by shifting the centre frequency to a higher value within the recorded frequency band.

Suitable filtering techniques for limiting the sidelobes of the focused images were

examined. In particular, apodization techniques including spatially variant apodization (SVA) were shown to be highly effective at removing sidelobes and did not produce and loss in resolution.

The auto-focusing algorithm clearly provides an effective way to image near-field targets and only requires a small bandwidth of data. It will be used in Chapters 5 and 6 of this work to focus data collected on a real measurement system.

Chapter 4

Imaging of Biophysical Objects with the Backward Propagation Algorithm

4.1 Introduction

Chapter 2 investigated the ability of the single frequency backward propagation imaging algorithm to focus data collected on a planar near-field scanner in an anechoic chamber. The aim of the work presented in this chapter is to implement the system described in Chapter 2 in a real situation. A full system description is presented and verification that the imaging algorithm works correctly and can be calibrated, is given. The system is then applied to the imaging of biophysical targets, namely trees and agricultural crops. Limited complementary transmission measurements are also carried out. By so doing, a better understanding of radar-target interaction, and polarimetric variations can be obtained.

4.2 Experimental Description

Figure 1.2 illustrated a typical arrangement for a planar imaging system. Such a system can be implemented in practice and the facility belonging to the Department of Electronic and Electrical Engineering at Sheffield University is described below.

4.2.1 Equipment

The experimental facility is housed in a microwave anechoic chamber which is 10m by 3.5m by 3m in dimensions and is clad with radar absorbing material (RAM) with a reflectivity of -50dB at a frequency of 10GHz. The chamber contains a high-precision, computer-controlled planar rectangular scanning aperture of dimensions 2m by 2m which is oriented in a vertical plane. Transmit and receive pyramidal horn antennas are mounted on the moveable carriage of the scanner as shown in the photograph in Figure 4.1. Their apertures are positioned diagonally next to each other to minimise direct coupling from the transmitter to the receiver. Changes in polarisation are achieved by manually rotating the horn antennas. Such an arrangement is simplistic but is more than adequate for the experiments described. A more accurate horn configuration will be presented in Chapter 5.

As shown in Figure 4.2, the transmit horn is driven by 10GHz Gunn diode oscillator with a nominal output power of 10mW. The diode is mounted on the carriage behind

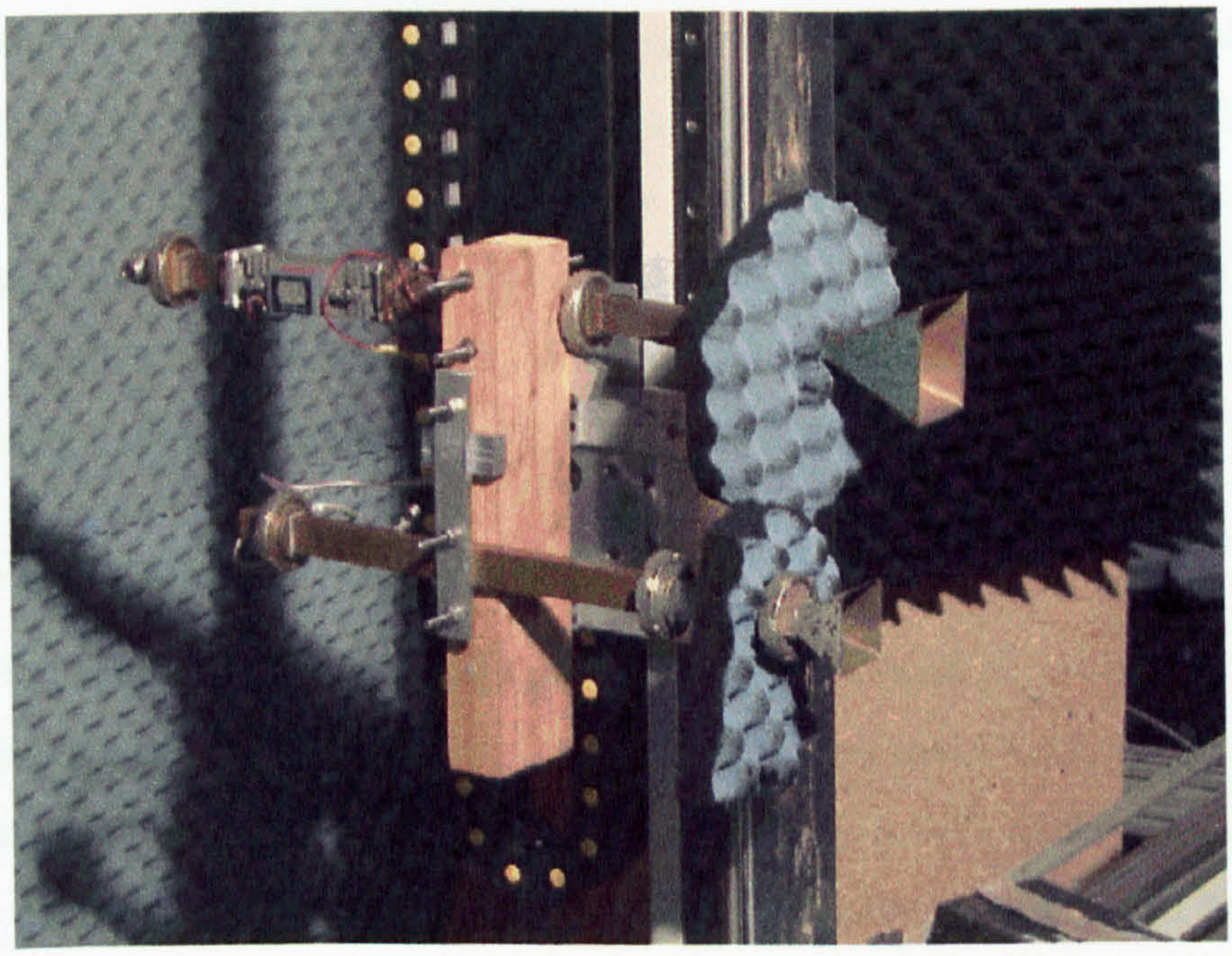

Figure 4.1 Photograph of Scanner Carriage

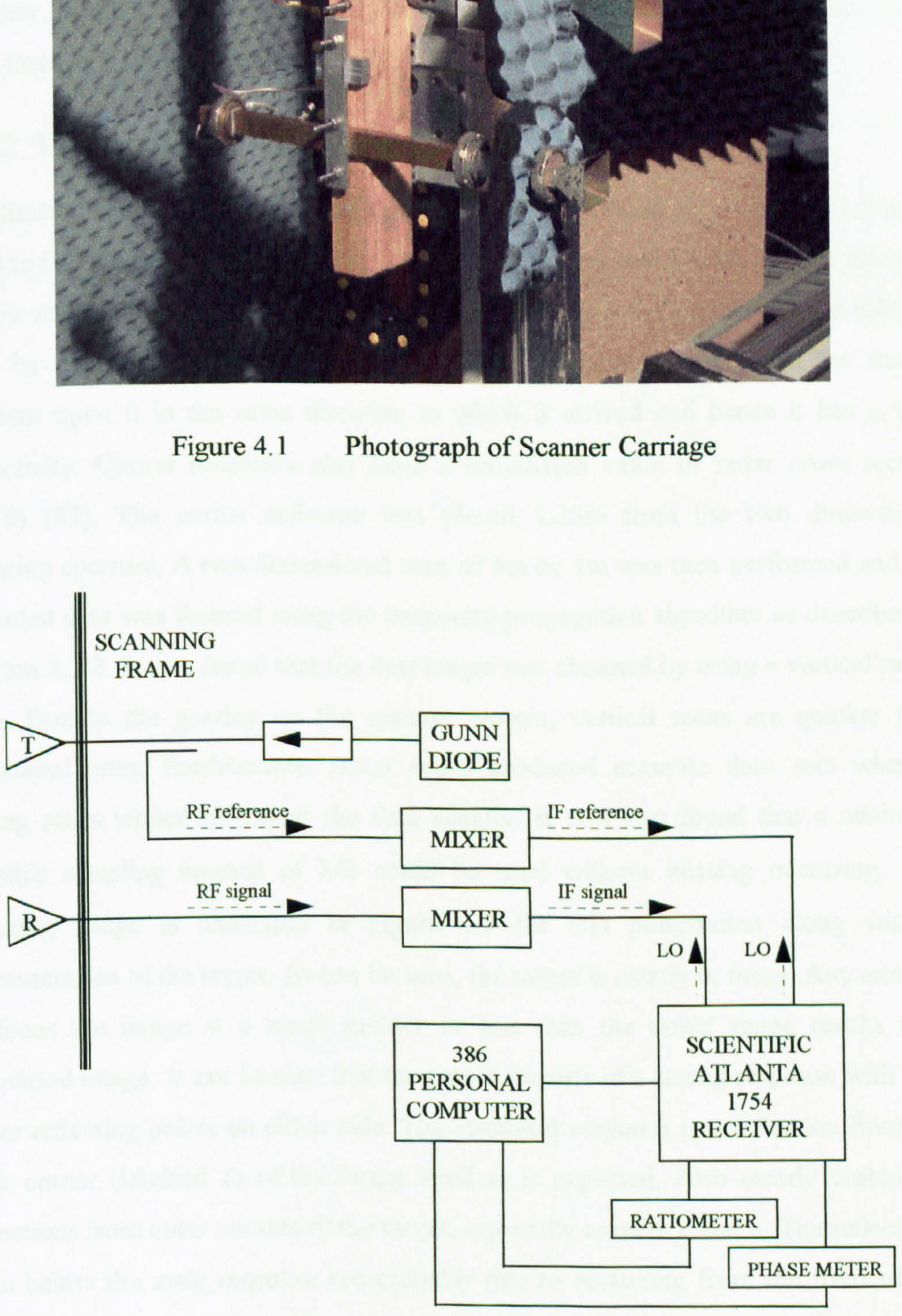

Figure 4.2 Experimental Setup

the transmit horn and a reference signal is derived from it using a directional coupler. Scientific Atlanta mixers are used both at the receive antenna and the coupler port to provide remote harmonic mixing. These mixers are driven through coaxial transmission lines by the local oscillator of a Scientific Atlanta 1754 phase amplitude receiver. A 386 PC is used to control the movement of the scanner and also to record data from the Scientific Atlanta 1833 ratiometer and 1823 phasemeter.

4.2.2 Verification of Algorithm

Verification that the backward propagation algorithm, described in Chapter 2, can be used to image real targets, was carried out by performing measurements on a trihedral corner reflector. This reflector was made of aluminium, 1.5mm thick and had sides of 8cm by 8cm. The reflector was chosen since, in theory, it returns all the energy incident upon it in the same direction in which it arrived and hence it has a high reflectivity. Corner reflectors also have a formulated value of radar cross section (RCS) [82]. The corner reflector was placed 1.33m from the two dimensional scanning aperture. A two dimensional scan of 1m by 1m was then performed and the recorded data was focused using the backward propagation algorithm as described in Section 2.2.3. It was found that the best image was obtained by using a vertical raster scan. Due to the gearing on the scanner motors, vertical scans are quicker than horizontal ones. Furthermore, raster scans produced accurate data sets whereas zigzag scans tended to distort the data slightly. It was also found that a minimum possible sampling interval of $\lambda/2$ could be used without aliasing occurring. The resulting image is illustrated in Figure 4.3 for HH polarisation along with a representation of the target. As can be seen, the target is clearly in focus. Any attempt to focus the image at a range greater or less than the target range results in a defocused image. It can be seen that the target consists of a strong response with two lesser reflecting points on either side. The strongest response is a reflection from the back corner (labelled 1) of the target itself as is expected. Also clearly visible are reflections from outer corners of the target, especially corners 2 and 4. The reflections from below the main response are probably due to scattering from the front of the reflector and from the supporting polystyrene. Figure 4.3 has been interpolated in the Fourier domain to give a clearer image as explained in Section 2.3.5.

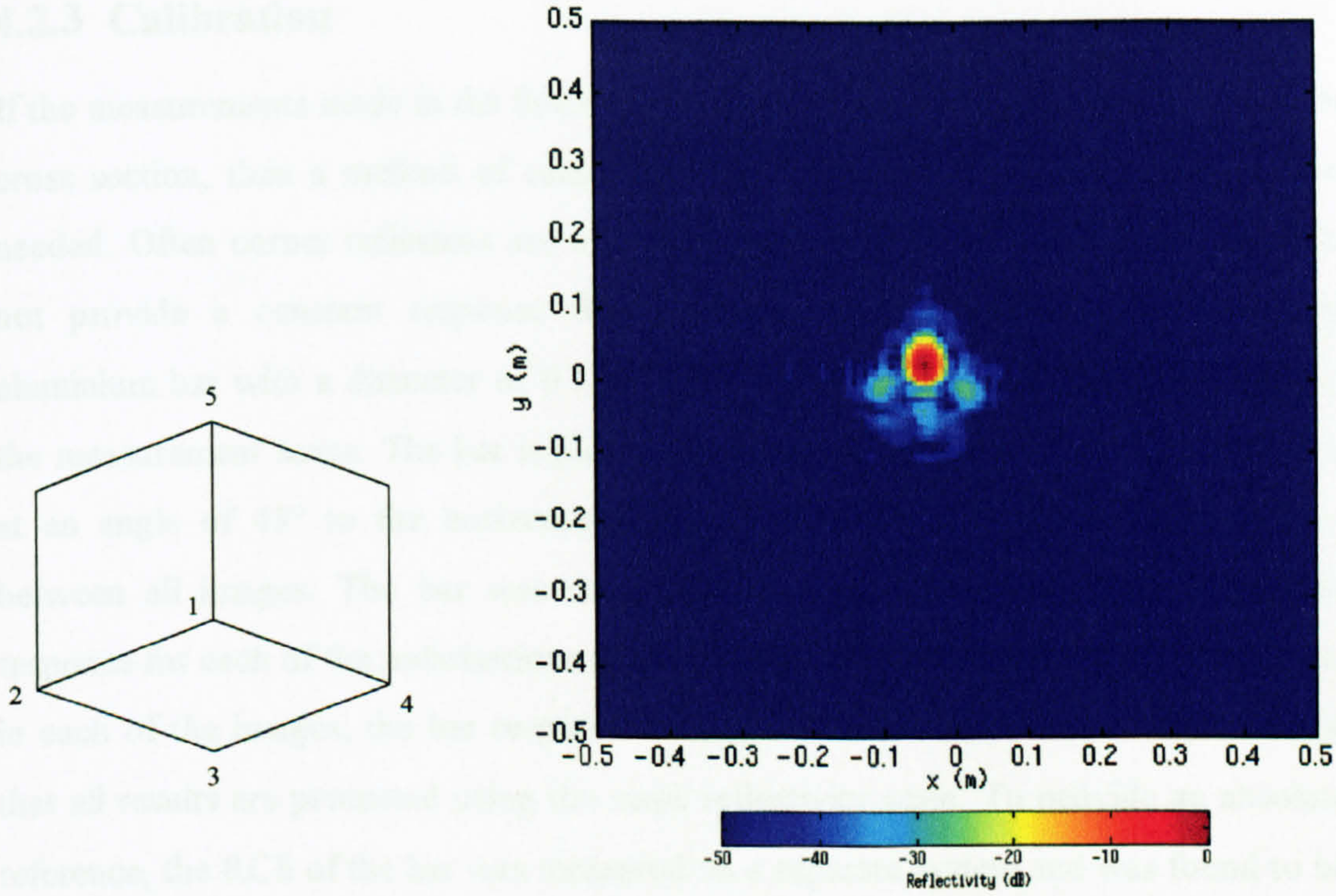

Figure 4.3 Schematic and Microwave Image of a Trihedral Corner Reflector

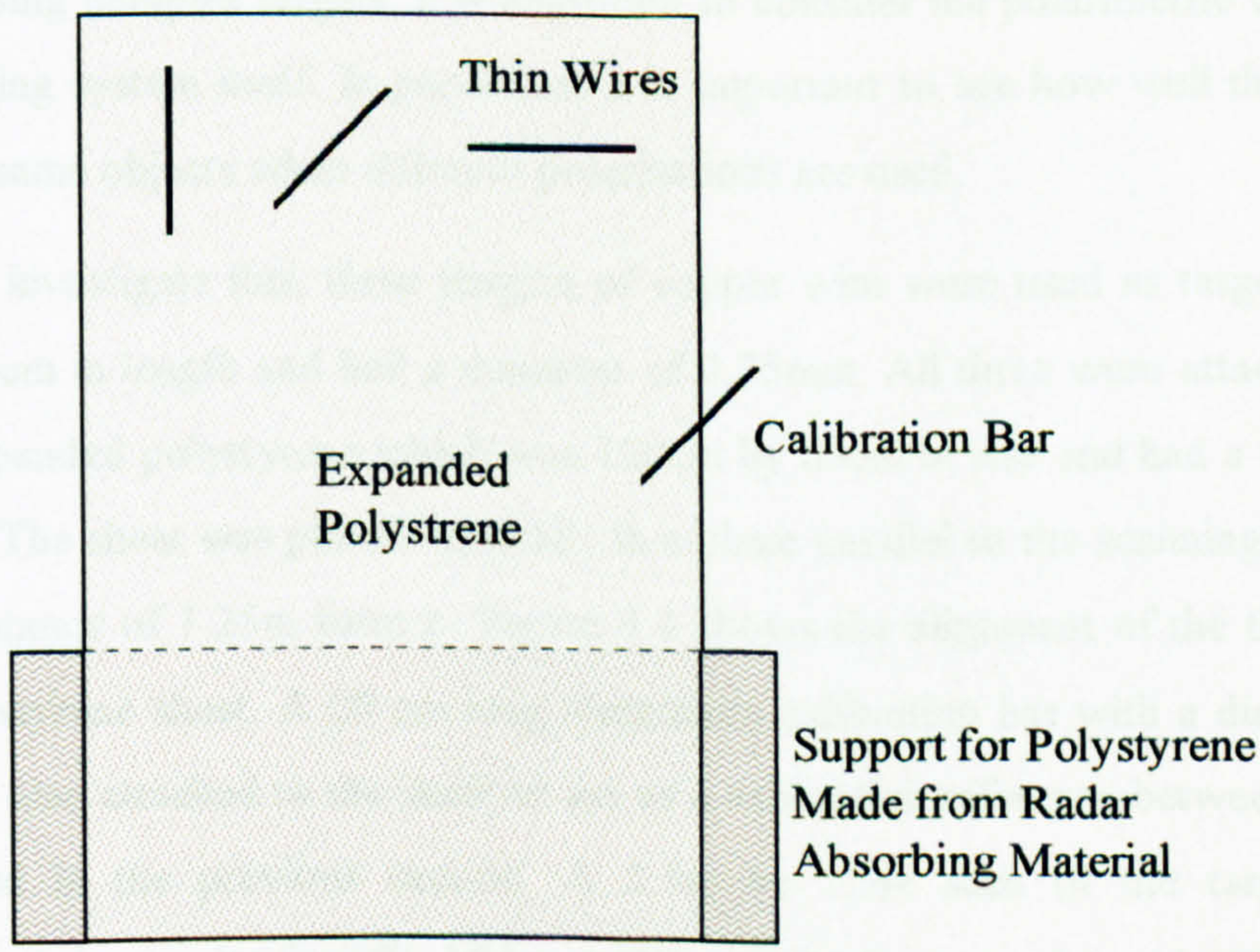

Figure 4.4 Configuration of Polarimetric Test Targets

4.2.3 Calibration

If the measurements made in the following sections are to have any relevance to radar cross section, then a method of calibrating the system to some known reference is needed. Often corner reflectors are used since they have a known RCS but they do not provide a constant response for all polarisations. Therefore, a 20cm long aluminium bar with a diameter of 0.5cm was chosen instead and included in each of the measurement scans. The bar is placed in a plane parallel to the scanning aperture at an angle of 45° to the horizontal and acts as a standard calibration reference between all images. The bar was utilised as it gives an almost identical level of response for each of the polarisations used, namely, VV, VH and HH [83]. Therefore, in each of the images, the bar response is assigned to the same reflectivity level, so that all results are presented using the same reflectivity scale. To provide an absolute reference, the RCS of the bar was measured on a separate system and was found to be -21dBm^2. This procedure is equivalent to a standard first-order calibration process, where a separate measurement is made of a known calibration standard and then subsequent measured data are divided by this response.

4.2.4 Polarimetric Sensitivity

Before utilising complex targets, it is important to consider the polarimetric variations of the imaging system itself. In particular, it is important to see how well the system images the same objects when different polarisations are used.

In order to investigate this, three lengths of copper wire were used as targets. Each one was 20cm in length and had a diameter of 0.75mm. All three were attached to a sheet of expanded polystyrene which was 120cm by 60cm in size and had a thickness of 2.54cm. The sheet was placed vertically in a plane parallel to the scanning aperture and at a distance of 1.25m from it. Figure 4.4 shows the alignment of the three bars on the polystyrene sheet. A 20 cm long aluminium calibration bar with a diameter of 0.5cm, was also attached to the sheet to act as a calibration reference between images as explained in the previous section. A 1.5m by 1.5m scan of the targets was measured and the results for VV, VH and HH polarisations are shown in Figure 4.5. The spatial resolution in the (x,y) plane is approximately 2cm.

VV

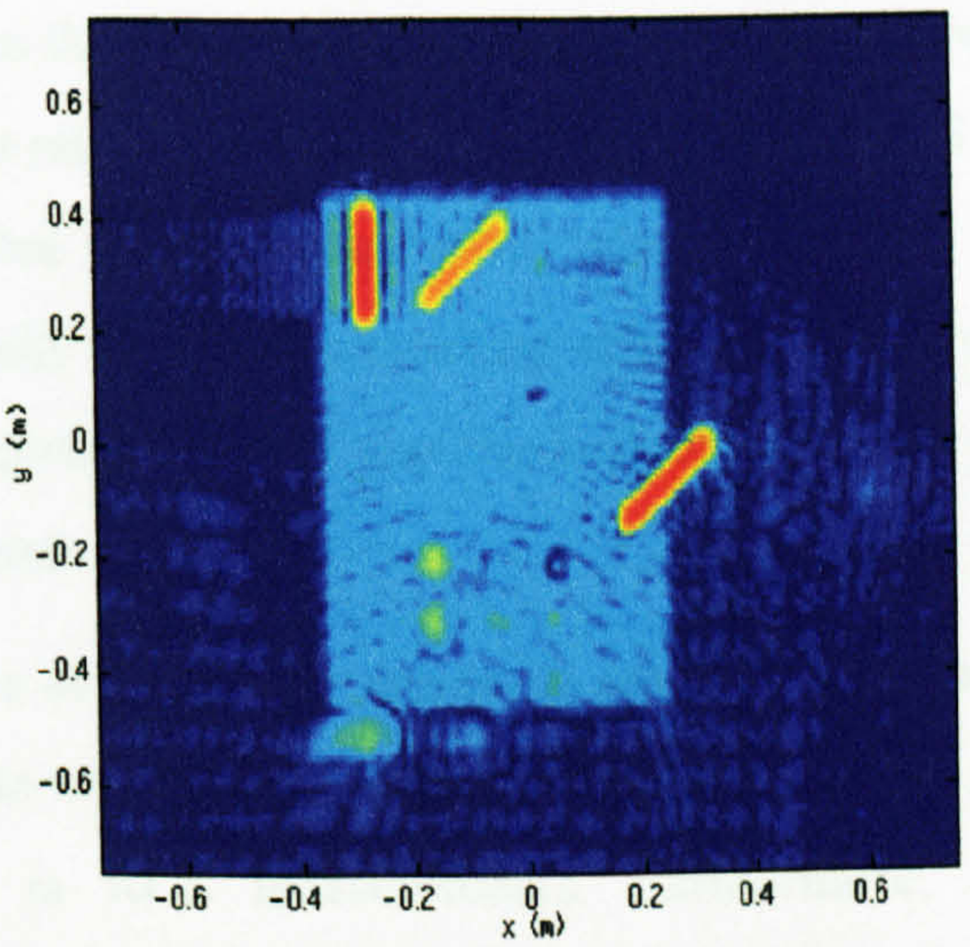

VH

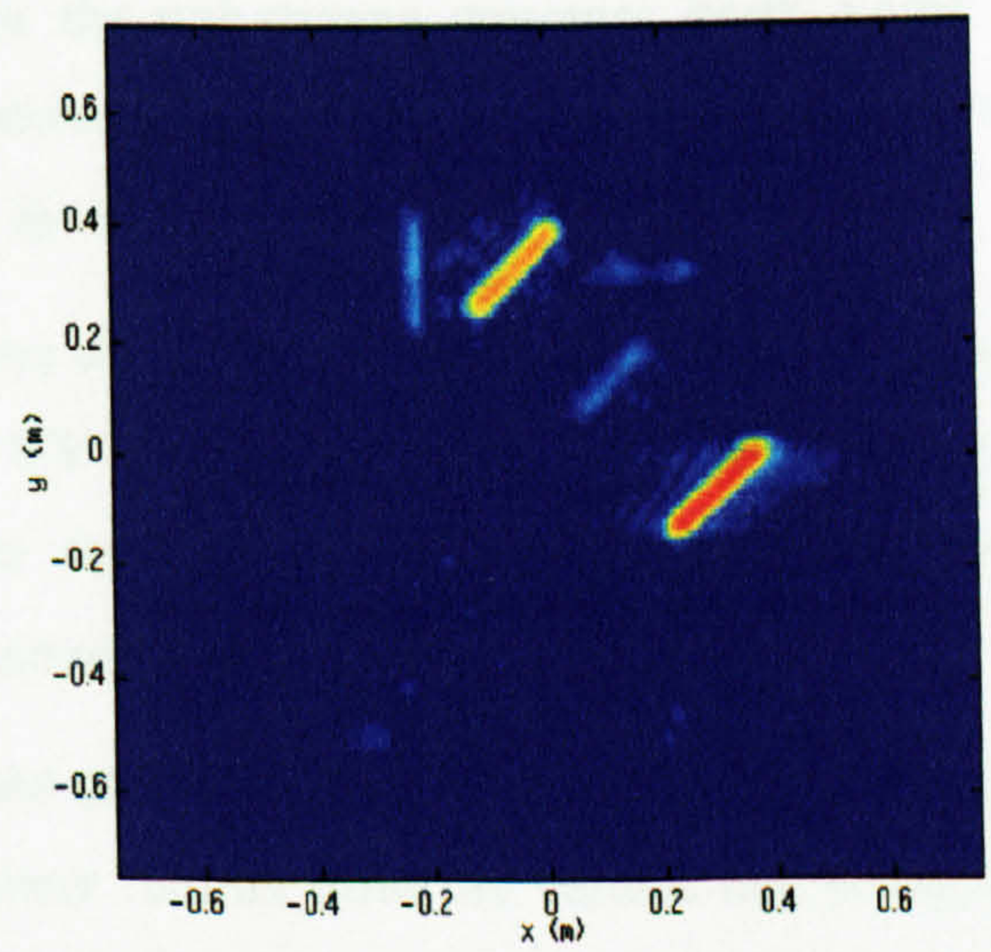

HH

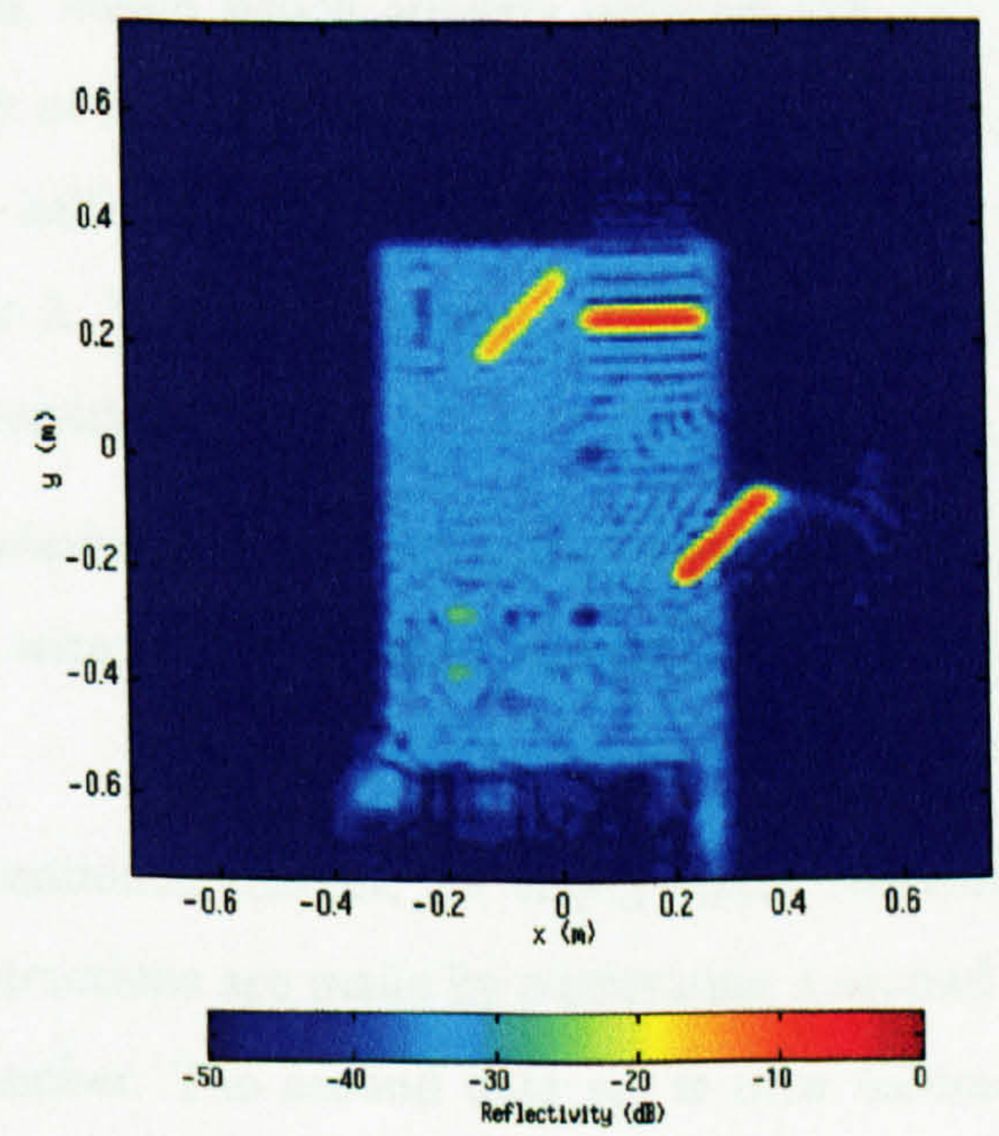

Figure 4.5 Results from Polarimetric Test Targets

The VV response clearly shows that the vertical wire has the strongest reflectivity and that the horizontal wire gives a relatively weak return. The wire oriented at 45° shows a reduction of 6.6dB below that of the vertical wire, which compares well with the expected value of 6dB, especially when the perturbing effects of the polystyrene sheet are considered. It is also just possible to see that the horizontal wire is re-radiating a cross polar response from its ends.

From the image, it can also be seen that the system is sensitive enough to image the polystyrene sheet as well as the wire targets. Polystyrene is traditionally used as a low reflectivity support material in RCS measurements. Furthermore, a number of anomalies can be seen within the polystyrene structure itself. Some of these are irregularities within the polystyrene sheet whilst others are due to absorber blocks placed behind the polystyrene sheet to support it.

The presence of the polystyrene sheet makes it difficult to assess the true polarisation purity of the system, but the VV image suggests that the return from the horizontal wire is 35-40dB below that from the vertical wire. This level of polarisation discrimination is sufficient to provide meaningful results.

The VH image shows that the greatest return at this polarisation is from the wire oriented at 45° with much lower returns from the vertical and horizontal wires. Of particular interest is the weak image which appears between the 45° wire and the calibration bar. This is a result of multiple scattering between the wire and the bar and gives rises to a virtual image half way between the two. Such a result was predicted by the simulations in Chapter 2. The polystyrene is not visible in this image since it does not have depolarising properties.

The HH image shows characteristics which are complementary to those of the VV image. Hence the horizontal wire has the highest reflectivity whilst the vertical wire has the lowest.

In each of the three aforementioned images, an empty room subtraction has been carried out. Empty room subtractions are made by performing a second scan with the target removed from the chamber. The second data set is then subtracted from the

data set containing the target. Such an operation removes many of the spurious reflections from the chamber and helps to remove any direct coupling that may exist between the transmit and receive horns on the scanning frame.

4.3 Reflection Measurements

The following section describes the application of the imaging system, described above, to the imaging of biophysical objects.

4.3.1 Imaging of Trees

Initially, three different species of tree were chosen for the experiment. The trees utilised were an ash tree (*Fraxinus excelsior* L.), a sycamore tree (*Acer pseudoplatanus* L.) and a willow tree (*Salix* species). The measurements were carried out during the winter months and each tree was essentially leafless. The trees were housed in round plastic pots to enable easy movement into the anechoic chamber. Their salient dimensions are given in Table I.

	Ash	Sycamore	Willow
Height of tree above soil level	120cm	104cm	162cm
Typical thickness of main axis	7 - 9.5mm	9.7 - 12.3mm	15.5 - 17.1mm
Typical thickness of main branches	4 - 5.4mm	5.5 - 7.5mm	6.5 - 13.8mm

Table I - Salient Dimensions of Tree Targets

As explained in Section 2.3.2, the depth of focus close to the aperture of a single frequency imaging system at 10GHz is in the order of only one to two centimetres. Therefore, the trees were sandwiched between two sheets of 2.54cm thick expanded polystyrene which were held together with masking tape. By so doing, all elements of the tree are constrained to lie in one plane from the aperture. The aluminium calibration bar was included with the tree to maintain a reference level between all the images. Measurements were made over a 1.5m by 1.5m scan for each of the three trees at polarisations of VV, VH and HH. Empty room subtractions were carried out for each image.

4.3.1.1 Ash Tree

Results for the ash tree are shown in Figure 4.6 from which it can be seen that the branches and main axis of the tree are in-focus and clearly visible above the background level. The VV and HH images show that the polystyrene sheet is again clearly visible along with small pieces of masking tape which can be seen at intervals along the vertical sides of the sheets. The optical image of the ash tree clearly shows the presence of two branches on the left hand side of the main axis, but these are not present in the microwave image. When examined, these branches were found to be dead and therefore likely to have a low water content, which is consistent with their low reflectivity. The same is true of the outer half of the lowest branch on the right-hand side of the main axis. The VV image also reveals the presence of a virtual image between the two uppermost parallel branches. This is caused by multiple reflections between the two branches and, noticeably, it does not extend beyond the shorter of the two branches.

The HH image produces a relatively strong return from the main axis because its diameter is approximately 0.3 wavelengths, but the return is much weaker from the upper branches which have a diameter of only 0.15 wavelengths. Localised high returns can be seen along these branches which appear to be consistent with the locations of buds where the local diameter is substantially increased thus giving a high return.

The VH image gives increased returns for tree components which are near to 45° relative to the horizontal. Multiple scattering terms can also be seen between the two uppermost branches of the tree corresponding to that seen in the VV image. Also visible are several nodes which have a high reflectivity where branches connect with the main axis. It is supposed that these nodes are the result of multiple scattering between the lower end of the branch and the main axis.

The high returns at the bottom of all three images are from the tree container and do not to carry information about the tree itself.

It is highly desirable to draw some quantitative results from the images presented in Figure 4.6 which relate the images to the power received at the aperture. This can be

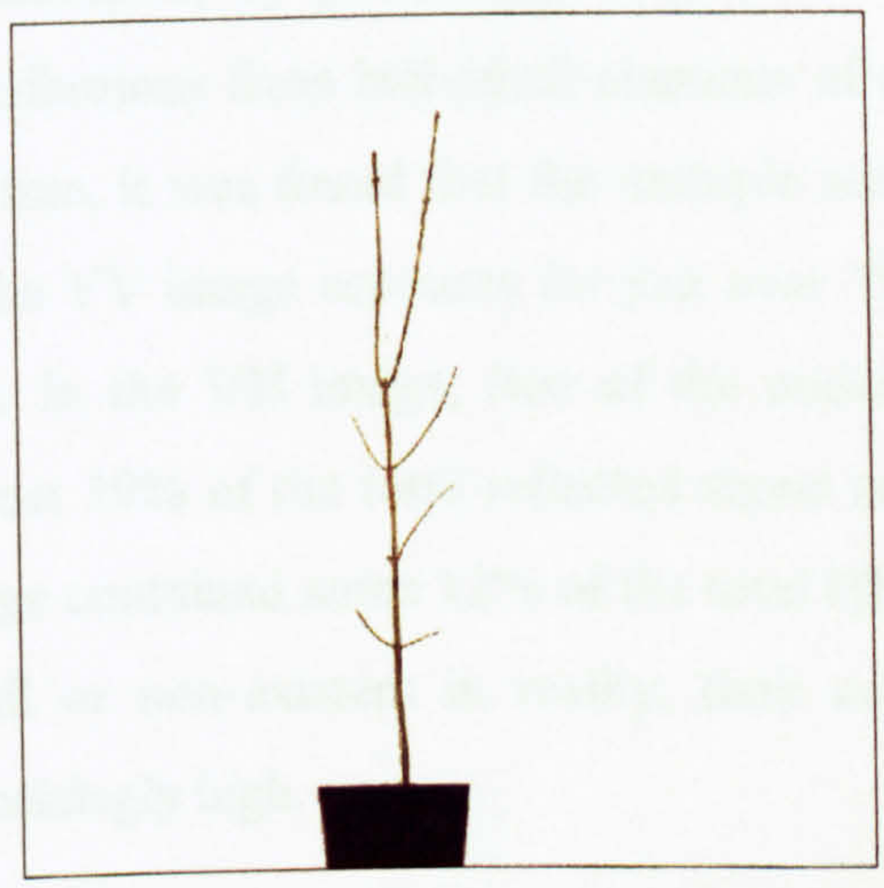

Optical Image

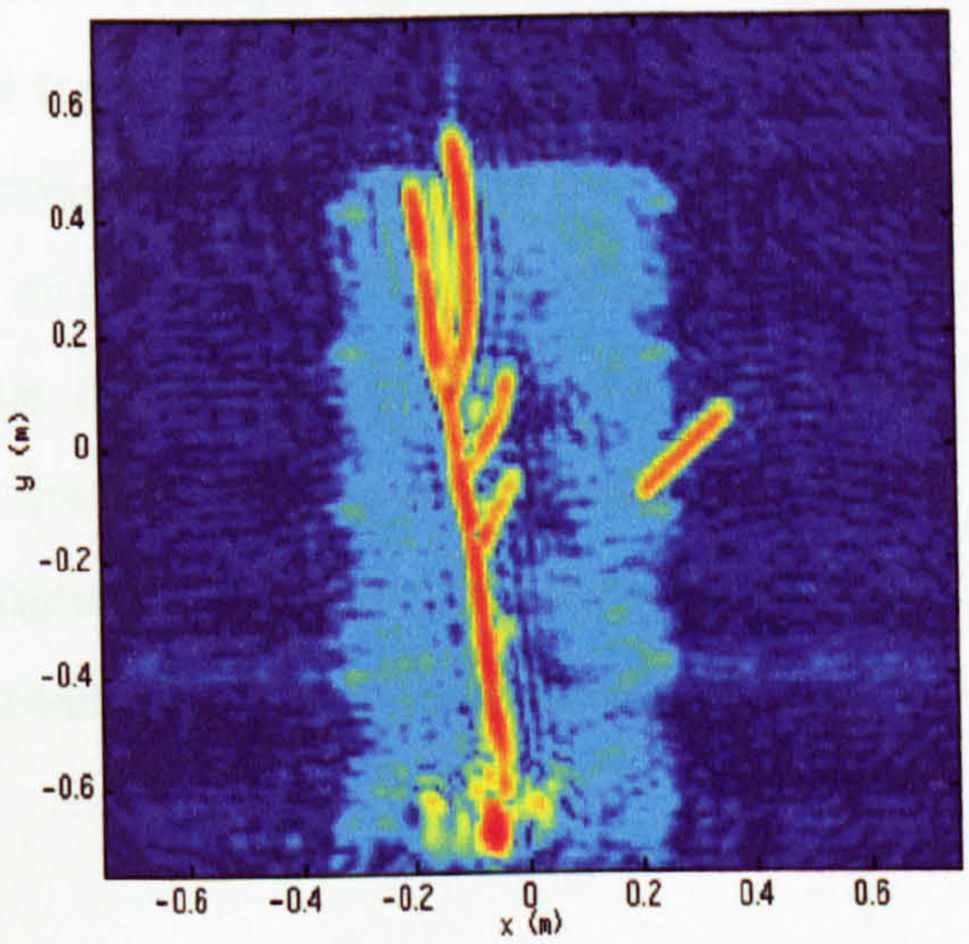

VV Image

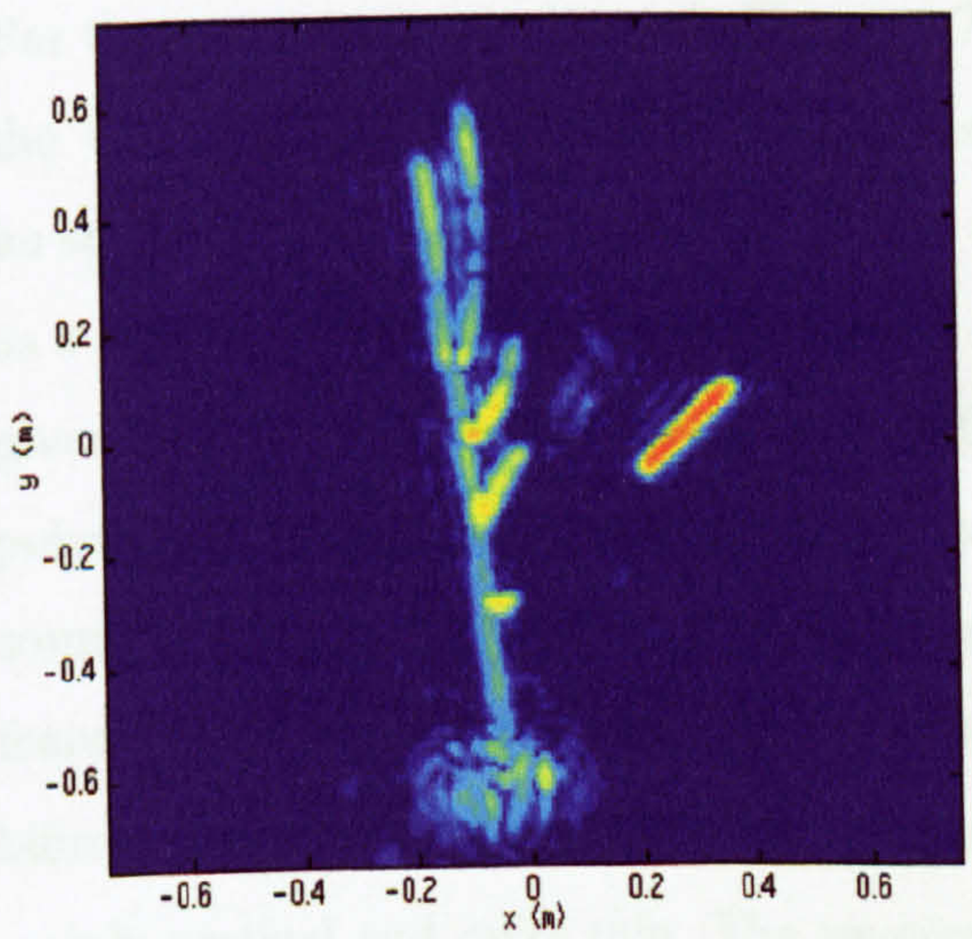

VH Image

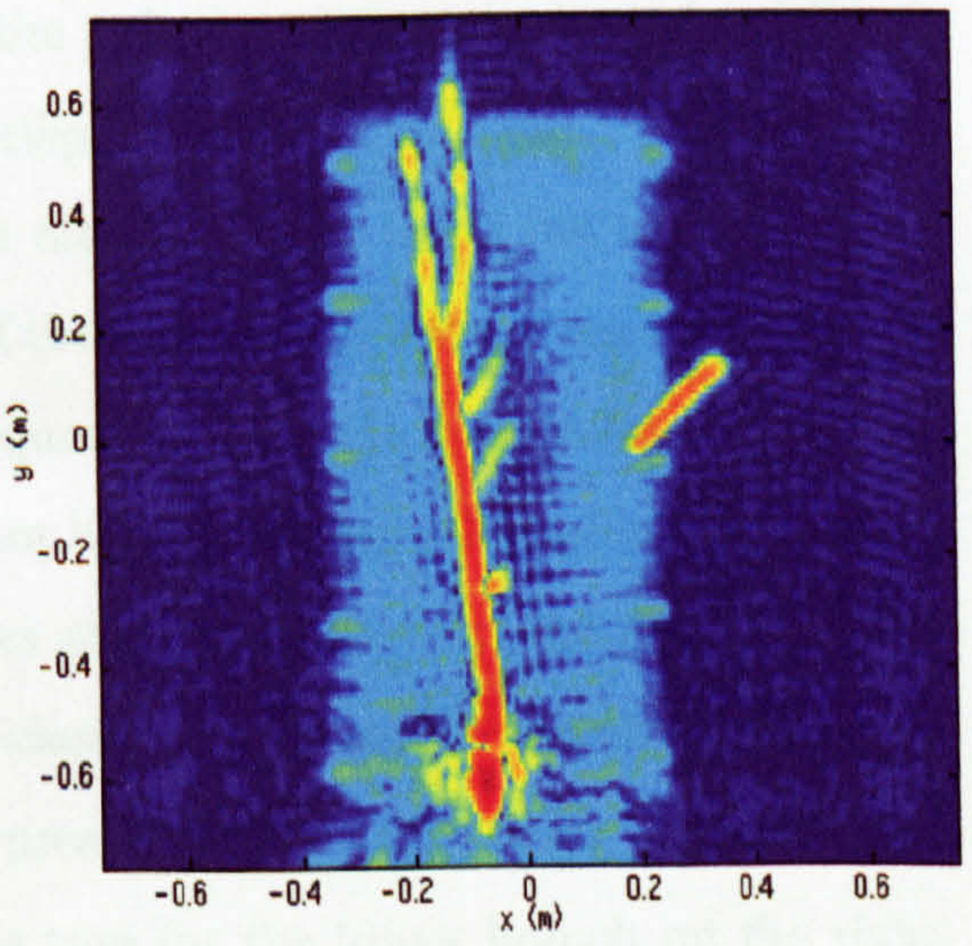

HH Image

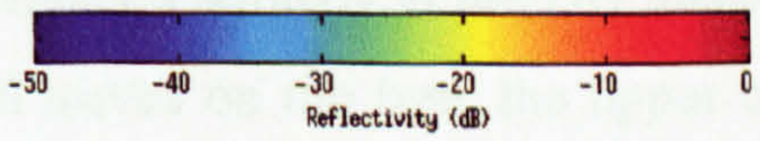

Figure 4.6 Results of Polarimetric Imaging of a Leafless Ash Tree

achieved by considering the complex sum of all the pixels in an image. By so doing it is possible to obtain an expression for the total power received from the whole tree. Furthermore, by performing a summation over selected regions of the image, the contributions from individual elements of the tree can be deduced. Therefore, for the ash tree, it was found that the multiple scattering term between the two top branches of the VV image accounts for just over 7% of the total VV signal reflected from the tree. In the VH image, two of the nodes on the main axis of the tree contributed almost 19% of the total reflected signal and the buds on the top branches of the HH image contained some 12% of the total HH signal. Considering that these artefacts are small or non-existent in reality, their contributions to the total reflected signal is surprisingly high.

4.3.1.2 Sycamore Tree

For the sycamore tree, shown in Figure 4.7, the polystyrene support is again visible in the VV and HH images, but in this case an elliptical area of very low reflectivity can be seen within it. This is particularly clear on the HH result. Here, the two sheets act as a sandwich radome, and over the locus of the ellipse they have a separation which gives 100% transmission at the operating frequency. Since the separation between the polystyrene sheets varies, other regions do not have the same value of separation and some reflection occurs. The VV image shows strong returns from the mainly vertical features and, in particular, distinguishes the cluster of thin stems just above the main bifurcation. However, these stems are not present in the HH image since they are mainly vertical and quite thin. The reverse is true for the lower branch on the right-hand side of the tree, which appears strongly in the HH image, but is weak in the VV image. There were two dead leaves on the tree, the upper one of which can just be seen in the HH image. Both were quite dry which is consistent with their low reflectivity.

In the VH image, the polystyrene is again invisible and the main axis of the tree has a very low reflectivity due to its orientation with respect to the polarisation. A virtual image can be seen between the top right branch and the calibration bar. Two nodes are also visible where the lower right branch connects with the main axis. This is

Optical Image

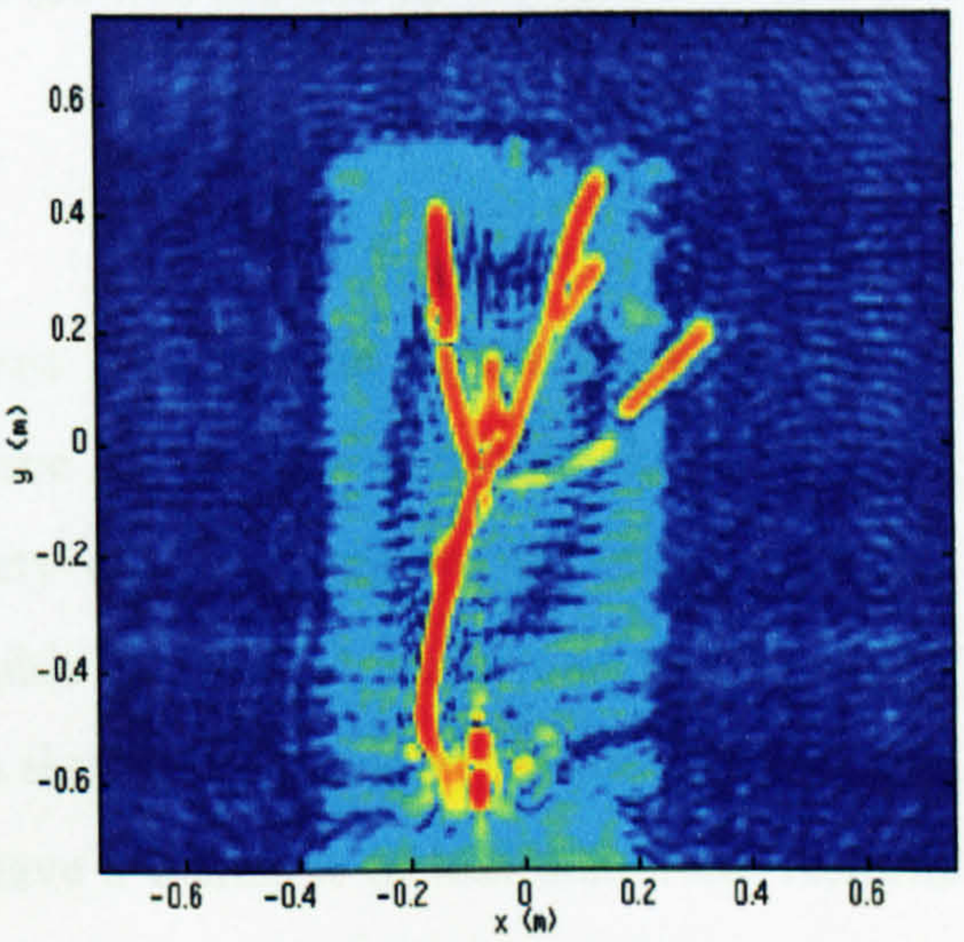

VV Image

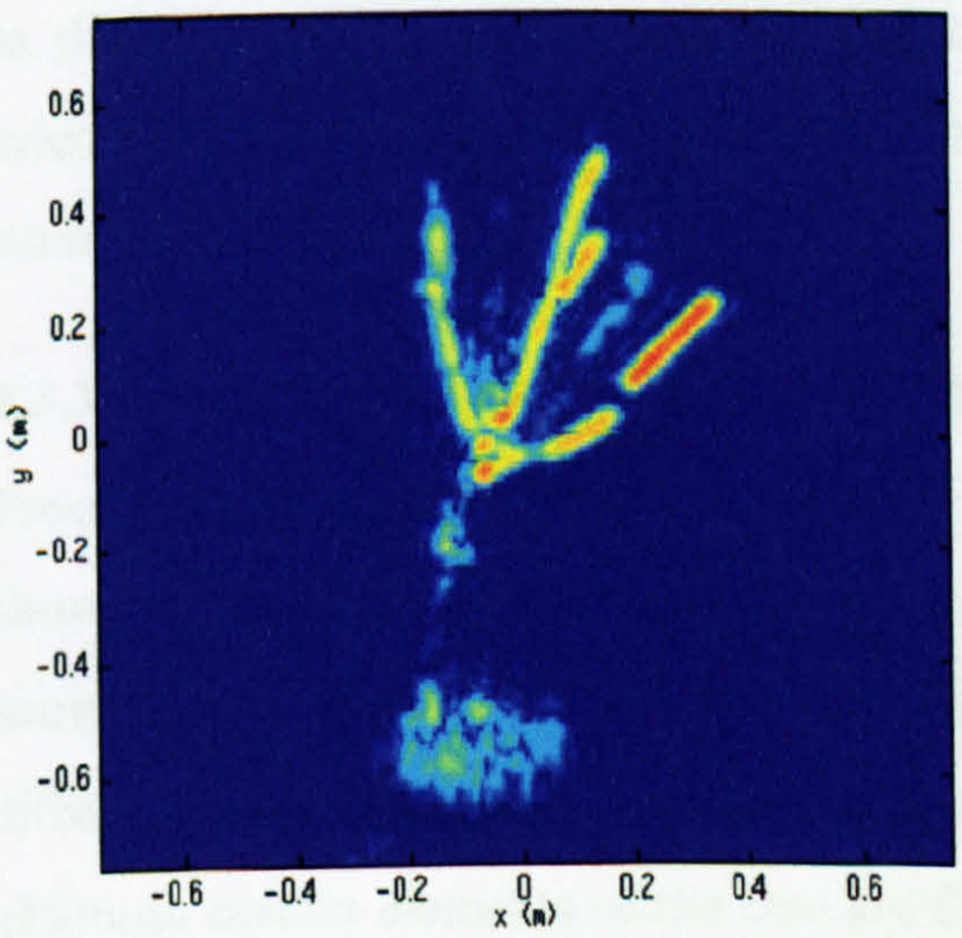

VH Image

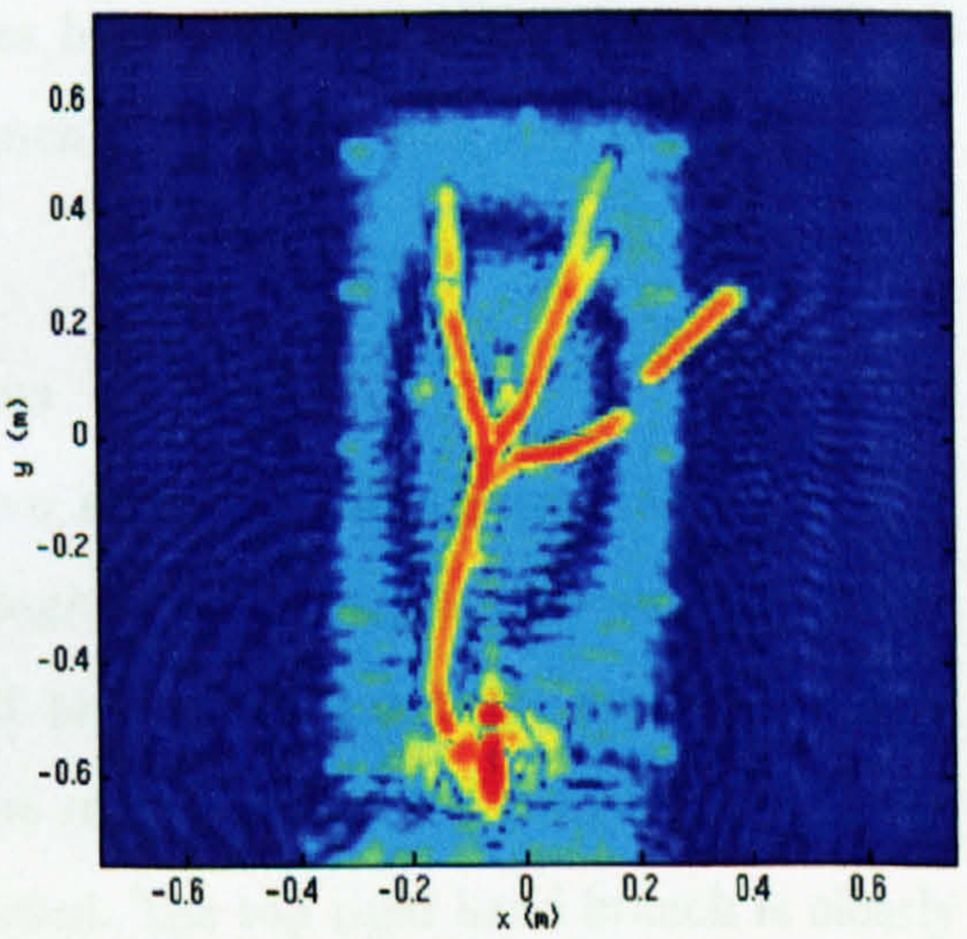

HH Image

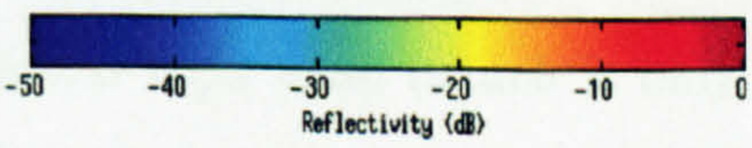

Figure 4.7 Results of Polarimetric Imaging of a Leafless Sycamore Tree

similar to the feature seen in the ash tree images, and it was found that these two nodes accounted for 8.5% of the total reflected signal from the tree.

Once again, the high returns from the base of the tree are due to the container and soil and provide no relevant information.

4.3.1.3 Willow Tree

The third tree measured was that of a willow tree and the results are presented in Figure 4.8. The complex features of this tree are clearly visible in the microwave images and show the polarisation sensitivity demonstrated by the other samples. Therefore, a high level of reflectivity is visible in the VV image due to the mostly vertical orientation of the branches whilst in the HH image the reflectivity of the top branches is considerably lower since many have a diameter of less than 1cm. Returns from the leaf clusters at the top of the tree can be seen for all polarisations.

In the VH image, one of the main branches has a very low reflectivity due to its orientation. However, a low level virtual branch can be seen mid way between to the main branches.

4.3.1.4 Proof of Depth of Focus Limitations

Proof that constraint of the tree between two sheets of polystyrene was essential is shown in Figure 4.9. Here the results of imaging an unrestrained sycamore tree are shown for VV polarisation. The backward propagator has been applied at three different distances and it is evident that none of the images are completely in focus although certain elements of the tree are focused. The top right hand branch is clearly focused when the focusing distance, z, is 1.25m, but the main axis is focused when z is 1.35m. Furthermore, the lower right hand branch is only just visible and is highly defocused since it is oriented at a large angle to the plane of the aperture.

The images also indicate the presence of a strong virtual image between the two main branches of the tree. No such virtual image is visible for the constrained sycamore tree of Figure 4.7 since the alignment of the two top branches is different in that case. (As noted in Chapter 2, the appearance of virtual images is dependent on the relative alignment and separation of target elements with respect to each other). It is also

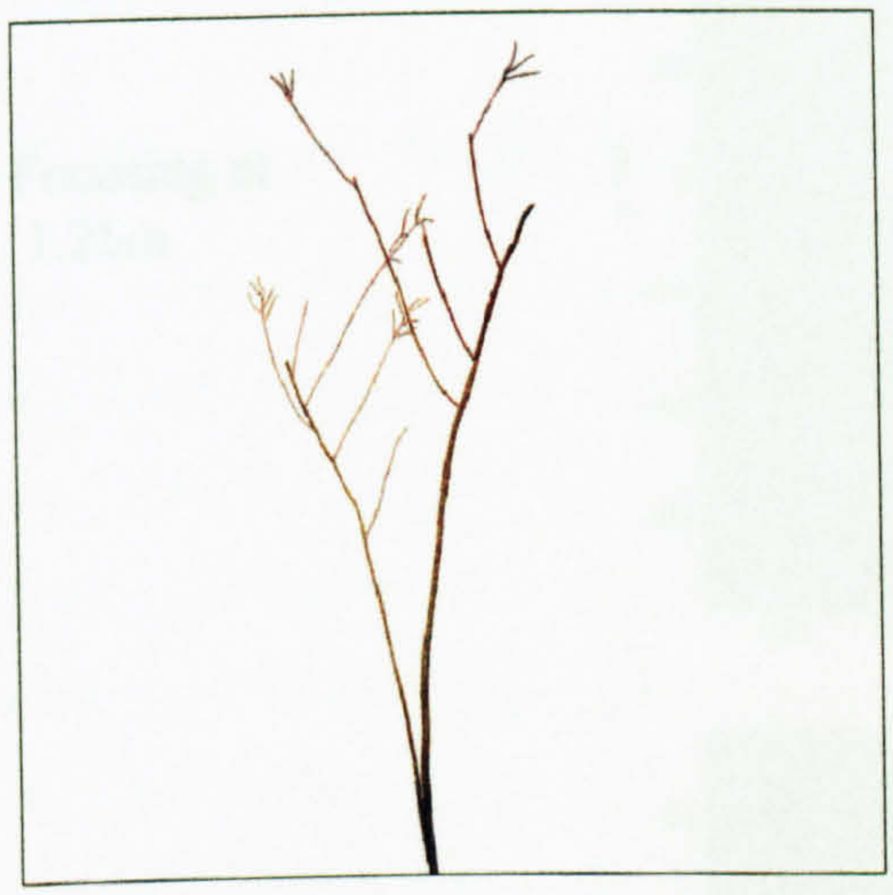

Optical Image

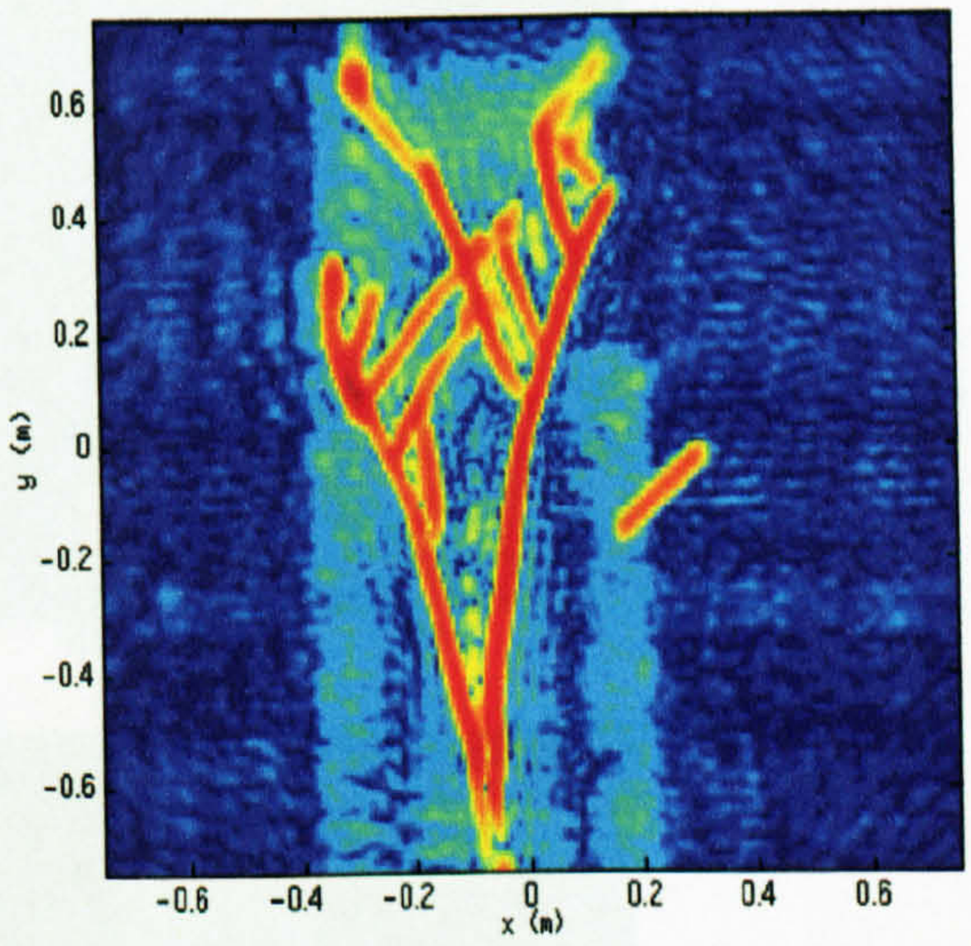

VV Image

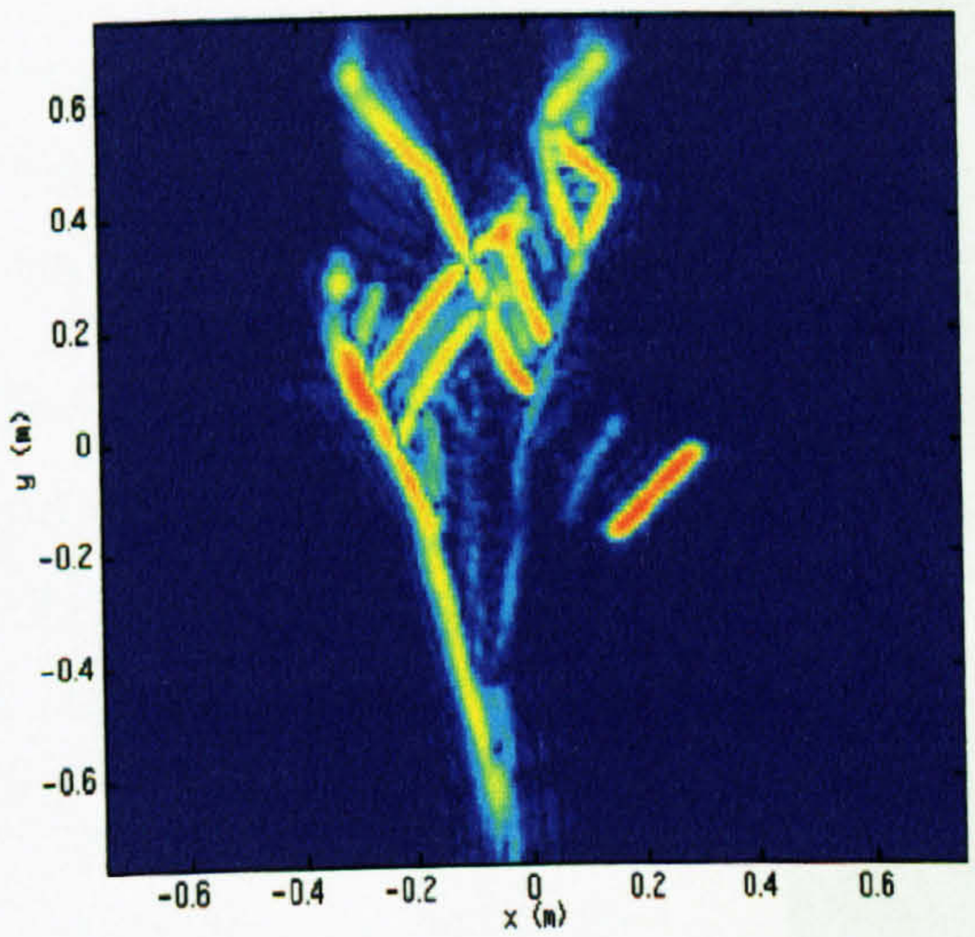

VH Image

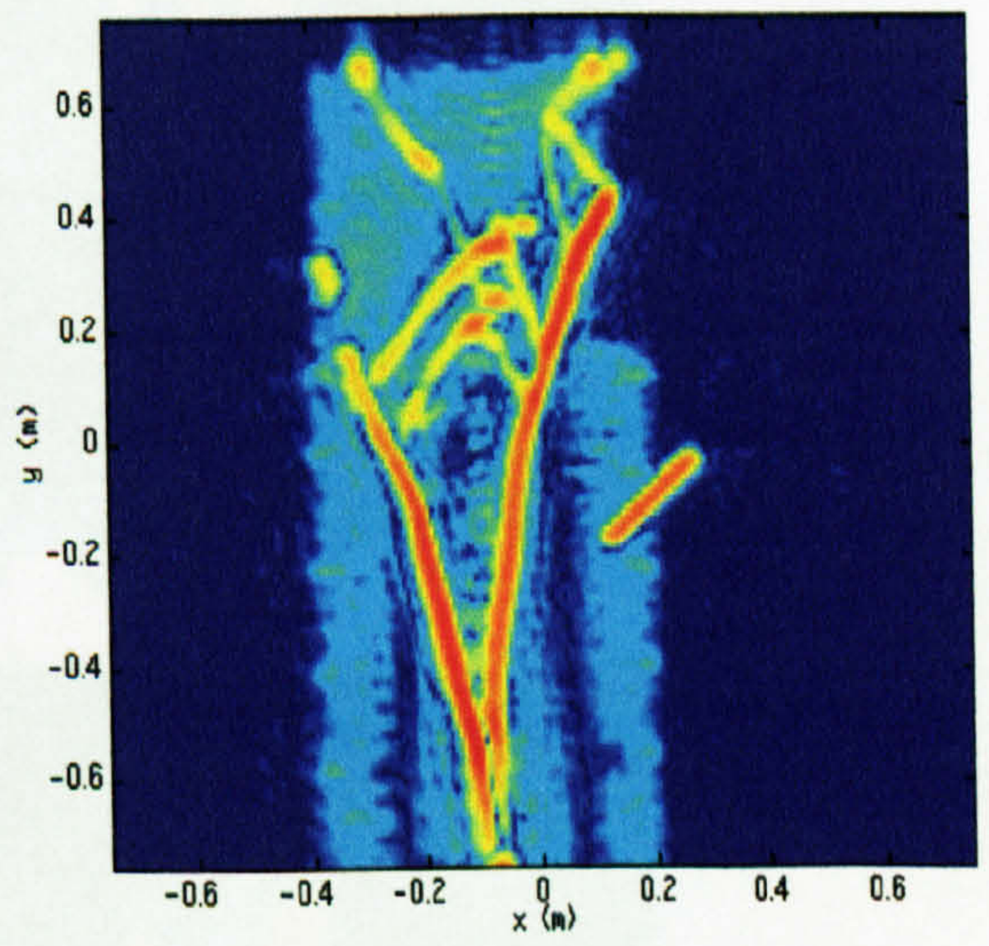

HH Image

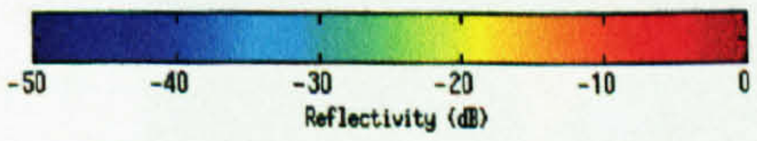

Figure 4.8 Results of Polarimetric Imaging of a Leafless Willow Tree

Focusing at
1.25m

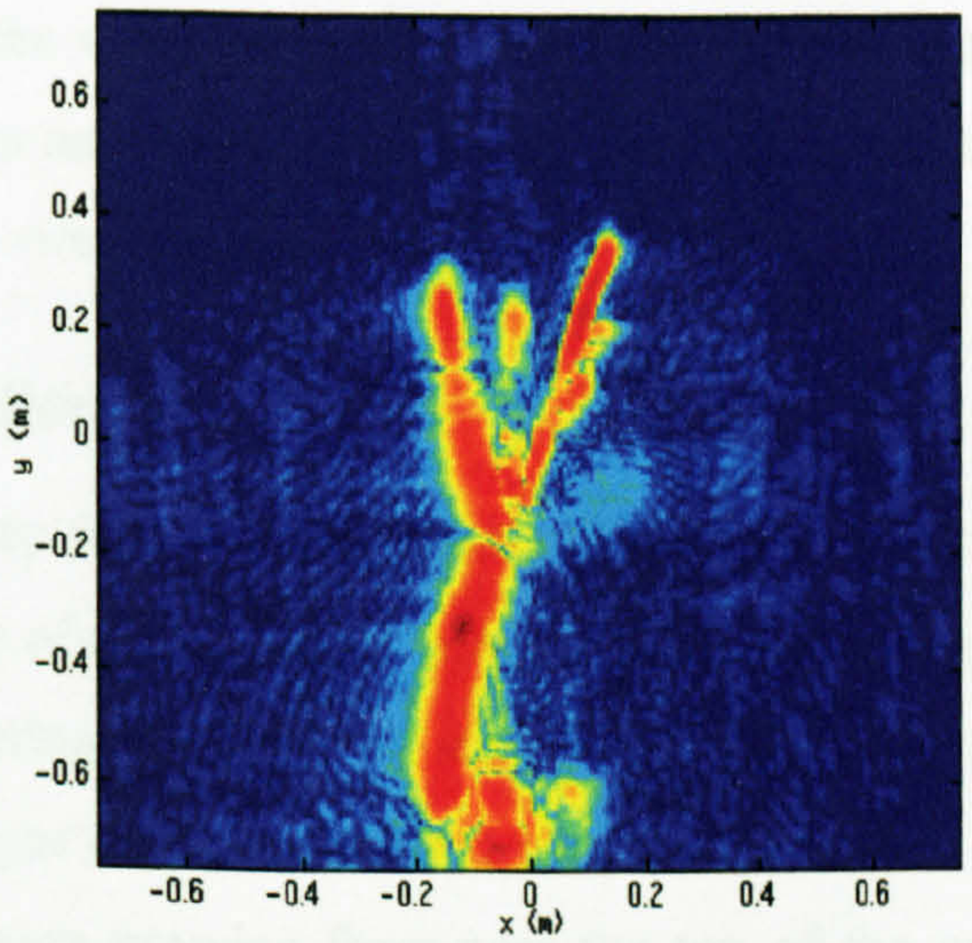

Focusing at
1.31m

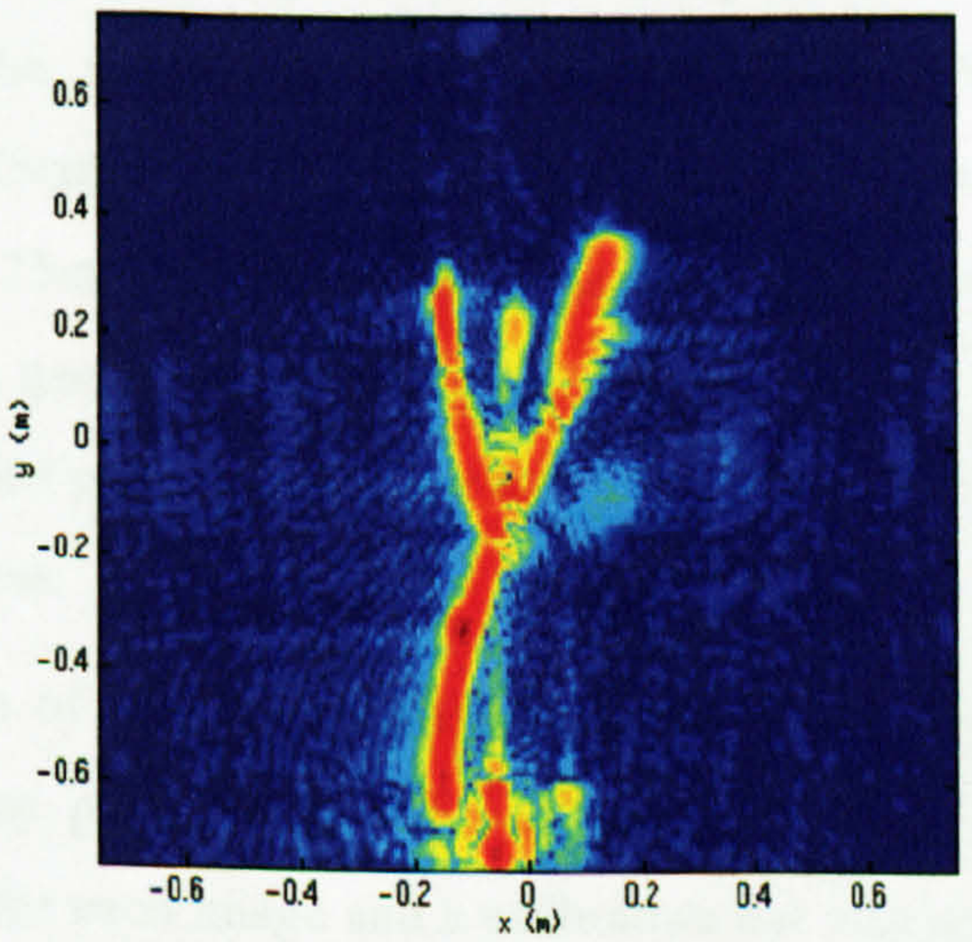

Focusing at
1.35m

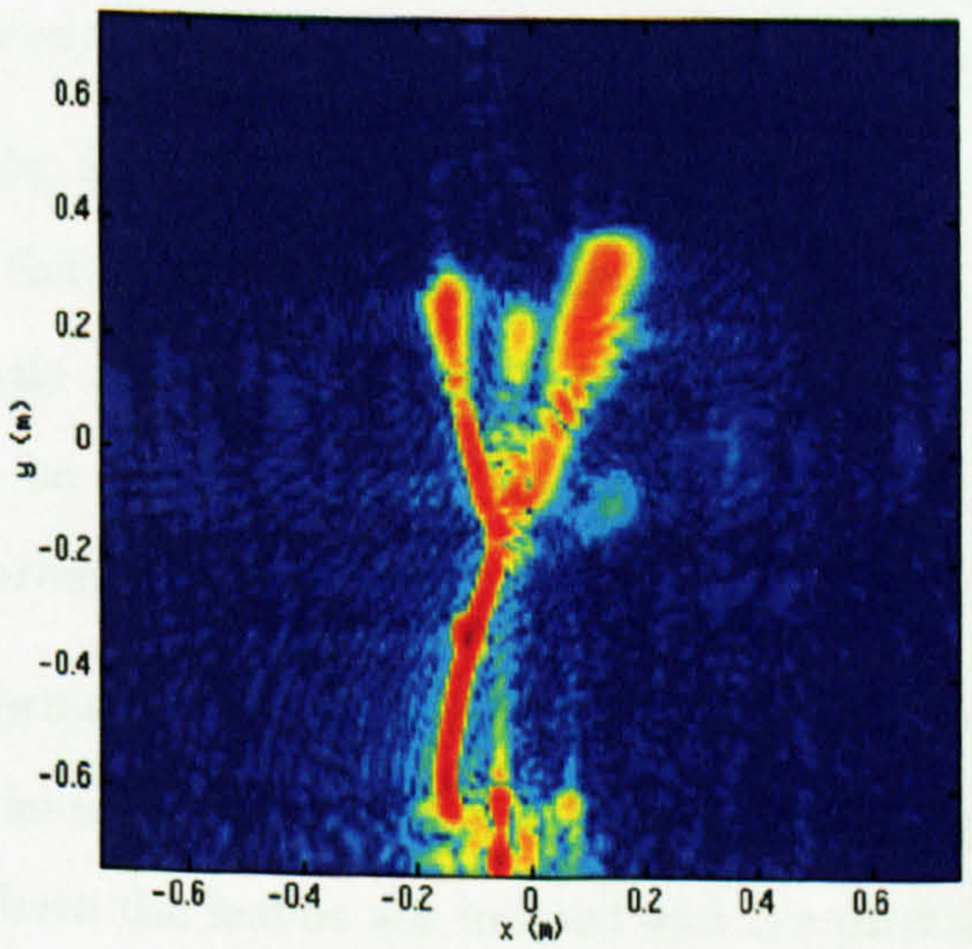

Figure 4.9 Results of Imaging an Unrestrained Sycamore Tree

evident from Figure 4.9 that the virtual image gives a return level comparable to the returns from real tree elements and without an optical image to refer to, it would be impossible to identify this as a virtual image.

4.3.2 Imaging of Sugar Beet

As part of an on-going study into the backscatter from agricultural crops [84], measurements were also made of a single sugar beet plant. The aim of such work was to determine the main scattering elements of such a plant and its variation with different polarisations. The sugar beet plant utilised was a mature plant and consisted of three large leaves which were growing from near the top of the main axis. The leaves were connected to the main axis by sturdy thin stalks. The plant was approximately 28cm tall and 25cm wide and the largest leaf was 12.5cm in length and 8cm in width. It was placed 1.25m from the aperture. As with the measurements made using the tree targets, it was necessary to place the sugar beet plant between two sheets of 2.54cm thick expanded polystyrene. Care was taken to ensure that the leaves remained flat during this process.

Figure 4.10 shows the results of collecting data over a 1m by 1m aperture for the sugar beet plant at the three polarisations of VV, VH and HH. Empty room subtractions were carried out for each image and a calibration bar was used to provide a fixed reference level between each image.

In both the VV and HH images, it can be seen that strong returns are received from each of the three leaves, with the strongest return coming from the central leaf. Also visible is the portion of the main axis which is above the soil. In the VV image, the stalks of the leaves can also be seen but these are not visible in the HH image. Spurious returns from the absorber material are also visible below the calibration bar.

The VH image is equally informative for what it does not show, namely, that the leaves of the plant are totally invisible at this polarisation. Only a few regions of low level backscatter are visible where the leaves are located and are probably caused by thick veins within the leaf structure. Evidently, leaves placed broadside to the radar do not cause depolarisation. The main axis of the plant is also invisible, but the stalks of two of the three leaves can be seen.

Optical Image

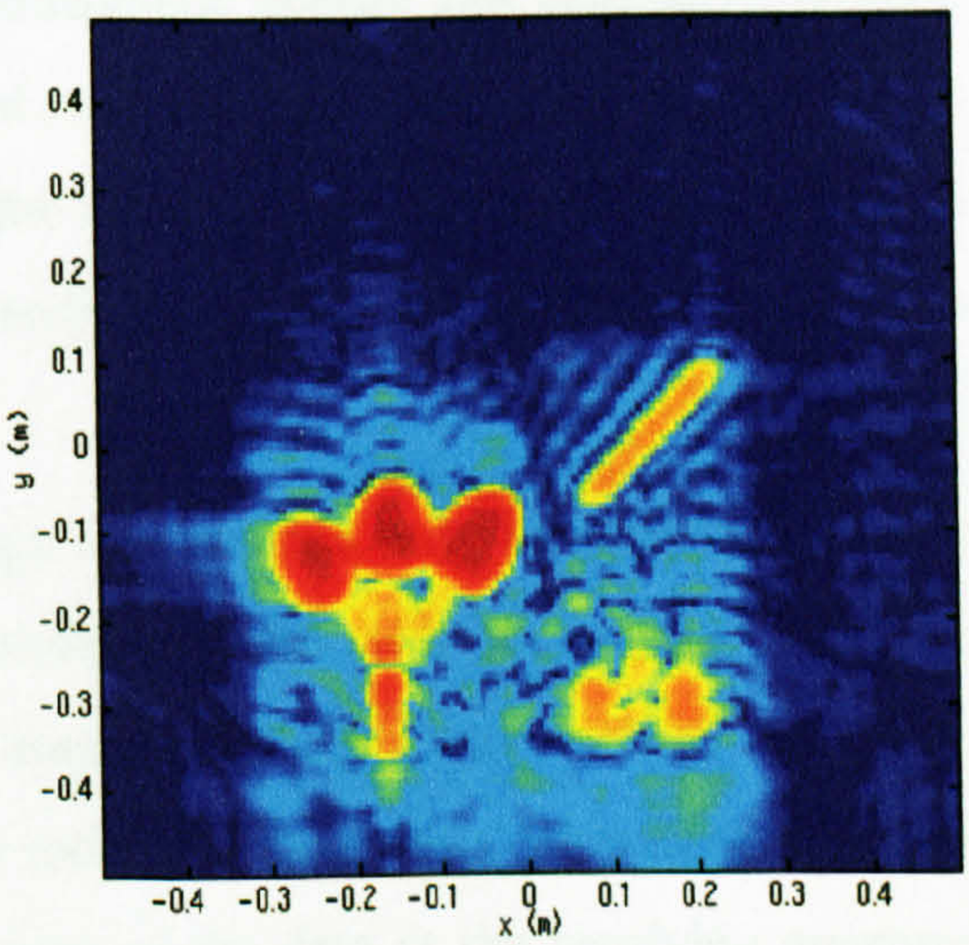

VV Image

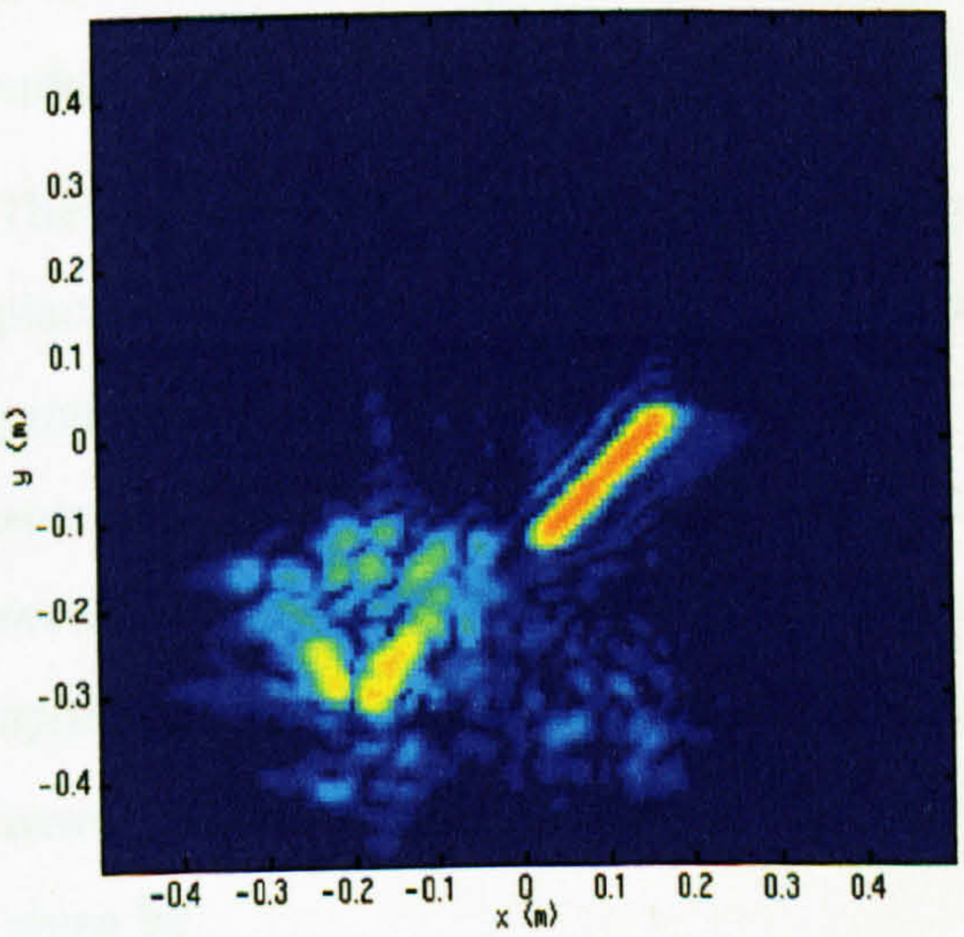

VH Image

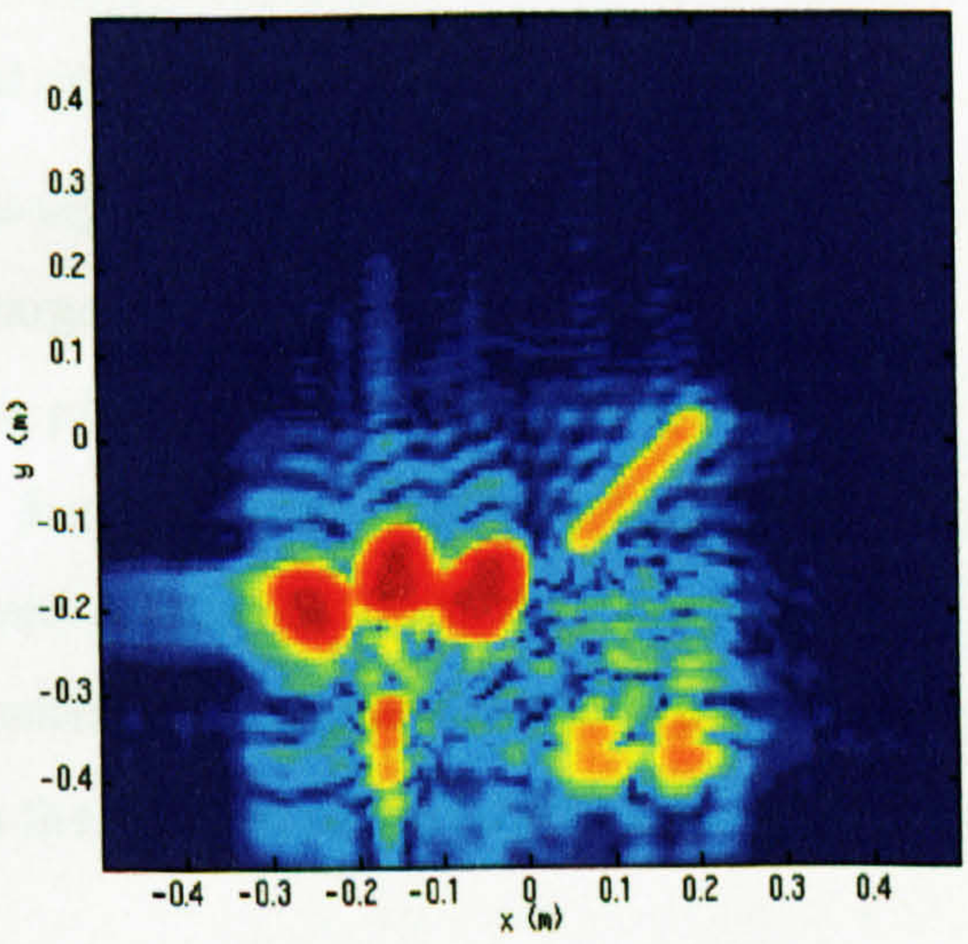

HH Image

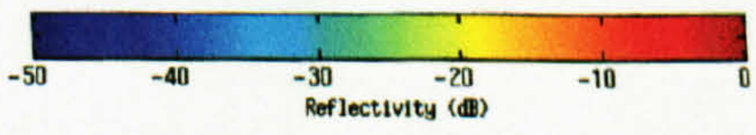

Figure 4.10 Results of Polarimetric Imaging of Sugar Beet

4.4 Transmission Measurements

The measurements made in Section 4.3 have provided a wealth of information about the nature of the interaction between electromagnetic energy and vegetative targets. In particular, the nature of the backscattered return was investigated. However, it is also important to examine the electromagnetic energy which travels through a target as well as that reflected from it. An understanding of such mechanisms is not easy to obtain.

A true representation of propagation through a target can only be achieved using a planar scanning aperture by having two apertures parallel with one another. Such an arrangement has one scanner to generate a transmitted plane wave behind the target and a second one in front of it to record the received plane wave. Therefore, for each single point on the transmit scanner, a full scan of the data at the receiving aperture must be made. Clearly, such an arrangement would be costly in terms of time and the volume of data involved and is not a practical option.

The next best scenario can be obtained by using a fixed transmitting source which is placed a considerable distance from the target and the receiver. A fixed source produces spherical waves as opposed to the plane waves synthesised by a scanning aperture. If the source is a considerable distance from both the target and the receiving aperture, then the spherical waves emanating from the source give an approximation to plane waves at the point where they encounter the target. In other words, the transmitter needs to be located in the far-field of the target. This distance is given by

$$R_{ff} = \frac{2D^2}{\lambda} \qquad (4\text{-}1)$$

where D is the largest dimension of the target. The disadvantage of using a fixed transmitter is that multiple scattering within the tree structure cannot be observed. As already mentioned, two separate parallel scanning apertures would be required for such an experiment.

4.4.1 Imaging of Trees

The sycamore tree studied in the reflection measurements was utilised again for the transmission experiments. As before, it was placed between two sheets of 2.54cm thick expanded polystyrene so that it lay in a plane parallel with the receiving aperture. A fixed transmitting horn antenna was placed some 3.7m behind the tree. The tree itself was located 1.3m from a scanning aperture where the receive antenna was located. According to equation (4-1), for a frequency of 10GHz, the distance between the sycamore tree and the transmitter should be in excess of 72m for the transmitter to be in the far-field of the target. Clearly, this cannot be achieved within the confines of the anechoic chamber. Therefore, the sycamore tree is illuminated with a spherical wave rather than a plane wave and this alters the phase of the reconstructed image. It does not, however, alter the magnitude of the image.

A scan of 1.5m by 1.5m of the tree was made for each polarisation and empty room subtractions were made for each data set. A 20cm long aluminium bar was used to provide a constant reference level between all the images as explained in Section 4.2.3.

The resulting images are shown in Figure 4.11 over 50dB dynamic range. From these, it is clear that there is a high background level which is due to the transmit horn located behind the tree. Despite using an empty room subtraction not all the transmitted signal has been eliminated leaving the defocused pattern of the transmit horn superimposed on the image. Although these images are not as good as had been hoped for, they still contain relevant information. It can be seen that the branches are a source of forward scattered signals, although the extent of this forward scattering depends on the orientation of the different tree elements with respect to the signal polarisation. Such polarimetric dependencies appear to be the same as those identified in the reflection measurements. Hence in the VV image there is very little forward scattered signal from the horizontal branch. The polystyrene sheets are again visible in the VV and HH images, although it is only the edge of the sheet that can be readily identified in the HH image. The resolution of these images is only half that of a transmit-receive system as was explained in Chapter 2.

VV

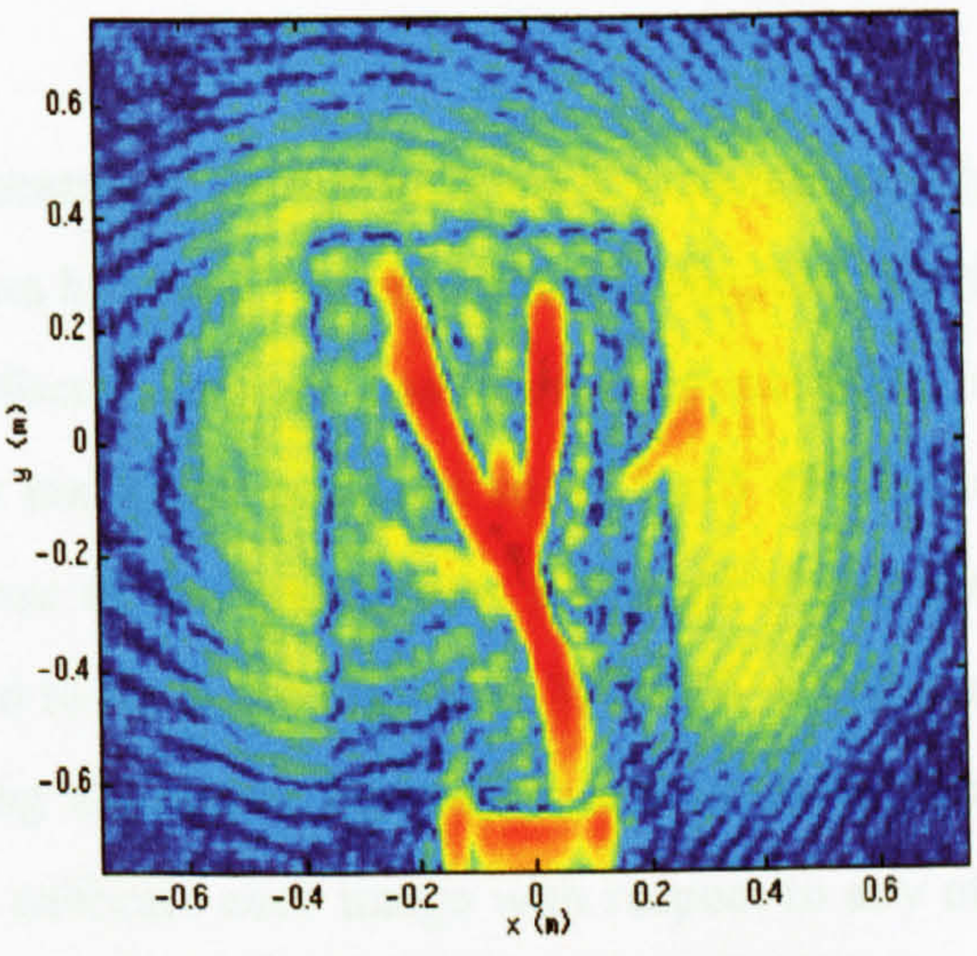

VH

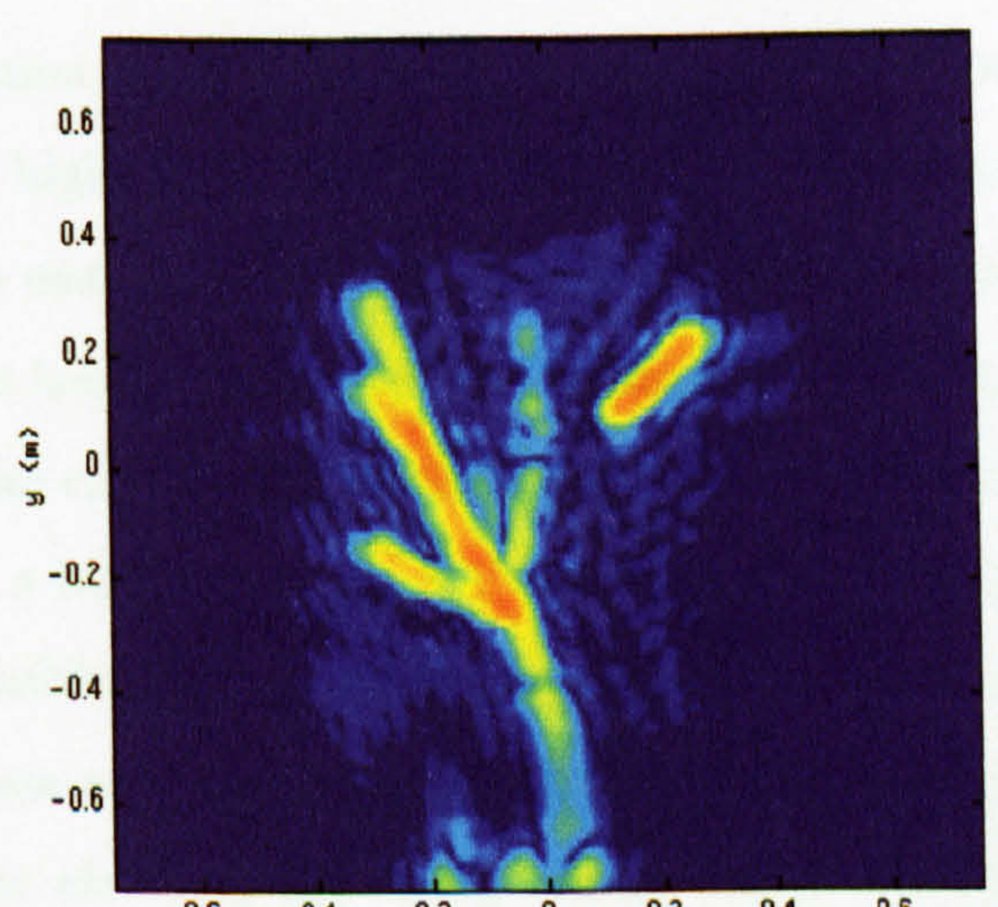

HH

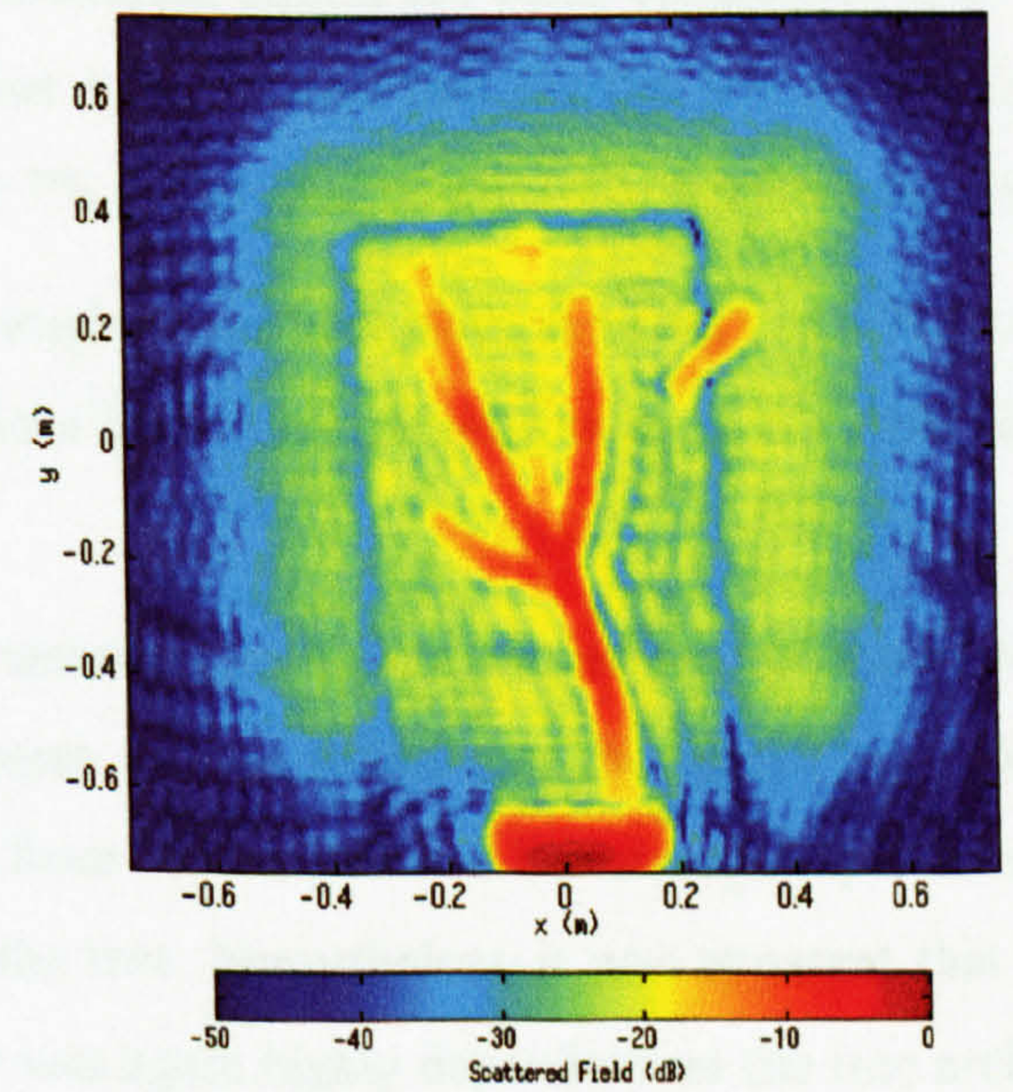

Figure 4.11 Results of Transmission Measurements Through a Leafless Sycamore Tree

4.5 Conclusions

An effective practical implementation of the backward propagation algorithm on a planar near field imaging system has been presented in this chapter. Verification that it can be used to produce in-focus imagery has been demonstrated, and a corner reflector was found to have a maximum response some 50dB above the background level. The polarimetric response of the system was investigated and the polarimetric purity of the system was found to be in the region of 35-40dB which provides a good level of isolation. A 20cm long aluminium bar was shown to be a suitable reference target which could be used to calibrate each image with respect to any other.

A series of polarimetric reflection measurements were then carried out on three trees. The system was shown to be highly sensitive and at VV and HH polarisations could image the polystyrene used to restrain the trees to a two dimensional plane. The trees were clearly visible above the background level and a number of interesting features were observed. Elements of the tree structures were highly dependent on polarisation, with vertical elements giving a high return for VV and visa versa. Small features on the trees were sometimes visible such as dead leaves, buds and nodes where the branches connected with a main axis. Significantly, the images also showed a number of incidences of virtual image elements appearing within the tree structures due to multiple scattering. Multiple scattering effects are often considered to be insignificant in terms of the total signal but it was found that for the VV ash tree, the multiple scattering term accounted for 7% of the total power reflected from the tree.

Images were also made of a single sugar beet plant showing that if leaves are parallel to the scanning aperture, then a high value of reflectivity is obtained from them for VV and HH polarisations.

Finally, limited transmission measurements were carried out on one of the trees used for the reflection measurements. It was found that the signal from the transmitter could not easily be removed from the images as it is a strong response in comparison to the forward scatter from the tree. Nevertheless, it was apparent that the scattered field recorded at the receiver was again highly dependent on the tree architecture with respect to the polarisation.

Chapter 5

Experimental Imaging with the Auto-Focusing Algorithm

5.1 Introduction

Chapter 3 presented the theory of a multifrequency near-field imaging system which utilised an auto-focusing algorithm to produce high resolution microwave images of targets. Application of this imaging algorithm to data collected on a real measurement facility is a complex task in which a number of factors have to be considered before accurate measurements can be obtained. The aim of this chapter is to examine these factors in detail and to develop the imaging process appropriately. Firstly, the effects of transmit and receive probe antennas on recorded data are examined by means of simulation in both one and two dimensions. A process known as probe compensation is utilised to remove these effects. In addition, the design of probe antennas is considered in relation to the auto-focusing algorithm and the experimental geometry so that appropriate antennas can be designed for the system. Equipment utilised for making actual measurements in an anechoic chamber is also described in this chapter along with practical considerations that must be taken into account when using it. Calibration of the system is explained and experimental validation of the algorithm is carried out by imaging two corner reflectors. Finally, the polarimetric sensitivity of the system is investigated.

5.2 Probe Antennas

Before any practical measurements can be made, it is important to examine the nature of the transmit and receive antennas which are mounted on the carriage of the scanning aperture. These probe antennas affect the recorded data values since the measured data is a convolution of the response of the target along with the response of the probe antennas. The effects of the probe antennas on the data need to be considered so that appropriate compensation can be carried out. Furthermore, the design of the probe antennas needs to be considered carefully in relation to the characteristics of the auto-focusing imaging algorithm and the geometry of the imaging system.

5.2.1 Probe Compensation

Every antenna has a particular electric field distribution across its aperture, which, along with the size and shape of the antenna, determines the antenna illumination pattern. This pattern defines the directivity of the antenna and hence affects the data which is transmitted or received through it. Therefore, for a transmit-receive synthetic aperture imaging system, the recorded data is not just the response of the target under test. Instead, it is a convolution of the response of the target with the effective aperture of the transmit-receive antenna system. This effective aperture is itself, the convolution of the patterns of the transmit and receive probe antennas.

In general, if the data recorded at the aperture are given by M(x,y,f) then

$$M(x, y, f) = U(x, y, f) \otimes \left[P_T(x, y, f) \otimes P_R(x, y, f) \right] \qquad (5\text{-}1)$$

where U(x,y,f) is the true response of the target at the aperture and P_T(x,y,f) and P_R(x,y,f) are the responses of the transmit and receive probe antennas respectively. Since the convolution and multiplication are related via the Fourier Transform [74], and given that the transmit and receive probe antennas are generally identical, equation (5-1) can be transformed to the spatial frequency domain so that

$$M(s_x, s_y, f) = U(s_x, s_y, f) \cdot P^2(s_x, s_y, f) \qquad (5\text{-}2)$$

It is evident from this equation that the effects of the probe antennas can be removed by dividing the measured data $M(s_x,s_y,f)$, by the square of the probe antenna response, $P^2(s_x,s_y,f)$, to obtain the true response of the target $U(s_x,s_y,f)$ [85]. This process is called probe compensation.

5.2.1.1 Probe Compensation for Pyramidal Horn Antennas

As already mentioned, the antennas utilised in this work are pyramidal horn antennas. These antennas have a constant amplitude illumination in one plane and a tapered cosine illumination in the other [86].

Since probe antennas only have a small aperture, their far fields are a few tens of centimetres from the aperture, as defined by equation (4-1). Therefore, targets are usually located in the probe antenna's far field, although they remain in the near field

of the scanning aperture. In the direction of uniform illumination, the one-dimensional far-field response of the probe antenna, $P_a(\theta)$, is a sinc function given by,

$$P_a(\theta) = \frac{D_a \sin\left(\frac{\pi D_a}{\lambda}\sin\theta\right)}{\frac{\pi D_a}{\lambda}\sin\theta} \qquad (5\text{-}3)$$

where D_a is the aperture size of the probe antenna in the plane of constant illumination and angle θ is defined in Figure 5.1 for ϕ=0. To remove the effects of the probe antenna, the equation must be transformed to the spatial frequency domain and substituted into equation (5-2). In the spatial frequency domain, $P_a(\theta)$ now becomes

$$P_a(s) = \frac{D_a \sin\left(\frac{\pi D_a s}{2}\right)}{\frac{\pi D_a s}{2}} \qquad (5\text{-}4)$$

Similarly, the one dimensional far-field response in the direction of cosine illumination, $P_b(\theta)$, is given by,

$$P_b(\theta) = \frac{\frac{2D_b}{\pi}\cos\left(\frac{\pi D_b}{\lambda}\sin\theta\right)}{1 - \frac{4D_b^2 \sin^2\theta}{\lambda^2}} \qquad (5\text{-}5)$$

where D_b is the aperture of the probe antenna in the plane of cosine illumination. Its spatial frequency domain response, $P_b(s)$, is then

$$P_b(s) = \frac{\frac{2D_b}{\pi}\cos\left(\frac{\pi D_b s}{2}\right)}{1 - D_b^2 s^2} \qquad (5\text{-}6)$$

To perform one-dimensional probe compensation on the measured data set M(x,y,f), equation (5-4) or (5-6) is substituted into equation (5-2) as appropriate, to obtain U(s,f). Simulations showing the effect of the probe pattern on the data and the results of applying probe compensation are presented in Section 5.2.3.

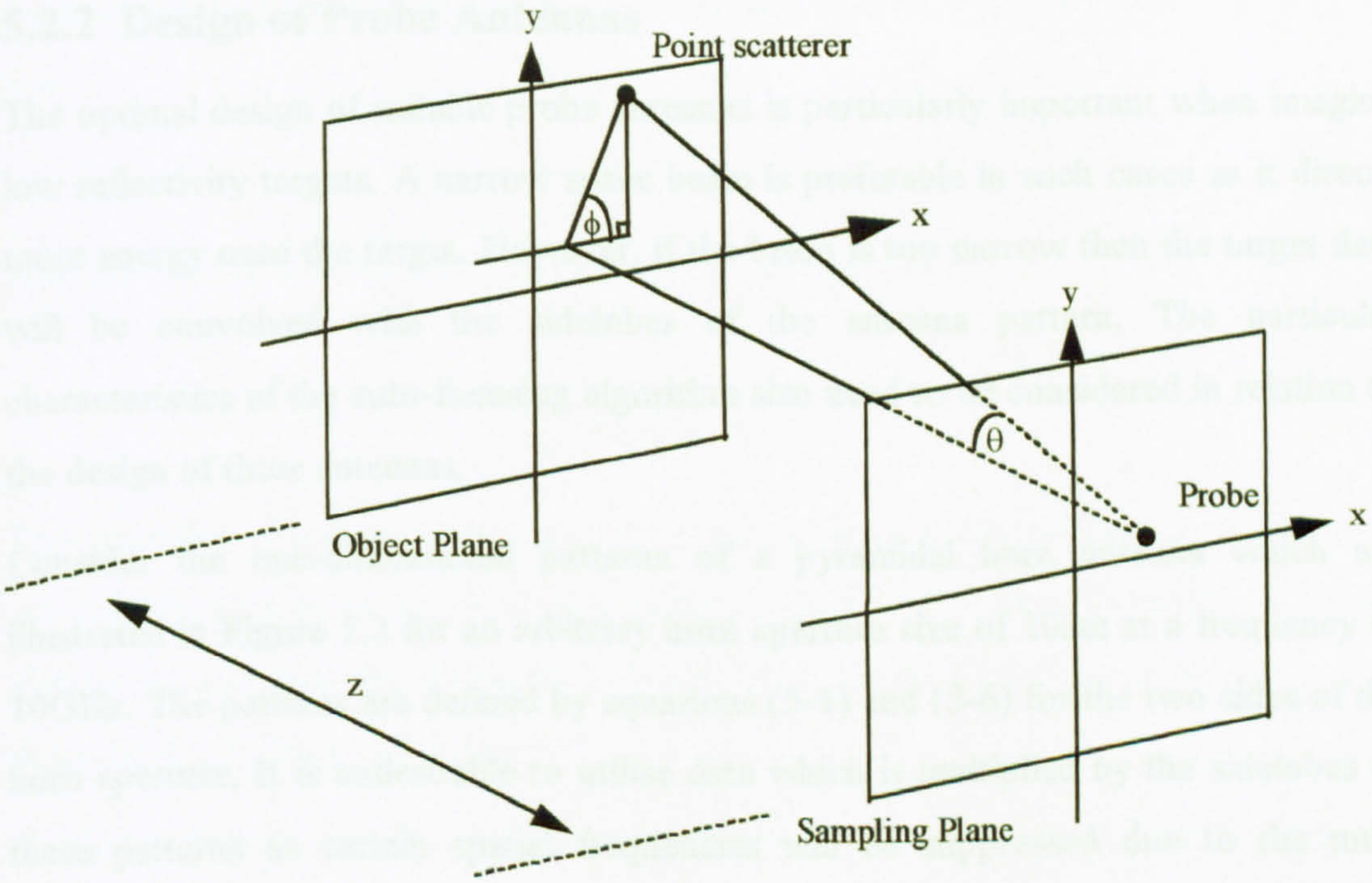

Figure 5.1 Definition of Theta and Phi

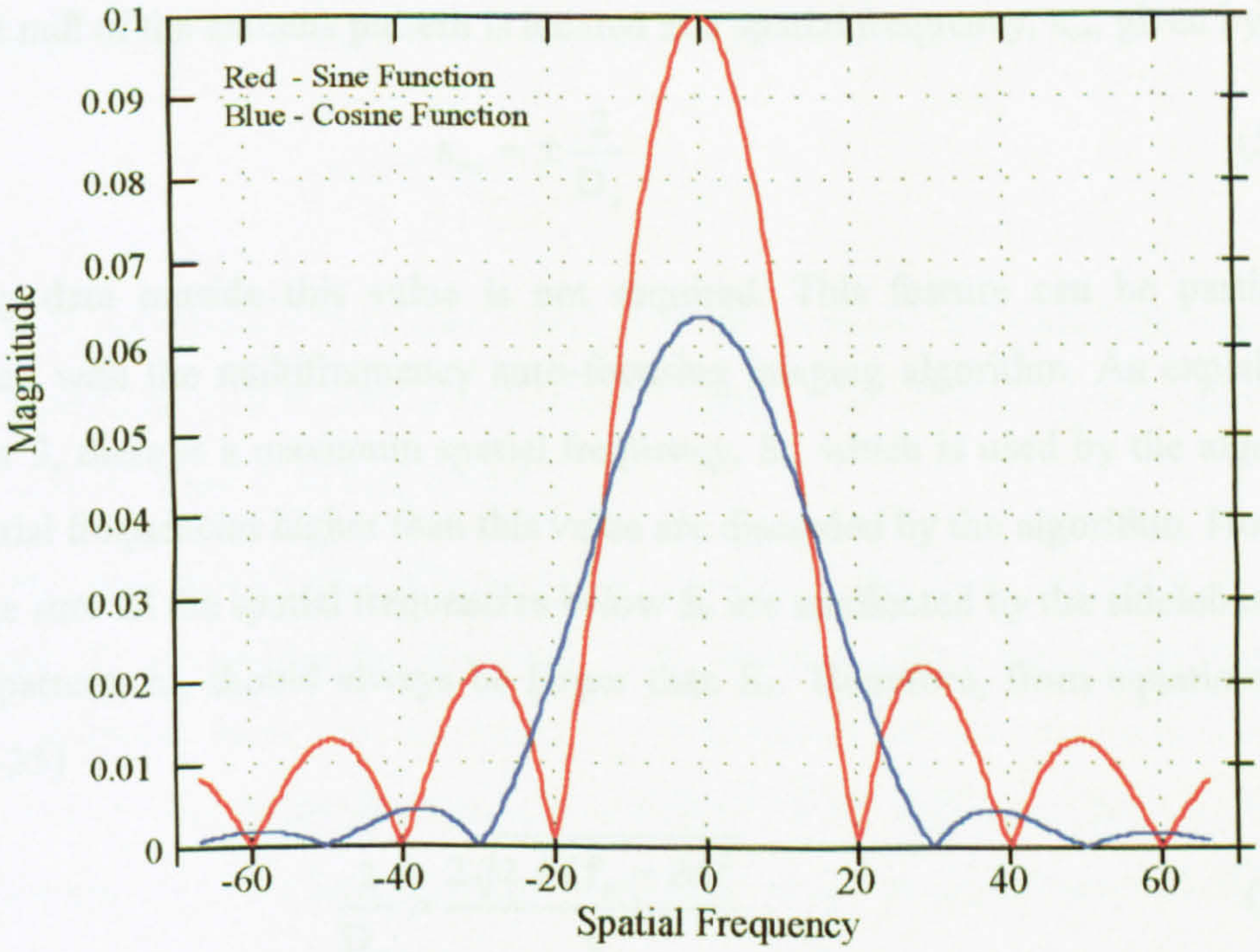

Figure 5.2 Far-Field Patterns of a Pyramidal Horn Antenna

5.2.2 Design of Probe Antennas

The optimal design of suitable probe antennas is particularly important when imaging low reflectivity targets. A narrow space beam is preferable in such cases as it directs more energy onto the target. However, if the beam is too narrow then the target data will be convolved with the sidelobes of the antenna pattern. The particular characteristics of the auto-focusing algorithm also need to be considered in relation to the design of these antennas.

Consider the one-dimensional patterns of a pyramidal horn antenna which are illustrated in Figure 5.2 for an arbitrary horn aperture size of 10cm at a frequency of 10GHz. The patterns are defined by equations (5-4) and (5-6) for the two sides of the horn aperture. It is undesirable to utilise data which is multiplied by the sidelobes of these patterns as certain spatial frequencies will be suppressed due to the nulls between the sidelobes. Hence only the data that falls within the main lobe of the antenna pattern is of use.

Consider first, the plane in which the probe antenna is uniformly illuminated and which has a spatial frequency domain response defined by equation (5-4). In this case the first null of the antenna pattern is located at a spatial frequency, s_{oa}, given by,

$$s_{oa} = \pm \frac{2}{D_a} \tag{5-7}$$

and any data outside this value is not required. This feature can be particularly exploited with the multifrequency auto-focusing imaging algorithm. As explained in Chapter 3, there is a maximum spatial frequency, S_c, which is used by the algorithm. All spatial frequencies higher than this value are discarded by the algorithm. However, to make sure all the spatial frequencies below S_c are unaffected by the sidelobes of the probe pattern, s_{oa} should always be larger than S_c. Therefore, from equations (5-7) and (3-35)

$$\frac{2}{D_a} > \frac{2\sqrt{2\,\Delta f\, f_o - \Delta f^2}}{c} \tag{5-8}$$

where Δf is the effective bandwidth of the system as defined by equation (3-36). The

aperture of the probe antenna is normally specified in multiples of wavelength, n_a, so that

$$D_a = n_a \lambda \tag{5-9}$$

Substituting this into equation (5-8) and re-arranging gives

$$n_a < \frac{f_o}{\sqrt{2\,\Delta f\, f_o - \Delta f^2}} \tag{5-10}$$

This equation determines the size the probe antenna needs to be, in multiples of wavelength, to prevent loss of spatial frequency data in this plane. In reality, n_a should always be less than the maximum allowed by equation (5-10) to avoid applying a sharp tapering effect to the data.

Similarly, the first null, s_{ob}, across the second plane where the probe has a tapered cosine illumination, is given by

$$s_{ob} = \pm \frac{3}{D_b} \tag{5-11}$$

The above method can be used to find the maximum aperture size, n_b, across the second plane in terms of multiples of the wavelength. Therefore,

$$n_b < \frac{3f_o}{2\sqrt{2\,\Delta f\, f_o - \Delta f^2}} \tag{5-12}$$

From these equations it was found that, for the modified auto-focusing algorithm, with a bandwidth of 0.51GHz and a centre frequency of 10GHz, typical values of n_a and n_b were 3.57 and 5.36 respectively.

Once this information was obtained, the design of the horn antennas could be addressed. By considering the geometry of the imaging system, the typical target size and its distance from the aperture, the beamwidth of the antennas could be determined. It was found for the targets utilised in the following chapter, that the 10dB beamwidth of the horns needed to be 120° in the vertical plane and 68° in the horizontal plane.

Given the system geometry and the maximum antenna size defined in equations (5-10) and (5-12), two horn antennas were designed. By using two different antennas, the target could be illuminated in any polarisation with the same illumination pattern. The horn for vertically polarised signals was 3.5cm by 7cm and the horizontal one was 4.5cm by 5.5cm.

5.2.3 Simulation of Probe Antenna Effects

This section presents simulations of the effects of probe antennas on simulated data in both one and two dimensions.

5.2.3.1 One Dimensional Simulations

Figure 5.3 illustrates the effect of a pyramidal horn antenna on a single point scatterer focused using the modified auto-focusing algorithm. In this example, the horn antenna is assumed to be 2λ in size. Once again bandwidth of 0.51GHz is used around a centre frequency of 10GHz. The scatterer is set 1m away from a 1m scanning aperture and, in this particular case, it is the effect of uniform illumination which is simulated. It can be seen that, once the effect of the probe antenna is included in the simulation, then the width of the mainbeam increases and the sidelobe levels decrease. This occurs since the pattern of the horn antenna acts as a filter window on the data in the spatial frequency domain. However, if the probe effects are removed, by applying probe compensation, then the resolution now returns that of the theoretical response. The sidelobe levels also increase back to the theoretical response although there are some slight changes to the low valued sidelobes.

The results for a cosine illuminated aperture produce very similar results to those for the uniform illumination and therefore are not presented here.

5.2.3.2 Two Dimensional Simulations

Section 5.2.1.1 explained how probe compensation is applied in a one-dimensional plane. In reality, two-dimensional probe correction is needed in which case equations (5-3) and (5-5) can be re-written as,

a) Theoretical Response

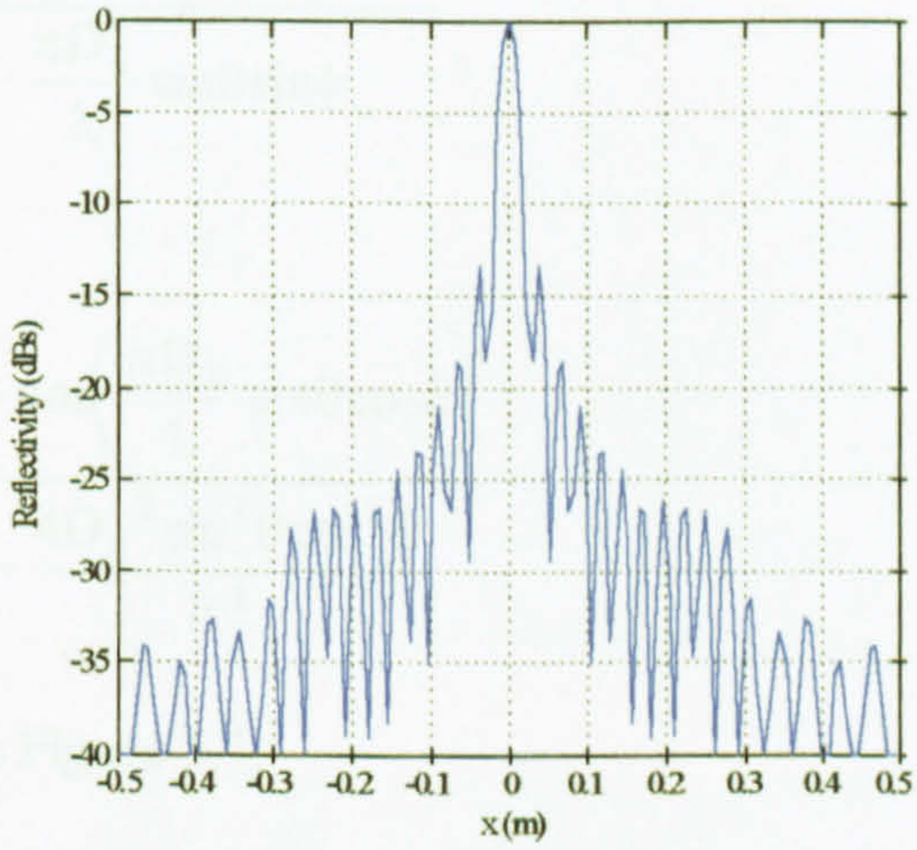

b) Response with Probe Effects Included

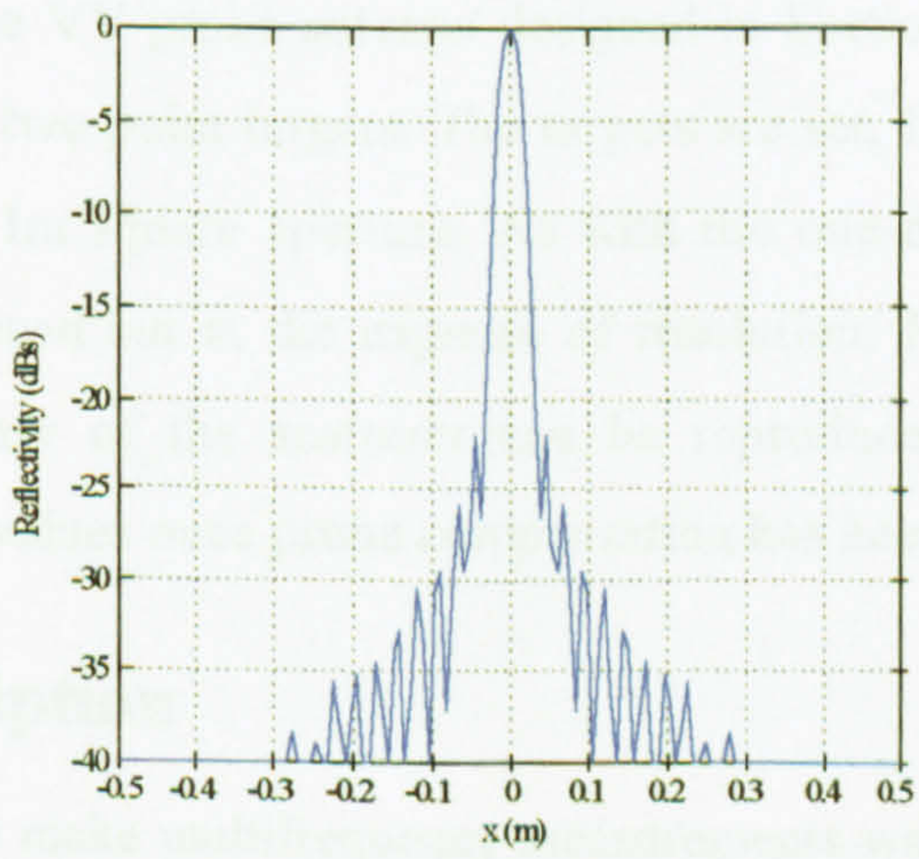

c) Response After Probe Compensation

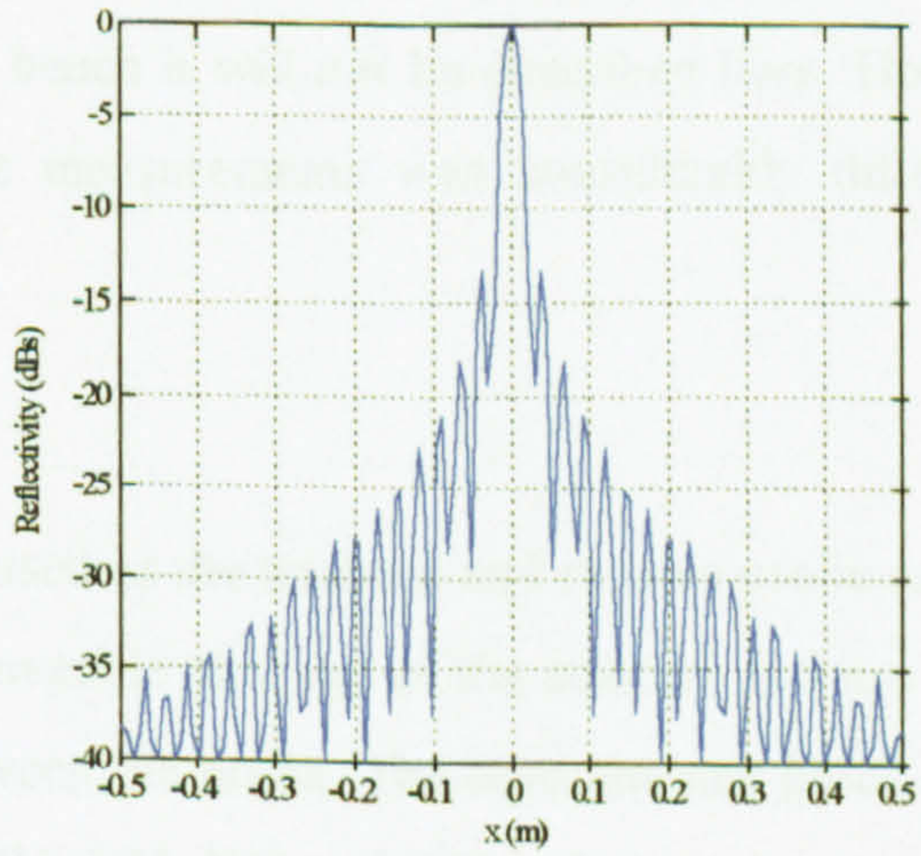

Figure 5.3 Illustration of the Effects of a Probe Antenna on a Single Point Scatterer

$$P_a(\theta,\phi) = \frac{D_a \sin\left(\frac{\pi D_a}{\lambda}\sin\theta\sin\phi\right)}{\frac{\pi D_a}{\lambda}\sin\theta\sin\phi} \qquad (5\text{-}13)$$

and

$$P_b(\theta,\phi) = \frac{\frac{2D_b}{\pi}\cos\left(\frac{\pi D_b}{\lambda}\sin\theta\cos\phi\right)}{1-\frac{4{D_b}^2\sin^2\theta\cos^2\phi}{\lambda^2}} \qquad (5\text{-}14)$$

where angles θ and ϕ are defined in Figure 5.1.

Figure 5.4b shows the effect of the VV probe antenna designed in Section 5.2.2 on the two-dimensional simulation of two point targets. The targets are set, from left to right, at 1.3m and 1.75m from a 1m square aperture. As with the one-dimensional simulations, the sidelobes are reduced but at the expense of resolution. Figure 5.4c illustrates that the correct response of the scatterer can be reproduced and the sidelobes restored to their original values once probe compensation has been applied.

5.3 Experimental Description

The experimental facility utilised to make multifrequency measurements was the same as that described in Chapter 4 and hence it will not be described here. However, the equipment employed to make the measurements was considerably different as is explained in the following section.

5.3.1 Equipment

The two pyramidal horn antennas, used as the transmit and receive probe antennas for the system, are mounted on the moveable carriage of the scanner and are positioned so as to minimise the coupling between the horns. The horn antenna block consists of four horn antennas which allows VV, VH, HH and HV polarimetric responses to be measured. The design of the horn antennas was considered in Section 5.2.2.

As shown in Figure 5.5, the transmit horn is driven via co-axial cables from an HP 8720DX network analyser. Initially, an HP 8404B network analyser was used but this

a) Theoretical Response

b) Response with Probe Effects Included

c) Response After Probe Compensation

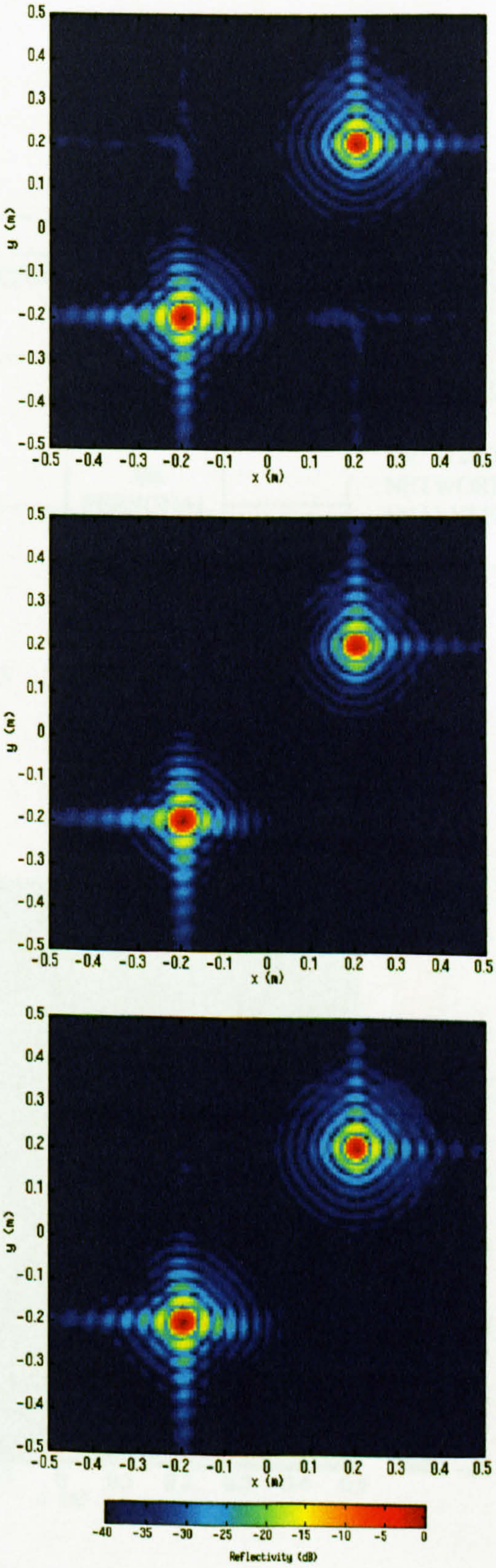

Figure 5.4 Effects of a Probe Antenna on a Two Dimensional Image of Two Point Scatterers

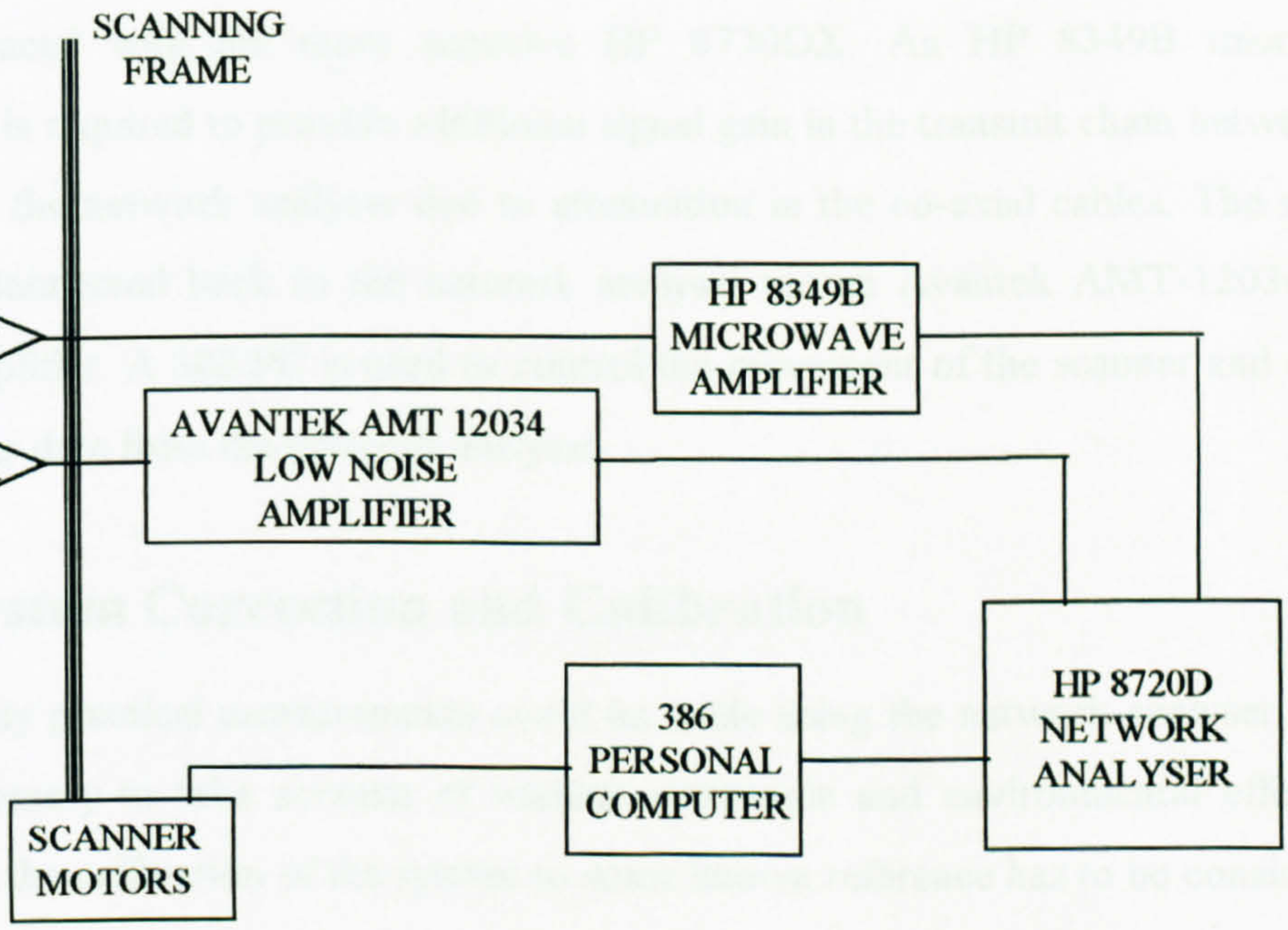

Figure 5.5 Experimental Setup

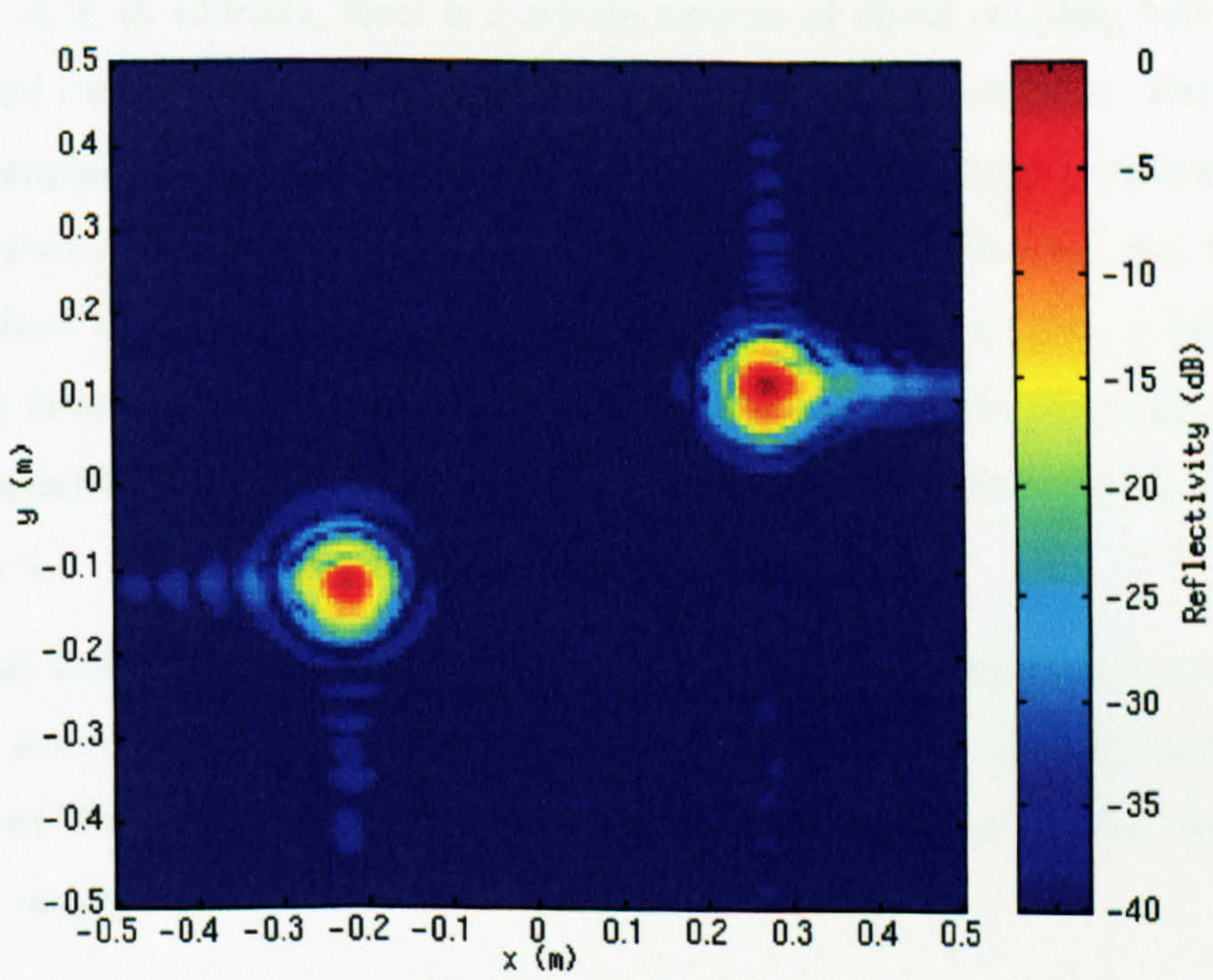

Figure 5.6 Results of Imaging Two Corner Reflectors

was replaced with the more sensitive HP 8720DX. An HP 8349B microwave amplifier is required to provide additional signal gain in the transmit chain between the horn and the network analyser due to attenuation in the co-axial cables. The receive horn is connected back to the network analyser via an Avantek AMT-12034 low-noise amplifier. A 386 PC is used to control the movement of the scanner and also to record the data from the network analyser.

5.4 System Correction and Calibration

Before any practical measurements could be made using the network analyser, it was first necessary to take account of various systematic and environmental effects. In addition, the calibration of the system to some known reference has to be considered.

5.4.1 System Correction

One of the main problems associated with making reflection measurements in an anechoic chamber is that there will be reflections from the chamber itself and the equipment in it. In addition, there is a certain amount of direct coupling between the transmit and receive horn antennas which are located next to each other. The amount of horn coupling depends on the polarisation used since different combinations of horn antennas are used for different polarisations. These reflections and coupling effects reduce the signal to noise ratio of the system and hence make it difficult to isolate the target response. They need to be removed before any processing can be carried out and this is achieved by performing an empty room subtraction as described in Chapter 4.

The system variation with changing frequency must also be accounted for including variations along the cables, waveguides and horns. Furthermore, the cable length must be removed from the system or the target under investigation will be incorrectly located in range.

The simplest way to compensate for these effects is to consider the signal recorded, $D_t(f)$, from a target located a distance r_t away from the aperture. $D_t(f)$ can be described by

$$D_t(f) = S(f)U_t(f)\exp(-jkb)\exp(-j2kr_t) \quad (5\text{-}15)$$

where S(f) accounts for the frequency response of the system, $U_t(f)\exp(-j2kr_t)$ is the true frequency response of a point in the target located a distance r_t from the aperture and b is the total length of cable in the system.

Equally, a target such as a corner reflector located a distance r_c from the aperture would have a frequency response $D_c(f)$. Therefore,

$$D_c(f) = S(f)U_c(f)\exp(-jkb)\exp(-j2kr_c) \quad (5\text{-}16)$$

where $U_c(f)\exp(-j2kr_c)$ is the true frequency response of the corner reflector. Dividing (5-15) by (5-16) gives

$$\frac{D_t(f)}{D_c(f)} = \frac{U_t(f)}{U_c(f)}\exp(-j2k(r_t - r_c)) \quad (5\text{-}17)$$

which removes the frequency dependence of the system, S(f), and the cable length effects. $U_c(f)$ can be computed since the radar cross section of a corner reflector has a well known and formulated value [82]. In short, $U_c(f)$ can be described by

$$U_c(f) = Kf \quad (5\text{-}18)$$

where *K* is a constant. Therefore, substituting this into equation (5-17) gives

$$D(f) = \frac{U_t(f)}{Kf}\exp(-j2k(r_t - r_c)) \quad (5\text{-}19)$$

Ultimately, all terms relating to the corner reflector should be removed in order to obtain the true target response. This can be achieved by multiplying the above equation by $f.\exp(-j2kr_c)$ to give $U_t(f)\exp(-j2kr_t)$.

The whole system correction process, applied to a two-dimensional data set, can thus be described as follows

i. Record response of a corner reflector for one (x,y) position over the frequency bandwidth.
ii. Record the response at the same (x,y) position with the target removed and subtract it from the first set to give $D_c(f)$.

iii. Record the two dimensional data of the target under investigation.

iv. Record an empty room set with the target removed and subtract from the data set to give $D_t(f)$.

v. Divide the data set by the response of the corner reflector to remove the system frequency response and cable length effects.

vi. Multiply by $f.\exp(-j2kr_c)$ to obtain the true target response.

Thereafter, focusing can be applied to the data to generate in-focus imagery.

5.4.2 Phase Compensation

Despite the corrections described above for removing system errors, there are still irregularities that occur during the measurement process. These must also be considered. The measurement of phase on the network analyser is highly sensitive to changes in temperature and changes of just 1°C can cause phase variations of 0.02rad for the cable lengths utilised in this work. The temperature variation during the measurement process may be significant especially as data collection for a large target may take in excess of two hours. The problem is compounded by the fact that the empty room subtraction process requires a second data set to be acquired and hence the total variation in temperature from the start of the data set to the end of the empty room set may be considerable.

The accepted method for compensating for these variations in phase is to take several lines of extra data at the end of each measurement set. These are known as tie-scans. The phase of these extra lines is compared with the phase of the same points in the data set and a general compensation curve to correct the whole data set is then constructed. This has been shown to work well for single frequency antenna measurements. However, with the auto-focusing algorithm, a large number of different frequencies are required and compensation would be required at each frequency for both the data and empty room measurements. Such an operation was found to require more time than could reasonably be allocated to it and was therefore not used in this work.

Investigations of the measured data revealed that variations in phase across individual data sets were reasonably small or non-existent, despite the fact that some data sets

took over two hours to collect. However, there could be significant variations in phase between the target data and the empty room data. Such variations between these two data sets could result in the background level of focused images being considerably higher than was expected. It was found that this variation could be limited by applying a small phase correction, normally of one or two degrees, across the whole of the empty room set thus minimising the average variation in phase between the two data sets. As this method is simple and fast and produces good results, it is applied to some of the data which will be presented in this chapter and the next.

5.4.3 System Calibration

The data recorded on the system described in Section 5.3 needs to be calibrated to some known reference value. Corner reflectors are often used for this purpose but in this case a 20cm aluminium bar oriented at 45° to the horizontal was utilised. This is the same reference that was used for the single frequency measurements and which was known to have a radar cross section of -21dBm^2. The choice of this reference has already been discussed in Section 4.2.3. As with the single frequency measurements, the calibration bar was included in each data set thus allowing all images to be displayed over the same colour scale.

5.5 Proof of Algorithm

Validation that the auto-focusing algorithm worked correctly was carried out by imaging a three-dimensional test target in the anechoic chamber. The target consisted of two trihedral corner reflectors each with a side length of 8cm. The reflectors were set 50cm apart in range and were positioned at (-0.225m,-0.125m) and (0.275m,0.125m) in the x and y directions. The nearest reflector was 1.3m from the aperture. Measurements were made using a 0.51GHz bandwidth at a centre frequency of 10GHz. The aperture size was 1m square and the polarisation was HH. System correction was implemented and probe compensation was carried out. The auto-focusing algorithm was then applied to generate the image shown in Figure 5.6. It should be noted that although the centre frequency of the recorded bandwidth was 10GHz, the modified auto-focusing algorithm described in Section 3.5 was used to

focus the image and this uses a frequency of 10.15GHz. In order to keep the sidelobe levels down, dual apodization techniques have been applied to this data. From the figure, it can be seen that the two corner reflectors are both in-focus although they do display slightly different sidelobe structures since they are located at different ranges.

5.6 Polarimetric Sensitivity

The polarimetric sensitivity experiments carried out in Chapter 4 were repeated for the multifrequency system. It was important to repeat the measurements since a new horn cluster had been employed and its polarimetric purity was unknown.

In order to examine the polarimetric response of the system, a test target consisting of three thin wires at different orientations was imaged. This target was the same as that used in Chapter 4, where each wire was 0.75mm in diameter and 20cm in length and were mounted on an expanded polystyrene sheet 120cm by 60cm as shown in Figure 4.4. A calibration bar was included in each measurement set to act as a constant reference and measurements were made over a scan aperture of 1.095m by 1.155m. For each data set, an empty room subtraction was also made. The results of imaging the target at VV, VH and HH polarisations are shown in Figure 5.7 over a 40dB dynamic range and should be compared with the results obtained in Chapter 4 for the single frequency system. It should be noted that these images have been probe compensated and filtered using dual apodization techniques which were not applied to the single frequency measurements.

In the VV image, the vertically oriented wire has the strongest response and the horizontal wire cannot be seen. The wire at 45° has a response approximately 5.5dB below that of the vertical wire which again compares well with the expected value of 6dB. The polystyrene sheet supporting the wires is also visible demonstrating that the measurement system is highly sensitive. Of particular interest is the weak return located half way between the wire at 45° and the calibration bar. This is a virtual image generated by multiple scattering between the bar and the wire and is slightly defocused. Such a result was predicted by the simulations in Chapter 3. To verify that it this image was indeed a result of multiple scattering, a single frequency reconstruction at the centre frequency of the system was carried out. It was found that

VV

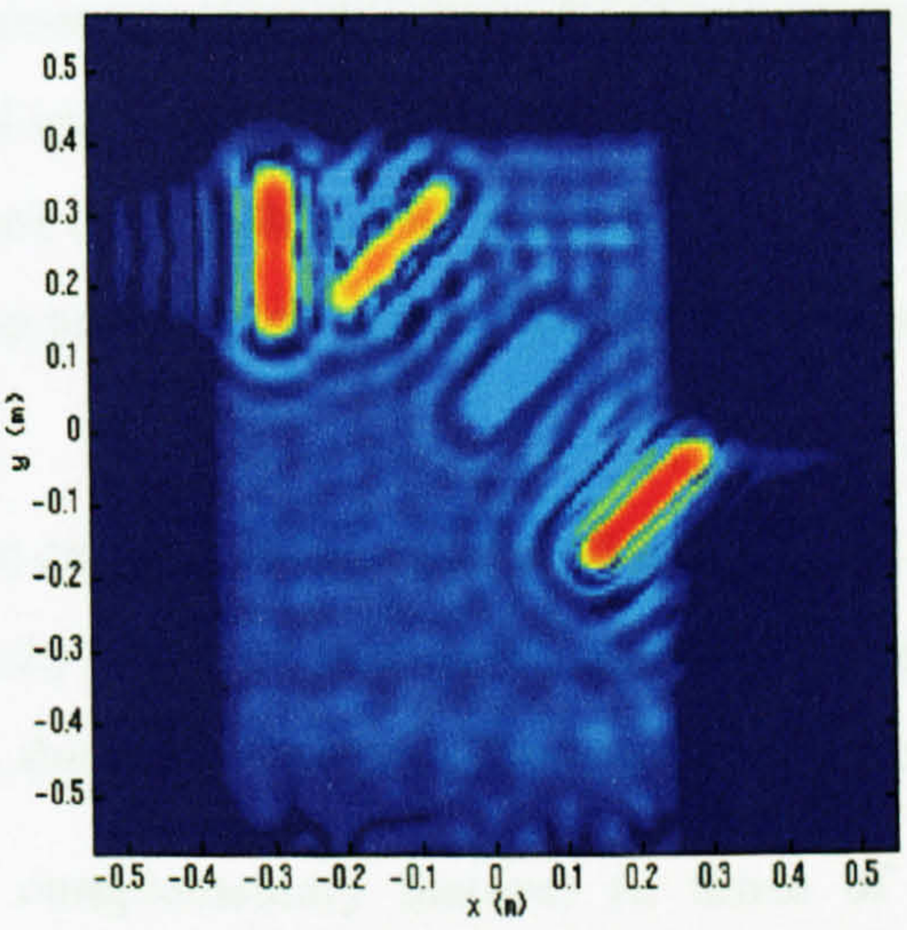

VH

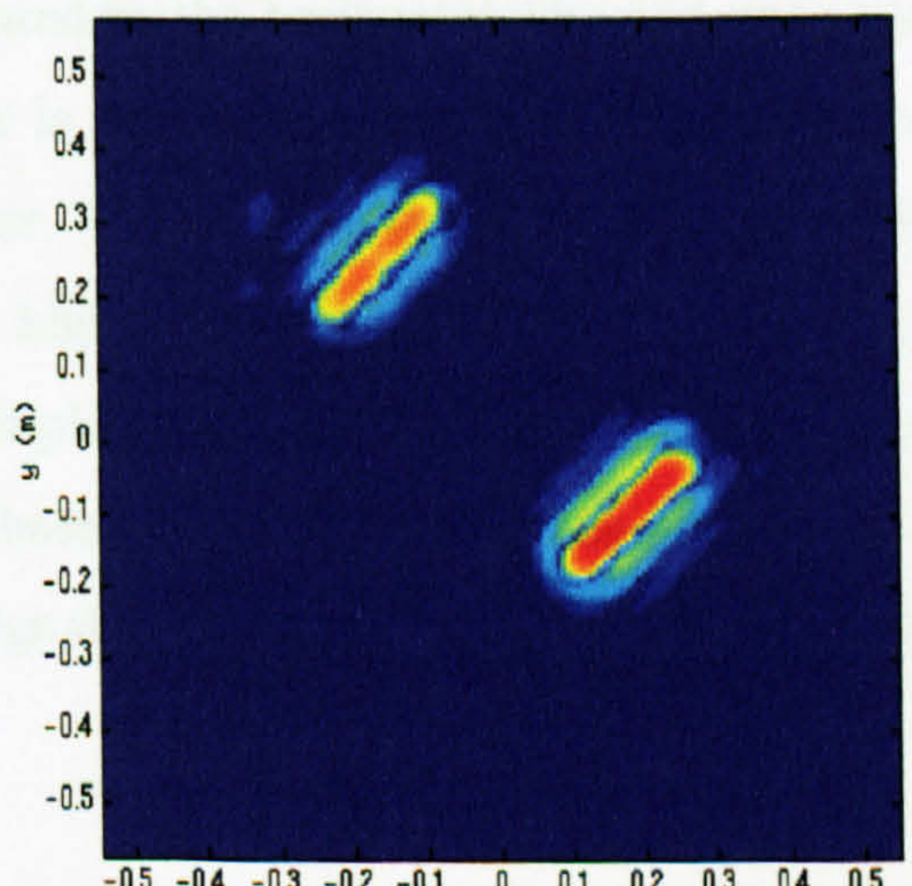

HH

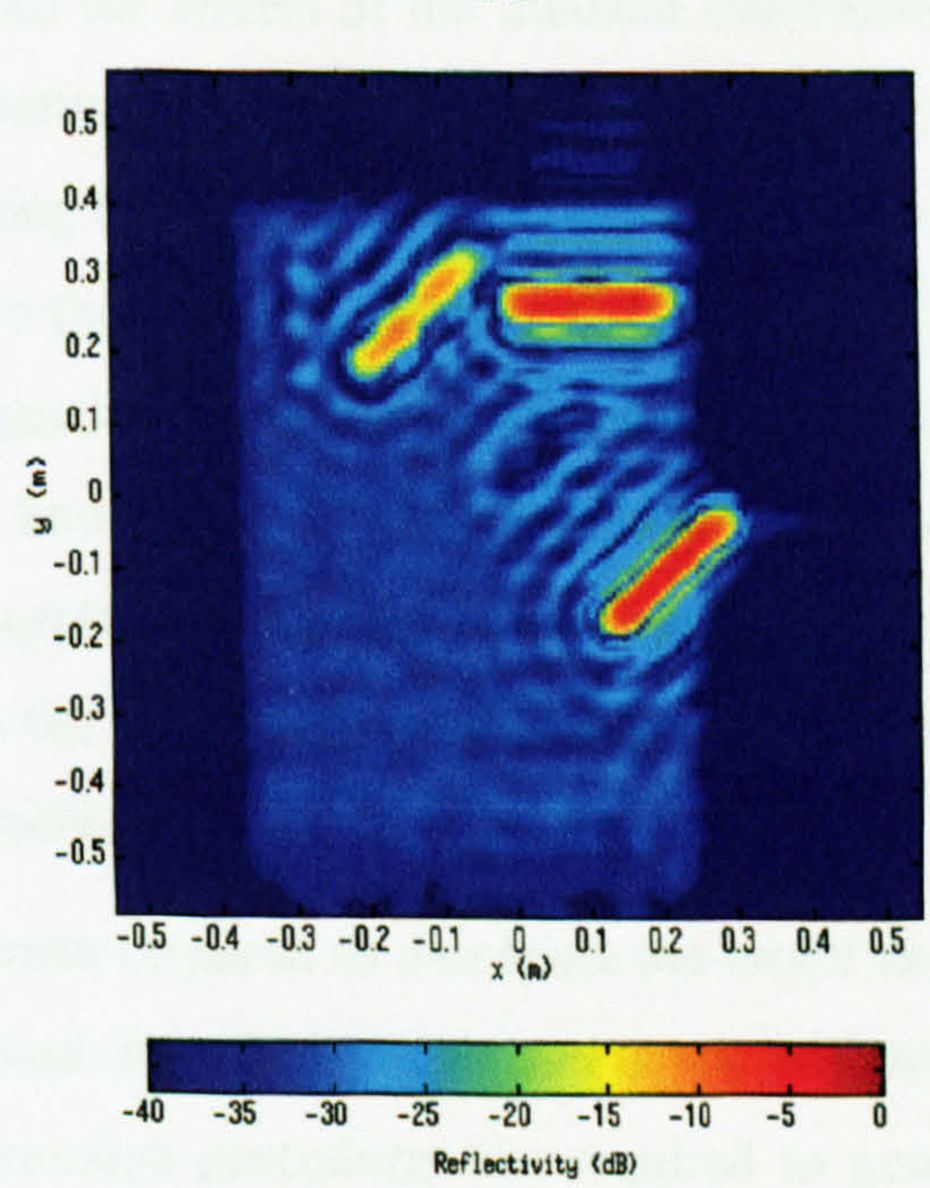

Figure 5.7 Results from Polarimetric Test Targets

the virtual image was reconstructed by the single frequency approach and hence it was concluded that the virtual image was the result of multiple scattering and not a result of constructive interference of sidelobes. The presence of the polystyrene in the image makes a calculation of the polarimetric purity difficult, but again, it is in the region of 30 to 35dB.

In the VH image, only the calibration bar and the wire at 45° are visible, the other two wires having a reflectivity so low that they cannot be seen. Furthermore, the polystyrene, as expected, does not depolarise the signal and hence is also invisible.

The HH image, shows complementary features to those of the VV image. The strongest return is generated by the horizontal wire and once again, the polystyrene is visible. In addition, there is an area of very low return half way between the wire at 45° and the calibration bar. This is in the same location as the virtual image in the VV image, but in that case a high return was generated. In fact, this region of low return is also the result of multiple scattering. In this case, it is supposed that the virtual image has an opposite phase to the return from the polystyrene at the same location. Consequently, the two signals cancel and leave a region of very low reflectivity.

5.7 Conclusions

This chapter has examined the effects of the transmit and receive probe antennas on the recorded data. The pattern of these antennas acts as a filter window in the spatial frequency domain, reducing the sidelobe level and the resolution. Probe compensation can be applied to remove these effects and was shown, by simulation, to be effective in both one and two dimensions. Suitable probe antennas for the experimental system were designed from a knowledge of the illumination pattern of pyramidal horn antennas along with an appreciation of the limited spatial frequency domain response of targets focused with the auto-focusing algorithm. The geometry of the imaging system also had to be considered.

The experimental equipment required to illuminate the target and record the reflected signal from it, has also been described. An automatic network analyser forms the core part of this system. Correction procedures are required to generate valid data from such a system and, in particular, the variations with changing frequency and the

effects of the cable length on the apparent location of the target have to be accounted for. This correction is achieved by dividing the measured data set by the measured response from a corner reflector.

Proof that the imaging process can produce in-focus imagery of a three-dimensional target has been presented in the form of an image of two corner reflectors set at different ranges from the aperture. The polarimetric sensitivity of the system has also been investigated and demonstrated the presence of virtual images caused by multiple scattering. The polarimetric purity of the system was found to be in the order of 30 to 35dB.

Chapter 6

Imaging of Biophysical Targets with the Auto-Focusing Algorithm

6.1 Introduction

The investigations carried out in the previous chapter demonstrated the ability of the multifrequency auto-focusing imaging algorithm to generate in-focus imagery from data collected over a planar aperture. The work presented in this chapter involves the application of such a system to the imaging of different trees. Firstly, a sycamore tree is imaged and then a larch tree and a beech tree are utilised for the rest of the work. The particular species of tree were chosen with care to include one coniferous tree and one deciduous tree. Polarimetric measurements are made of both trees to obtain a better understanding of the nature of radar-target interaction. In addition, measurements of the two trees are made over a period of several months to monitor the changes in the trees' biophysical properties and how they affect the backscattered signal. Investigations are also carried out to determine the variation of backscatter with radar incidence angle for the beech tree.

6.2 Initial Measurements

Before measurements were made on the larch and the beech trees, the sycamore tree utilised in the single frequency measurements of the previous chapter, was imaged. By so doing, the response of the multifrequency system to a known biophysical target could be observed and compared with that obtained on the single frequency system. The experiment was made in May, several months after the single frequency measurements. The tree was in full leaf at this time and there had been little change in its size over the intervening months.

The tree was imaged by utilising the vertical planar scanner system described in Chapter 5. A two-dimensional data set (76.5cm by 151.5cm) was collected over a 0.51GHz bandwidth at a centre frequency of 10GHz. The polarisation used was VV. Empty room subtractions were made and a calibration bar was included in the measurement scan. A calibration set was taken to remove the system frequency and cable length effects. The data was then transferred from the PC in the chamber control room to a Unix platform and focused using the modified auto-focusing algorithm described in Chapter 3.

The initial results for the tree are shown in Figure 6.1a. The tree is clearly visible above the background level, even though it is a comparatively low reflectivity target. However, the sidelobes of the reconstructed image are relatively high and are possibly obscuring features of the target. Therefore, the result of applying dual and tri-apodization filters and SVA filters, as described in Chapter 3, are also shown in Figure 6.1. From this, it can be seen that all the filtering techniques produce a noticeable reduction in the sidelobe levels around the tree. The SVA filter, as expected, produces the best result although there are still some sidelobes visible in the image. SVA will be applied to all other tree images presented in this chapter.

Careful examination of Figure 6.1d shows a number of interesting features relating to the tree itself. The main axis is clearly visible as an area of high reflectivity. The two main top branches can also be identified but do not give such a high level of reflectivity. It is supposed that this is because they are partially obscured by the leaves around them. The leaves themselves cannot be seen in the image as they are mostly oriented horizontally in the x-z plane and hence appear 'edge on' to the radar. Since they present such a small surface area to the radar, they are almost invisible to it although some points of low reflectivity can be identified in the regions around the branches. The lower right hand branch of the tree cannot be seen as it is oriented away from the radar. However, there is a strong response from the end of the branch which corresponds well with the simulations presented in Chapter 3. The calibration bar is visible in the bottom right hand corner.

6.3 Larch Tree Measurements

The common or European larch tree (*Larix decidua* Miller) is a coniferous tree which is native to the mountainous regions of Europe. It is also widely planted for timber, shelter along roads and for ornament in parks. When mature, it is a narrowly canonical tree typically reaching up to 40m in height [87]. The larch was chosen for the experimental work presented here as it has an unusual characteristic, namely, that it sheds its needles every winter as deciduous trees do. There are only a few conifer trees which do this and the larch is the only one native to Europe. This characteristic makes it an ideal subject with which the relative contribution of needles and branches

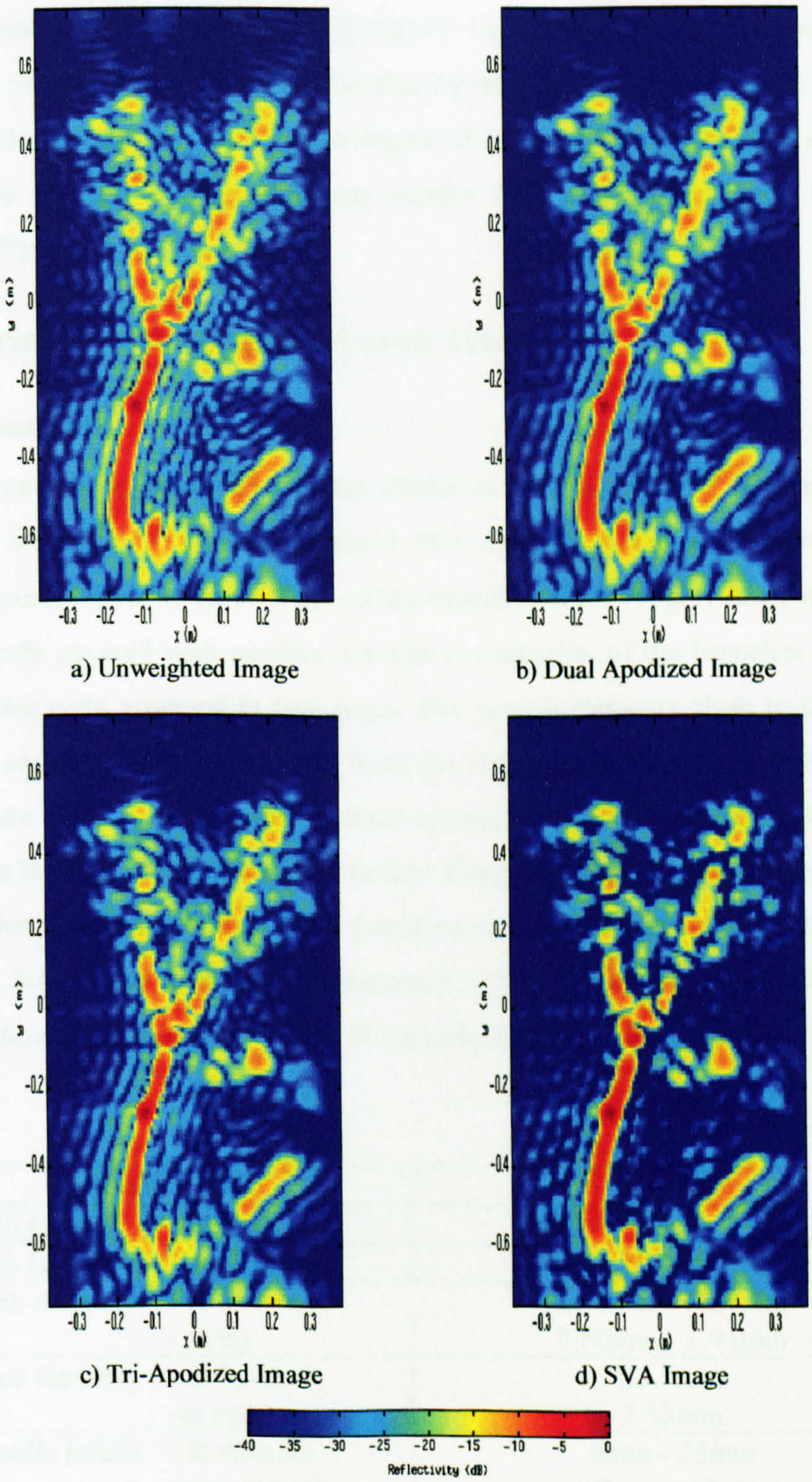

a) Unweighted Image

b) Dual Apodized Image

c) Tri-Apodized Image

d) SVA Image

Figure 6.1 Image of a Sycamore Tree at VV Polarisation - May 1997

to the backscattered signal can be investigated. Since the larch naturally loses its needles in winter, their effect on the backscattered signal can be determined. Previously published literature [6][15][16][17] has attempted to determine the contributions of the needles to the backscatter by manually removing all the needles from a tree. Clearly, this may cause some degree of stress to the tree and will alter the flow of water through it Therefore, any results from such experiments may be misleading [17].

6.3.1 Polarimetric Imaging of a Larch Tree

6.3.1.1 August 1997

Initial measurements on the larch tree were carried out in August 1997. The larch tree at that time, was 114cm tall and consisted of a main stem and approximately 40 branches connected directly to it. Most of the branches were roughly horizontal and were completely covered with needles. Careful examination of the branches showed that the needles were arranged in two ways. The branch elements close to the main axis did not consist of any new wood from the then current growing season. The needles in these areas were arranged in small clusters along the branches, with about 35-40 needles in each cluster. However, further along the branches, where new wood had grown that year, the needles were found to be singly arranged by themselves. Furthermore, the needles from this new seasonal growth were longer and softer than those which formed in clusters. A table of typical dimensions from the tree is shown below.

Height		114cm
Width (as seen by the radar)		80cm
Depth (as seen by the radar)		97cm
Branch diameter	- at main axis - at tip	2.08mm - 6.24mm 0.60mm - 1.91mm
Main axis diameter	- at bottom -at top	23.7mm 2.43mm
Typical needle length	- in clusters -new growth	8mm - 35mm 17mm - 49mm

The tree was kept outside and was watered on a regular basis. It was brought inside

for measurements to be made. The same process was employed for imaging the larch tree as was used to image the sycamore tree. Therefore, measurements were made over a 0.51GHz bandwidth at a centre frequency of 10GHz. The scan size was 109.5cm by 142.5cm and, in this case, measurements were taken for the three polarisations of VV, VH and HH. Empty room subtractions and calibration sets were taken for each polarisation. Probe compensation was applied to the data and focusing was carried out using the modified auto-focusing algorithm described in Chapter 3. The same technique and parameters (with the exception of scan size) are utilised for all further measurements presented in this chapter.

The results of the larch tree imaging process are shown in Figure 6.2. The images have been filtered using the SVA filtering technique and are each displayed over the same colour scale.

The VV image shows a high return from areas along the main axis, particularly from the leading shoot. Given the resolution of the system, the diameter of the main axis and its parallel orientation to the aperture, it should be possible to see a continuous response from most of the main axis. However, certain areas along the main axis are not visible and hence it is concluded that these areas are obscured by the needles surrounding them. It is not clear whether the needles are absorbing the energy from the radar or whether they are scattering it away from the receive antenna. It is likely that a combination of both processes is occurring. Certain areas of high reflectivity are also seen along the branches. The majority of the branches have a small diameter and since they are oriented orthogonally to the incident polarisation, it is expected that they may give a low reflectivity to VV polarisation. Indeed, only isolated returns are visible from along the branches. In some cases, these returns are from the very ends of branches which are angled steeply with respect to the x,y plane in which the aperture is located. In other places, the returns come from areas along the branches. It is supposed that these areas of reflectivity are due to both the branches and the needles although it is likely that most reflected energy comes from the needles.

In both the VV and HH responses, the rectangular feature at the bottom of the images is the reflection from a sheet of RAM included in an attempt to obscure the tree pot from the image.

Optical Image

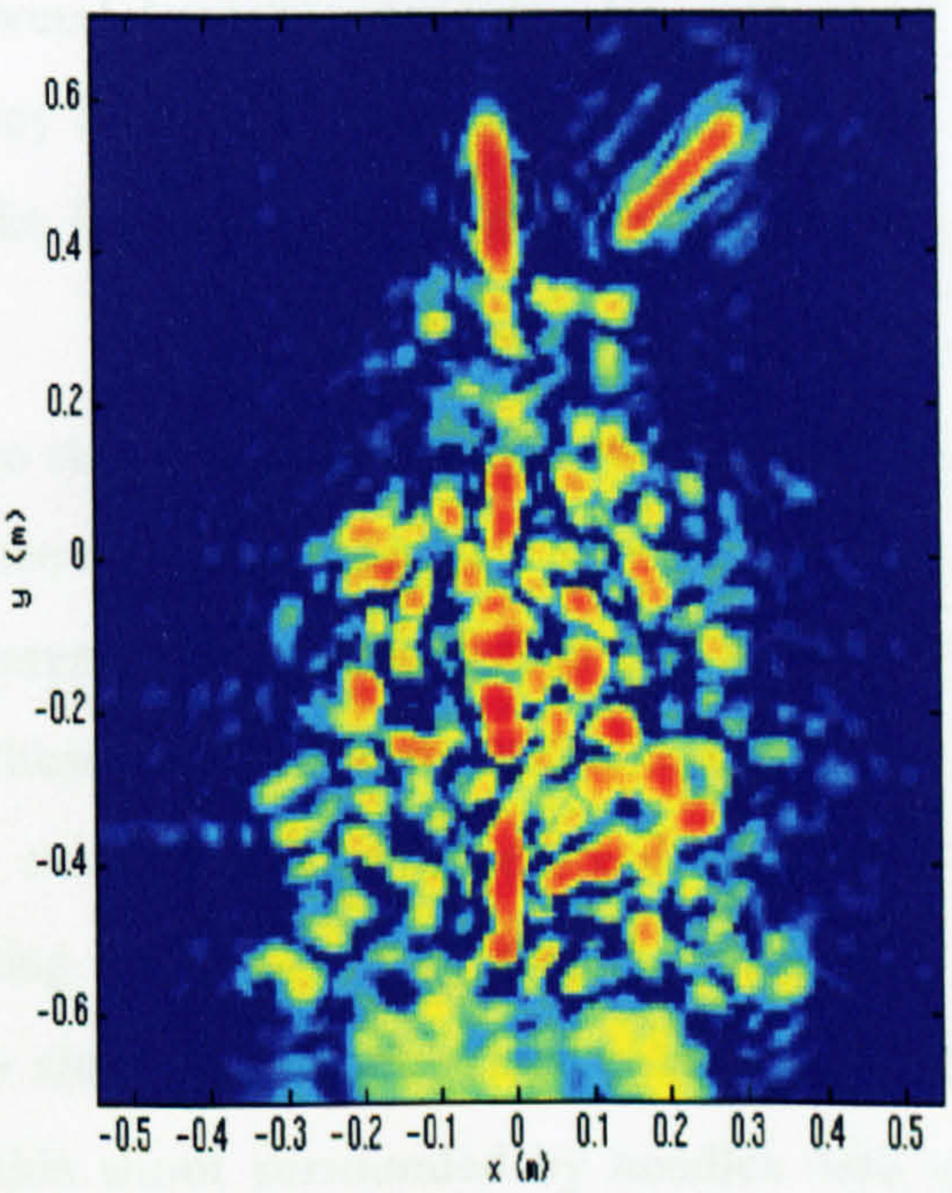

VV Image

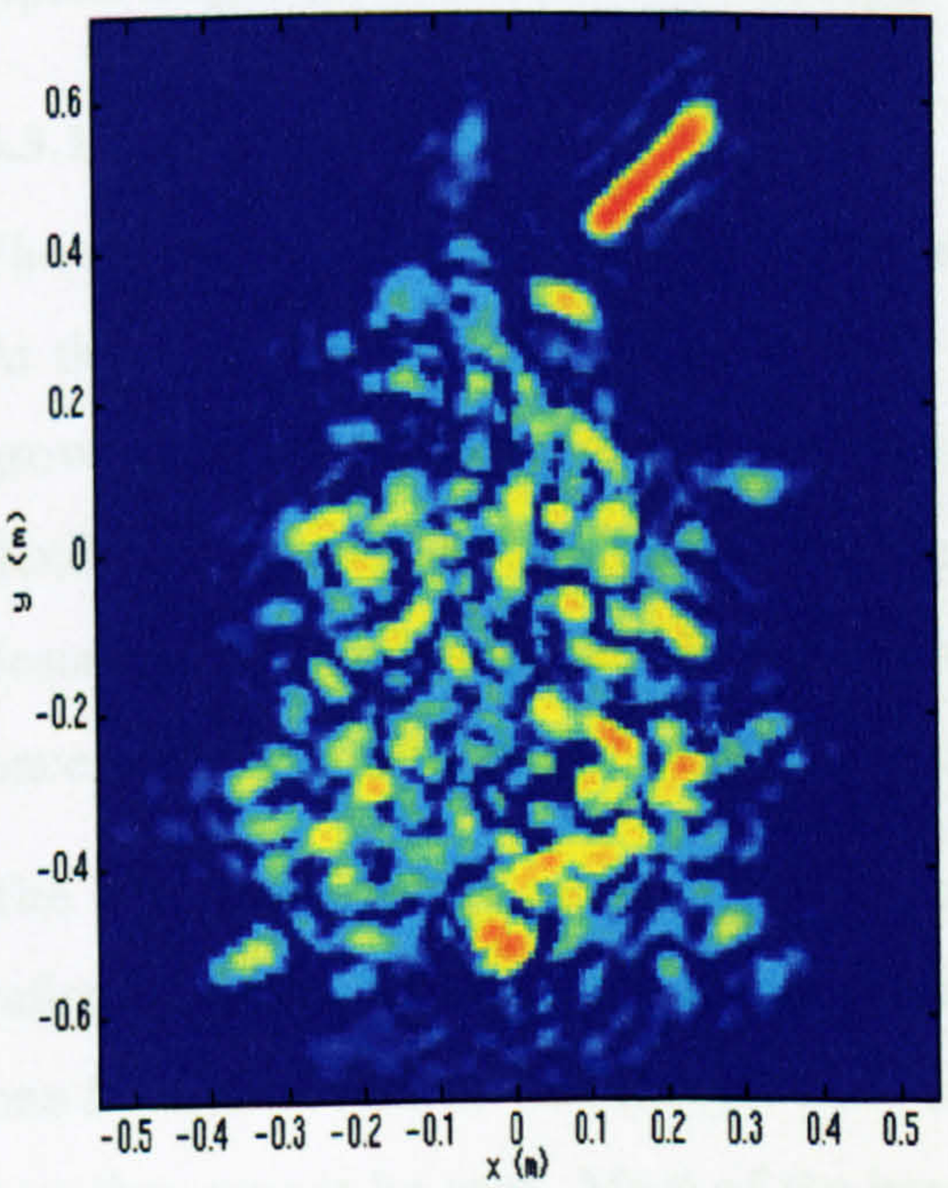

VH Image

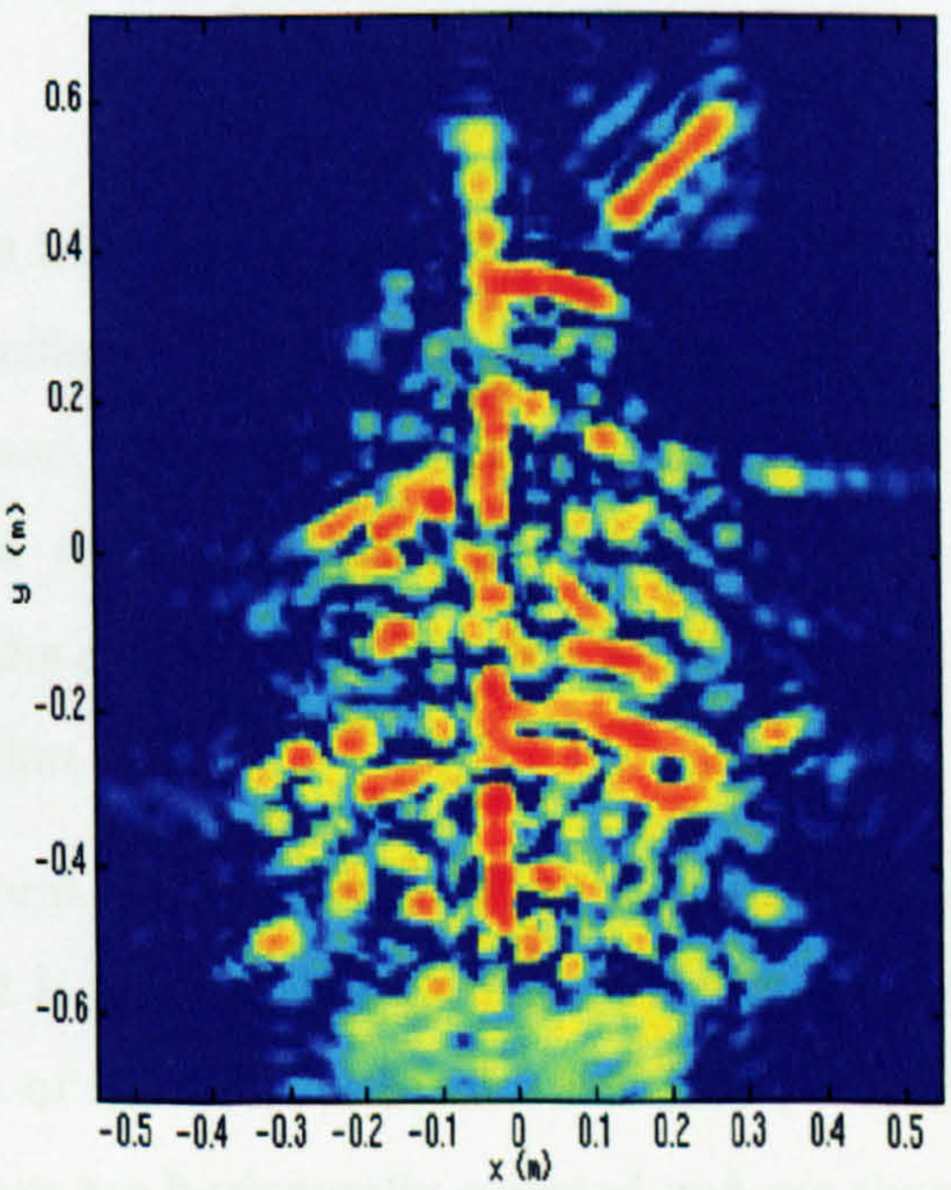

HH Image

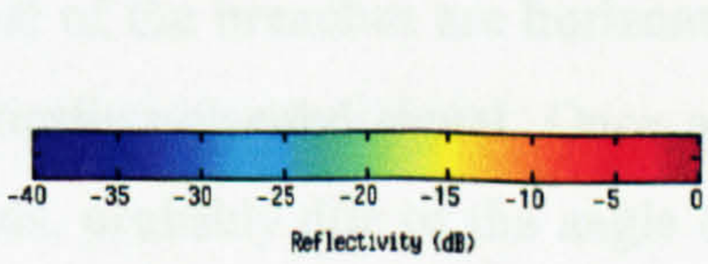

Figure 6.2 Polarimetric Imaging of a Larch Tree - August 1997

The VH image shows a much lower level of return from the tree as a whole and the main axis cannot be easily identified. Very low level responses from the top of the main axis are just visible. The ends of several branches can also be seen, most noticeably is the one isolated by itself half way down the tree on the right hand side. There is an area of higher reflectivity at the bottom of the tree which may be a reflection from the bottom of the main axis.

In contrast to the VV image, the HH response clearly indicates the presence of several branches especially on the right hand side of the main axis. The ends of other branches can also be identified. Returns from other areas along the branches can be clearly seen, although it is unclear as to whether these are caused by reflections from the needles or the branches or both. The main axis of the tree is resolved as it has a relatively large diameter, although the leading shoot is not as clear as in the VV response. Instead, isolated nodes are visible along this shoot. Close examination of this shoot, revealed it to be made up of a thin shoot surrounded by needles with a typical length of 4cm and which were individually arranged and evenly spaced.

6.3.1.2 October 1997

The second set of measurements on the larch tree were carried out in October 1997. At this time, the tree was still covered in needles, although it was no longer actively growing as it was the end of the growing season. The needles were no longer soft and flexible indicating a biophysical change in them. Measurements were made as described in the previous section and the results are shown in Figure 6.3. The data has once again been filtered with the SVA algorithm.

The VV image shows a strong reflection from the main axis of the tree and other reflections from the branches and needles. It is just possible to make out the line of one horizontal branch on the right hand side of the tree but in all other cases, whole branches cannot be seen. Most of the branches are horizontally oriented and are thus too thin to be seen by a vertically polarised signal. Once again, there are noticeable returns from some branch ends, probably due to the angle of the branch with respect to the plane of the scanning aperture. This effect was simulated in Chapter 3.

Optical Image

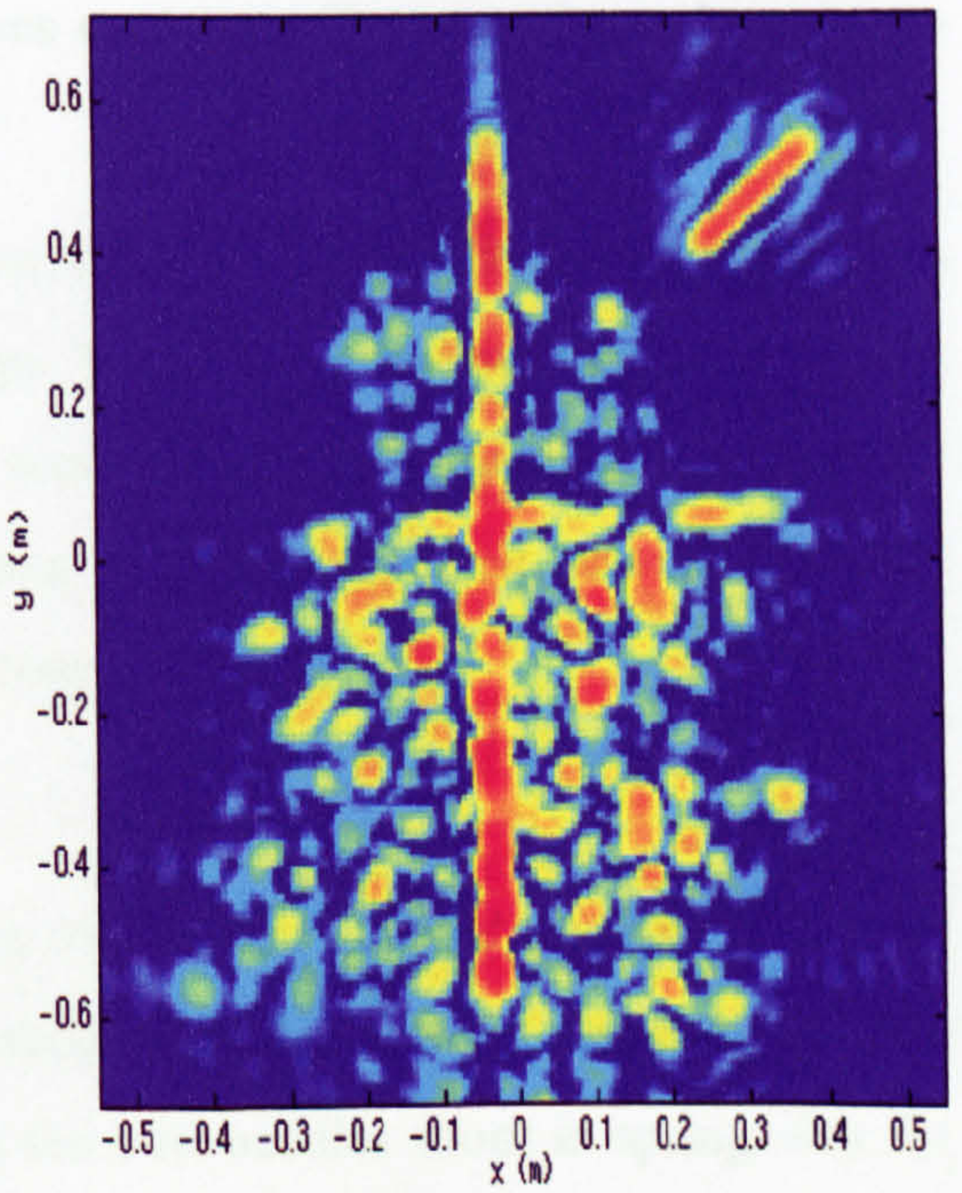

VV Image

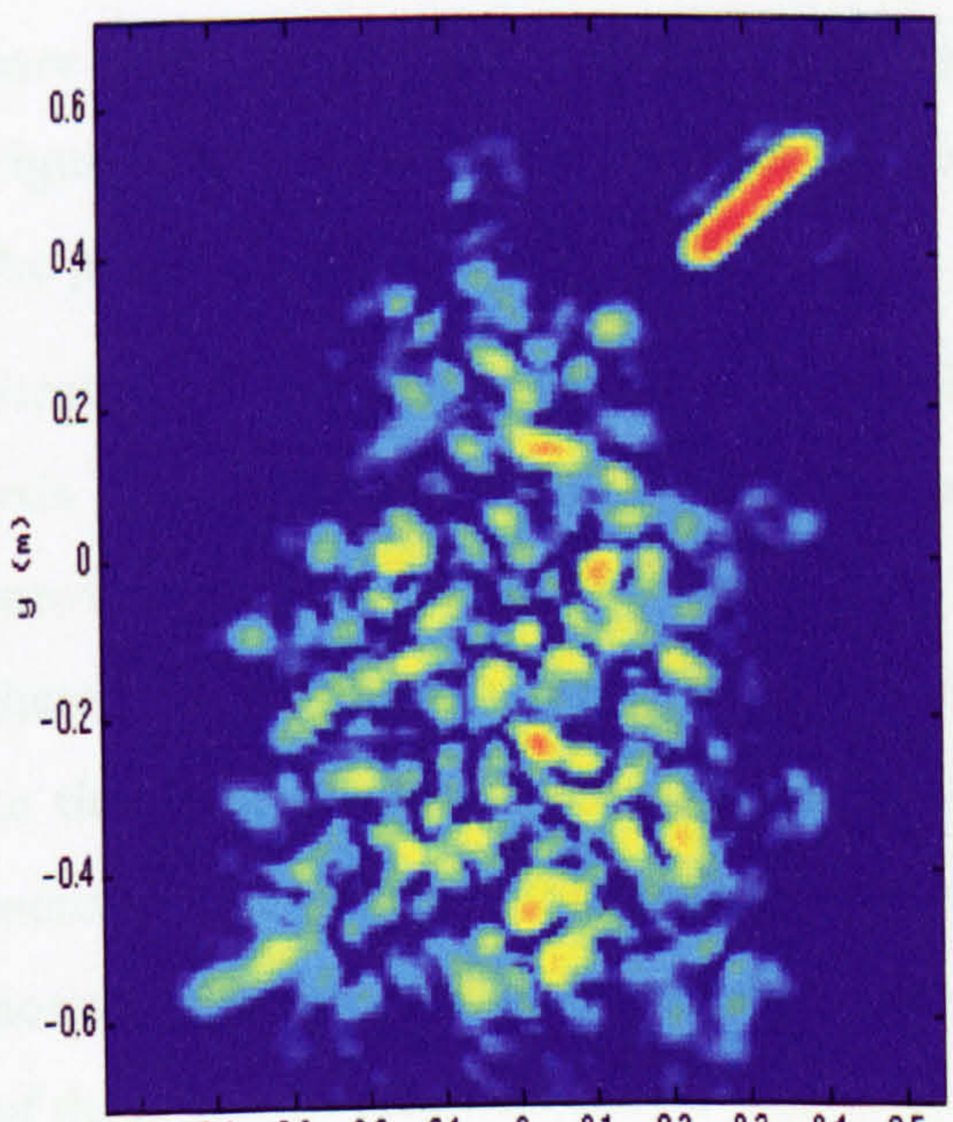

VH Image

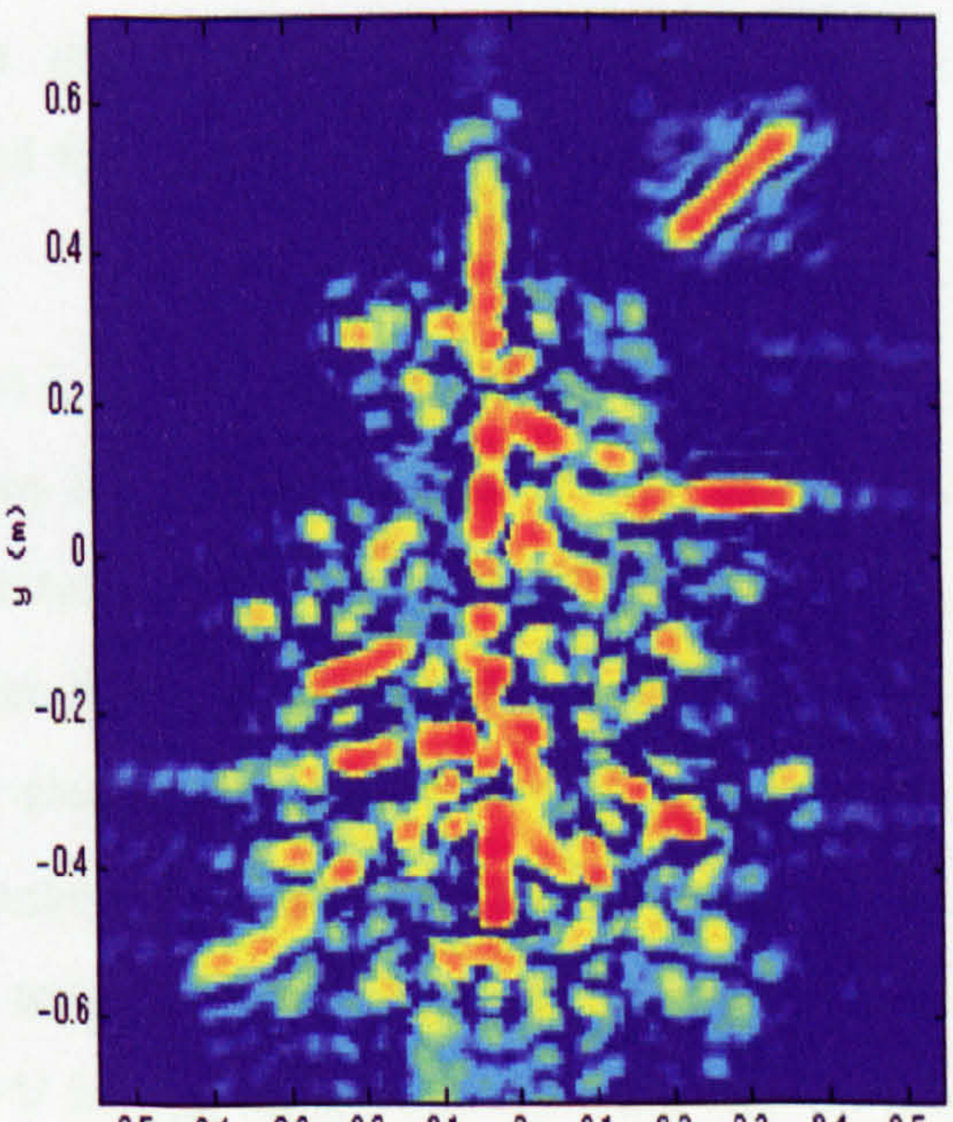

HH Image

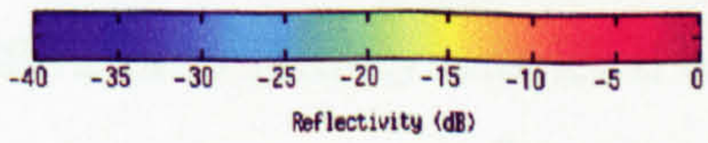

Figure 6.3 Polarimetric Imaging of a Larch Tree - October 1997

The main axis is not easily identifiable in the VH image in Figure 6.3. Here, most of the response comes from the area around the branches and the needles, although again it is not clear whether the branches themselves or the needles contribute the most to the reflected signal.

In the HH image, the main axis can be clearly seen, although it does not have as strong a response as it does in the VV image. This is most noticeable at the leading shoot, the top of which cannot be clearly seen. However, a number of horizontal branches can be identified in the image along with the expected returns from the branch ends and other returns from regions along the branches.

6.3.1.3 January 1998

The next measurements were made in January 1998 when the tree was bare and there were no needles attached to it. Once the needles on larch trees die, they tend to remain attached to the tree and fall off when the new needles shoot in spring. For the purposes of this experiment, the dead needles were all removed to give a completely bare tree. Polarimetric images were again generated and the results shown in Figure 6.4. The size of the tree was unchanged from the previous measurements made the preceding October.

From the VV image, it can be seen that there is a very striking return from the main axis of the tree and very low areas of return from the branches. It was evident in previous images, that as the branches are horizontal, the radar has difficulty in seeing them with VV polarisation. It is supposed that, in this case, the branches are invisible to the radar as there are no needles on the tree to generate reflected energy or to increase the effective diameter of the branches. Not all the branch elements are horizontally oriented, since certain branches tend to 'droop' down at an angle. Some of these branch elements can be seen in the VV image, most noticeable are two on the right hand side.

In the VH image, it is again difficult to identify individual branches and the main axis cannot be seen. However, there are numerous isolated returns from areas along the branches and three branches can be clearly seen on the top right corner of the tree. Some of the areas with high reflectivity, or 'hot spots', on the branches may be

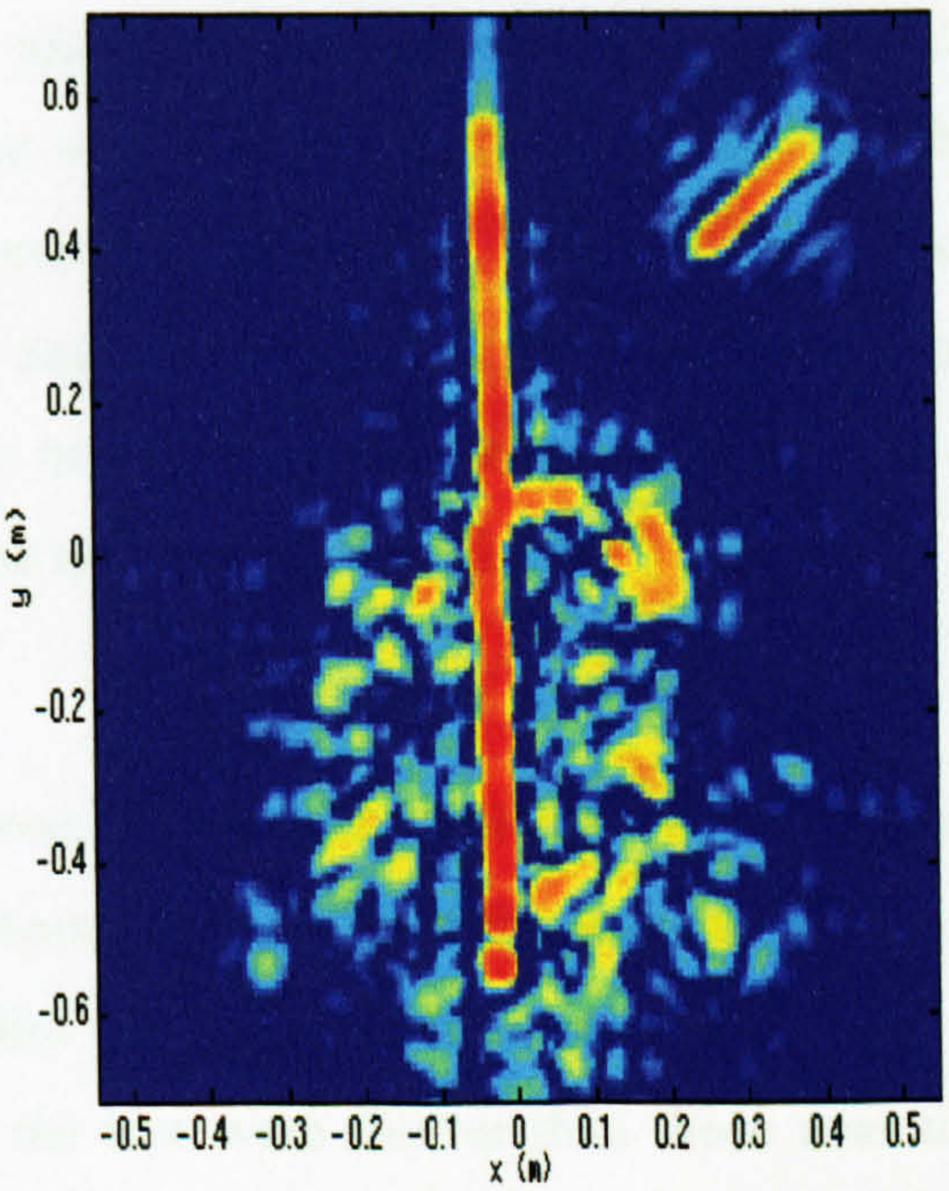

VV Image

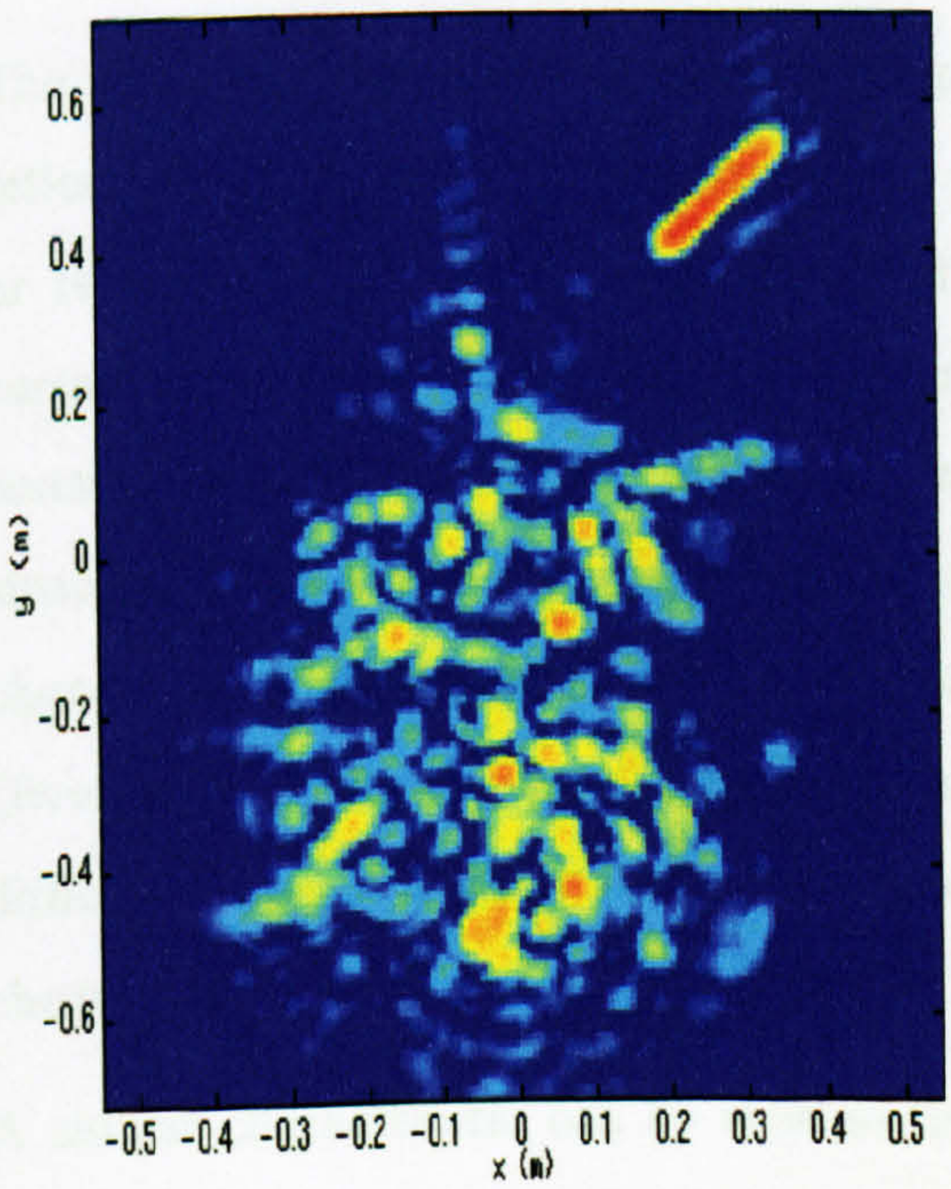

VH Image

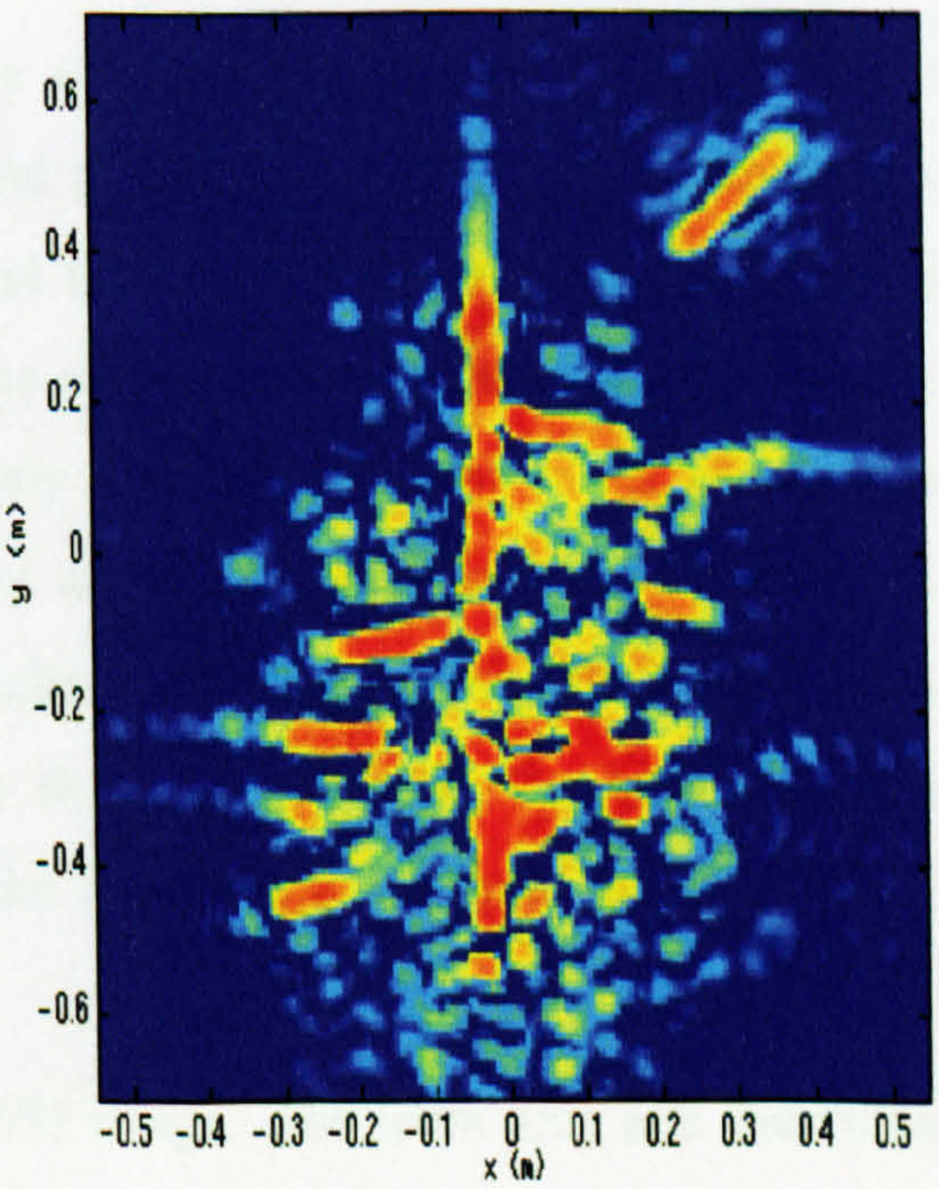

HH Image

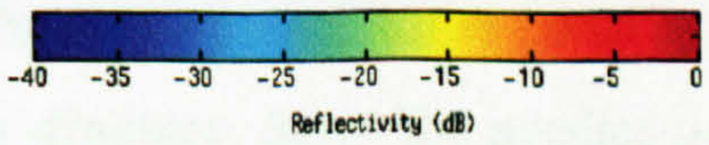

Figure 6.4 Polarimetric Imaging of a Larch Tree - January 1998

generated from regions where a branch splits into two smaller branches. Such a result was demonstrated in the single frequency scenario in Chapter 4.

In contrast to the VV and VH images, the HH image shows the presence of several branches. Again, these are visible since they are horizontally oriented and hence interact well with a horizontal polarisation. Other returns come from branches which are oriented at a large angle to the plane of the aperture and hence cannot be imaged completely. The main axis can be seen although the leading shoot becomes too narrow at the top of the tree to be clearly visible.

6.3.1.4 April 1998

The final image data was collected in April 1998 when the needles on the larch tree were just starting to shoot. The needles at this stage were all in clusters and were soft and flexible. The needles were also found to be quite short, in the order of 1cm. The needles at the top of the tree were shorter than those near the bottom as they had sprouted later.

The main axis, in the VV image of Figure 6.5, gives a noticeably high level of reflectivity. However, there is also a high level of reflectivity from the branches. One or two branches can be clearly identified and the isolated returns from the ends of certain other branches can also be seen. On the whole, the response from the branches consists of high reflectivity 'hot spots', evenly distributed across much of the tree structure. It is supposed that these hot spots are either reflections from the needle clusters or reflections from areas on the branches which are not obscured by needles. Given that in the previous data set, where the tree was bare, the branches were difficult to see, it is likely that in this case, the hot spots are returns from the needle clusters.

A similar characteristic can be seen in the VH image. The main axis and individual branches cannot be identified, as expected in a cross polar image. However, as with the VV image, the response from the branch areas consists of a large number of hot spots distributed over the tree structure. Since the needles occur in small clusters, it is supposed that they may cause a strong depolarising effect on the incident signal giving rise to the hot spots visible in the image.

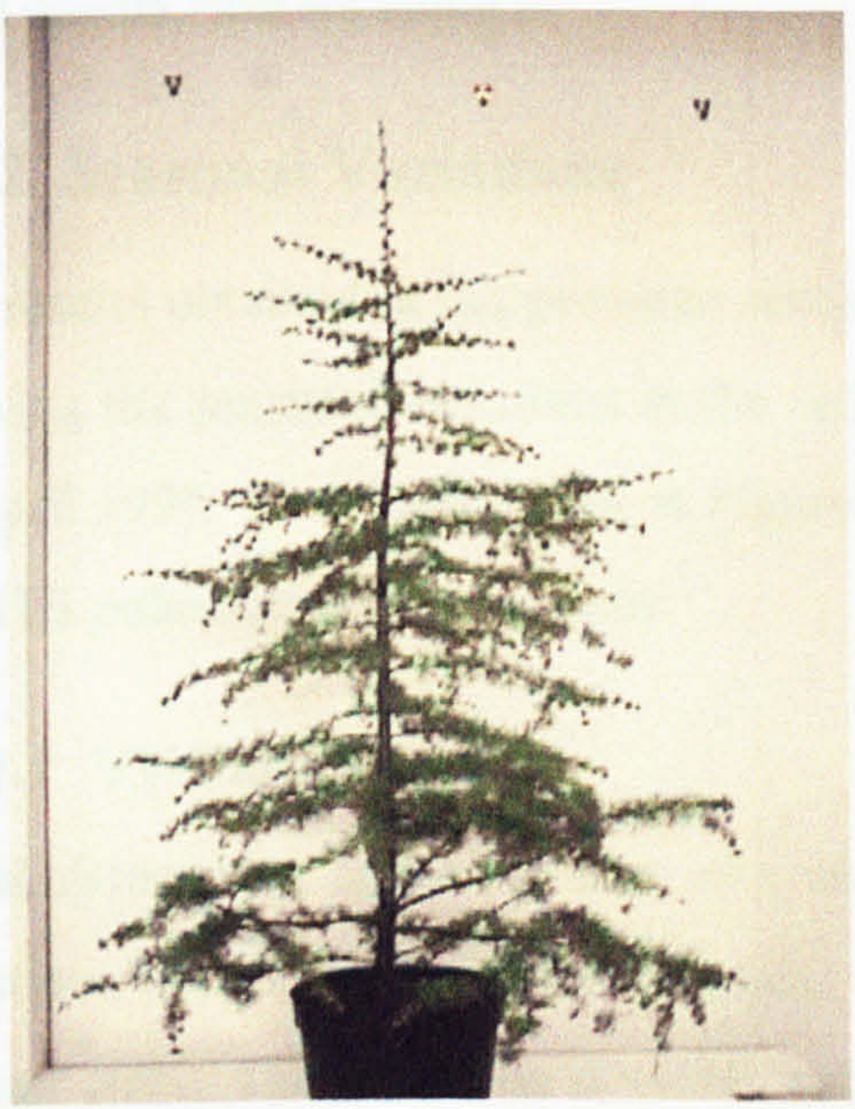

Optical Image

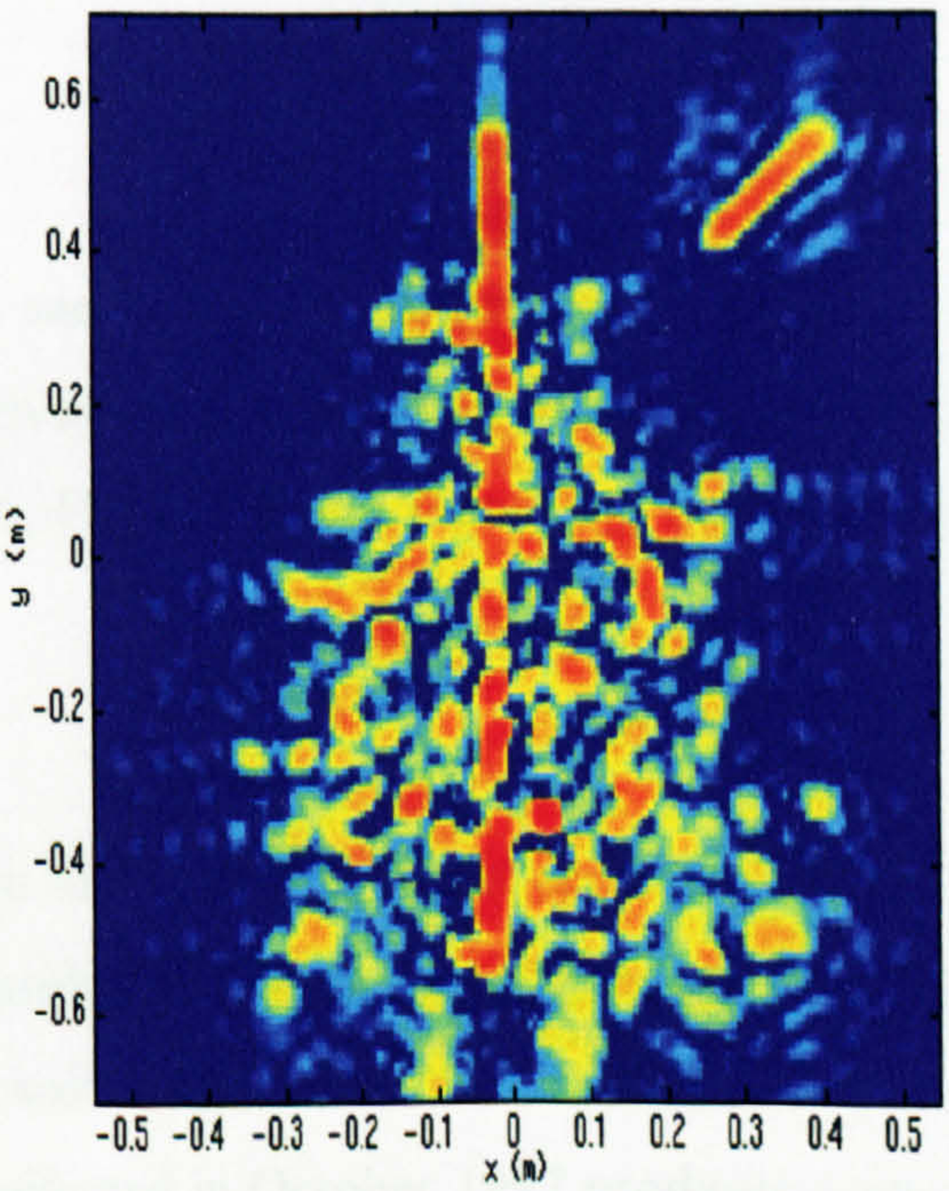

VV Image

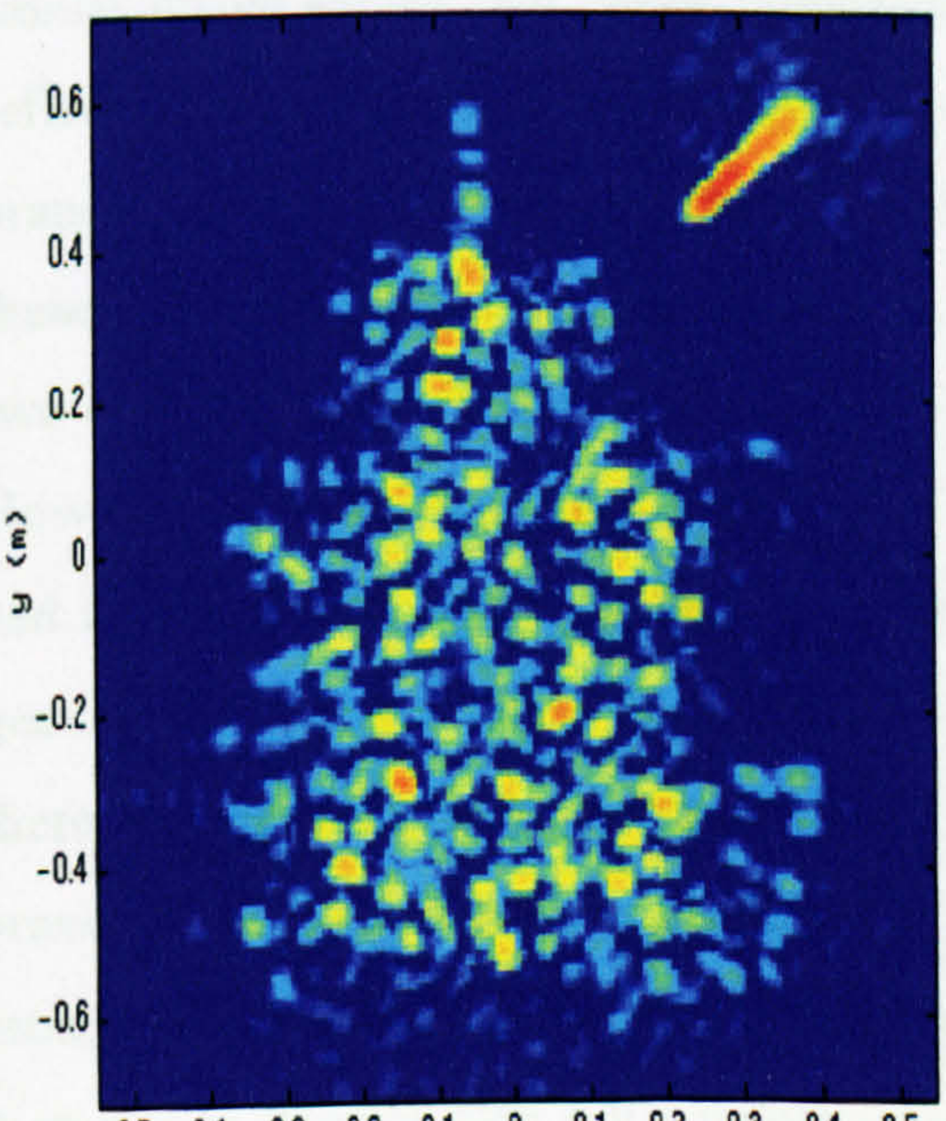

VH Image

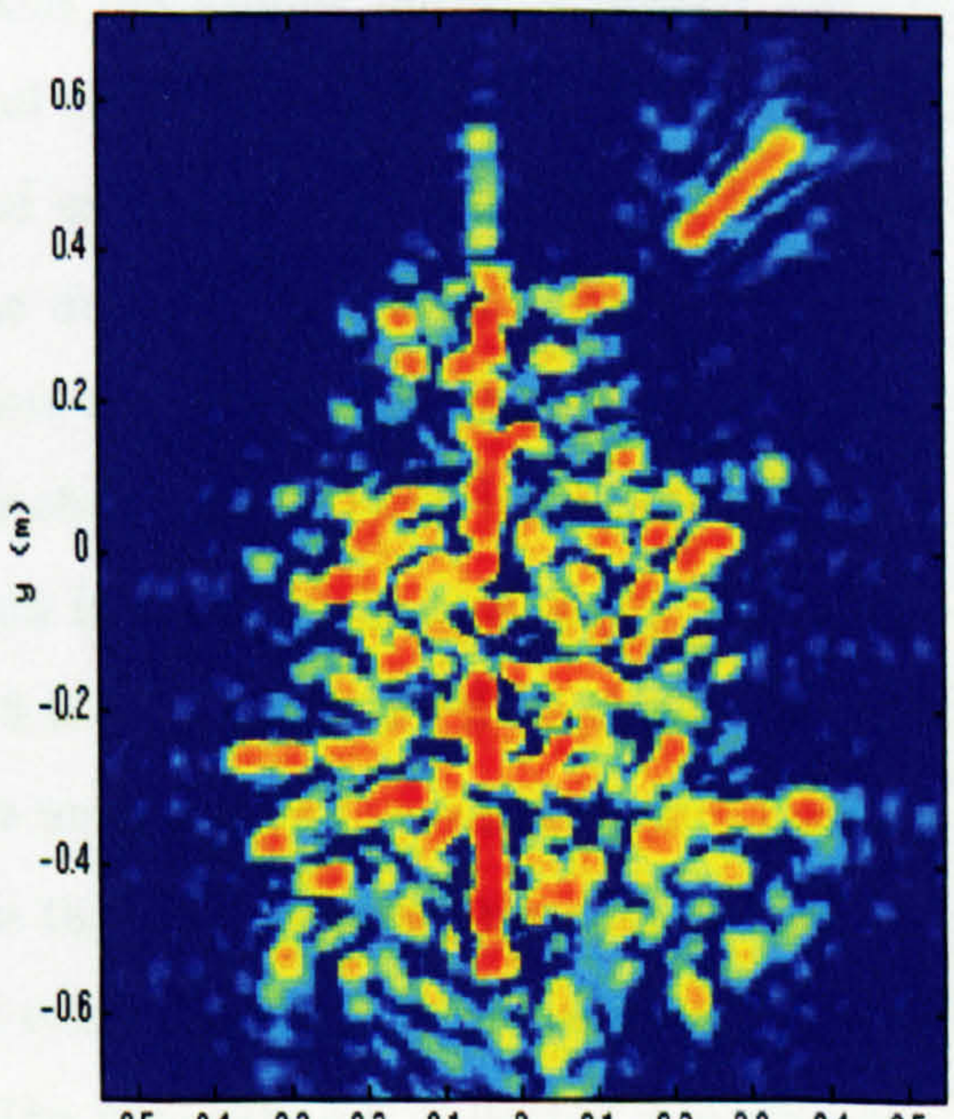

HH Image

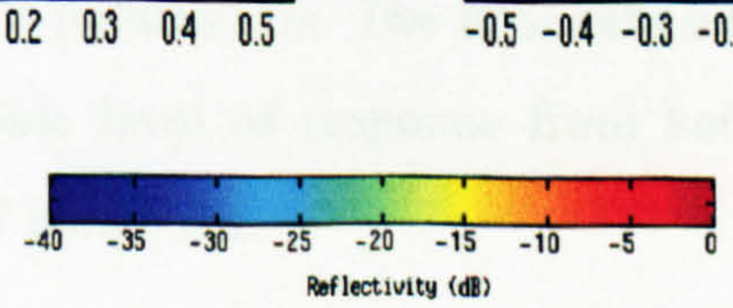

Figure 6.5 Polarimetric Imaging of a Larch Tree - April 1998

The HH image shows high levels of reflectivity from both the main axis and individual branches. The leading shoot is visible as four points which may be returns from the small needle clusters along it.

6.3.2 Seasonal Variations

The results obtained in the previous sections can be collated to form a set of images, showing the seasonal variations in the reflectivity of the larch tree from August 1997 to April 1998. These are shown in Figure 6.6, Figure 6.8 and Figure 6.9 for VV, VH and HH polarisations respectively.

6.3.2.1 VV Variations

Initial observation of the VV data sets, shown in Figure 6.6, reveal several interesting variations between the different images. Consider initially the measurements made in August 1997. The main axis is visible and considerable returns can also be seen from around the branches. The measurement set collected in October 1997 produces a very similar image except that, when compared with the August image, a greater level of reflectivity is obtained from the main axis and a lower level from the area where the branches are located. Since the tree is covered in needles in both cases, it is likely that these variations are caused by changes in the orientation of the needles between the two data sets. The needles in October are more spread out than they were in August. However, it was noted that the needles in October were all fairly brittle and may have had a lower water content which would result in a change in reflectivity. The image generated from data collected in January 1998 is a very different from the first two, as there is a very striking high response from the main axis and very little return from the branches. The tree was bare of needles at this time and evidently the radar cannot see most of the branches as they are horizontally oriented and do not have a large enough diameter to interact with a VV polarisation. The final data set, collected in April 1998, once again shows a reasonable level of response from both the main axis and the branches, as the August 1997 image did.

In order to draw some more quantitative results from these images, it is necessary to find a measure of the total power reflected from the tree or its constituent components. A representation of the total power can be obtained by performing a

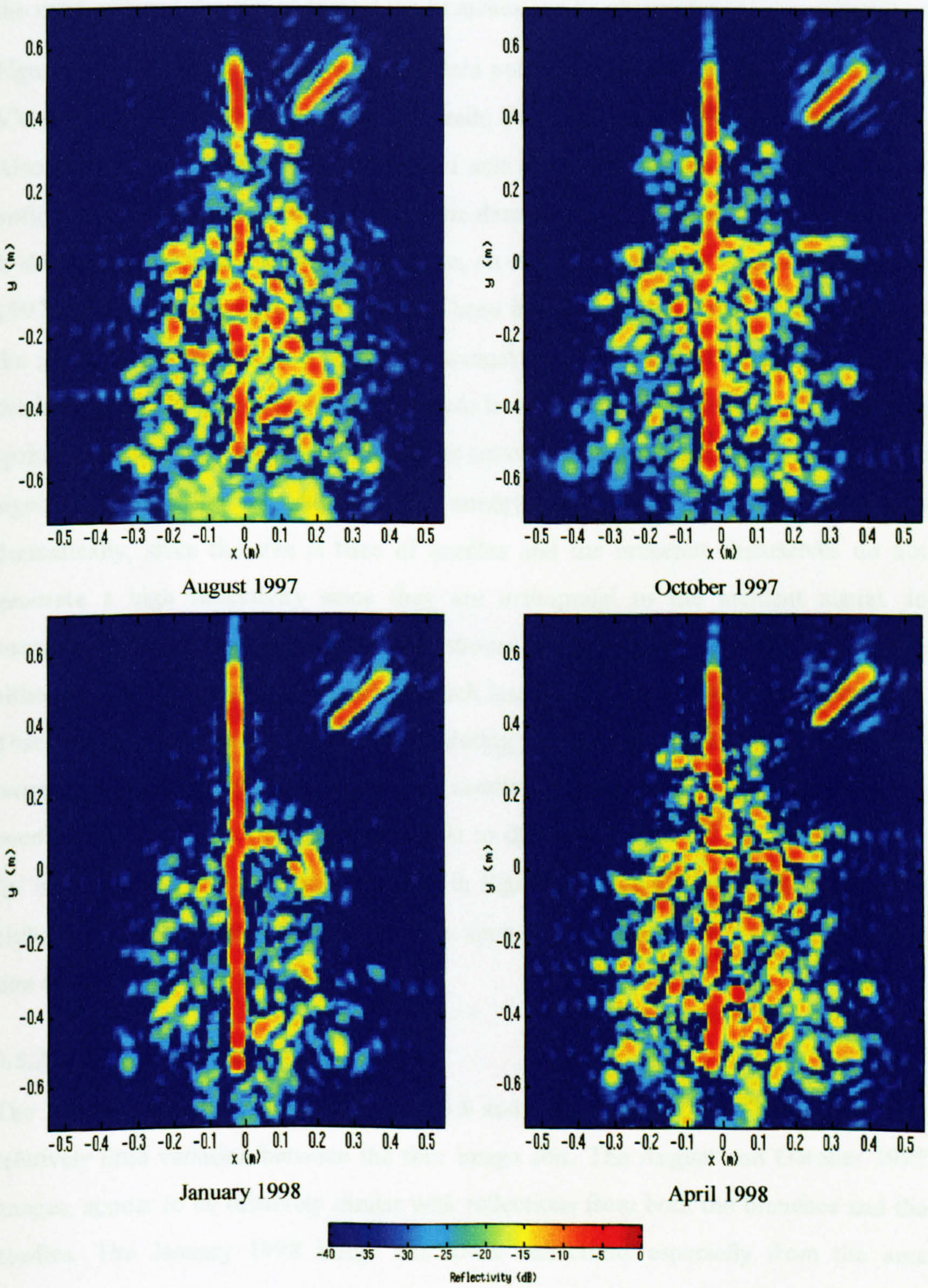

Figure 6.6 VV Images of a Larch Tree Over a Growing Season

complex summation of all the data values which make up the tree image. A similar process can be repeated for individual tree elements and by so doing the returns from the main axis and the region around the branches can be obtained.

Figure 6.7 shows a summation of all the data points which make up the tree images at VV polarisation, for the measurements made between August 1997 and April 1998. Also shown are the returns from the main axis and the branches over the same time period. Lines have been drawn between the data points to illustrate the general trend. It should be noted that, at VV polarisation, an extra data set was made in September 1997 and the reflectivity of this data has been included in the graph. Examination of the graph shows that there is a strong seasonal variation in the VV reflectivity from the larch tree. The responses from the whole tree and from the branches are highest in spring and summer. At this time the tree is covered in needles and these clearly cause significant reflection of the incident energy. In winter, the reflectivity falls dramatically, since the tree is bare of needles and the branches themselves do not generate a high reflectivity since they are orthogonal to the incident signal. In contrast, the response from the trunk shows a maximum in the winter months, although the total seasonal variation is much less than was exhibited by the branches. This behaviour can be explained by considering that the trunk is a strongly reflecting target which is mostly obscured by the needles. In winter, however, there are no needles and the whole trunk is then visible to the radar. It should also be noted that for each of the three summations shown in Figure 6.7, the values in April 1998 are higher than those from August 1997. It is supposed that this is due to the increased size of the tree caused by natural growth.

6.3.2.2 VH Variations

The VH images are all shown in Figure 6.8 and in contrast to the VV images, show relatively little variation between the four image sets. The August and October 1997 images, appear to be relatively similar with reflections from both the branches and the needles. The January 1998 image has fewer reflections especially from the area around the top of the tree. A few hot spots can be seen from the junctions of two branches and various linear features can be seen due to returns from the bare branches. The April 1998 image is a somewhat different from the other three in that

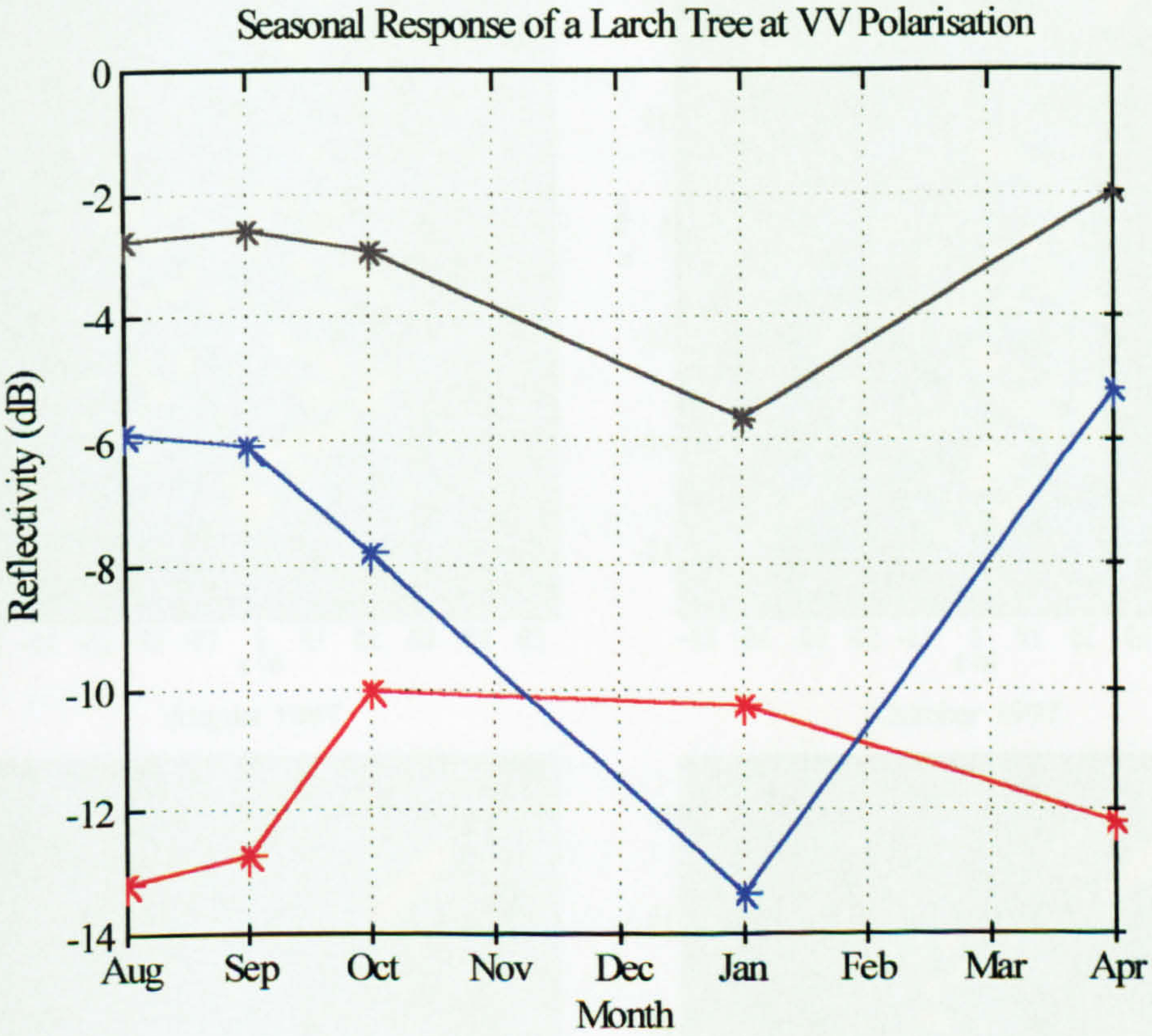

Figure 6.7 VV Reflectivity of the Larch Tree over Several Months

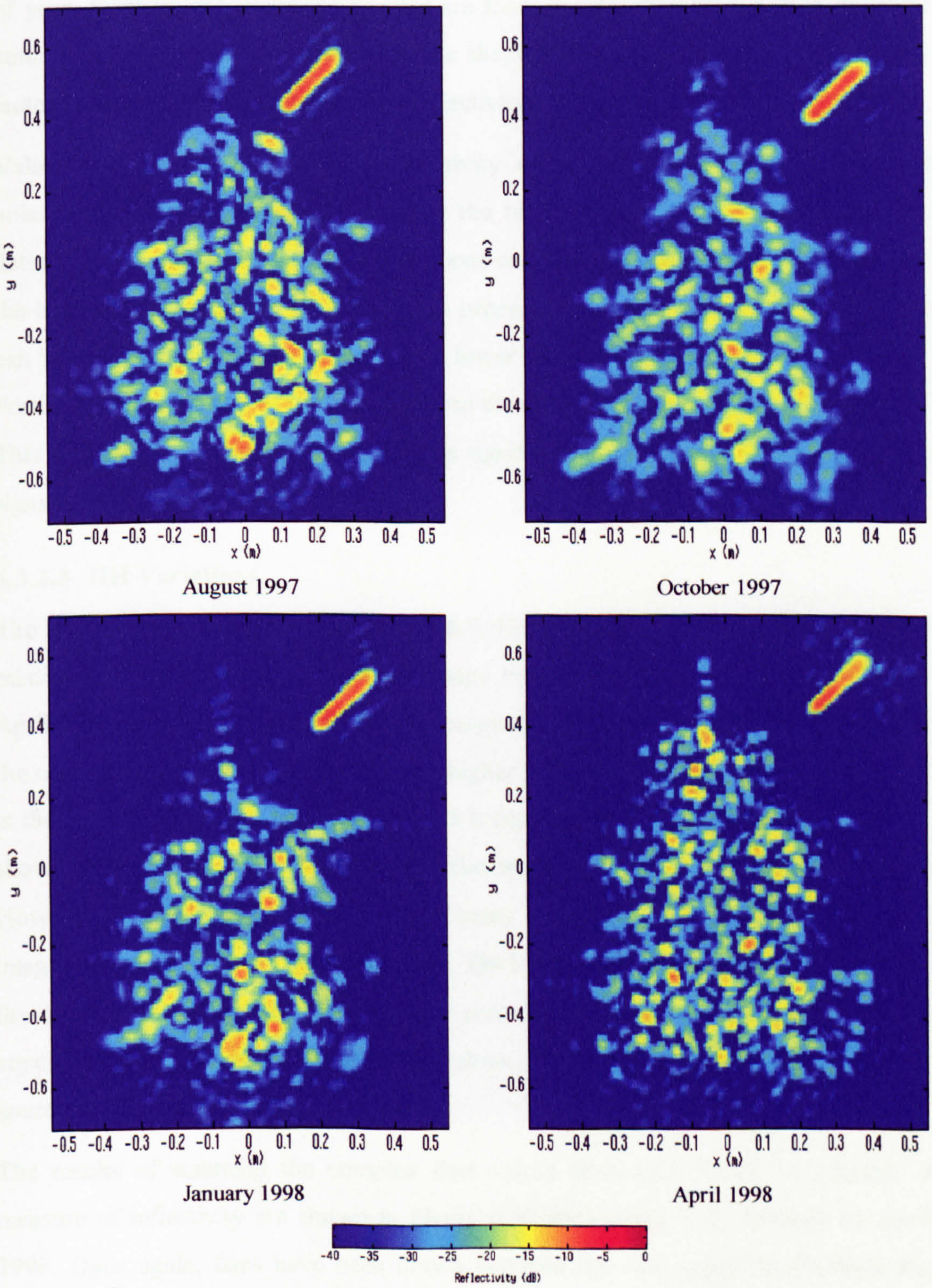

Figure 6.8 VH Images of a Larch Tree Over a Growing Season

there are a multitude of small returns scattered across the whole tree area. This is due to the needles on the tree, all of which are arranged in small tight clusters at this time of year. Furthermore, since the needles are fresh shoots, they have a high moisture content. It is supposed, however, that the shape of the needle clusters is the critical factor in determining the nature of the reflectivity.

Values representing the seasonal reflectivity of the tree were calculated at VH polarisation. In this particular case only the total reflectivity of the tree could be determined as the branches and the main axis could not be separately distinguished in the images. The results of the summation process are shown in Figure 6.11 where it can be seen that the VH response is much lower that the VV response, as is expected. Furthermore, the shape of the VH response closely follows that of the VV response. This suggests that the needles contribute a significant proportion of the backscattered signal at VH polarisation.

6.3.2.3 HH Variations

The HH image sets are shown in Figure 6.9. From these, it can be seen that there is relatively little difference between the image sets of August and October 1997 and April 1998. In all three cases, there is a reasonable return from both the branches and the main axis, although there is perhaps a higher level of reflectivity from the branches in the April 1998 image. The January 1998 image, when the tree was bare of needles, shows a much stronger response from the main axis and from certain branches. However, the reflectivity at the ends of many branches is lower than in the other images due to the lack of needles on them. The leading shoot cannot be clearly seen in the January image either, whereas it is seen in all the others. Hence, it can be concluded that the needles on the leading shoot and some thin branches, are the main source of backscatter at this polarisation.

The results of summing the complex data values from each image to generate a measure of reflectivity are shown in Figure 6.10 for August 1997 through to April 1998. Once again, lines have been drawn between the data points to illustrate the general trend. In contrast to the VV data, these results show little seasonal variation. There is a general increasing trend across the graph but this is likely to be due to

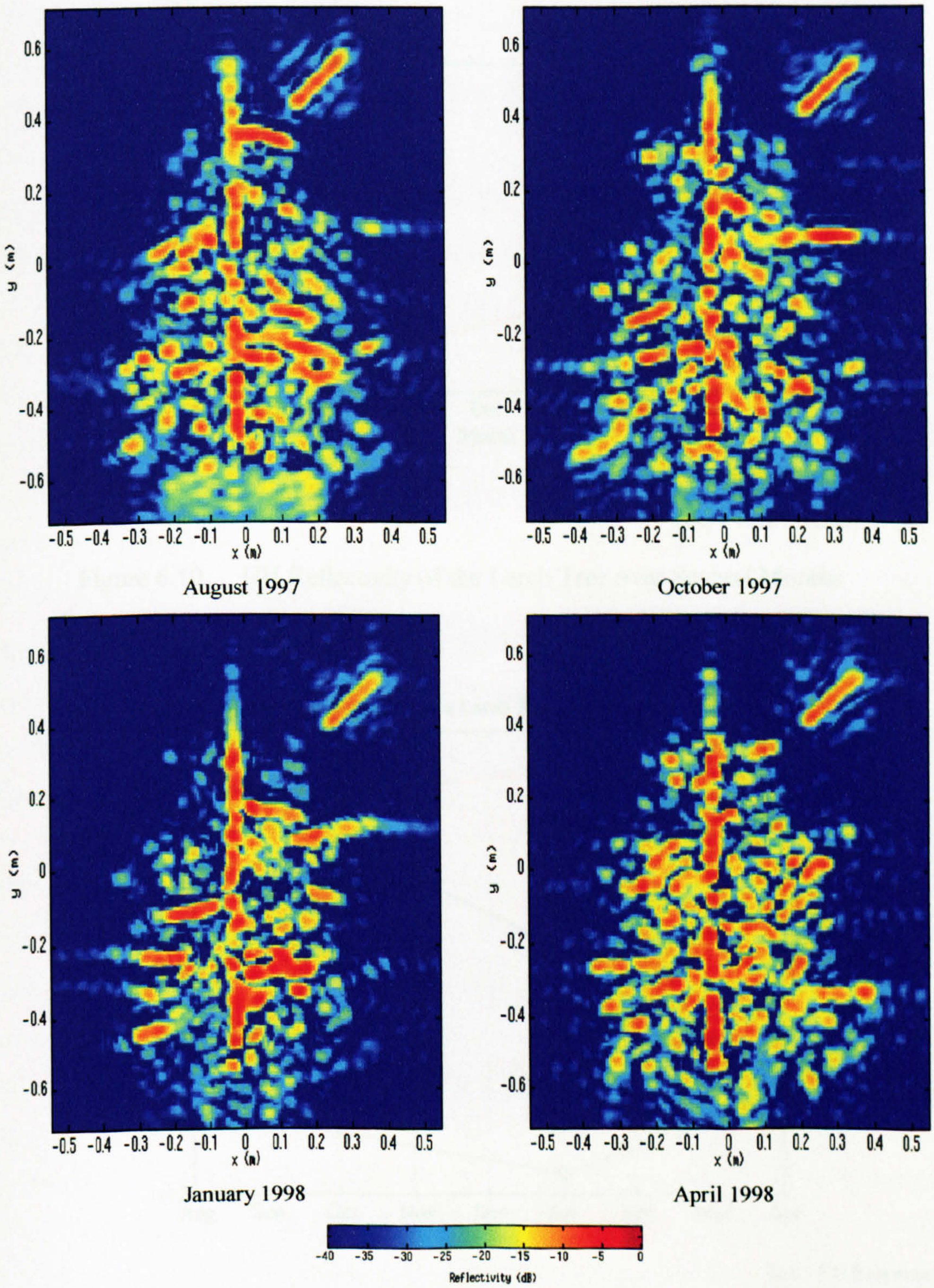

Figure 6.9 HH Images of a Larch Tree Over a Growing Season

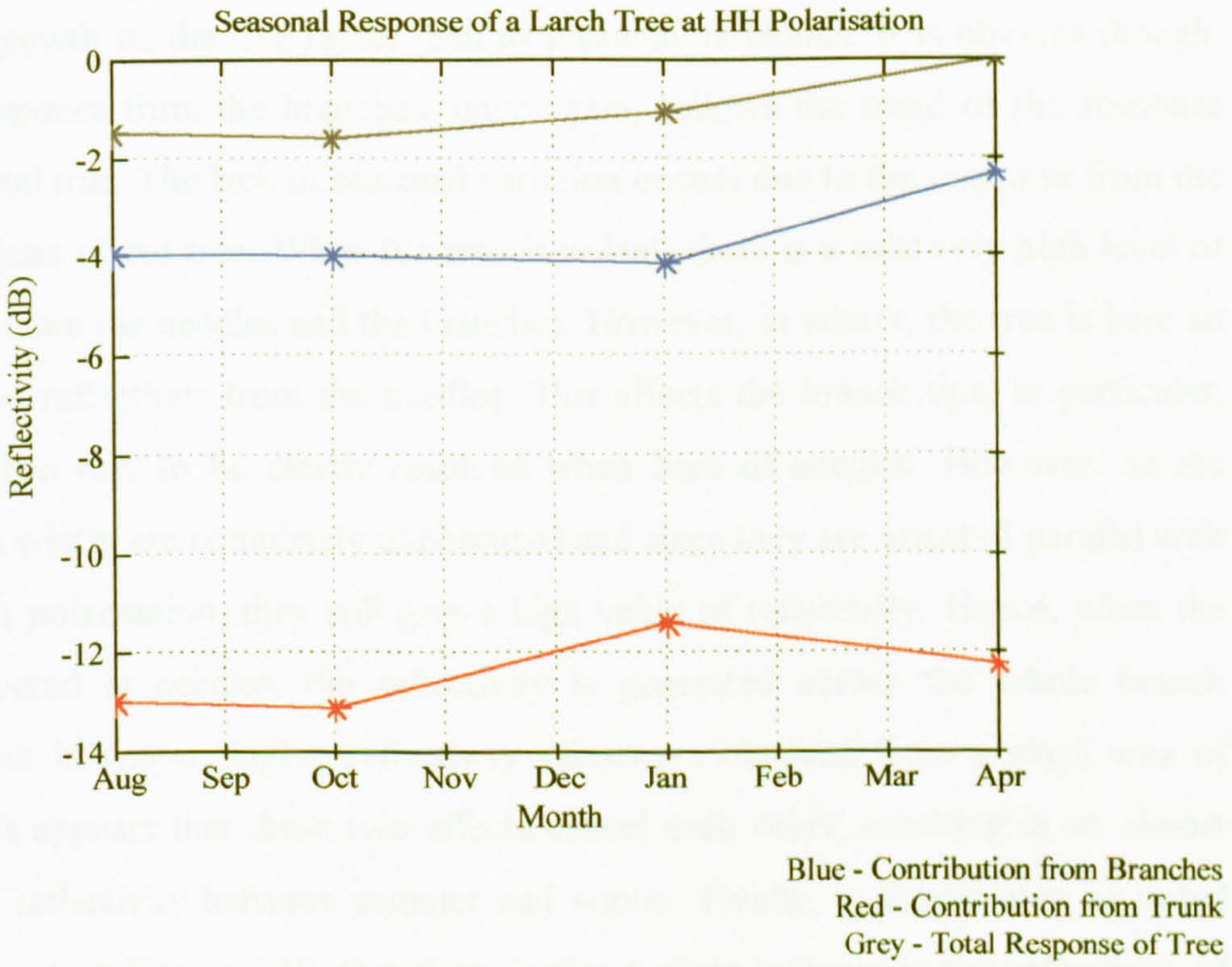

Figure 6.10 HH Reflectivity of the Larch Tree over Several Months

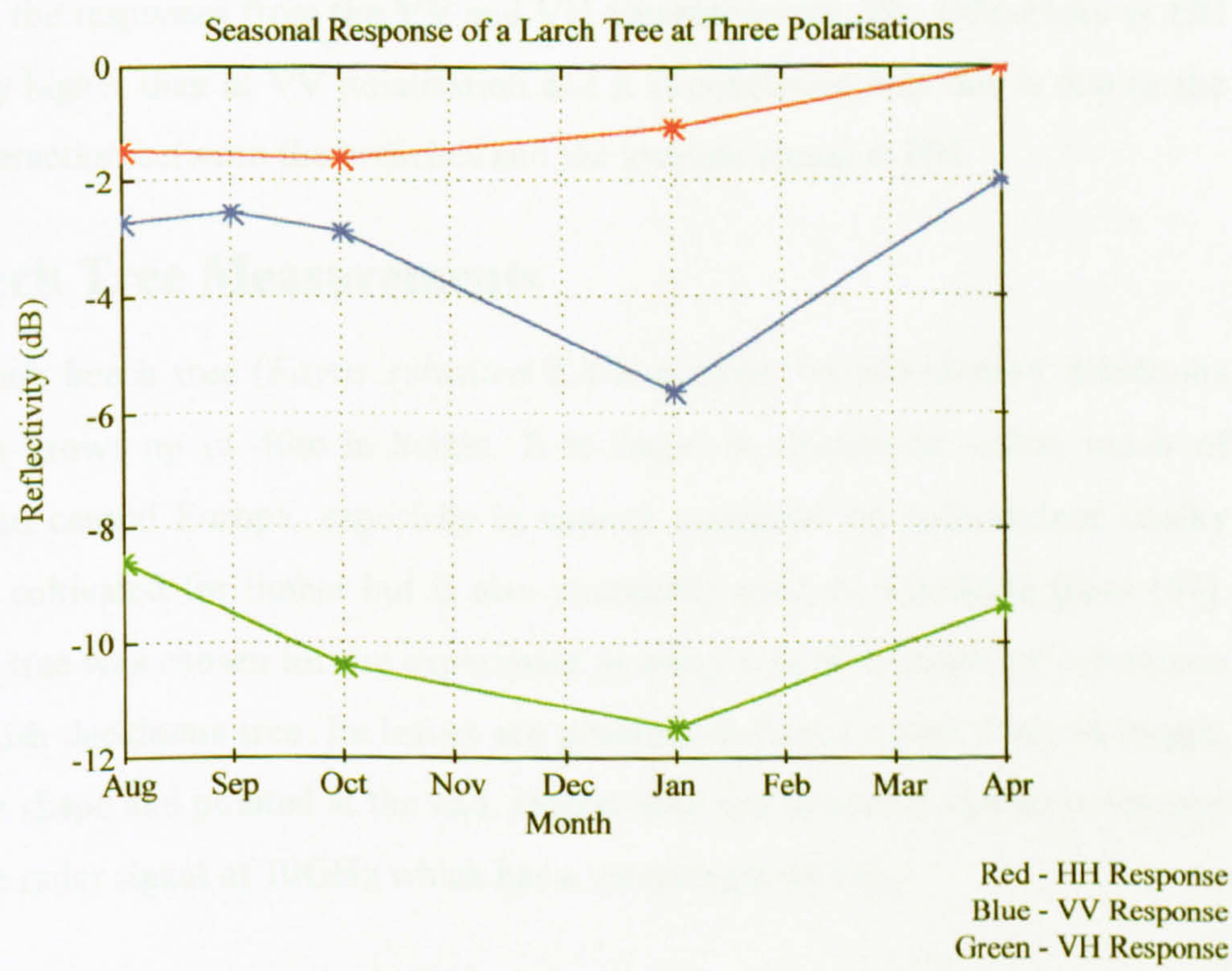

Figure 6.11 Comparison of the Seasonal Reflectivity of the Larch Tree at VV, VH and HH Polarisations

increased growth on the tree rather than to seasonal variations. It is obvious though, that the response from the branches, once again, follows the trend of the response from the total tree. The lack of seasonal variation occurs due to the response from the branch regions of the tree. When the tree is in leaf, there is a relatively high level of reflectivity from the needles and the branches. However, in winter, the tree is bare so there are no reflections from the needles. This affects the branch tips, in particular, which are too thin to be clearly resolved when bare of needles. However, as the branches in winter are completely unobscured and since they are oriented parallel with the incident polarisation, they still give a high value of reflectivity. Hence, when the tree is covered in needles, the reflectivity is generated across the whole branch structure but in winter, higher reflectivity values are obtained from a small area of branches. It appears that these two effects cancel each other, resulting in an almost unchanged reflectivity between summer and winter. Finally, it should also be noted from the graph in Figure 6.10, that there is also a slight increase in the reflectivity of the trunk in the winter months since it is not obscured by needles.

The HH reflectivity from the whole tree is also plotted on the graph in Figure 6.11 along with the responses from the VV and VH measurements. The reflectivity at HH is evidently higher than at VV polarisation and it is concluded that this is due to the greater interaction between the branches and the incident signal at HH.

6.4 Beech Tree Measurements

The common beech tree (*Fagus sylvatica* L.) is a large, broadly-domed deciduous tree which grows up to 40m in height. It is found in abundance across much of western and central Europe, especially in natural woodland on well-drained chalky soils. It is cultivated for timber but is also commonly used as a hedging plant [87]. The beech tree was chosen for the experiment as being a good example of a common native British deciduous tree. Its leaves are generally between 4 and 10cm in length, elliptical in shape and pointed at the end. Hence, they are of such a size as to interact well with a radar signal of 10GHz which has a wavelength of 3cm.

6.4.1 Polarimetric Imaging of a Beech Tree

The beech tree utilised for this experiment was a small tree, initially some 120cm in height. It consisted of a main axis and a number of horizontal branches connected to it and is shown in Figure 6.12. At the top of the main axis was a bifurcation where the axis split into two main branch clusters, both of which were oriented between 25° and 30° to the vertical just above the bifurcation. Initial dimensions of the tree are given below

Height		120cm
Width (as seen by the radar)		57cm
Depth (as seen by the radar)		62cm
Branch diameter	- at main axis	2.08mm - 9.20mm
	- at tip	1.01mm - 2.98mm
Main axis diameter	- at bottom	28.1mm
	-at bifurcation	11.68mm

6.4.1.1 August 1997

The first set of measurements were made on the tree in August 1997 when the tree was in full leaf. The leaves were mostly horizontal and were connected to the branches with short stalks. There were no leaves connected directly to the main axis. The tree was imaged using a 121.5cm by 133.5cm scan with a 0.51GHz bandwidth at a centre frequency of 10GHz. Once empty room and system corrections had been performed, the data was focused using the modified auto-focusing algorithm as previously described. The images were filtered using the SVA technique and are shown for three polarisations in Figure 6.12.

The VV image clearly shows the presence of the main axis of the tree. In contrast, there are relatively low levels of return from the area around the branches. The branches themselves, especially those below the bifurcation, are oriented orthogonally to the incident polarisation and hence a low level of reflectivity is expected. The leaves are hard to identify since they are 'edge on' to the radar and hence only present it with a very small surface area. There are some returns from the areas around the branches below the bifurcation. These may be returns from non-horizontally oriented leaves or from small areas on the branches themselves. Above the bifurcation, a

Optical Image

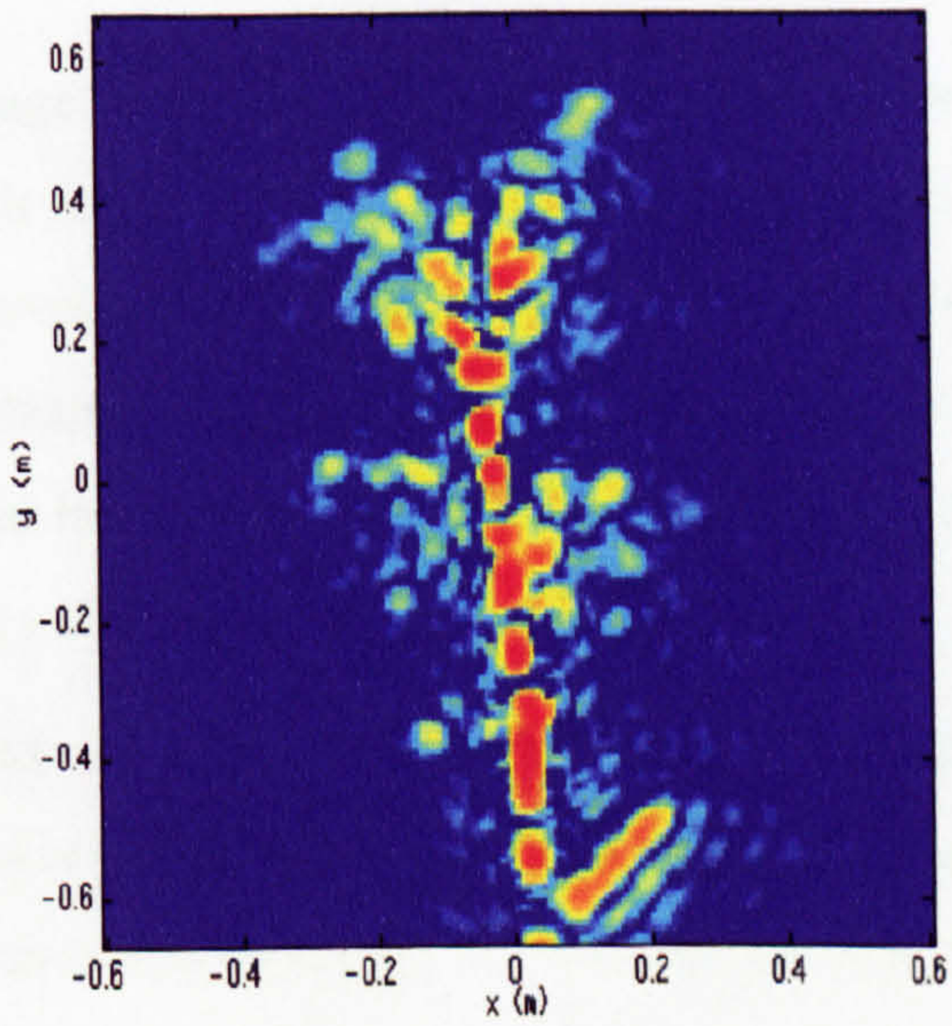

VV Image

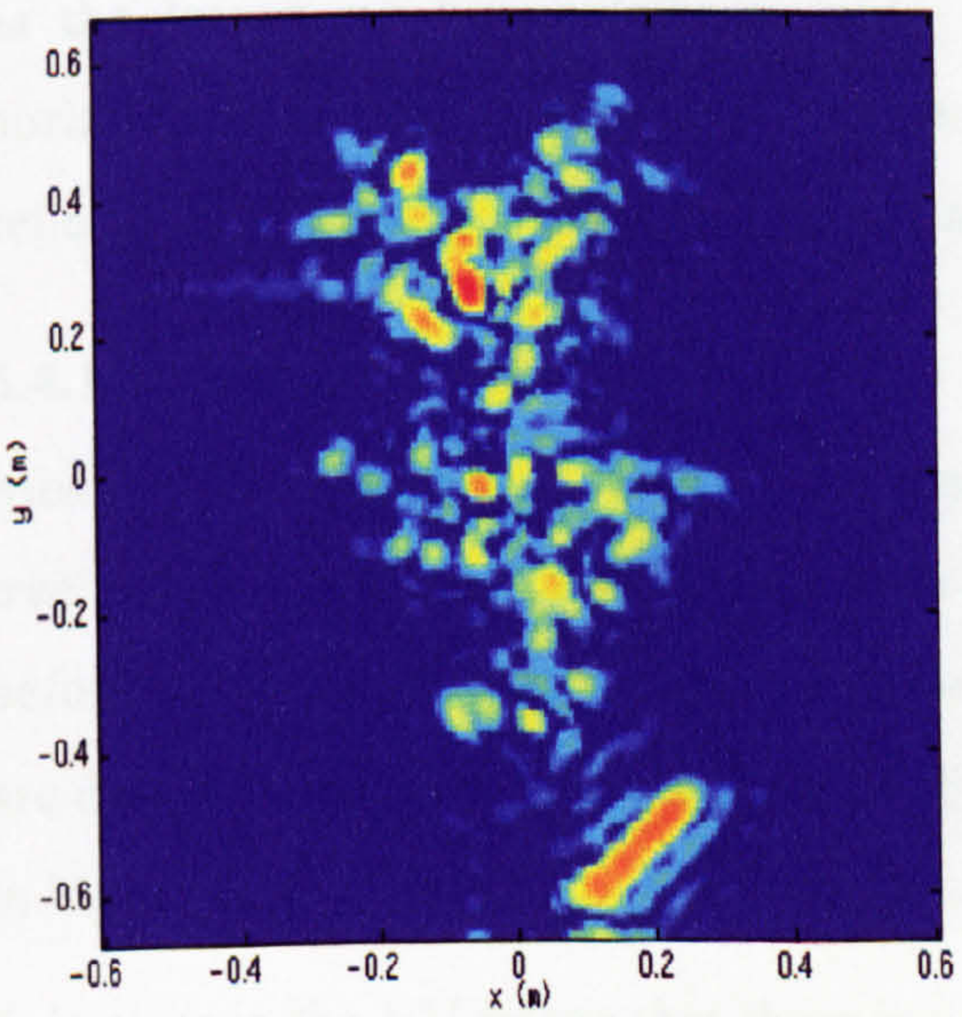

VH Image

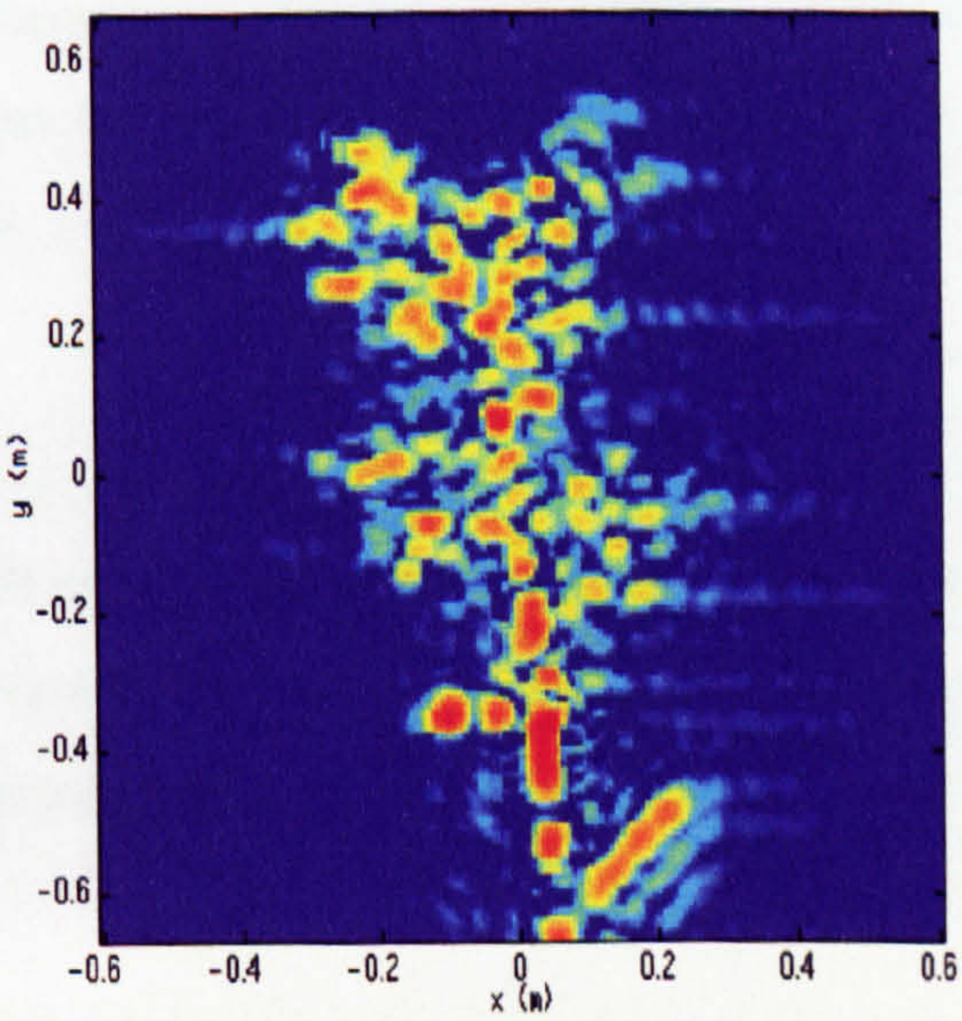

HH Image

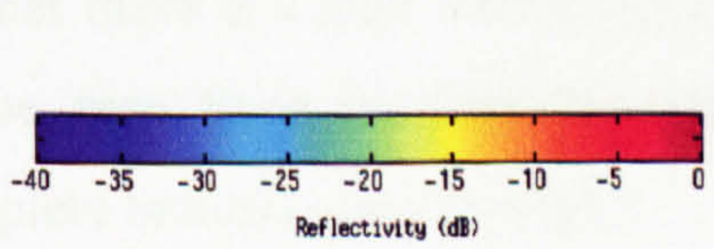

Figure 6.12 Polarimetric Imaging of a Beech Tree - August 1997

greater level of reflectivity can be observed. The branches in this area are oriented at approximately 25° - 30° to the vertical and hence interact much better with a VV signal than the horizontal branches do.

The main axis cannot be seen in the VH image. Instead, only isolated returns can be seen from the areas around the branches. It is supposed that, these returns are mostly from the branches themselves. The highest levels of reflectivity come from just above the main bifurcation and are reflections elements of some of the branches which are oriented at angles approaching 45°. As noted in Chapters 4 and 5, elements oriented at 45° provide the greatest reflectivity at VH polarisation.

In the HH image, the lower half of the main axis is clearly visible and has a high reflectivity since there are no leaves around this region. The upper regions of the main axis are more difficult to identify as the leaves are obscuring it. The leaves clearly interact well with the incident radar signal at this polarisation. This is to be expected as the leaves are horizontally oriented. Therefore, a number of reflections from horizontally oriented branches and leaves can be seen in this image and they have reflectivities of similar values to the main axis.

6.4.1.2 January 1998

Measurements were also made of the beech tree in January 1998. The leaves on the tree were all dead and dried up and were still attached to the tree but were removed before imaging took place. The same parameters were used for the imaging process as are described previously and the results of the polarimetric imaging process are shown in Figure 6.13.

It is clear in the VV image that there is a high return from the main axis of the tree. Some reflections can also be seen from the branches both below and above the bifurcation, although no complete branches can be seen.

The VH image does not show the presence of the main axis, but instead has a high response from the area around the main bifurcation. As already mentioned, some of the branches at this point are oriented close to 45° and hence give a strong response to a VH signal. Other areas of isolated returns can be seen around the rest of the branches. Clearly, some of the branches cause strong depolarising effects.

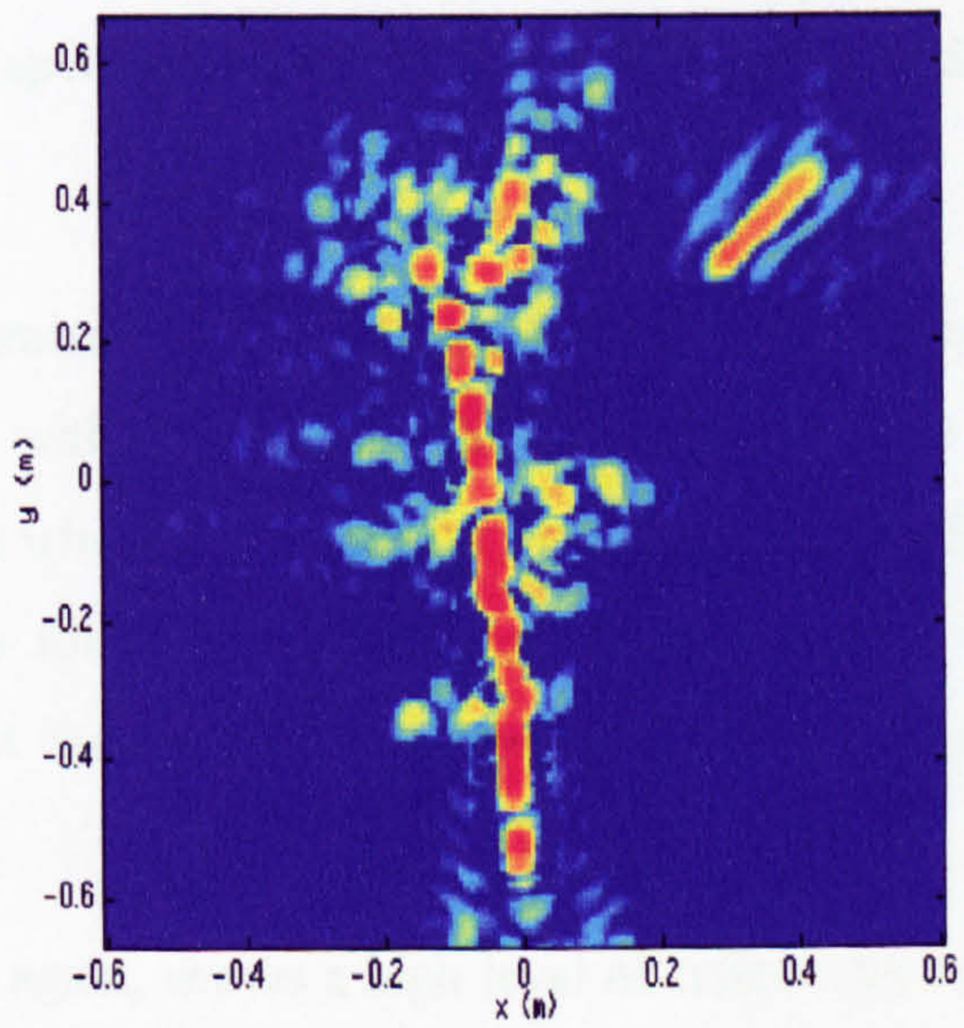

Figure 6.13 Polarimetric Imaging of a Beech Tree - January 1998

In the HH image, the main axis can be clearly seen since its diameter is large enough to allow good interaction with the incident wave. Several of the branches can also be seen and those branches which cannot be seen are angled towards or away from the plane of the scanning aperture and hence only their ends are visible.

6.4.1.3 April 1998

The final set of polarimetric measurements on the tree were made in April 1998 when the tree was covered with new leaves. The leaves at this time were soft and flexible and were smaller than when measurements were made the previous August. A number of these leaves were found to be hanging downwards and were not horizontally oriented, especially at the ends of branches. The images generated at this time are shown in Figure 6.14.

The VV image, once again, shows a high level of reflectivity from the main axis. The bifurcation of the main axis can be seen along with the lower ends of three branches just above it. There is also a wide spread area of lower level returns from the branches and leaves. Given the small number of branches visible at VV polarisation in the January images, it is likely that most of these returns are from the leaves. As already explained, some of the leaves were drooping downwards and hence were oriented in such a way that they would interact well with a VV signal.

The VH image shows a wide area of scattering from the leaves of the tree. The main axis cannot be seen, but some returns from the branches at the bifurcation can be identified. Clearly, the leaves at this time of year are effective at depolarising signals.

The highest returns from the branch-leaf regions occur in the HH data set. The horizontal branches of the tree cannot be seen in this image, since they are obscured by the leaves surrounding them. It is supposed that the reflectivity in these regions is from both the unobscured branch elements and suitably oriented leaves. The main axis can be seen at the bottom of the tree where there are no leaves around it.

6.4.2 Angular Imaging of a Beech Tree

The work so far has concentrated on observing radar-target interactions by generating images of trees in a plane parallel to the direction of growth of the tree. In such a

Optical Image

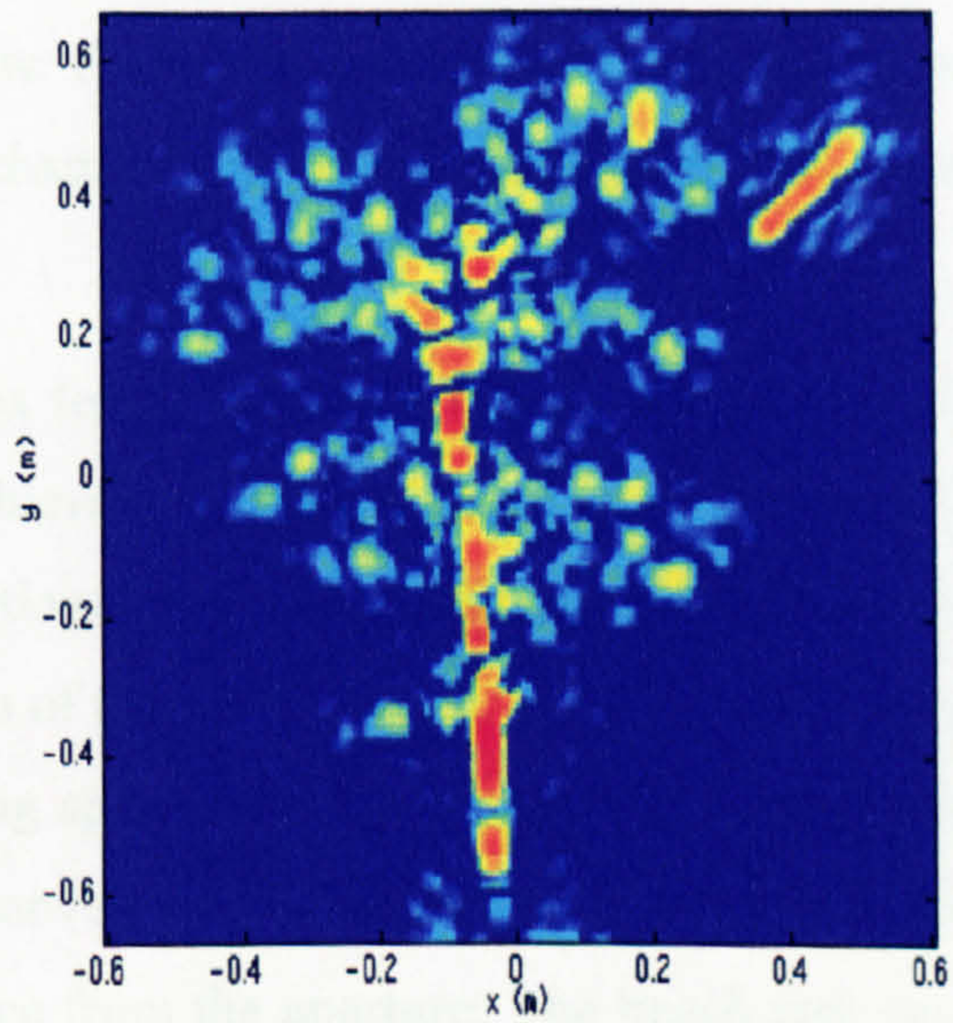

VV Image

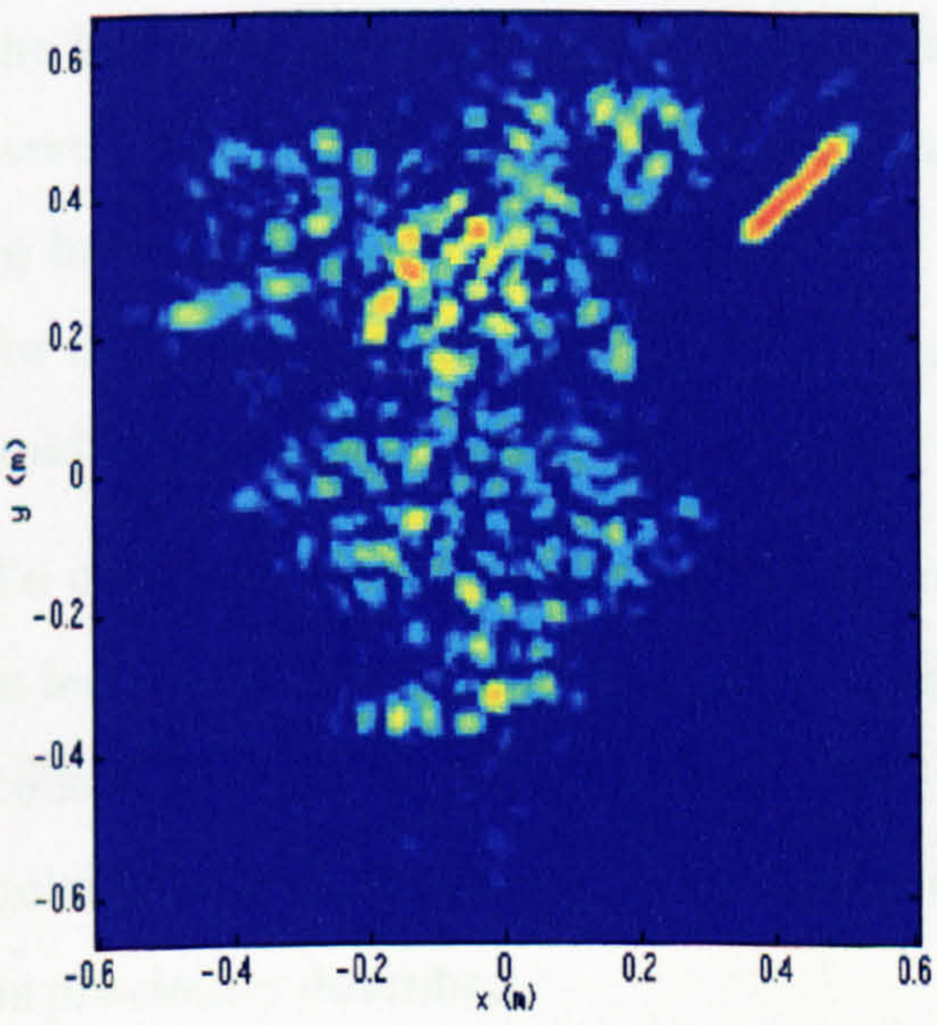

VH Image

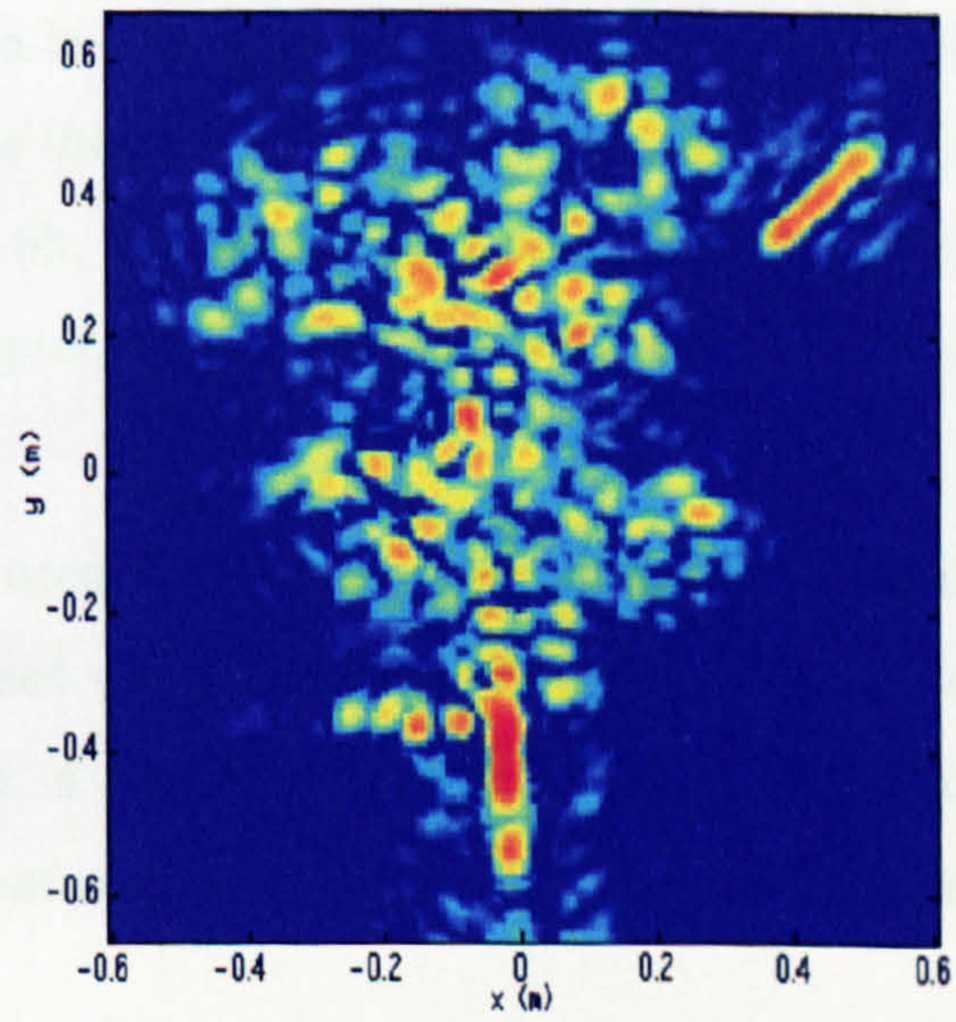

HH Image

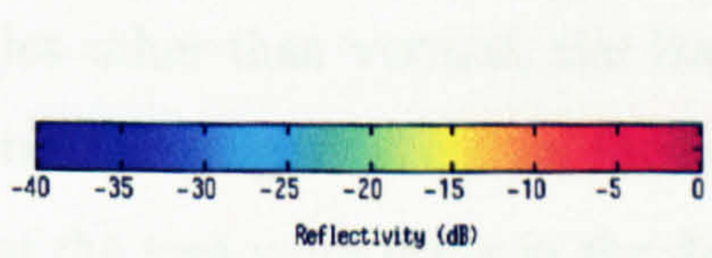

Figure 6.14 Polarimetric Imaging of a Beech Tree - April 1998

case, the radar illuminates the tree from the side. However, in order to relate these high resolution near-field images to those taken by aircraft and satellites, it is necessary to generate a second group of images from an overhead view above a tree to complement those taken from a side view. Such an experiment would require an overhead scanner located in an anechoic chamber and suitable equipment was not available.

An alternative solution to this problem was to tilt the angle of the tree instead of tilting the angle of the scanner. This was achieved by fixing a single beech tree into a cradle which is connected to a rotating positioner unit. The cradle attaches the pot of tree to the positioner unit so that the bottom of the tree is kept fixed whilst the top of the tree is tilted towards the vertical scanning aperture. At each new angle of tilt, the cradle and its attached positioner unit are moved away from the scanner so that the top of the tree is always at the same distance from the aperture. The beech tree was utilised for this experiment as the results obtained in the previous sections suggest that the leaves of the beech cannot easily be seen in side view images. The measurements were made in September 1997 at which time the tree was found to be sturdy enough to hold its shape regardless of the angle of tilt. This experiment was not carried out for the larch tree described earlier in the chapter, as the larch was not rigid enough to hold its shape when tilted.

To carry out the experiment, the beech tree used was placed in the cradle and imaged in increments of 15 degrees. The scan size used was 97.5cm by 130.5cm and data was collected over a 0.51GHz bandwidth at a centre frequency of 10GHz. The polarisation utilised was VV and empty room and calibration corrections were made as previously described.

When a tree is tilted to angles other than vertical, the leaves attempt to alter their positions to maximise the amount of light falling on the leaf surface. To avoid this problem, the measurements of the tree were made in the dark at night. All plants are sensitive to changes in gravity, as well as light, but the effect on a small tree in an autumnal month should be minimal. Nevertheless, the tree was only left at a tilted angle for a few hours at a time.

The results of the imaging process are shown in Figure 6.15 and the corresponding optical images are presented in Figure 6.16. The images show the tree at tilted angles of 0°, 15°, 30°, 45°, 60° and 75° which corresponds to incidence angles of 90°, 75°, 60°, 45° and 30° respectively. For the rest of this section, the angles of incidence will be referred to.

It is apparent that when the tree is vertical, the radar has a side view of it. At this point the incidence angle is 90°. From the figure, it can be seen that, the main axis of the tree is clearly visible and gives a high level of reflectivity. However, the branches and the leaves of the tree cannot be easily detected.

When the angle of incidence is decreased to 75°, the response from the main axis deteriorates slightly. There is now no longer a continuous response from it as some parts of it are invisible to the radar.

The main axis disappears completely when the incidence angle reaches 60°. At this point the tree is oriented at 30° to the plane of the aperture. Therefore, the reflections from the main axis are directed away from the scanning aperture. It is also clear from this image, that there is now a noticeable response from the region around the leaves. Evidently, as the tree is tilted forwards, the backscattered energy from the leaves is now being directed back towards the scanning aperture resulting in their presence in the image.

The response from the leaves increases further still as the incidence angle decreases. The highest levels of reflectivity from the leaves are achieved when the incidence angle drops to 45° and 30°. At these angle, the leaves present a large surface area to the radar.

Therefore, it is clear that leaves are good reflectors of electromagnetic energy, provided that they are oriented in such a way as to provide a large surface area to the transmitted radar energy. To understand more about the variation of backscatter from the leaves, a single leaf was removed from the beech tree and its variation in backscatter with changing incidence angle was measured. The resulting graph is shown in Figure 6.17. Here, it can be seen that when the radar is pointing directly to the flat surface of the leaf, then the backscatter is at a maximum of ~-26dBm^2. As the

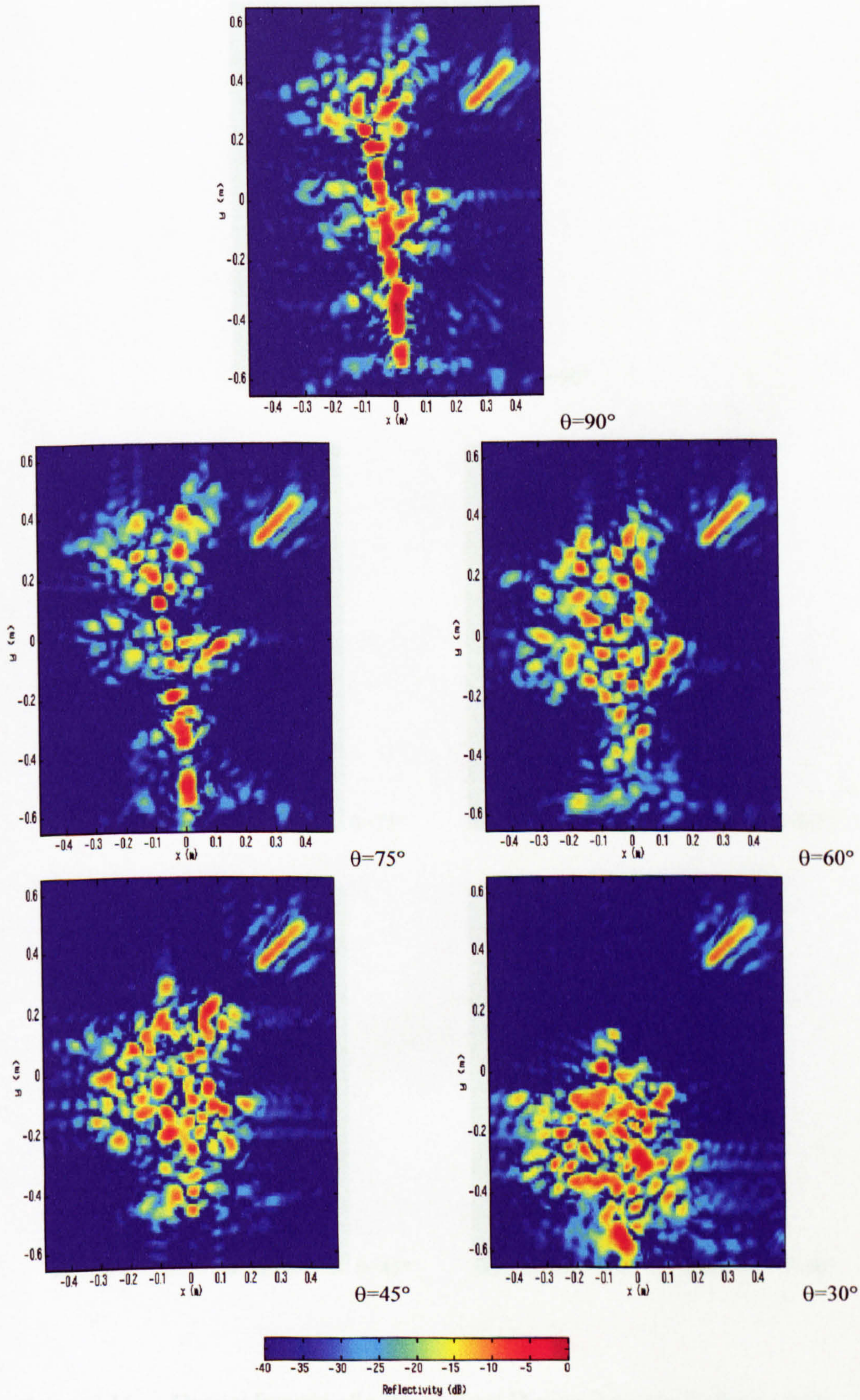

Figure 6.15 Angular Imaging of a Beech Tree at VV Polarisation - Sept. 1997

θ=90°

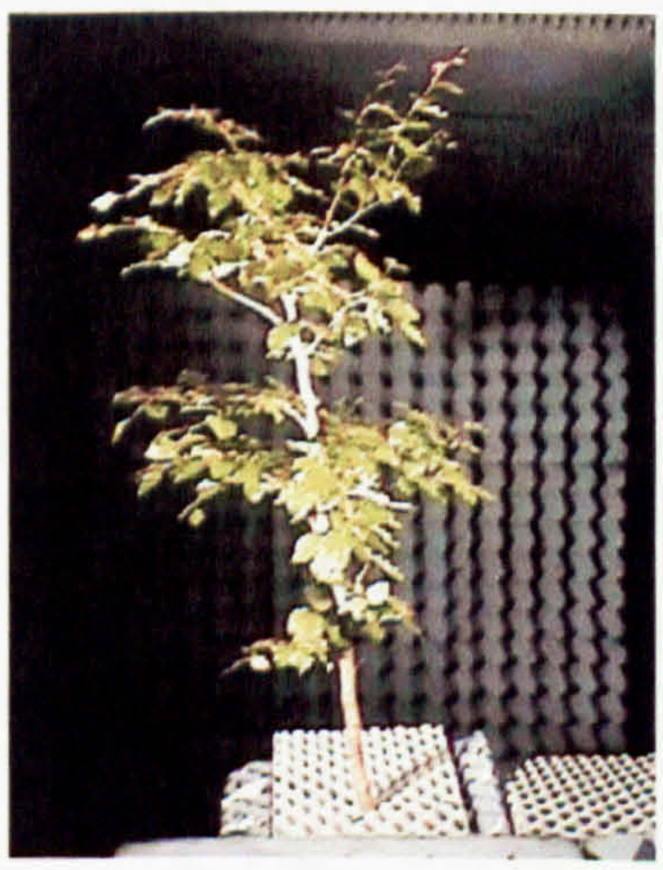

θ=75°

θ=60°

θ=45°

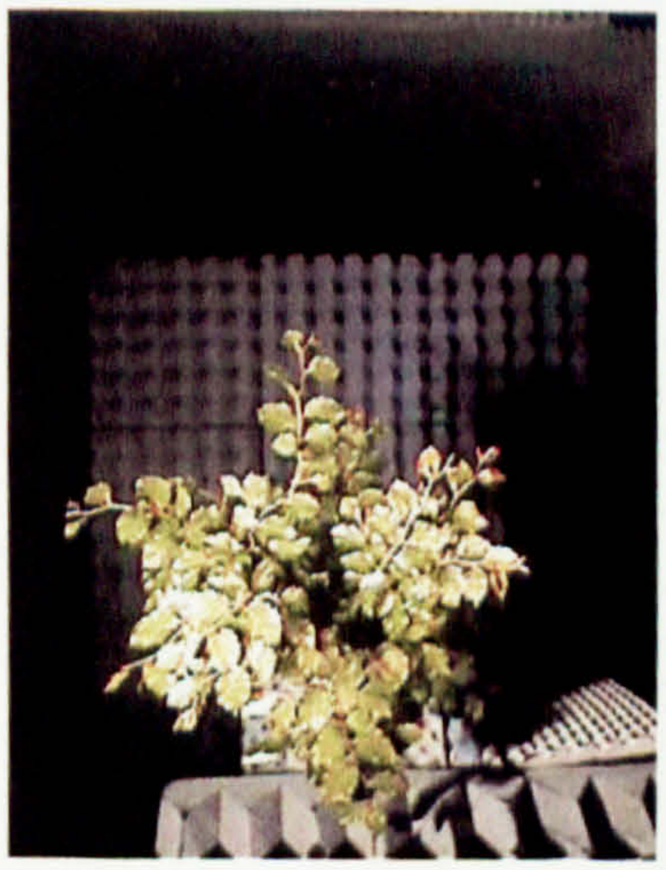

θ=30°

Figure 6.16 Optical Images of a Beech Tree During Angular Measurements

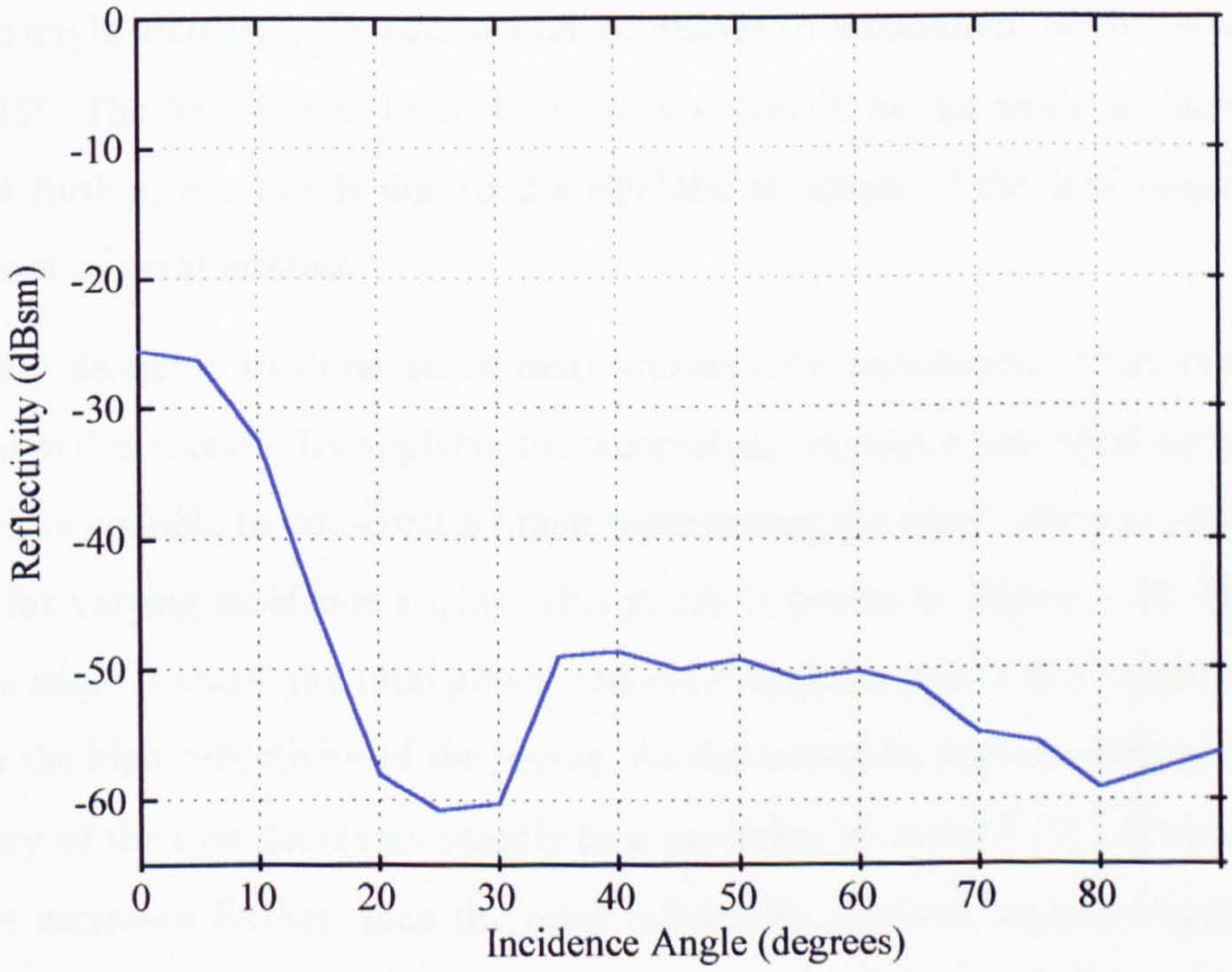

Figure 6.17 Variation of Backscatter from a Single Beech Leaf with Incidence Angle

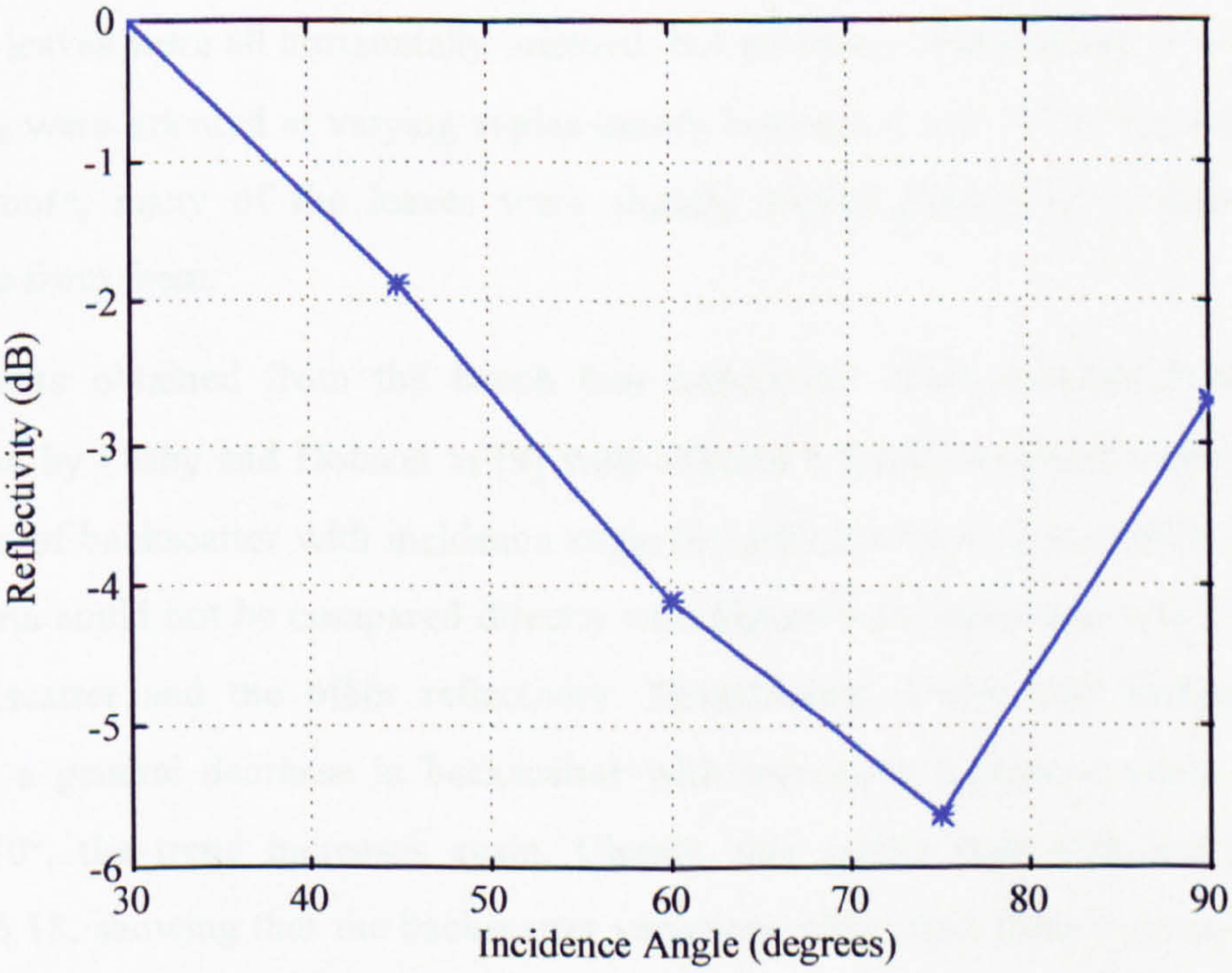

Figure 6.18 Total Variation in Reflected Energy with Changes in Incidence Angle

incidence angle increases, the backscatter decreases to a minimum below -60dBm^2 at around 25°. The backscatter level the increases slightly as the angle of incidence is increased further, but this is due to the sidelobe structure of the leaf response and hence is not of great interest.

It is highly desirable to draw some more quantitative conclusions from the images presented in this section. By applying the summation technique described earlier in the chapter, it is possible to construct a graph representing the total reflected power from the tree for varying incidence angles. This graph is shown in Figure 6.18. When the incidence angle is small, the total power reflected from the tree is at a maximum. This is due to the high reflectivity of the leaves. As the incidence angle increases, the total reflectivity of the tree decreases sharply to a minimum at around 75°. If the angle of incidence increases further, then the total reflectivity starts to increase again as the main axis of the tree is now contributing to the reflected signal. It should also be noted that the angle at which the minimum of the tree response occurs (75°) is much greater than the minimum of an individual leaf response (25°) as shown above. It is probable that this is due to the orientation of the leaves on the tree. It was assumed that the leaves were all horizontally oriented, but on closer examination, it was found that they were oriented at varying angles mostly between 0 and 30° to the horizontal. Furthermore, many of the leaves were slightly curved leading to a non-uniform response from them.

The results obtained from the beech tree experiment were compared with data published by Ulaby and Dobson in [9] who collated a whole series of results for the variation of backscatter with incidence angle for different types and groups of trees. Their data could not be compared directly with Figure 6.18, since one was a measure of backscatter and the other reflectivity. Nevertheless, Ulaby and Dobson's data showed a general decrease in backscatter with increasing incidence angle until, at about 70°, the trend increases again. Clearly, this agrees well with the graph in Figure 6.18, showing that the backscatter variations with angle from a group of trees correspond well with the reflectivity from a single tree.

6.4.3 Seasonal Variations

As with the larch tree, the data from the beech tree was collated to try and determine the seasonal variations present in the images. It should be noted that the September 1997 measurement was made at VV polarisation only.

6.4.3.1 VV Variations

Examination of the VV images in Figure 6.19 shows that there appears to be little variation between the first three images (August, September and January). The leaves present a very small surface area to the radar and hence cannot be seen in the August and September images. Therefore, the image data collected in January is little different, even though, at the time, there were no leaves present on the tree. The main axis can be seen very clearly in all the first three images but the returns from the branch-leaf regions are low. The image generated from the data collected in April 1998, is different in that it shows a much more extensive tree structure and a greater returns from the region around the branches. It is supposed that this is due to reflections from the leaves, many of which were soft and flexible and drooping at an angle, making them more visible to the radar than usual.

6.4.3.2 VH Variations

From the VH images, presented in Figure 6.20, it is clear that there is again little difference between the August 1997 and January 1998 data sets. The only noticeable feature, is the large return from the branches around the bifurcation in the January image. This cannot be seen in the August image, possibly due to the obscuring effect of the leaves. The April 1998 image, also shows the highest valued returns being generated at the bifurcation. Otherwise, the image provides a different result from the first two, with numerous hot spots across most of the tree structure. It is supposed that these are reflections from the young leaves.

6.4.3.3 HH Variations

The seasonal results at HH polarisation, as shown in Figure 6.21 provide the most information about the seasonal variation of the beech tree. In August 1997, the main axis of the tree cannot be clearly identified except at the bottom of the tree where

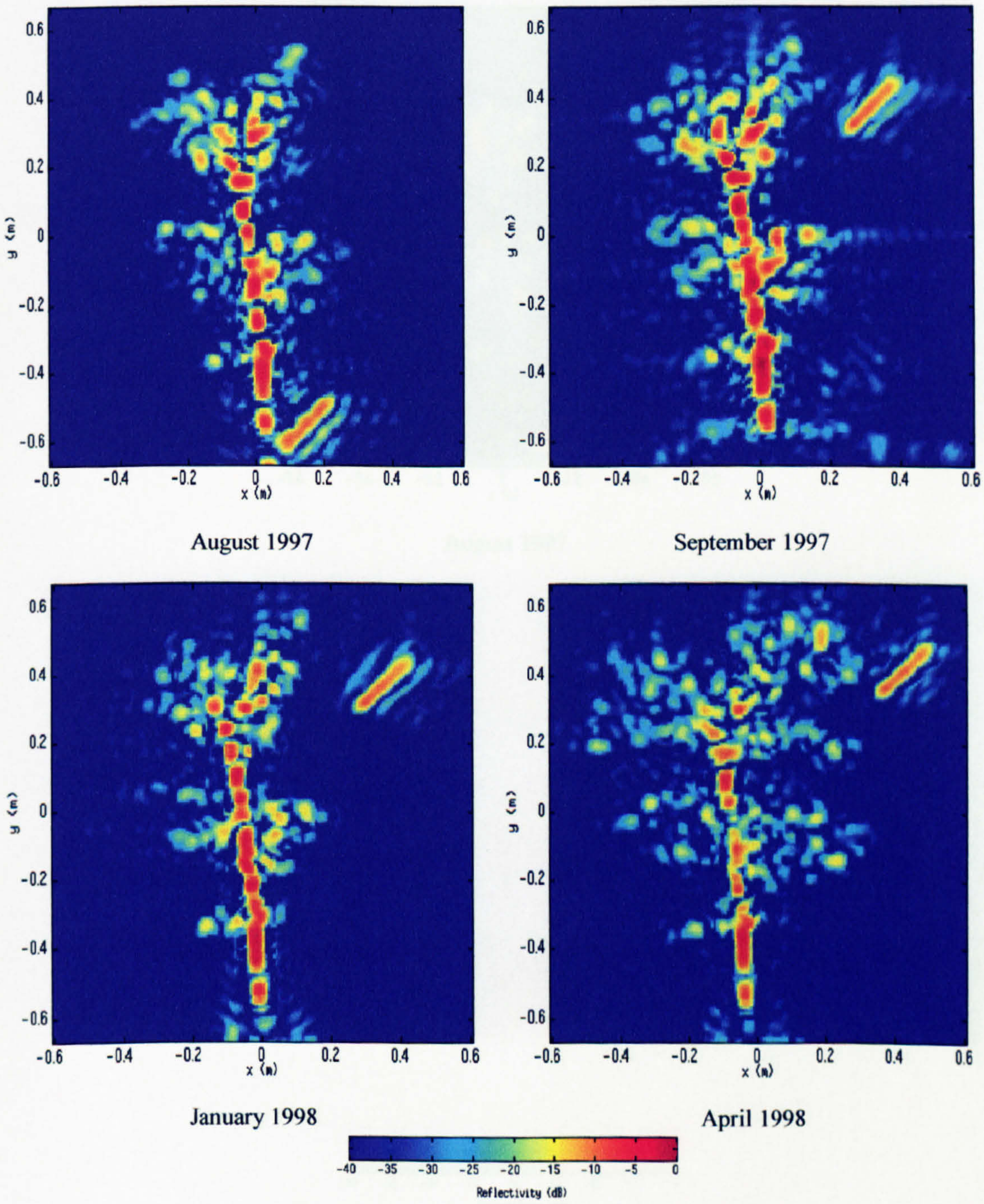

Figure 6.19 VV Images of a Beech Tree Over a Growing Season

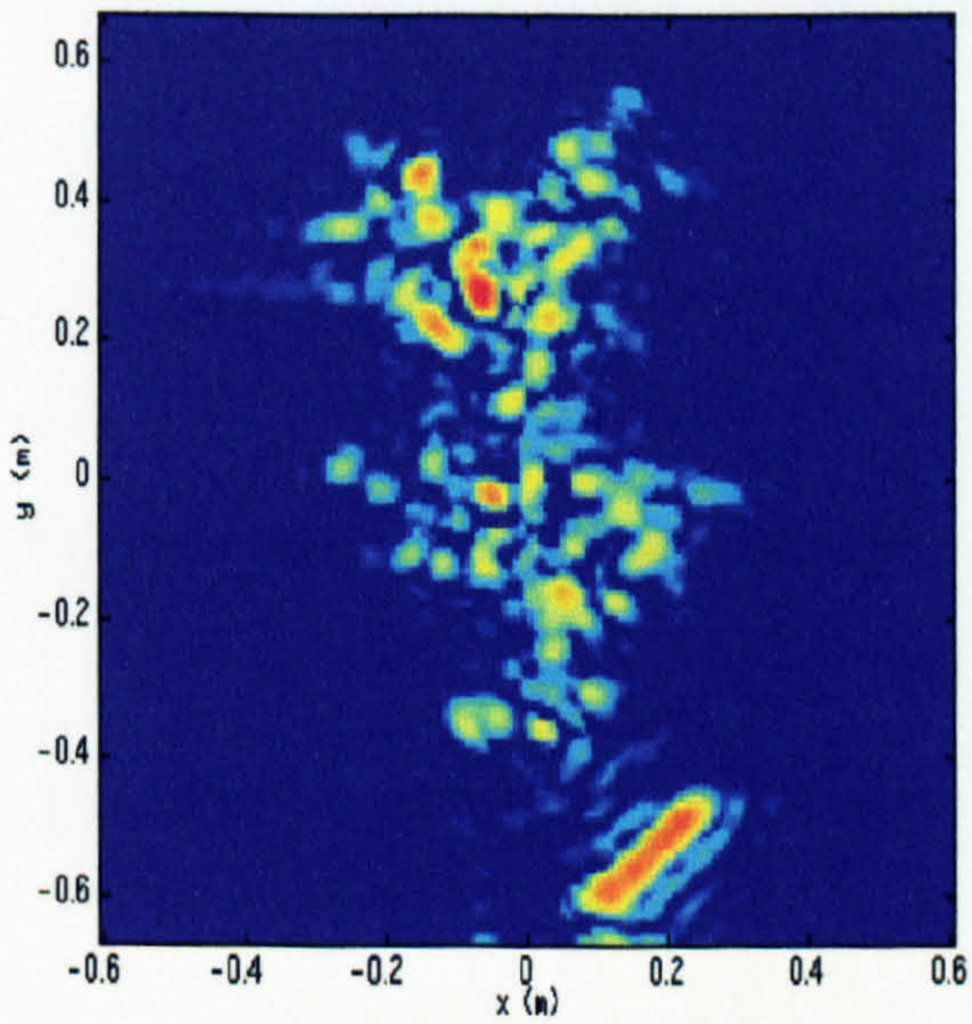

Figure 6.20 VH Images of a Beech Tree Over a Growing Season

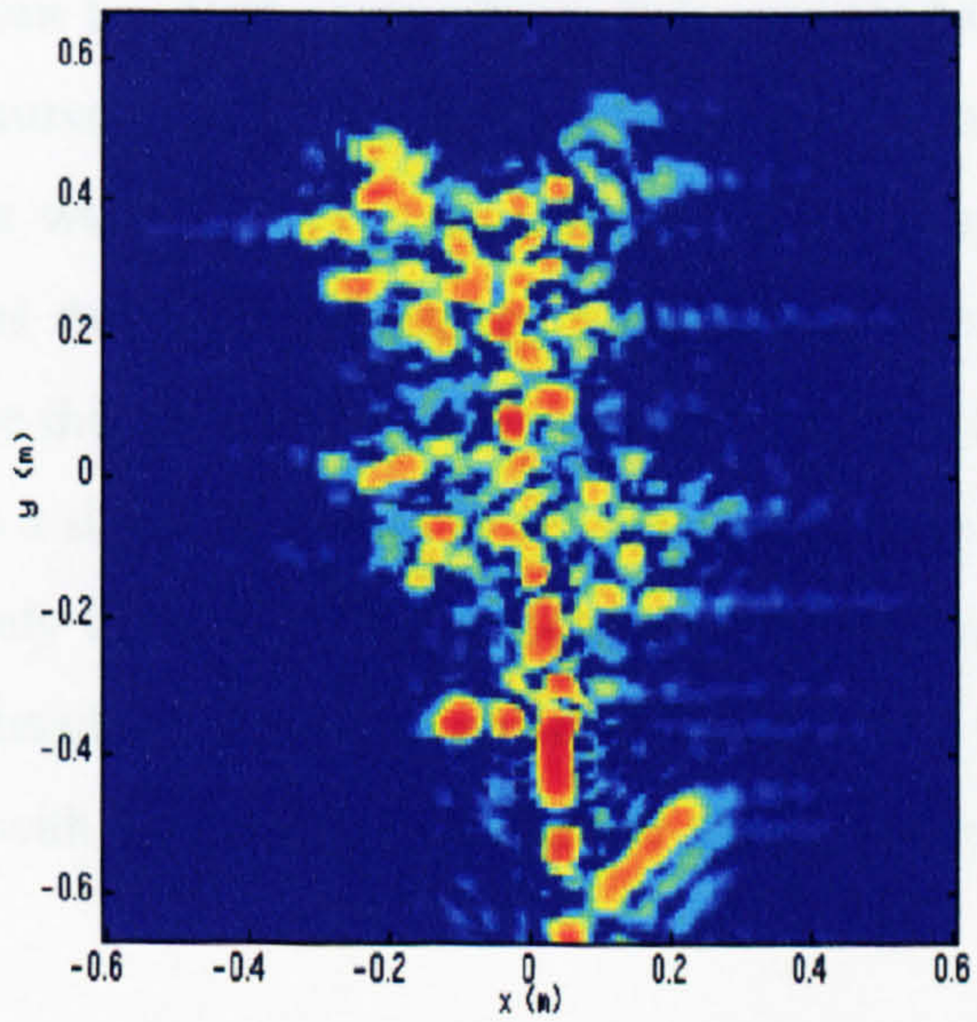

Figure 6.21 HH Images of a Beech Tree Over a Growing Season

there are no leaves. Higher up the tree, the response from the main axis diminishes greatly and is lost amongst the reflections from the branches and the leaves. No individual branches can be clearly seen either. It is supposed that the reflections are from both the unobscured branch elements and the leaves. In the image data collected in January 1998, the whole of the main axis can be seen, in contrast to the data collected the previous August. Furthermore, a number of individual branches can be clearly identified since there are no leaves obscuring them. The final data set, collected in April 1998, shows a similar response to the data from the previous August, in that the main axis can only be seen at the bottom and the returns from the leaves are evidently obscuring details of the branch structure higher up. It is clear, therefore, that leaves interact well with a horizontally polarised signal generating a relatively high level of reflectivity.

6.5 Conclusions

This chapter has demonstrated that the modified multifrequency auto-focusing imaging algorithm provides an effective method of imaging biophysical targets illuminated from a planar scanner. A sycamore tree was imaged to verify that low reflectivity targets could be seen above the system background level. Experimental proof that the SVA algorithm performs well on such targets was also demonstrated.

Polarimetric measurements were made on two trees, a larch tree and a beech tree. From these it was found that the response of the trees to the radar is highly dependent on the orientation of the tree elements with respect to the system polarisation. This was true of both the tree itself and the leaves on it. For example, the main axis gave a high reflectivity in VV images whilst the horizontally oriented leaves on the beech tree gave a good level of reflectivity at HH. These results were anticipated from the single frequency measurements of Chapter 4.

A set of measurements was also conducted to investigate the effect of incidence angle on the backscattered return from the beech tree. From this, it was discovered that as the incidence angle is increased, the total reflectivity of the tree is decreased as leaf surface area seen by the radar decreases. The reflectivity reaches a minimum around

70° and then starts to increase as reflections from the main axis of the tree start to become significant. It was shown that these results correspond to other published results.

The data collected from the polarimetric measurements were collated to try and identify seasonal changes in the reflectivity of the trees. For the larch it was found that, at VV polarisation, the main axis gave strongest response, especially in winter. At other times it was slightly obscured by the needle clusters. The VH images showed little variation with season although the nature of backscatter in spring was clearly determined by the shape of the needles. The winter VH image also identifies hot spots at bifurcations as predicted by the measurements made in Chapter 4. The HH image showed little seasonal variation although the strongest response from the main axis and branches occurs in winter when the tree is bare. The greatest response from the needles seems to occur in spring.

From these measurements, it can be concluded that backscatter is caused by both the needles and tree elements such as the branches and main axis. The total contribution of each, depends on the season and the polarisation. Clearly, when the tree is bare the branches and main axis have the highest response. At other times, the needles cause significant backscatter although the total contribution depends on the size and shape of the needles.

Seasonal variations for the beech tree were much harder to identify than for the larch tree. This was due to the fact that the radar was illuminating the tree from the side and hence the leaves could not easily be seen by the radar. This was especially true for the VV and VH polarisations. However, at HH polarisation, where the leaves were easy to identify, it was noted that the leaves obscure the response from the main axis and branches in spring and summer. This obscuring effect was greatest in spring whilst the highest level of reflectivity from the tree branches and main axis were found to be in winter.

Chapter 7

Discussions and Conclusions

7.1 Introduction

This chapter presents a brief overview of the key points of this work. Some general conclusions are drawn relating to the sources of the backscatter from trees and some suggestions for further work are given.

7.2 Simulations

The backward propagation algorithm was simulated in Chapter 2 in both one and two dimensions. Apart from the obvious limitation of poor depth of focus, the algorithm provides excellent resolution and is fast and simple to implement in practice. Multiple scattering effects were also modelled and, although they were generally in-focus, their presence prevented accurate far-field information being derived from the data. It is generally recognised that near-field measurements of multiple interactions using synthetic aperture techniques result in a loss of information which prevents a true far-field response being obtained [76].

Investigations of the multifrequency auto-focusing algorithm, presented in Chapter 3, were highly informative and provided a clear relationship with the backward propagation algorithm. The simple computational and data requirements of this algorithm make it ideal for generating high resolution images and it only requires a narrow bandwidth. For images in a microwave eye format, the alternative would be to use an ISAR system, in which case the motion of the target during the angular rotation process may cause errors. A cylindrical or spherical SAR system could also have been used, but a suitable system was not available.

The difficulty of using the auto-focusing algorithm is that it has an inherent redundancy of data in it which leads to some deterioration in the resolution. This can only be circumvented by using a wider bandwidth. The algorithm also has relatively high sidelobe levels although these can be reduced by application of suitable filtering techniques. Multiple interactions were also modelled in Chapter 3 and once again, it was found that this prevented accurate far-field data being derived from near-field simulations.

7.3 Single Frequency Measurements

The first set of experimental work employed a two-dimensional scanner to collect data reflected from targets in an anechoic chamber at a single frequency. Initially, polarimetric measurements were made of a series of wires oriented at different angles. This demonstrated the polarimetric sensitivity of the system and the polarimetric purity was found to be between 35 and 40dB. The system was also found to be highly effective at imaging low reflectivity targets since the polystyrene support sheet for the wires was clearly visible in two of the images. Of particular interest in the images were multiple scattering terms which could be identified between different wires. These had been expected from the simulations although there appears to be no published literature where such virtual terms have been clearly resolved in images.

The results of the single frequency measurements on the ash, sycamore and willow trees were highly successful. The images generated from the measurements had a high level of resolution with low sidelobe levels and a good signal to noise ratio. The images clearly demonstrated that the backscatter was dependent on the orientation of the tree elements relative to the polarisation of the system. Thus, vertical elements gave the highest reflectivity at VV whilst horizontal ones were better observed with HH polarisation.

The resolution of the system was high enough to distinguish very small features on the tree such as the location of nodes on the upper branches of the ash tree shown in Figure 4.6. In addition, the presence of several nodes, where the branches connected with the main axis, could be observed on two of the VH images. These nodes accounted for between 8 and 18% of the total signal reflected from the tree and thus are an important source of backscatter. The virtual images apparent within the tree structure of Figures 4.6 - 4.9 also contribute to the total backscattered signal. It is difficult to know how much these small effects would contribute to the backscatter from more mature trees and at different frequencies. It is clear though that these effects should be considered with more care when models of the backscatter from forested areas are developed.

Transmission measurements made on the sycamore tree were less successful but still demonstrated the dependence of the response on the tree geometry relative to the system polarisation.

The difficulty in using the single frequency system is that it has a poor depth of focus and biophysical targets need to be constrained to lie at a single range from the aperture. The problem can be alleviated by using the multifrequency auto-focusing algorithm.

7.4 Multifrequency Measurements

It was shown that the auto-focusing algorithm could be used experimentally to generate an in-focus image of a three-dimensional target. Two corner reflectors set at different ranges from the scanning aperture were used for this. In addition, the polarimetric purity was investigated by repeating the measurements made at a single frequency of several wires arranged at different orientations. This second experiment again revealed the presence of virtual images caused by multiple interactions between the targets. The virtual images were slightly defocused in this case, although the simulations showed that they may also be in-focus, depending on the separation between the real targets. Of particular interest, was the area of low reflectivity shown in Figure 5.7 which is also a result of multiple scattering. Here the virtual image has been cancelled out by the return from the polystyrene sheet at that location. This has important implications for the measurements made on biophysical targets in Chapter 6. Clearly, it is possible that multiple scattering may lead to virtual images being generated where there is no scatterer present but equally, it may cause a valid scatterer to be cancelled out if a virtual image occurs at the same x,y co-ordinates as a real scatterer.

The multifrequency measurements have also provided valuable information about the nature and origin of the backscatter from trees.

7.4.1 Sycamore Tree

The initial measurements performed on the sycamore tree showed that the multifrequency experimental system was highly effective at imaging biophysical

objects. As predicted, the sidelobes of the image were very high but could be effectively limited by using the SVA algorithm. The drawback of using this technique is in verifying that it produces valid imagery. The SVA algorithm individually examines each pixel in the image and identifies each one as a mainlobe pixel, a sidelobe pixel or as an unknown. The mainlobe pixels are unaltered, the sidelobe pixels are set to zero whilst the unknowns are filtered with a Hanning window. It is the status of this third set of unidentified pixels that may give cause for concern. Such pixels generally contain a mainlobe pixel response with some sidelobe energy in it although this may not be the case. Therefore, to apply a Hanning window to it may result in a mainlobe pixel being reduced in magnitude whilst other mainlobe pixels are left unaltered. Such a situation could conceivably destroy the integrity of the image. Indeed, it is possible in the aforementioned image of the sycamore tree, that the SVA algorithm has removed returns from the leaves around the upper branches. However, it is impossible to determine in Figure 6.1a-c whether the returns in this area are from sidelobes or leaves and hence the extent of the problem cannot be determined. Given that SVA is still a relatively new technique, it is likely that further work may provide a solution to this problem.

7.4.2 Larch Tree

The measurements made on the larch tree clearly show a strong dependence on polarisation. As expected, vertical elements such as the main axis, give high reflectivities at VV whereas the horizontally oriented branches can scarcely be seen in some cases. The reverse is true for HH. The real difficulty with the measurements lies in identifying how much of the reflectivity is due to the needles and how much is due to the branches. It is clear though, that the needles are an important source of backscatter. This is especially true in the VV and, to a lesser extent, in the VH data where there is a noticeable reduction in the total reflectivity from the tree in the winter months when it is bare of needles. Examination of Figure 6.7 indicates that, at VV polarisation, the needles account for around 50% of the backscattered signal from the branches. However, it is also clear that, although the needles are a good source of backscatter, they obscure the branches and main axis of the tree. Hence, in the winter months the reflectivity of the main axis increases, a trend which is noticeable in both

the VV and HH data. Such conclusions are no surprise as the penetration depth of coniferous trees at X-band is known to be very small [6][7].

The only parameters that could not be accounted for in these measurements were the changes in the biophysical properties of the tree itself over the nine months of the experiment. Therefore, any contributions due to changes in water content of the tree itself or its needles could not be determined. As mentioned in Chapter 1, it is known that both deciduous and coniferous trees have a changing water content depending on the time of year [18][19][20]. However, this could not be measured without causing damage to the larch tree itself. It was also noticed that the needles of the larch tree which were short, soft and flexible in spring, became long and firm in autumn. On reflection, it may have been useful to measure the water content of the needles as each measurement set was collected. Individual needles could be removed without affecting the total response from the tree. It should be noted though, that the response from the main axis increases in winter despite the fact that the water content of the trunk is lowest at this time of year. Therefore, it is reasonable to suppose that the nature of the foliage covering a tree has a greater effect on the backscatter than the moisture content of the tree.

The seasonal responses from the larch tree made at VV polarisation demonstrated a dramatic fall in reflectivity from the branches in the winter months. In contrast, the HH data shows almost no seasonal variations, due to the continuous response from the branches in both summer and winter. It is likely that these differences would be much smaller for a more mature tree which has a more complex architecture. In particular, the VV response from a mature tree may be higher in winter due to better interaction with the branch structure. Examination of Figure 6.11 also shows that the total reflectivity from the tree is always higher at HH than at VV. Measurements made by Mougin *et al.* [7] agree well with this. They demonstrated that VV and HH responses could be significantly different on a tree with fairly simple architecture, but that the differences were less marked on trees with more complex geometries. The VH data shown in Figure 6.11 also showed seasonal variations although they were not as marked as in the VV response. It is clear that both the needles and the branches again contribute to the backscatter at this polarisation. Of particular interest, was the

data set made in January 1998 shown in Figure 6.8 where a number of strongly reflecting hot spots are visible. Some of these are likely to be generated from points of branch bifurcation which would agree well with results observed in the single frequency case.

The trend shown in the seasonal larch measurements can be compared with other work on the seasonal variation in backscatter from forests. In particular, the measurements made by Ahern *et al.* [21] at C-band over Tamarack forested areas are of particular interest. Tamarack (*Larix laricina* (Du Roi) K. Koch) is also known as the American or Alaskan Larch and is smaller than its European counterpart. Nevertheless, in common with all larch species, it loses its needles in winter. Ahern *et al.* measured the backscatter over a Canadian plantation of Tamarack at HH polarisation in August and October 1987 and February and May 1988 using an incidence angle of approximately 70°. Their results show a minimum in the winter and a maximum in spring and summer. The greatest backscattered values obtained were for the spring measurements. This trend corresponds well with the results obtained in this work for the reflectivity of a single larch tree at VV polarisation and not with those made at HH. However, it does support the theory that the needles contribute a significant portion of backscattered signal from a larch tree and that, on the whole, a higher level of backscatter could be expected in summer rather than in winter. These conclusions are also supported by results of defoliating spruce and pine trees which generally show a small reduction in backscatter when the needles are removed [6][15][16][17].

There were a number of problems associated with making the larch tree measurements which undoubtedly have some effect on the results. In particular, it was found to be very difficult to position the tree in exactly the same place relative to the scanner for each measurement set. Even positioning errors of 1° can cause significant alterations in the final image distribution. This also prevented any difference measurements being made between images. In addition to the positioning errors, the larch tree showed a tendency to change the orientation of the leading shoot and certain branches very rapidly which again may have led to unexpected changes in the final images.

7.4.3 Beech Tree

As with the larch tree measurements, the beech tree images showed a strong dependence on system polarisation. In particular, it was noticeable that only the main axis of the tree could be seen at VV. The branches and the leaves were almost invisible (except in the April 1998 image) due to their orthogonal orientation to the incident wave. It is therefore not surprising that little in the way of seasonal variations could be observed. A better solution to the problem would be observe the seasonal changes from an overhead position although the equipment to do this was not available.

The VH data also showed relatively little seasonal variation although the response in the spring data set was noticeably different from the first two. This difference was due to the size and orientation of the leaves on the tree at this point in time. In all the VH images, the highest reflectivity is obtained from the area just above the bifurcation, which is not surprising given the orientation of the branches in this area. Conversely, the main axis is invisible in all the VH images, but this is expected given the VH results obtained at single frequency.

The most successful imaging of the beech tree occurred at HH polarisation as seasonal variations are more easily identifiable in this data. These results indicate that the leaves, when visible to the radar, are an important source of backscatter. As with the data from the larch tree they obscure the main axis and the branches especially in spring.

The experiment to image the beech tree at different incidence angles was constructed to try and address the problems associated with making side view images. The results demonstrated that the reflections from the leaves were readily identifiable at incidence angles less than 70° and that information about the total variation in backscatter with incidence angle could be obtained. The general decrease in reflectivity with increasing incidence angle, indicated that the surface area of the leaves presented to the radar is critical in determining the total backscatter from a tree. However, at angles greater than ~70°, the main axis and branches become significant. The results obtained from the small tree utilised in this work may vary to some extent to those obtained from a

mature tree. However, the underlying trend is likely to be unaltered and as already mentioned, the results obtained in Chapter 6 agree well with other published data [6][9]. Due to time constraints, it was not possible to investigate the angular variation at other polarisations.

7.5 Further Work

In retrospect, more conclusive data, with respect to seasonal variations, could have been obtained by measuring the larch and beech trees at more regular intervals. It would then have been possible to obtain graphs for the total reflectivity of the beech tree and improve the ones generated for the larch.

The greatest difficulty associated with this work has been the difficulty in observing certain elements of the tree when making measurements from a side view. Although such measurements provide important information about the polarimetric response of trees, seasonal variations of deciduous trees are difficult to determine. Clearly, an overhead scanner would be preferable, and in particular, one which could be used to make measurements at different incidence angles would be highly desirable. If such a system existed, it would be worth repeating the angular variations on the beech tree at all polarisations and over a growing season. This would provide valuable data that could more easily be related to data collected from airborne SARs over forested areas.

The multifrequency system described above along with the auto-focusing algorithm provide a valuable tool for generating high resolution near-field images. The applications of such a system are multitudinous and are only limited by constraints of time and money. In terms of imaging biophysical objects, an enormous amount of information can yet be obtained. For example, difference measurements denoting the respective contributions of a tree at different polarisations could be made or investigations into the effect of water stress or disease on plants could be monitored. Such measurements will continue to aid understanding of radar-target interaction and will lead to more representative and accurate models.

References

[1] Sabins, F.F., (1997), *Remote Sensing: Principles and Interpretation*, W.H. Freeman, New York.

[2] Ulaby, F.T., Moore, R.K. and Fung, A.K., (1982), *Microwave Remote Sensing, Active and Passive. Vol. 2. Radar Remote Sensing and Surface Scattering and Emission Theory*, Artech House, Reading, MA.

[3] Ulaby, F.T., Moore, R.K. and Fung, A.K., (1986), *Microwave Remote Sensing, Active and Passive. Vol. 3. From Theory to Applications*, Artech House, Reading, MA.

[4] Pitts, D.E., Gautam, D.B., Reyna, E., Zoughi, R., Wu, L. and Moore, R.K., "Estimation of X-Band Scattering Properties of Tree Components", *IEEE Transactions on Geoscience and Remote Sensing*, Vol. 26, No. 5, September 1988, pp. 612-616.

[5] Hirosawa, H., Matsuzaka, Y., Daito, M. and Nakamura, H., "Measurement of Backscatter from Conifers in the C and X Bands", *International Journal of Remote Sensing*, Vol. 8, No. 11, 1987, pp. 1687-1694.

[6] Hirosawa, H., Matsuzaka, Y. and Kobayashi, O., "Measurement of Microwave Backscatter From a Cypress With and Without Leaves", *IEEE Transactions on Geoscience and Remote Sensing*, Vol. 27, No. 6, November 1989, pp. 698-701.

[7] Mougin, E., Lopes, A., Mostafa, A.K. and Fung, A.K., "Effect of Tree Structure on X-Band Microwave Signature of Conifers", *IEEE Transactions on Geoscience and Remote Sensing*, Vol. 31, No. 3, May 1993, pp. 655-667.

[8] Ranson, K.J. and Saatchi, S.S., "C-band Microwave Scattering from Small Balsam Fir", *IEEE Transactions on Geoscience and Remote Sensing*, Vol. 30., No. 5, September 1992, pp. 924-932.

[9] Ulaby, F.T. and Dobson, M.C., (1989), *Handbook of Radar Scattering Statistics for Terrain*, Artech House, Norwood, MA.

[10] Narayanan, R.M., Nelson, S.E. and Dalton, J.P., "Azimuthal Scattering Pattern of Trees at X-Band", *IEEE Transactions on Aerospace and Electronic Systems*, Vol. 29, No. 2, April 1993, pp. 588-593.

[11] Al-Nuaimi, M. and Hammoudeh, A., "Theoretical and Experimental Study of Attenuation and Scatter of Microwave Signals by Trees", *8th International Conference on Antennas and Propagation*. Heriot-Watt University, UK, 30 March-2 April 1993, pp. 808-811

[12] Hammoudeh, A. and Al-Nuaimi, M., "Scattering Cross-Section Characterisation of Vegetation Media at Microwave Frequencies", *Electronics Letters*, Vol. 30, No. 11, 26th May 1994, pp. 903-904.

[13] Al-Nuaimi, M.O. and Hammoudeh, A.M., "Measurements and Predictions of Attenuation and Scatter of Microwave Signals by Trees", *IEE Proceedings on Microwaves, Antennas and Propagation*, Vol. 141, No. 2, April 1994, pp. 70-76.

[14] Elachi, C., (1988), *Spaceborne Radar Remote Sensing: Applications and Techniques*, IEEE Press, New York.

[15] Pulliainen, J., Heiska, K., Hyyppä, J. and Hallikainen, M., "Detection of Spruce Defoliation with Microwave Radar Techniques", *22nd European Microwave Conference*, Helsinki University of Technology, Espoo, Finland, 24-27 August 1992, pp. 939-944.

[16] Zoughi, R., Bredow, J., Osman, S. and Moore, R.K., "Fine Resolution Signatures of Coniferous and Deciduous Trees at C Band", *International Journal of Remote Sensing*, Vol. 10, No. 1, 1989, pp. 147-169.

[17] Pulliainen, J., Heiska, K., Hyyppä, J. and Hallikainen, M., "Laboratory and Tower-Based Microwave Measurements of Spruce Defoliation", *IGARSS '92*, Houston, Texas, USA, 26-29 May 1992, pp. 1177-1180.

[18] Constantz, J. and Murphy, F., "Monitoring Moisture Storage in Trees Using Time Domain Reflectometry", *Journal of Hydrology*, Vol. 119, No. 1-4, 1990, pp. 31-42.

[19] Wullschleger, S.D., Hanson, P.J. and Todd, D.E., "Measuring Stem Water Content in Four Deciduous Hardwoods with a Time-Domain Reflectometer", *Tree Physiology*, Vol. 16, No. 10, October 1996, pp. 809-815.

[20] Gates, D.M., "Water Relations of Forest Trees", *IEEE Transactions on Geoscience and Remote Sensing*, Vol. 29, No. 6, November 1991, pp. 836-842.

[21] Ahern, F.J., Leckie, D.J. and Drieman, J.A., "Seasonal Changes in Relative C-Band Backscatter of Northern Forest Cover Types", *IEEE Transactions on Geoscience and Remote Sensing*, Vol. 31, No. 3, May 1993, pp. 668-679.

[22] Way, J., Paris, J., Dobson, M.C., McDonald, K., Ulaby, F.T., Weber, J.A., Ustin, S.L., Vanderbilt, V.C. and Kasischke, E.S., "Diurnal Change in Trees as Observed by Optical and Microwave Sensors: The EOS Synergism Study", *IEEE Transactions on Geoscience and Remote Sensing*, Vol. 29, No. 6, November 1991, pp. 807-821.

[23] Dobson, M.C., DeLaSierra, R. and Christensen, N., "Spatial and Temporal Variation of the Microwave Dielectric Properties of Loblolly Pine Trunks", *IGARSS '91*, Espoo, Finland, 3-6 June 1991, pp. 1107-11110.

[24] Salas, W.A., Ranson, J.K., Rock, B.N. and Smith, K.T., "Temporal and Spatial Variations in Dielectric Constant and Water Status of Dominant Forest Species from New England", *Remote Sensing of Environment*, Vol. 47, No. 2, February 1994, pp. 109-119.

[25] Bergen, K.M., Dobson, C.M., Pierce, L.E. and Ulaby, F.T., "Effects of Within-Season Dielectric Variations on Terrain Classification Using SIR-C/X-SAR", *IGARSS '97*, Singapore, 3-8 August 1997, Vol. 2, pp. 1072-1074.

[26] Moore, R.K., Osman, M.S. and Zoughi, R., "Measurements of Radar Backscatter from an Artificial Tree: An Indication of Azimuthal Variations and Polarisation Sensitivity of Trees", *IGARSS '88*, 13-16 September 1988, Edinburgh, Scotland, pp. 681-682.

[27] Nance, C.E. and Blanchard, A.J., "Backscatter Measurements from a Vegetation-Like Structure", *International Journal of Remote Sensing*, Vol. 11, No. 7, 1990, pp. 1205-1222.

[28] Moore, R.K., Osman, M.S., Zoughi, R. and Bredow, J., "Measurements of Radar Backscatter from an Artificial Tree: An Indication of Azimuthal Variations and Polarization Sensitivity of Trees", *International Journal of Remote Sensing*, Vol. 12, No. 3, 1991, pp. 401-417.

[29] Lang, R.H., "A Tree Scattering Experiment", *European Microwave Signature Laboratory Newsletter*, No. 9, November 1996, pp. 1-3.

[30] Fortuny, J. and Sieber, A.J., "Radar Reflectivity of a Fir Tree Measured by Three-Dimensional SAR Imaging", *European Microwave Signature Laboratory Newsletter*, No. 10, May 1997, pp. 1-3.

[31] Lang, R.H., Nesti, G., Landry, R., Franchois, A. and Sieber, A., "A Radar Tree Scattering Experiment", *Progress in Electromagnetic Research Symposium*, Cambridge, Massachusetts, USA, 7-11 July, 1997

[32] Kim, H., Johnson, J.T. and Baertlein, B., "Ka Band Backscatter Measurements and Modeling of Tree Foliage", *IGARSS '98*, 6-10 July 1998, Seattle, USA. pp. 2086-2088.

[33] Schwering, F.K., Violette, E.J. and Espeland, R.H., "Millimeter-Wave Propagation in Vegetation: Experiments and Theory", *IEEE Transactions on Geoscience and Remote Sensing*, Vol. 26, No. 3, May 1988, pp. 355-367.

[34] Al-Nuaimi, M.O. and Hammoudeh, A.M., "Attenuation Functions of Microwave Signals Propagated Through Trees", *Electronics Letters*, Vol. 29, No. 14, 8th July 1993, pp. 1307-1308.

[35] Al-Nuaimi, M.O. and Stephens, R.B.L., "Estimation of the Effects of Hilltop, Singly Distributed, Trees on the Path Loss of Microwave Signals", *Electronics Letters*, Vol. 33, No. 10, 8th May 1997, pp. 873-874.

[36] Seville, A., "Vegetation Attenuation: Modelling and Measurements at Millimetric Frequencies", *10th International Conference on Antennas and Propagation*, Heriot-Watt University, UK, 14-17 April, 1997, pp. 2.5-2.8

[37] Stephens, R.B.L. and Al-Nuaimi, M.O., "Attenuation Measurement and Modelling in Vegetation Media at 11.2 and 20 GHz", *Electronics Letters*, Vol. 31, No. 20, 28th September 1995, pp. 1783-1785.

[38] White, M.O., "Radar Cross-Section: Measurement, Prediction and Control", *IEE Electronics and Communication Engineering Journal*, Vol. 10, No. 4, August 1998, pp. 169-180.

[39] Cown, B.J. and Ryan, C.E., "Near-Field Scattering Measurements for Determining Complex Target RCS", *IEEE Transactions on Antennas and Propagation*, Vol. 37, No. 5, May 1989, pp. 576-585.

[40] Skolnik, M.I., (1962), *Introduction to Radar Systems*, McGraw-Hill Kogakusha, Ltd. Tokyo.

[41] Edde, B., (1993), *Radar: Principles, Technology, Applications*, PTR Prentice Hall, Englewood Cliffs, New Jersey.

[42] Wehner, D.R., (1987), *High Resolution Radar*, Artech House, Inc., Norwood, MA.

[43] Mensa, D.L., (1991), *High Resolution Radar Cross-Section Imaging*, Artech House, Inc., Dedham, MA.

[44] Chen, C.C. and Andrews, H.C., "Multifrequency Imaging of Radar Turntable Data", *IEEE Transactions on Aerospace and Electronic Systems*, Vol. 16, January 1980, pp 15-22.

[45] Mensa, D. and Vaccaro, K., "Two-Dimensional RCS Image Focusing", *AMTA*, Ninth Annual Meeting and Symposium, Seattle, Washington, 28 September - 2 October 1987, pp.164-170.

[46] Ausherman, D.A., Kozma, A., Walker, J.L., Jones, H.M. and Poggio, E.C., "Developments in Radar Imaging", *IEEE Transactions on Aerospace and Electronic Systems*, Vol. 20, No. 4, July 1984, pp. 363-400.

[47] Scudder, H.J., "Introduction to Computer Aided Tomography", *Proceedings of the IEEE*, Vol. 66, No. 6, June 1978, pp. 628-637.

[48] Adams, M.F. and Anderson, A.P., "Synthetic Aperture Tomographic (SAT) Imaging for Microwave Diagnostics", *IEE Proceedings*, Vol. 129, Pt. H, No. 2, April 1982, pp. 83-88.

[49] Knaell, K.K. and Cardillo, G.P., "Radar Tomography for the Generation of Three-Dimensional Images", *IEE Proceedings on Radar, Sonar and Navigation*, Vol. 142, No. 2, April 1995, pp. 54-60.

[50] Munson, D.C., O'Brien, J.D. and Jenkins, W.K., "A Tomographic Formulation of Spotlight-Mode Synthetic Aperture Radar", *Proceedings of the IEEE*, Vol. 71, No. 8, August 1983, pp. 917-925.

[51] Mensa, D.L., Halevy, S. and Wade, G., "Coherent Doppler Tomography for Microwave Imaging", *Proceedings of the IEEE*, Vol. 71, No. 2, February 1983, pp. 254-261

[52] Li, H. and Lin, F., "Near-Field Imaging for Conducting Objects", *IEEE Transactions on Antennas and Propagation*, Vol. 39, No. 5, May 1991, pp. 600-605.

[53] Odendaal, J.W. and Joubert, J., "Radar Cross Section Measurements Using Near-Field Imaging", *IEEE Transactions on Instrumentation and Measurement*, Vol. 45, No. 6, December 1996, pp. 948-954.

[54] El Assad, S., Lakkis, I. and Saillard, J., "Holograhpic SAR Image Formation by Coherent Summation of Impulse Response Derivatives", *IEEE Transactions on Antennas and Propagation*, Vol. 41, No. 5, May 1993, pp. 620-624.

[55] Broquetas, A., DePorrata, R., Sagués, L., Fàbregas, X. and Jofre, L., "Circular Synthetic Aperture Radar (C-SAR) System for Ground-Based Applications", *Electronics Letters*, Vol. 33, No. 11, 22nd May 1997, pp. 988-989.

[56] Broquetas, A., Palau, J., Jofre, L. and Cardama, A., "Spherical Wave Near-Field Imaging and Radar Cross-Section Measurement", *IEEE Transactions on Antennas and Propagation*, Vol. 46, No. 5, May 1998, pp. 730-735.

[57] Fortuny, J., "An Efficient Three Dimensional Near Field ISAR Algorithm Using the Method of Stationary Phase", submitted to *IEEE Transactions on Aerospace and Electronic Systems*, May 1997.

[58] Voles, R., "Radar Target Imaging by Rotation about Two Axes", *Proceedings of the IEE*, Vol. 125, No. 10, October 1978, pp. 919-921.

[59] Joy, E.B., (1989), "Near-Field RCS Measurement Ranges", *Radar Reflectivity Measurements Techniques and Applications*, ed. N.C. Currie, Artech House, Inc., Norwood, MA.

[60] Fortuny, J. and Sieber, A.J., "Fast Algorithm for a Near-Field Synthetic Aperture Radar Processor", *IEEE Transactions on Antennas and Propagation*, Vol. 42, No. 10, October 1994, pp. 1458-1460.

[61] Goodman, J.W., (1968), *Introduction to Fourier Optics*, McGraw-Hill Book Company, New York.

[62] Bennett, J.C. and Morrison, K., "Development of a Ground-Based, Polarimetric Synthetic Aperture Radar", *IEEE Aerospace Applications Conference*, Aspen, Colorado, USA, 1996, Vol. 4, pp. 139-146.

[63] Yamani, A., (1984), *Depth of Field Improvements and Automatic Focusing in Long Wavelength Imaging Systems*, Ph.D. thesis, University of Sheffield, UK.

[64] Clarke, R.H. and Brown, J., (1980), *Diffraction Theory and Antennas*, Ellis Horwood Limited, Chichester.

[65] Jull, E.V., (1981), *Aperture Antennas and Diffraction Theory*, Institution of Electrical Engineers, London.

[66] Booker, H.G. and Clemmow, P.C., "The Concept of an Angular Spectrum of Plane Waves, and its Relation of that of Polar Diagram and Aperture Distribution", *IEE Proceedings* Vol. 97, Part III, 1950, pp. 11-17.

[67] Adams, M.F., (1982), *Synthetic Aperture Techniques for Diffraction Tomographic Imaging with Microwaves and Ultrasonics*, Ph.D. thesis, University of Sheffield, UK.

[68] Busse, L.J., "Three-Dimensional Imaging Using a Frequency-Domain Synthetic Aperture Focusing Technique", *IEEE Transactions on Ultrasonics, Ferroelectrics, and Frequency Control*, Vol. 39, No. 2, March 1992, pp. 174-179.

[69] Wang, J.J.H., "An Examination of the Theory and Practices of Planar Near-Field Measurements", *IEEE Transactions on Antennas and Propagation*, Vol. 36, No. 6, June 1988, pp. 746-753.

[70] Ylitalo, J.T. and Ermert, H., "Ultrasound Synthetic Aperture Imaging: Monostatic Approach", *IEEE Transactions of Ultrasonics, Ferroelectrics, and Frequency Control*, Vol. 41, No. 3, May 1994, pp. 333-339.

[71] Special Issue on Near-Field Scanning Techniques, *IEEE Transactions on Antennas and Propagation*, Vol. 36, No. 6., June 1988.

[72] Hecht, E., (1987), *Optics*, Addison-Wesley Publishing Company. Reading, Massachusetts.

[73] Yamani, A., (1981), *A Technique for Improving The Depth of Field in Ultrasonic Imaging Systems*, BSc thesis, University of Sheffield, UK.

[74] Brigham, E.O., (1988), *The Fast Fourier Transform and Its Applications*, Prentice-Hall International, Inc., Englewood Cliffs, N.J.

[75] Davis, J.C. and Sheffield, L., "Improved Validation of IER Results", *AMTA*, Nineteenth Meeting and Symposium, Boston, MA., 12-17 November 1997, pp. 346-351.

[76] Mensa, D.L. and Vaccaro, K., "Near-Field to Far-Field Transformation of RCS Data", *AMTA*, Seventeenth Meeting and Symposium, Williamsburg, Virginia, USA, 13-17 November 1995, pp. 155-161.

[77] Harris, F.J., "On the Use of Windows for Harmonic Analysis with the Discrete Fourier Transform", *Proceedings of the IEEE*, Vol. 66, No. 1, January 1978, pp. 51-83.

[78] Stankwitz, H.C., Dallaire, R.J. and Fienup, J.R., "Nonlinear Apodization for Sidelobe Control in SAR Imagery", *IEEE Transactions on Aerospace and Electronic Systems*, Vol. 31, No. 1, January 1995, pp. 267-278.

[79] Carrara, W.G., Goodman, R.S., and Majewski, R.M., (1995), *Spotlight Synthetic Aperture Radar Signal Processing Algorithms*, Artech House, Inc, Boston, Mass. Appendix D.

[80] Dezellem, R., Adams, J., Mensa, D. and Vaccaro, K., "Non-Linear Windowing for ISAR Images", *AMTA*, Sixteenth Annual Meeting and Symposium, Long Beach, California, 3-7 October 1994, pp. 320-325.

[81] Jung Ah, C.L. and Munson, D.C., "Effectiveness of Spatially-Variant Apodization", *Proceedings of the International Conference on Image Processing*, Washington, DC, 23-26 October 1995, pp. 147-150.

[82] Kingsley, S.P. and Quegan. S., (1992), *Understanding Radar Systems*, McGraw-Hill Book Company, Berkshire, UK.

[83] Wiesbeck, W. and Kähny, D., "Single Reference, Three Target Calibration and Error Correction for Monostatic Polarimetric Free Space Measurements", *IEEE Proceedings*, Vol. 79, No. 10, October 1991, pp. 1551-1558.

[84] Morrison, K. and Bennett, J.C., "Recent Developments in Ground-Based, Polarimetric Synthetic Aperture Radar Imaging at the University of Sheffield", *IEE Colloquium*, 1995, No. 239, pp. 8/1-8/4

[85] Joy, E.B. and Paris, D.T., "Spatial Sampling and Filtering in Near-Field Measurements", *IEEE Transactions on Antennas and Propagation*, Vol. 20, No. 3, May 1972, pp. 253-261.

[86] Kraus, J.D., (1988), *Antennas*, 2nd edition, McGraw-Hill, New York

[87] Humphries, C., Press, J. and Sutton, D., (1989), *The Hamlyn Guide to Trees of Britain and Europe*, Hamlyn, London.